Control of Electrical Systems Using Artificial Intelligence for More Electric Aircraft Applications

Habibu Hussaini (BEng., MSc.)

Thesis submitted to the University of Nottingham for the degree of Doctor of Philosophy

October 2023

Acknowledgements

I would like to start by expressing my deepest and most sincere gratitude to my supervisors, Dr Tao Yang and Professor Serhiy Bozhko for their immense and invaluable guidance and support throughout my PhD study. Also, I would like to acknowledge Dr Alan Watson, my internal assessor, for his review of my annual reports, critical assessment, and suggestions on different aspects of my research throughout this study. I would like to express my special thanks to Dr Lin Jiang for generously devoting his time to act as my thesis examiner and for offering valuable insights to improve the quality of the thesis.

I would also like to acknowledge my friends and colleagues at the Aerospace Technology Centre and Power Electronics and Machine Centre building including Dr Cheng Wang, Dr Yuan Gao, Dr Matias Urrutia-Ortiz, Dr Mohamed A. A. Mohamed, Ge Bai, Yiren Zhu, Shengyu Cao and others for the great discussions and exchange of ideas that made my research work interesting and exciting. Special thanks to Dr Cheng Wang for our many fruitful discussions and the great support he offered me throughout this research work.

I would like to sincerely acknowledge and appreciate the management of the Petroleum Technology Development Fund (PTDF), Nigeria, for their sponsorship of my PhD study. I would also like to thank the Federal University of Technology, Minna management staff for granting me a study fellowship for my PhD study.

I would like to sincerely thank my parents for their support throughout my education and for always encouraging me to aim for greater heights. Thanks also to my siblings for their emotional support and encouragement throughout this study.

Finally, I would like to sincerely appreciate and thank my wife, Amina, for her many sacrifices, motivation and emotional support which made my research work easier. Many thanks also to our daughter, Kawthar, for her beautiful distractions while working on my thesis.

Habibu Hussaini

Nottingham, United Kingdom, 2023.

Abstract

The increasing demand for fuel efficiency and environmental sustainability has driven the emergence of More Electric Aircraft (MEA) concepts, aiming to reduce weight, fuel consumption, environmental pollution, and operational costs. To achieve this, aircraft propulsion systems are transitioning towards electrical energy, resulting in a high demand for efficient power management and control. In this context, DC microgrids (MGs) have gained attention for power distribution in MEA due to their simplicity and the single-bus high voltage direct current (HVDC) electrical power system (EPS) architecture has been identified as a promising solution. Droop control is commonly employed in this architecture to achieve autonomous power management among power-generating sources without the need for a communication network. However, traditional droop control methods have limitations that require innovative and intelligent solutions. The primary goal of this thesis is to overcome the limitations of traditional droop control methods and enhance the power management, overall performance, and stability of the MEA EPS HVDC distribution network. To achieve this, the study focuses on the application of artificial intelligence (AI) techniques and introduces the following proposed approaches:

1. This thesis develops an advanced droop settings design strategy using AI-based optimisation with artificial neural networks (ANNs). This approach optimises droop coefficient settings offline, leveraging a trained ANN-based surrogate model to enhance voltage regulation and power sharing among power-generating sources.
2. A real-time tuning approach for droop control using reverse data training of an ANN-based surrogate model is presented. By directly predicting optimal droop gain settings based on specific performance requirements, the controller can adapt in real-time to reference changes, enhancing flexibility and responsiveness in dynamic conditions.
3. An innovative AI-based hierarchical control design strategy to address voltage deviations and improve overall voltage regulation under various operating conditions is proposed. The trained ANN-based surrogate model computes optimal droop and voltage compensation coefficients based on desired power-sharing ratios and bus voltage regulation requirements.

4. A new approach utilising two ANNs to address controller limitations in the presence of varying line resistance conditions is presented. One ANN optimises droop gain settings, while the second estimates real-time interconnecting cable resistances to compensate for terminal voltage deviations, leading to accurate current sharing and enhanced voltage regulation in DC MGs.

Extensive simulations and hardware-in-the-loop (HIL) experiments are conducted to validate the effectiveness and reliability of the AI-based approaches in improving droop control performance, offering promising prospects for enhancing the operation of MEA EPS.

Table of Contents

Chapter 1 Introduction 1

1.1 Background 1

1.1.1 Overview of the Conventional Aircraft Power System 2

1.1.2 Challenges with the Conventional Aircraft EPS 4

1.2 The More Electric Aircraft Concept 5

1.3 Challenges of MEA Electrical Power System Management 8

1.3.1 Load Power Sharing 10

1.3.2 DC Bus Voltage Control 11

1.4 Aims and Objectives 12

1.5 Proposed Approaches and Contributions 12

1.5.1 Optimal Droop Control Design Using ANN 13

1.5.2 Real-Time Tuning of Optimal Droop Gain Using ANN 13

1.5.3 Artificial Intelligence-Based Hierarchical Control Design 14

1.5.4 Real-time Line Resistance Identification with Artificial Intelligence 14

1.6 Thesis Outline 15

Chapter 2 Literature Review 17

2.1 Electrical Power System in the MEA 17

2.1.1 Evolution of Electrical Power Generation Systems in MEA 17

2.1.2 Overview of Power Distribution Architectures 29

2.1.3 Power Consumption and Electric Loads on Aircraft 34

2.1.4 Single Bus-based Multi-Generator Electrical Power System 35

2.2 Power Sharing Control Methods 43

2.2.1 Centralised control 44

2.2.2 Distributed control 46

2.2.3 Decentralised control 48
2.3 Artificial intelligence techniques in power electronics and control 54
2.3.1 Metaheuristic methods 55
2.3.2 Machine Learning 56
2.3.3 Artificial Neural Networks (ANN) 58
2.4 Summary 61
Chapter 3 Optimal Droop Control Design using ANN. 62
3.1 Introduction 62
3.2 System Description 65
3.3 Problem Formulation 67
3.3.1 Degradation of the DC Bus Voltage 68
3.3.2 Degradation in the Current Sharing Accuracy 69
3.4 Proposed ANN-based Droop Coefficient Design Approach 70
3.4.1 Methodology 71
3.4.2 ANN Structure and Training 72
3.5 Application of the Proposed Approach in the Droop Coefficient Design for the MEA EPS 73
3.5.1 Data generation 74
3.5.2 ANN-based Surrogate Model Development 76
3.5.3 Design Examples with Different Fitness Functions 77
3.6 Simulation Results 82
3.7 Summary 89
Chapter 4 Real-Time Tuning of Optimal Droop Gain Using ANN. 90
4.1 Introduction 90
4.2 System Description 94
4.3 Proposed Droop Gain Design Approach and Comparison with Conventional ANN Optimisation-Based Design 95

4.3.1 Procedure 96
4.3.2 ANN Structure and Training 98
4.4 Optimal Droop Gain Design for the MEA EPS 100
4.4.1 Data generation 100
4.4.2 Development of the Surrogate Models 102
4.4.3 Design Examples 104
4.4.4 Computational Burden 106
4.5 Simulation Results 108
4.5.1 Equal Power Sharing with Three Generators 108
4.5.2 Equal Power Sharing with Four Generators 110
4.6 Summary 114
Chapter 5 Artificial Intelligence-Based Hierarchical Control Design 115
5.1 Introduction 115
5.2 Proposed Bus Voltage Compensation 119
5.3 Proposed ANN-based Hierarchical Control Design Approach 122
5.3.1 Methodology 123
5.3.2 Design Consideration and Stability Concerns 125
5.3.3 Computational Burden 126
5.4 Design Examples and Validation Using Simulation 127
5.4.1 Design Examples 127
5.4.2 Simulation Results 128
5.5 Summary 136
Chapter 6 Real-time Line Resistance Identification with Artificial Intelligence 138
6.1 Introduction 138
6.2 Modified Droop Control Algorithm 141
6.3 Proposed Approach for Enhanced Droop Control 142
6.3.1 Rational for Using Artificial Intelligence (AI) 142

6.3.2 Proposed AI-Based Online Line Resistance Estimation 144
6.3.3 Implementation of the Proposed Online Line Resistance Estimation 154
6.4 Simulation Results 155
6.4.1 Cable Resistance identification 156
6.4.2 Equal Current Sharing 157
6.4.3 Performance Under Fault Condition 159
6.5 Summary 161
Chapter 7 Controller Hardware-In-the-Loop (C-HIL) Setup and validation 162
7.1 Hardware-in-the-loop (HIL) Experimental Setup 162
7.1.1 DSP Control card 164
7.1.2 Interface board 165
7.1.3 Embedded Coder Support Package for Texas Instruments C2000 Processors 166
7.1.4 HIL 604 device 169
7.2 HIL Experimental Results for Optimal Droop Control Design using ANN. 171
7.2.1 Validation of Optimal Droop Setting Design 171
7.2.2 Comparison with traditional droop coefficient 173
7.2.3 Load fluctuations 174
7.2.4 Fault condition 174
7.2.5 Robustness to DC-link Capacitance Parameter variations 176
7.2.6 Robustness to variation in line resistance and inductance 176
7.2.7 Performance evaluation under different converter ratings 178
7.3 HIL Experimental Results for Realtime Tuning of Optimal Droop Gain Settings . 179
7.3.1 HIL experimental validation of the offline computed optimal droop gain settings 180
7.3.2 Evaluation of Real-Time Implementation Performance 187
7.4 HIL Experimental Results for AI-Based Hierarchical Control Design. 191
7.4.1 Equal power sharing and bus voltage compensation 192

7.4.2 Unequal power sharing and bus voltage compensation 193
7.4.3 Traditional Droop Control Method 195
7.4.4 Fault Scenario 196
7.4.5 Parameter Uncertainty 197
7.4.6 Comparison with the method in [94] under Parameter Uncertainty 201
7.4.7 Analysis of the impact of variation between simulation and HIL parameters 203
7.5 HIL Experimental Real-time Line Resistance Identification Using AI 204
7.5.1 Validation of the Online Initial Line Resistance identification 204
7.5.2 Validation of the Accuracy of the Identification Model 205
7.5.3 Load Current Sharing 206
7.5.4 Fault Scenario 208
7.5.5 Comparison with Conventional Droop Control 209
7.6 Summary 210
Chapter 8 Conclusion and Future Work 211
8.1 Conclusion and Discussion 211
8.2 Future Work 213
Appendix A List of Publications 215
Appendix B Reference Frame Transformation 217
Appendix C Voltage Equations for Stator Windings of a Permanent Magnet Machine in the DQ Frame 218
References 221

List of Figures

Figure 1.1 The non-propulsive power system in the conventional large civilian aircraft 3

Figure 1.2 The non-propulsive power system in the More Electric Aircraft.....6

Figure 1.3 Single bus HVDC power distribution system architecture for the future MEA [35] 9

Figure 1.4 Schematic of a twin-spool, high-bypass turbofan engine connected to a single HVDC bus [43]. 11

Figure 2.1 Constant frequency constant speed using IDG. 19

Figure 2.2 VGSCF system with a power converter. 20

Figure 2.3 Variable speed variable frequency generation system. 21

Figure 2.4 AC generator with AC-DC converter. 22

Figure 2.5 Overall Architecture of the Starter-Generator System. 23

Figure 2.6 Diagram of the three-stage wound-field synchronous machine [70]. 24

Figure 2.7 Induction motor construction [74]. 25

Figure 2.8 Structure of stator and rotor of the switched reluctance machine [77]. 26

Figure 2.9 Structure of a permanent Magnet Machine [77]. 28

Figure 2.10 Power distribution system in conventional aircraft and B787 [15]. 30

Figure 2.11 Conventional B767 aircraft power distribution system [83]. 30

Figure 2.12 Electrical Power Distribution Architecture for MEA in the MOET Project [89].32

Figure 2.13 Flexible power distribution architecture with modular and identical PECs [89]. 32

Figure 2.14 Single bus electrical power distribution system [91]. 33

Figure 2.15 A single bus EPS architecture for future MEA applications. 35

Figure 2.16 Control block diagram of PMSM. 36

Figure 2.17 Current Controller Transfer Function 39

Figure 2.18 Two-level three-phase active front end (AFE) rectifier. 40

Figure 2.19 Model of a two-level active front-end (AFE) power converter in dq frame. 41

Figure 2.20 DC-link model 42

Figure 2.21 Load model combining constant impedance load (CIL) and constant power load (CPL) 43

Figure 2.22 Centralised control operating principle in DC EPS. 44

Figure 2.23 Control scheme of centralised control. 45

Figure 2.24 Control scheme of master-slave control. 46

Figure 2.25 Operating principles of distributed control in DC EPS. 47

Figure 2.26 Operating principles of decentralised control in DC MGs. 48

Figure 2.27 Droop characteristics (a) V-I droop (b) I-V droop. 50

Figure 2.28 Two-source single load DC MG 51

Figure 2.29 Trade-off between power sharing accuracy and voltage regulation. 52

Figure 2.30 Application of some AI methods in power electronic systems (PES) 54

Figure 2.31 Artificial neural network representation. 59

Figure 3.1 Typical Single bus Multi-source HVDC architecture for future MEA EPS. 65

Figure 3.2 Control diagram of the PMSG-AR system controlled using the voltage-mode droop control scheme. 66

Figure 3.3 Steady-state equivalent circuit model of a droop-controlled DC MG formed by two (PMSG-AR) systems and one resistive load. 67

Figure 3.4 Flowchart of the proposed ANN-based design of the droop coefficient in droop control of power converters. 72

Figure 3.5 Structure of the three-layer FFNN-based surrogate model. 73

Figure 3.6 Comparison between the 1,331 targeted data obtained from the detailed simulation model shown in Figure 3.2 and the predicted output of the trained ANN model shown in Figure 3.5. 76

Figure 3.7 Optimal droop coefficient setting for the fitness function in (3-12) (a) The plot of the integrated function *d* and position of its minimum value at 267,697. (b) Optimal droop coefficient settings that minimise *d* are indicated with a red dot. 80

Figure 3.8 Optimal droop coefficient setting for the fitness function (3-15) (a) The plot of the integrated function *e* and position of its minimum value at 409,704. (b) Optimal droop coefficient setting that minimizes e is indicated with a red dot. 82

Figure 3.9 Simulation results for current sharing and voltage regulation using the optimal droop coefficient from (a) the first design example and (b) the second design example. 83

Figure 3.10 Current sharing and bus voltage regulation using (a) Traditional fixed and identical droop gains. (b) Optimal droop gain settings from the first design example. 84

Figure 3.11 Simulation results for current sharing and bus voltage regulation using the optimal droop coefficient from the second design example under source fault conditions. 86

Figure 3.12 (a) Ramp load (b) Current sharing and bus voltage regulation using optimal droop gain settings from the first design example under a ramped load. 87

Figure 3.13 Summary of the optimal droop coefficient settings performance against different line resistance variations. 88

Figure 4.1 (a) Local PMSG-AR primary controller (b) MEA EPS HVDC grid 95

Figure 4.2 Flowchart of the comparison of the proposed design approach and conventional ANN optimisation-based design of the droop coefficient in droop control of power converters. 97

Figure 4.3 Schematics of the FFNN (a) Proposed design approach (b) Convectional ANN optimisation-based design [186]. 99

Figure 4.4 ANN model training profile for (a) Proposed design approach and (b) ANN optimisation-based design approach. 101

Figure 4.5 Comparison of the regression plot of the trained ANN showing the relationship between the targeted data (o) and the surrogate model prediction (blue line) for (a) Proposed design approach and (b) ANN optimisation-based design approach. 102

Figure 4.6 Simulation results of a comparison of the current sharing and bus voltage regulation performance using droop gain settings from the (a) Conventional ANN optimisation-based design and (b) Proposed design approach. 109

Figure 4.7 Simulation results for current sharing and bus voltage regulation using the proposed design approach for equal power sharing among four generators. 111

Figure 4.8 Block diagram of the proposed control strategy for the PMSG-ARi systems in the MEA EPS distribution network. 112

Figure 4.9 Step response: (a) Desired system response (ANN model's input) and computed optimal droop gain settings by ANN model (b) Current sharing and bus voltage regulation. 113

Figure 5.1 Single-bus HVDC distribution network utilised in the MEA EPS.....116

Figure 5.2 Proposed Hierarchical Control scheme for the MEA EPS DC grid. 119

Figure 5.3 Flowchart for the design of the droop and compensation coefficients using the ANN approach. 122

Figure 5.4 Case study setup 123

Figure 5.5 Schematic of the NN-based surrogate model. 124

Figure 5.6 Simulation results of the case study for load sharing and bus voltage regulation using Optimal control coefficient from (a) Design example 1 (b) Design example 2. 129

Figure 5.7 (a) ramp load (b) Simulation results of the case study for load sharing and bus voltage regulation using optimal control coefficient from design example 1. 130

Figure 5.8 Simulation results of the case study for load sharing and bus voltage regulation comparison between (a) Proposed method [212] (b) Approach presented in [94]. 132

Figure 5.9 Simulation results showing the plug-in and plug-out capability of the proposed approach. 134

Figure 5.10 Effect of variation in cable resistance on current sharing accuracy and bus voltage regulation of the proposed approach. 136

Figure 6.1 Flowchart diagram depicting the proposed methodology for online estimation of interconnecting cable resistances. 143

Figure 6.2 FFNN structure of the ANN1-based surrogate model. 146

Figure 6.3 Simulation results for current sharing and voltage regulation using (a) Traditional fixed and identical droop gains (shown in Table 6-1) (b) Optimal fixed droop gain settings obtained using the proposed approach. 147

Figure 6.4 Online estimations of the initial line resistances. 150

Figure 6.5 FFNN structure of the ANN2-based surrogate model. 152

Figure 6.6 Comparison between the simulation data and the surrogate model prediction. ...153

Figure 6.7 Proposed approach implementation on the studied MEA EPS HVDC architecture. 154

Figure 6.8 The results of interconnecting cable resistances identification 156

Figure 6.9 Output currents of the three PECs and the total load current using optimal droop gain settings and the proposed control algorithm under a variation in the initial line resistances. 157

Figure 6.10 Output voltages of the three PECs and the main bus voltage using optimal droop gain settings and the proposed control algorithm under a variation in the initial line. resistances. 158

Figure 6.11 Online estimation of the line resistances using the ANN2-based identification model.....158

Figure 6.12 Simulation results using the proposed control algorithm under fault condition (a) output currents of the three PECs and the total load current (b) output voltages of the three PECs and the main bus voltage.....160

Figure 7.1 (a) C-HIL experimental setup; (b) Simplified block diagram of the C-HIL setup. 163

Figure 7.2 Texas Instruments F28379D control card 164

Figure 7.3 HIL DSP 180 Interface board layout. 165

Figure 7.4 ADC module in Simulink. 166

Figure 7.5 HIL device output settings.....167

Figure 7.6 SVPWM Simulink implementation for code generation.....168

Figure 7.7 Model of the Inverter and PMSM implemented in Typhoon HIL schematic editor. 169

Figure 7.8 Externally controlled properties (a) Three-phase inverter (b) PMSM 170

Figure 7.9 HIL Experimental results for steady-state current sharing and bus voltage regulation using the optimal droop coefficient from (a) the first design example and (b) the second design example. 172

Figure 7.10 HIL experimental results for steady-state current sharing and bus voltage regulation using the conventional droop coefficient. 173

Figure 7.11 HIL experimental results for current sharing and bus voltage regulation using the optimal droop coefficient from the first design example under load variation conditions. ...175

Figure 7.12 HIL experimental results for current sharing and bus voltage regulation using the optimal droop coefficient from the second design example under source disconnection condition. 175

Figure 7.13 HIL experimental results for current sharing and bus voltage regulation using the optimal droop coefficient from the first design example. A response to a 20% reduction in C_b. 176

Figure 7.14 HIL experimental results for current sharing and bus voltage regulation to validate the robustness of the optimal droop coefficient settings to a (a) 50% decrease in the line resistance and inductance (b) 50% increase in line resistance and inductance.....178

Figure 7.15 HIL experimental results for unequal current sharing and bus voltage regulation. 179

Figure 7.16 Comparative performance assessment using optimal droop gain settings from the first design example. (a) ANN optimisation-based design [186] (b) Proposed design approach. 181

Figure 7.17 Comparative performance assessment under fault conditions using optimal droop gain settings from the first design example. (a) ANN optimisation-based design [186] (b) Proposed design approach.....182

Figure 7.18 Comparative performance assessment under line resistance variation using optimal droop gain settings from the first design example. (a) ANN optimisation-based design [186] (b) Proposed design approach. 183

Figure 7.19 Comparative performance assessment using different droop gain settings (a) Traditional identical fixed droop gain settings (b) Optimal droop gain settings for case 1...185

Figure 7.20 HIL experimental results demonstrating unequal current sharing and bus voltage regulation using the optimal droop gain settings from Case 2.....186

Figure 7.21 Block diagram of the proposed approach for the real-time tuning of the optimal droop gains.....187

Figure 7.22 Transient-state HIL experimental results under CPL = 40-kW. (a) ANN model references. (b) Computed optimal droop gain settings by the ANN model (c) Current sharing and bus voltage regulation. 189

Figure 7.23 Transient-state HIL experimental results under CPLs = 40-kW and 20-kW. (a) ANN model references. (b) Computed optimal droop gain settings by the ANN model (c) Current sharing and bus voltage regulation. 191

Figure 7.24 HIL experimental results for mixed load with equal current sharing and bus voltage regulation using the proposed approach (a) without bus voltage compensation (b) with bus voltage compensation.....193

Figure 7.25 HIL experimental results for mixed load with unequal current sharing and bus voltage regulation using the proposed approach (a) without bus voltage compensation (b) with bus voltage compensation. 195

Figure 7.26 HIL experimental results for power sharing and bus voltage regulation using the conventional droop control method. 196

Figure 7.27 HIL experimental results for fault scenario with equal current sharing and voltage regulation using the proposed approach. 197

Figure 7.28 HIL experimental results for load sharing and bus voltage compensation using the proposed control method, a response to (a) a 30% decrease in the cable parameters and (b) a 30% increase in the cable parameters. 198

Figure 7.29 HIL experimental results for load sharing and bus voltage compensation using the proposed control method, a response to (a) a 30% decrease in the dc-link capacitance and (b) a 30% increase in the dc-link capacitance. 199

Figure 7.30 HIL experimental results for current sharing and bus voltage compensation. The response to a +/- 30% variation is shown for both (a) the proposed method and (b) the method described in [94]. 200

Figure 7.31 Summary of the deviations in control performance resulting from the variations between the line resistances used in data generation and the HIL setup. 202

Figure 7.32 HIL experimental result of the online estimation of the initial line resistances. 204

Figure 7.33 Comparison between emulated line resistance and identification model estimation. 205

Figure 7.34 Percentage error in the estimation of the emulated line resistances. 206

Figure 7.35 HIL experimental result of load current sharing and bus voltage regulation while using the optimal droop gain settings and under the proposed control approach. 207

Figure 7.36 HIL experimental result of the online estimation of the line resistances by the identification model. 207

Figure 7.37 HIL experimental result of load current sharing and bus voltage regulation under a generator failure. 208

Figure 7.38 Experimental result of load current sharing and bus voltage regulation using the traditional fixed and identical droop gain. 209

List of Tables

Table 2-1 Recent Advances in Aircraft Power Generation Systems [21] 18

Table 2-2 Comparison of Various Control Principles 52

Table 3-1 Parameters of the system used as a case study in simulations and HIL experiments. 75

Table 3-2 Range and sampling step used in data generation. 75

Table 3-3 Range and sampling step used in optimisation.....77

Table 4-1 Fundamental differences between the proposed approach and the ANN optimisation-based design. 98

Table 4-2 Other design examples 105

Table 4-3 Comparison between the conventional droop gain design, conventional ANN optimisation-based design and proposed design approach for the design of three control variables, k_{d1}, k_{d2} and k_{d3}. 107

Table 5-1 Simulation Input Variables Ranges for Data Generation 124

Table 5-2 Comparison of branch current and transmission loss of the method in [94] and proposed control approach. 133

Table 6-1 Parameters of the system used as a case study in simulations and HIL experiments. 145

Table 6-2 Error in current sharing ratios and voltage deviation for different variations in line impedance. 148

Table 6-3 Design range based on initially estimated line resistance. 151

Table 6-4 Changes in the interconnecting cable resistances.....156

Table 7-1 Comparison of performance metrics. 173

Table 7-2 Comparison between proposed control strategy and different techniques for online line resistance identification. 209

List of Acronyms

AC	Alternating Current
ACO	Ant Colony Optimisation
ADC	Analog-to-Digital Converters
AEGART	Aircraft Electrical Starter-Generation System with Active Rectification Technology
AFE	Active Front End
AI	Artificial Intelligence
ANN	Artificial Neural Network
ANNs	Artificial Neural Networks
AO	Analog Outputs
APU	Auxiliary Power Unit
AR	Active Front-End Controlled Rectifier
ARM	Advanced RISC Machine
ARs	Active Rectifiers
BTB	Bus-Tie Breaker
C-HIL	Controller Hardware-In-the-Loop
CCL	Constant Current Loads
CCS	Code Composer Studio
CF	Constant Frequency

CIL	Constant Impedance Loads
CO2	Carbon Dioxide
CPL	Constant Power Loads
CPU	Central Processing Unit
CSD	Constant Speed Drive
DB	Dead-Band
DC	Direct Current
DCL	Digital Communication Links
DG	Distributed Generation
DI	Digital Inputs
DO	Digital Outputs
DSP	Digital Signal Processor
ECS	Environmental Control System
EHAs	Electro-Hydrostatic Actuators
EPS	Electrical Power System
ESS	Energy Storage System
ETOPS	Extended Range Twin-Engine Operations Performance
EU	European Union
EV	Electric Vehicle
FCS-MPC	Finite Control Set Model Predictive Control
FFNN	Feedforward Neural Network

FMI	Functional Mock-Up Interface
FMU	Functional Mock-up Unit
FNN	Fuzzy Neural Networks
FPGAs	Field Programmable Gate Arrays
FW	Flux Weakening
GA	Genetic Algorithm
GPD	General Piecewise Droop
HEV	Hybrid Electric Vehicle
HIL	Hardware-In-The-Loop
HP	High-Pressure
HPCs	High-Pressure Compressors
HPS	High-pressure shaft
HPT	High-pressure Turbine
HSEC	High-Speed Electrical Connector
HVDC	High-Voltage Direct Current
IDG	Integrated Drive Generator
IG	Induction Generators
IM	Induction Machines
IPSO	Improved Particle Swarm Optimisation
kVA	kilovolt-amperes
LC	Local Controller

LBC	Low Bandwidth Digital Communication
LP	Low-Pressure
LPC	Low-pressure Compressor
LPS	Low-pressure Shaft
LPT	Low-Pressure Turbine
MCPEC	Modular Cell Power Electronic Converter
MEA	More Electric Aircraft
MG	Microgrid
ML	Machine Learning
MMmt	Million Metric Tons
MOET	More Open Electrical Technologies
MOO	Multi-Objective Optimisation
MOOPs	Multi-Objective Optimisation Problems
MPPT	Maximum Power Point Tracking
MTDC	Multi-Terminal DC
NN	Neural network
NPC	Neutral Point Clamped
NSGA	Non-dominated sorted genetic algorithm
PC	Primary Control
PCC	Point of Common Coupling
PEC	Power Electronic Converter

PES	Power Electronic Systems
PI	Proportional-Integral
PM	Permanent Magnet
PMGs	Permanent Magnet Generators
PMMs	Permanent Magnet Machines
PMSGs	Permanent Magnet Synchronous Generator
PMSG-AR	Permanent Magnet Synchronous Generator-Active Front End Rectifier
PMSM	Permanent Magnet Synchronous Motor
POA	Power Optimised Aircraft
PSO	Particle Swarm Optimisation
PWM	Pulse Width Modulation
RAT	Ram Air Turbine
RISC	Reduced Instruction Set Computing
RL	Reinforcement learning
RLS	Recursive Least Squares
RMSE	Root Mean Square Error
RNN	Recurrent Neural Networks
RTS	Real-Time Simulator
RVM	Relevance Vector Machine
SC	Secondary Control
SCADA	Supervisory control and data acquisition

SG	Starter/Generator
SiC	Silicon Carbide
SNR	Signal-to-Noise Ratio
SO	Single Objective
SOC	State of Charge
SRM	Switched Reluctance Machines
SRSGs	Switched Reluctance Starter/Generators
SVM	Support Vector Machine
SVPWM	Space Vector PWM
TI	Texas Instrument
TIMES	Totally Integrated More Electric Systems
TRUs	Transformer Rectifier Units
UART	Universal Asynchronous Receiver-Transmitter
VF	Variable Frequency
VFGs	Variable Frequency Generators
VGSCF	Variable Speed Constant Frequency
VSCF	Variable-Speed Constant-Frequency
VSVF	Variable Speed Variable Frequency
WFSM	Wound Field Synchronous Machine
WBG	Wide Band Gap
WIPS	Wing Ice Protection System

List of Symbols

C_b	DC-link capacitance
C_i	Local DC-link capacitance
f_c	Switching frequency
i_d	d-axis current
i_q	q-axis current
i_c^{max}	Maximum phase current
i_{dc}	DC current before the capacitor
i_o	Load current after the capacitor
I_{dci}	Output current of the converter #i
I_L	Load current
k_c	Bus voltage compensation coefficient
k_{di}	Droop coefficients/gains of the converter #i
k_{di}^{opt}	Optimal droop coefficients/gains of the converter #i
k_{ic}	Integral gain of the current regulator
k_{pc}	Proportional gain of the current regulator
L_d	d-axis inductance
L_q	q-axis inductance
M	Maximum modulation index
m_d	d-axis modulation indices

m_q	q-axis modulation indices
n_i	Current sharing ratio between two AC-DC converters
P	Active power
P_{cpl}	Total power of the CPL
P_{res}	Total power of the resistive load
R_{ci}	Interconnecting Cable resistance of converter #i
R_{res}	Resistance of the resistive load
R_s	Stator resistance
T_d	Dead time of Converter #i
V_{bus}	Voltage of common DC bus
V_c	AC voltage
V_c^{max}	Maximum phase voltage amplitude at the fundamental frequency
v_d	d-axis stator voltage
v_q	q-axis stator voltage
V_{dci}	DC terminal voltage for converter #i
V_{dci}^*	Calculated voltage reference for converter #i
V_{dc}^*	Nominal voltage
ζ	Damping ratio
φ_m	Flux linkage of the permanent magnet
ω_e	Electrical rotor angular velocity
ω_n	Natural bandwidth

Chapter 1 Introduction

1.1 Background

The evolution of modern aircraft has been marked by numerous developmental changes since their inception over a hundred years ago [1]. These aircraft have revolutionised transportation, providing passengers with a convenient and safe means of travelling long distances in short periods, thanks to their exceptional speed compared to other modes of transportation. As a result, the aviation industry has experienced a significant surge in passenger travel, and it is projected that by 2030, approximately 27,000 new aircraft will take to the skies [2]. This exponential growth underscores the immense importance of the aircraft industry on a global scale. Not only does it facilitate the seamless movement of individuals across borders, but it also plays a vital role in stimulating economic growth and reducing unemployment rates in numerous countries.

However, despite the remarkable advantages associated with the aircraft industry, it is also recognised as one of the major contributors to greenhouse gas emissions, raising serious concerns about its environmental and climatic impacts. Currently, commercial aviation emits an estimated 186 million metric tons (MMmt) of carbon dioxide (CO_2), and this figure is projected to reach 209 MMmt by 2050 [3]. Furthermore, the aviation sector accounts for 13.9% of emissions within the transportation sector, positioning it as the second-largest contributor to transport emissions, following road transport [4]. Therefore, the pursuit of enhanced energy efficiency, reduced emissions (CO_2 and NO_x), and minimised noise from aircraft has become imperative to mitigate the threats to quality of life. To ensure a sustainable future, the aircraft industry must strive to develop energy-efficient and environmentally friendly air transportation while also working towards reducing operational costs [5]. Failure to address these challenges could result in sanctions, leading to increased airfares and decreased competitiveness within the industry. Additionally, achieving lower emissions, noise levels, and overall operational costs necessitates a re-evaluation of aircraft development and design.

To overcome these challenges, the aircraft industry has directed its attention towards the development of technologies that promote more efficient and greener solutions. One notable

advancement is the shift towards more electric aircraft (MEA) driven by progress in power electronics, electrical machines, and drives [6, 7, 8, 9]. MEA represents a significant breakthrough in addressing environmental and climatic concerns within the aircraft industry [10]. To achieve significant efficiency gains, various aspects of the aircraft need to be optimised, including power generation, distribution, onboard energy management, utilisation, aerodynamics, and weight considerations [11, 12]. These optimisations are important for advancing the industry's objectives and aligning it with the principles of sustainability.

1.1.1 Overview of the Conventional Aircraft Power System

To comprehend the advantages associated with the transition to MEA, it is important to first provide an overview of conventional aircraft electrical power systems (EPS). These systems encompass both primary and secondary power sources, each playing a distinct role in the aircraft's operation and functionality. This section aims to shed light on conventional power systems before delving into the advancements of MEA.

Conventional aircraft primarily rely on gas turbine engines as their primary power source. These engines generate the necessary propulsion and supply most of the aircraft's power needs. However, alongside the primary source, there exist secondary power sources that contribute to various systems and passenger comfort. These secondary sources encompass pneumatic, hydraulic, mechanical, and electrical power systems, all derived from the primary power source, as shown in Figure 1.1. Collectively, these secondary sources account for approximately 5% of the total fuel consumption during flight operations. The secondary power sources are vital for ensuring the aircraft's safe operation and enhancing passenger comfort [13], [12]. They support a range of critical functions and systems within the aircraft, contributing to its overall performance and reliability. However, it is important to note that jet fuel remains the primary power source used for aircraft take-off and propulsion.

Pneumatic power, also known as "Bleed air", is derived from aircraft engines. This form of power is primarily utilised for the operation of the Environmental Control System (ECS), air-conditioning, cabin pressurisation, engine start-up, and the Wing Ice Protection System (WIPS) [14], [15]. In particular, the "Bleed air" provides hot air for wing de-icing, with the WIPS system functioning in either Anti-Icing or De-icing mode. However, the pneumatic power system finds it difficult to detect leaks and has low efficiency. The low efficiency is more

noticeable in the bleeding compressors and cabin pressurisation [6]. The low-efficiency results in increased fuel consumption [16]. Furthermore, the traditional pneumatic power system tends to extract more power than required, which results in unutilised energy being dumped overboard the aircraft [15].

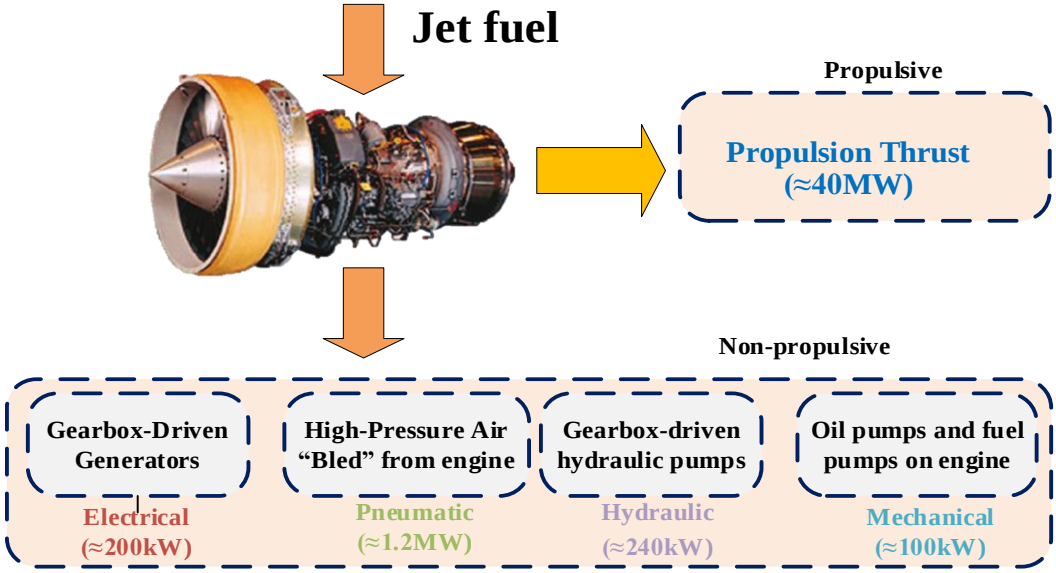


Figure 1.1 The non-propulsive power system in the conventional large civilian aircraft

Mechanical power, on the other hand, is obtained by extracting energy from a shaft driven by the aircraft engine. This mechanical power is then distributed throughout the aircraft via an accessory gearbox. It serves as the driving force for various subsystems, such as central hydraulic pumps, fuel pumps, engines, and other mechanically driven components. Nevertheless, the accessory gearbox from which it is generated is heavy and complex, expensive to maintain, and it must be completely replaced if any component becomes faulty. Besides, the accessory gearbox is an essential medium for the transmission of power for electrical and hydraulic systems. To minimise bearing friction in the gearbox, additional oil pumps are used to facilitate the circulation of oil through the rotating bearings within the mechanical system [17].

Hydraulic power is generated through the operation of hydraulic pumps driven by the accessory gearbox. This power is essential for both primary and secondary flight control actuation, utility actuation, and landing gears. The central hydraulic pump distributes hydraulic power to the actuation systems, ensuring precise control and movement of various aircraft components. The

hydraulic system is known to have high power density and robustness; however, its main drawback is related to the transmission pipes that connect to loads. The pipes are usually inflexible, heavy, and prone to leaks. In addition, the pipes are very long (from the engine to the aft of the aircraft). Furthermore, the hydraulic systems have no leakage detection mechanism in place, and this makes it difficult to maintain [6].

Electrical power, another vital power source, is generated by electrical machines connected to the accessory gearbox. The electrical power system is responsible for generating, controlling, and distributing power for avionic systems, in-flight entertainment, flight-deck displays, and commercial loads, including galleys, cabin electronics, lighting, avionics, utility actuators, and flight control equipment onboard the aircraft. While the aircraft is on the ground, power is supplied by an auxiliary power unit (APU) generator located at the aft of the aircraft. In emergencies or in the event of an engine failure, a ram air turbine (RAT) is utilized to provide power. It is worth noting that electrical power represents a relatively small percentage of the total power in conventional aircraft as shown in Figure 1.1.

1.1.2 Challenges with the Conventional Aircraft EPS

To understand the potential advantages and driving factors behind the development of more efficient and environmentally friendly electrical power systems in aircraft, it is essential to examine the limitations inherent in conventional power systems. Conventional power systems, while effective in enabling aircraft functionality, face certain challenges that require attention. These challenges include issues related to energy efficiency, environmental impact, and overall system performance. In terms of energy efficiency, conventional power systems often exhibit inefficiencies due to the presence of multiple power sources and complex distribution networks. The utilisation of pneumatic, mechanical, hydraulic, and electrical power sources, each with its energy conversion processes, can result in suboptimal energy utilisation and unnecessary fuel consumption [16]. Consequently, there is a growing need to develop power systems that maximise energy efficiency and minimise waste. Also, the combustion of jet fuel in gas turbine engines releases carbon dioxide (CO_2) and other pollutants into the atmosphere, contributing to climate change and air pollution. As concerns about environmental sustainability grow, there is an urgent demand for more environmentally friendly power systems that reduce emissions and minimise the industry's ecological footprint [18]. Furthermore, conventional power systems may encounter limitations in terms of overall system

performance and reliability. The complex interdependencies between different power sources and subsystems can introduce potential points of failure and reduce overall system robustness. Moreover, it becomes difficult to find and correct faults in time, thus reducing the system's reliability and increasing its downtime. Addressing these limitations requires innovative approaches to power generation, distribution, and system integration.

Based on the limitations of conventional power systems, it has become apparent to develop more efficient, sustainable, and reliable electrical power systems in aircraft. The subsequent sections will delve into the advancements and potential solutions offered by MEA technologies, which aim to overcome these limitations and pave the way for a greener and more efficient future of air transportation.

1.2 The More Electric Aircraft Concept

The fundamental principle behind the MEA concept is the replacement of traditional non-electric systems with electrical alternatives, thereby minimising the reliance on hydraulic, pneumatic, and mechanical power sources [8]. MEA aims to take advantage of the advancements in power electronics, electrical machines, and drives to create a more integrated and electrically driven aircraft system [10]. At the core of the MEA concept is the notion of electrical power as the primary source for various aircraft functions and operations. By transitioning from mechanical and hydraulic power to electrical power, several benefits can be achieved. Firstly, electrical power systems are inherently more efficient, offering higher power density and improved energy utilisation compared to their conventional counterparts. This increased efficiency translates into reduced fuel consumption, lower emissions, and enhanced overall energy management [9]. Furthermore, the electrification of aircraft systems allows for more accurate control and modulation of power delivery, resulting in improved system responsiveness, reliability, and fault tolerance. Electric systems also offer greater flexibility in terms of power distribution, enabling optimised power routing and the elimination of bulky and complex mechanical components [16]. This reduction in weight and complexity can contribute to lower maintenance requirements, reduced system complexity, and improved overall aircraft performance [9].

The MEA concept encompasses various aspects of aircraft systems, including propulsion, environmental control, flight control, and auxiliary functions. For instance, electric propulsion

systems, such as electric motors or hybrid-electric configurations, hold the potential for enhanced propulsion efficiency and reduced emissions [19]. Electrically driven ECS can provide more accurate and efficient cabin temperature control, reducing the energy consumption associated with cabin pressurisation and air conditioning [9], [20]. Flight control systems, including primary and secondary flight control surfaces, can also benefit from electrical actuation, offering increased reliability, reduced weight, and improved manoeuvrability. Additionally, auxiliary functions like lighting, in-flight entertainment, and avionics can be powered by electrical systems as shown in Figure 1.2, providing greater flexibility, reliability, and improved passenger comfort [21], [22].

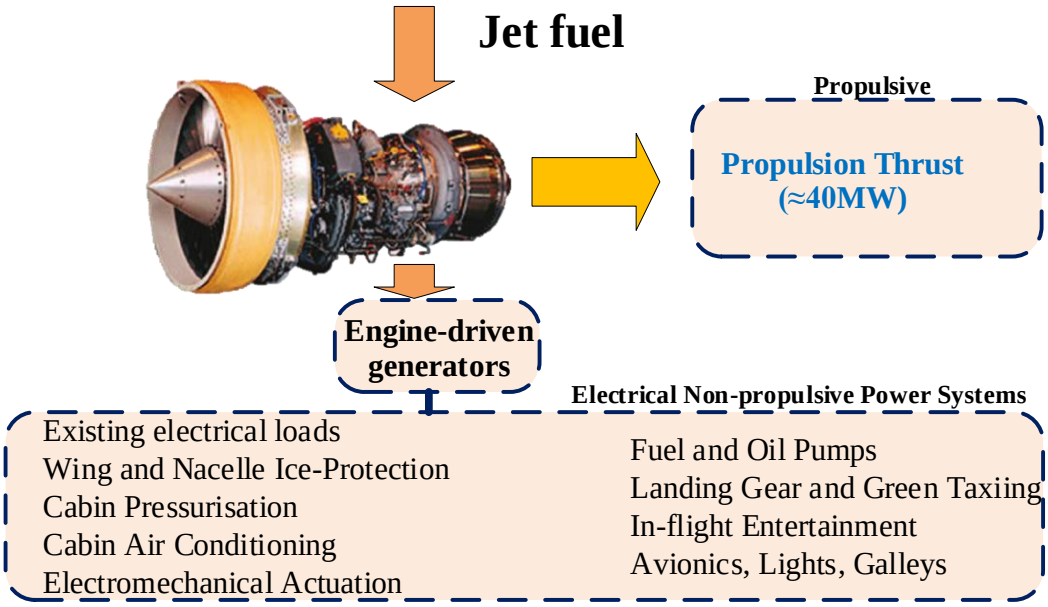


Figure 1.2 The non-propulsive power system in the More Electric Aircraft

The concept of MEA has a long history [13], with renewed interest in the 1990s due to advancements in power electronics technology [23]. Various research projects, such as Power Optimised Aircraft (POA) [24], Totally Integrated More Electric Systems (TIMES) [11], More Open Electrical Technologies (MOET) [23], and Cleansky initiatives [14], are driving innovation and pushing the boundaries of technology to create more energy-efficient, environmentally friendly, and economically viable aircraft. The POA project focuses on maximising the overall efficiency of aircraft systems through the integration of advanced electrical components, subsystems, and optimised power management techniques [24]. On the other hand, the TIMES project aims to develop fully integrated and intelligent electrical

systems, ensuring seamless communication and coordination among various aircraft components [25]. The MOET project set out to explore open-architecture electrical systems, allowing for greater flexibility, adaptability, and standardisation across the aircraft industry [21]. Meanwhile, the Cleansky initiative targets significant reductions in emissions and noise, promoting environmentally friendly aviation through the development of greener aircraft technologies [26]. The Cleansky 2 project represents a continuation of efforts to further enhance the performance and efficiency of aircraft systems, with a particular emphasis on sustainability and eco-friendly solutions [27]. Through these research and development efforts, the aviation industry is at the forefront of realizing the MEA vision, pushing the boundaries of technology and innovation to create aircraft that are more energy-efficient, environmentally friendly, and economically viable.

Commercial aircraft like the Airbus A380 and Boeing 787 (B787) serve as successful examples of MEA implementation [9]. They utilise electricity to power critical services and systems on board, resulting in improved efficiency and reduced fuel consumption. For instance, in the B787, electricity is predominantly employed to power services such as ECS, wing de-icing, cabin pressurisation, and even backup wing actuators [13]. Similarly, the Airbus A380 relies heavily on electricity to drive critical components such as flight-control actuators. To facilitate these advancements, both aircraft models have transitioned from conventional power generation systems that utilised integrated drive generators (IDGs) to more efficient variable frequency generators (VFGs) [15]. The integration of VFGs directly coupled to the engines has proven to be a significant step forward in enhancing power generation capabilities in these aircraft. One notable aspect of the B787 is its electrically powered cabin pressurisation system, which is a departure from traditional pneumatic systems. This shift to electric power contributes to the B787's impressive fuel-saving potential, estimated to be around 3% during cruise conditions [15]. The adoption of a no-bleed electrical system architecture in the B787 enables the aircraft to reduce fuel consumption while maintaining optimal performance levels. Furthermore, the B787 benefits from its construction using lightweight composite materials. These advanced materials offer significant weight reduction compared to conventional aircraft construction methods, enhancing overall fuel efficiency [15]. In addition, the engines of the B787 have been meticulously designed to minimise fuel consumption and maximise thrust power, further contributing to the aircraft's improved efficiency [15]. The successful

integration of MEA concepts in these commercial aircraft paves the way for further advancements and sets a benchmark for future aircraft development.

While the MEA concept offers numerous advantages, it also presents challenges that need to be addressed, including power management, power density, energy storage, thermal management, electromagnetic compatibility, and safety and reliability issues [6]. This thesis will focus on the challenges in the MEA EPS in terms of power management.

1.3 Challenges of MEA Electrical Power System Management

The implementation of MEA places greater demands on the aircraft EPS, including power generation, fault tolerance, power management, reliability and stability of both DC and AC power systems. These challenges necessitate innovations in power generation, distribution, processing, and management systems. The design of the aircraft EPS faces increasing complexities due to the growing number of power electronic loads. Architecture paradigms are being studied to address these challenges, with a focus on high-voltage DC (HVDC) networks that offer mass reduction and improved performance [28]. The use of HVDC networks allows for optimised coupling between generators and loads, regenerative load acceptance, and compliance with AC quality standards [29]. Furthermore, studies carried out under the MOET European Union (EU) project highlight the interest in HVDC architecture for MEA and prove the efficiency and controllability of the 270 V HVDC network [30, 31]. The evolution of power generation, distribution, and utilisation systems will be discussed in further detail in Chapter 2.

The choice of the HVDC system for the MEA EPS architecture is due to its several advantages when compared to the classical AC network system. The following are some of the advantages of the HVDC network [32, 33].

- ✓ MEA requires efficient power distribution and management systems to handle the growing demand for electrical power. Traditional AC power distribution systems are limited in their ability to manage power optimally and flexibly. DC MGs offer advantages in terms of higher power quality, lower losses, and improved control over power distribution, making them suitable for MEA applications.
- ✓ Power conversion efficiency plays a critical role in MEA, as it directly affects overall energy consumption and system performance. Conventional AC power systems involve multiple stages of power conversion, leading to increased power losses. DC MGs, on

the other hand, enable direct conversion of power from the source to the load, minimising conversion stages and improving overall efficiency.

- ✓ Aircraft have stringent weight and space limitations, making it challenging to accommodate additional power systems and components. AC power systems require bulky and heavy transformers and multiple conversion stages, adding to the overall weight and size. DC MGs offer a compact and lightweight solution, reducing the impact on weight and space constraints in MEA.
- ✓ MEA power systems should be flexible and scalable to accommodate changing power demands, system upgrades, and future advancements. DC MGs offer inherent flexibility, allowing for the integration of various power sources, and energy storage systems, and the easy addition or removal of loads. This scalability enables MEA to adapt to evolving power requirements and technological advancements.

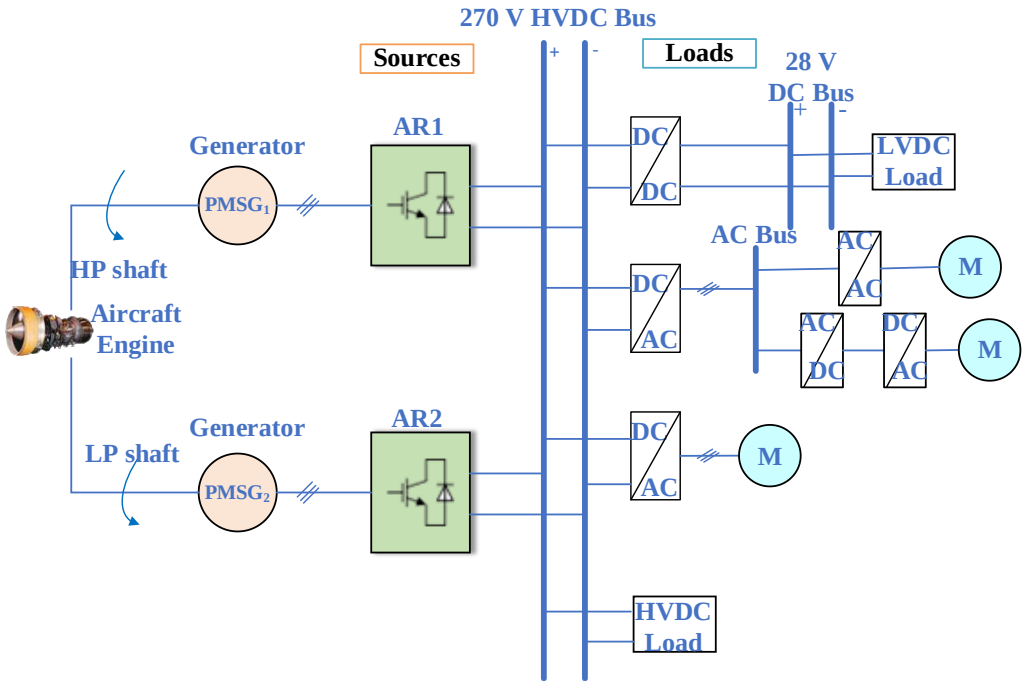


Figure 1.3 Single bus HVDC power distribution system architecture for the future MEA [35]

HVDC distribution systems have been widely adopted in various applications [34], leading to the proposal of different architectures such as single-bus, multi-bus, and ring-bus configurations [32]. Among these, the "single bus" architecture stands out due to its simplicity and is considered a promising candidate for future MEA. In this architecture, twin engine-

driven generators supply electrical power to the single DC bus through active rectifiers (ARs) as shown in Figure 1.3.

When multiple sources are connected in parallel as shown in Figure 1.3, it helps to enhance the redundancy and availability of the power system [36], [36], [37]. As shown in Figure 1.3, the converters are essential elements connecting electrical sources and loads. In such an EPS, the parallel-connected sources should operate in a coordinated way to regulate the DC bus voltage and share the electrical loads' current demand in proportion to their power ratings. Accurate sharing of the load power demand among the multiple sources is critical to prevent some of the sources from being overloaded and thermally stressed [37]. The control of these converters interfacing sources to the MG is a key issue in the MG's operation [38, 39], especially concerning the sharing of the load power demand among the sources and bus voltage regulation [40].

These issues can be summarised as [41]:

- proportional power sharing control among the multiple parallel-connected sources
- robust DC bus voltage control and maintaining power quality.

These issues will be further explored and discussed in the upcoming subsection, highlighting their significance in the context of MEA implementation.

1.3.1 Load Power Sharing

In a twin-shaft engine configuration, the low-pressure turbine (LPT) drives the fan and low-pressure compressor (LPC) through the LP shaft (LPS), while the high-pressure turbine (HPT) drives the axial and radial high-pressure compressors (HPCs) through the HP shaft (HPS). This arrangement is depicted in Figure 1.4. Traditionally, an electrical generator is connected to the gearbox associated with the HPS of the engine [7]. This is preferred due to the favourable characteristics of the HPS, such as high and relatively constant speed, which allows for smaller and lighter generators [42]. However, extracting a significant amount of power from the HPS can negatively impact the overall engine performance [43]. An alternative approach is to utilise the LPS as an additional power source by employing it to drive an additional electrical generator. This involves connecting the engine to dual generators, one through the LPS and the other through the HPS [44]. In a multi-source multi-load power system, ensuring appropriate

load power sharing becomes paramount and optimising the performance of both the engine and the HVDC grid. Achieving an optimal balance of power distribution among the various loads is essential in maximising efficiency and maintaining system stability [28]. Further details on the load-sharing methods will be provided in Chapter 2.

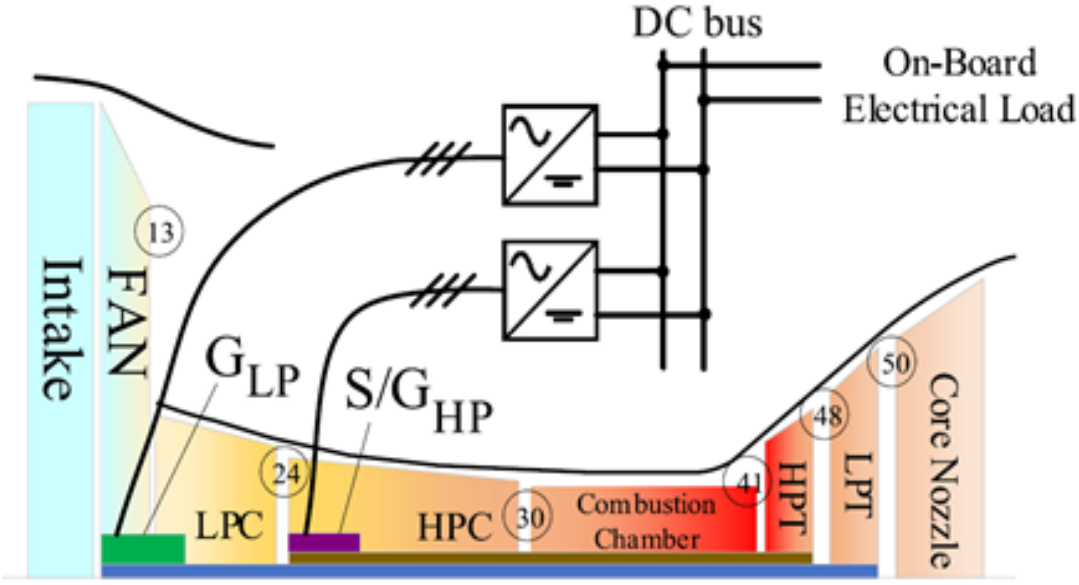


Figure 1.4 Schematic of a twin-spool, high-bypass turbofan engine connected to a single HVDC bus [43].

1.3.2 DC Bus Voltage Control

In a single-source-based system, there is only one source responsible for regulating the bus voltage. However, in systems with multiple sources and converters operating in parallel, at least one converter must regulate the DC bus voltage, while the others can operate in active power control mode. After an outage occurs in one or more converters, the remaining converters should share the resulting power deficit in an appropriate proportion [45]. To achieve this, it is beneficial for all converters to operate in the DC link voltage control mode, rather than strictly following their active power references. This highlights the need for cooperative voltage control among all power sources [28].

1.4 Aims and Objectives

The main aim of this research is to enhance power management and control in the MEA EPS HVDC distribution network by overcoming the limitations of the traditional droop control method through the application of artificial intelligence (AI) techniques.

The research objectives are as follows:

1. To develop an optimal droop control design strategy, utilising an artificial neural network (ANN) optimisation-based method, to overcome the limitations of traditional droop control affected by mismatched cable parameters, and enhance power management in the MEA HVDC distribution network.
2. To propose a new approach utilising an ANN for real-time tuning of the droop gain parameters in a hardware control platform, enabling dynamic and efficient control of the MEA HVDC distribution network.
3. To design and develop an AI-based hierarchical control strategy for the MEA DC MG that optimises voltage regulation and power-sharing under various operating conditions, incorporating droop and bus voltage compensation coefficients for power sharing and bus voltage restoration while addressing the trade-off between current-sharing accuracy and bus voltage regulation in traditional droop control methods.
4. To investigate the impact of line resistance variation on control performance and develop an AI-based approach using ANN models to optimise droop gain settings and estimate real-time interconnecting cable resistances for compensation.
5. To validate the proposed methodologies through extensive simulations and experiments using advanced power system simulation tools and hardware-in-the-loop (HIL) setups.

The research primarily focuses on aircraft onboard power systems, akin to islanding DC MGs, but the study's findings and analysis can be extended to other DC MGs like marine power systems, and the methodologies can also be applied to terrestrial DC MGs or shipboard DC power systems.

1.5 Proposed Approaches and Contributions

This research is dedicated to enhancing the droop control performance in the MEA DC MG by introducing optimal droop control design using AI techniques, enabling real-time tuning of

droop gain parameters, implementing hierarchical control design for improved voltage regulation, and utilising AI for accurate current sharing and enhanced voltage regulation by identifying real-time line resistance. The primary objective is to improve the stability and efficiency of transient and steady-state operations in the MEA DC MG, leading to more effective power management and control in the aircraft's EPS.

1.5.1 Optimal Droop Control Design Using ANN

Proposal of an alternative solution using ANN-based optimisation for offline design and selection of optimal droop gain settings for power converters in DC MGs (Chapter 3). This approach effectively improves droop control performance without adding computational burden on the EPS or elongating the design process. It leverages a trained ANN-based surrogate model to evaluate a user-defined fitness function and obtain optimal droop coefficient settings, offering more robust and practical designs for various MG scenarios compared to existing model-based approaches. The method also avoids the risk of local optima observed in other intelligent optimisation techniques and directly provides optimal designs for any additional sub-design space without the need for further data collection and training. Extensive simulations and HIL experiments have been conducted to validate the effectiveness of this proposed approach.

1.5.2 Real-Time Tuning of Optimal Droop Gain Using ANN

The heuristic methods and ANN optimisation-based design have some drawbacks which are undesirable in a practical implementation. The heuristic optimisation techniques require time-consuming simulation or experimental results for specific design points, while ANN optimisation-based design involves processing large datasets to find the best droop gain settings. To overcome these challenges, this thesis presents a quicker and real-time method enabling real-time tuning of droop gain parameters in a hardware control platform (Chapter 4). The proposed approach utilises reverse data training of an ANN, allowing direct determination of the optimal droop gain settings based on the power sharing ratio and bus voltage regulation references. This contribution facilitates automatic updates of droop gains in local controllers, ensuring quick adaptation to reference changes and achieving the desired control performance. A detailed comparison between the proposed approach and the ANN optimisation-based design has been performed, which shows the simplicity, flexibility, and low computational burden of

the proposed design approach. Comprehensive simulation and HIL experimental results further validate the effectiveness and practical applicability of this approach.

1.5.3 Artificial Intelligence-Based Hierarchical Control Design

The limitations of droop control cannot be fully overcome by simply adjusting the droop gains. Therefore, a new AI-based design strategy is proposed to address these drawbacks through a hierarchical control design (Chapter 5). This approach incorporates both the primary droop control and a secondary control method. In the proposed design strategy, a methodology is developed using an ANN to compute the optimal settings of the droop and bus voltage compensation coefficients based on desired power sharing and bus voltage regulation. The proposed strategy aims to achieve both bus voltage compensation and improved load sharing simultaneously, avoiding the shortcomings of conventional secondary control methods with high droop gains that may compromise robustness and reliability in case of source faults or secondary control failure.

1.5.4 Real-time Line Resistance Identification with Artificial Intelligence

The unknown and varying interconnecting cable resistance in low-voltage DC MGs, impacts the effectiveness of conventional droop control methods. Therefore, this thesis presents an AI-based line resistance identification techniques, utilising advanced data-driven algorithms, particularly neural networks (Chapter 6). The approach leverages optimal droop gain settings to determine initial line resistance values and creates an identification model based on ANN using generated data. This model establishes a mapping between current sharing ratios and line resistances within a predefined design range. As a result, during EPS operation, the ANN-based identification model can accurately identify new line resistance values, allowing real-time adjustment of converter voltage references to achieve accurate current sharing and improved voltage regulation. The proposed method offers high estimation accuracy without compromising system stability or adding computational complexity. Additionally, it reduces the need for extra sensors, as the only required parameter for measurement is the output current of the converter used for normal control and operation of the EPS. This contribution enables more effective and reliable optimal droop control performance in low-voltage DC MGs.

1.6 Thesis Outline

Chapter 2 provides a comprehensive literature review covering various aspects of the electrical power system in a MEA. It discusses the power generation and distribution systems, as well as the electrical starter/generator system and potential electrical machine candidates. The chapter also presents models for individual components, such as permanent magnet synchronous generators (PMSGs) and AC-DC converters. The paralleling of generation channels and load-sharing methods are explored, along with a detailed examination of the limitations of droop control in DC MGs and the proposed solutions found in the literature. Furthermore, the review explores different AI techniques applied in power electronics and control, with a particular focus on their applications for enhancing power management.

Chapter 3 (based on publication J1) introduces the methodology for designing optimal droop control using an ANN-based surrogate model. The chapter outlines the process of optimisation design based on ANNs and formulates the droop control optimisation problem. It introduces ANNs and their training algorithms. It demonstrates how the surrogate model is implemented to determine the optimal droop gains and compares the accuracy of the created ANN surrogate with simulation and HIL experimental results. The chapter also presents simulation results to evaluate the performance of the proposed droop control design and compares it with traditional droop control methods.

Chapter 4 (based on publications J2 and C3) presents a new approach for real-time tuning of droop gain parameters by exploring reverse data training of ANNs. The chapter discusses the integration of the ANN model into the hardware control platform. Additionally, a comprehensive comparison between the proposed design strategy and ANN optimisation-based design (presented in Chapter 2) is provided. The chapter includes simulation validation and analysis to evaluate the effectiveness and efficiency of the real-time tuning approach.

Chapter 5 (based on publications J3) introduces a methodology for hierarchical control design using ANNs. The chapter explores the concept of hierarchical control and its significance in the context of the MEA DC MG. It formulates the computation of optimal droop and bus voltage compensation coefficients to enhance power sharing and bus voltage restoration. The chapter provides simulation results, highlighting the improved power sharing and bus voltage restoration achieved through the proposed hierarchical control design.

Chapter 6 (based on publications J4, C2, and C5) focuses on addressing the issue of line resistance variation in the MEA DC MG and its impact on control performance. The chapter presents a new approach utilising two ANNs models to tackle the challenges associated with accurate current sharing and voltage regulation in DC MGs. It discusses the training and implementation of ANN models to achieve accurate current sharing and voltage regulation. The effectiveness of the proposed approach is evaluated through simulation studies under various line resistance scenarios.

Chapter 7 (based on publications J1, J2, J3, and J4) focuses on the HIL experimental validation of the theoretical and simulation results presented in the previous chapters. It provides a detailed explanation of the hardware-in-the-loop (HIL) setup used for the experiments. The chapter presents the HIL experimental results, which serve to corroborate and reinforce the analytical and simulation findings discussed in earlier chapters.

Chapter 8 presents a summary of the research findings and their implications. It reflects on the achieved research objectives and highlights the contributions of the study. The chapter also discusses potential future research directions.

Chapter 2 Literature Review

This chapter presents a thorough overview of aircraft electrical power systems, encompassing power generation, distribution, and utilisation. It examines various power generation options and compares electric machines used in starter/generator applications. The review includes control strategies for the DC power system and methods for power sharing among parallel generation sources. Additionally, the chapter discusses the application of AI in power electronics systems.

2.1 Electrical Power System in the MEA

Recent years have seen substantial advancements and transformations in the electrical power system of MEA. This section presents a comprehensive overview of the MEA electrical power system, encompassing its components, power generation, and distribution.

2.1.1 Evolution of Electrical Power Generation Systems in MEA

The power generation systems have witnessed significant developments to meet the increasing demand for electrical power on board. Historically, aircraft power generation began with the use of DC generators, driven by aircraft engines and equipped with electromagnets for power generation. The DC power generated was distributed through a commutator, and the voltage level was maintained with the support of onboard batteries [46]. However, to address the need for higher speeds, reduced aircraft size, and increased electrical power requirements, a shift from DC to AC power generation occurred in the 1960s. AC power generation offered advantages such as improved power density, reliability, and the ability to operate at higher voltages [47], [48]. The standard voltage and frequency adopted since then, and still in use today, is 115/200 V at 400 Hz, as set by the United States Air Force in 1959 [49].

In commercial aircraft, each engine typically drives one electrical generator for power generation. In some cases, there may be multiple generators connected to each engine, serving as backups to ensure redundancy and compliance with operational standards like extended range twin-engine operations performance (ETOPS) [50], [51]. Additionally, an auxiliary power unit (APU), which is a small gas turbine-driven generator, serves as an additional power

source. The APU provides power while the aircraft is on the ground and can act as an emergency power source during flight [52]. Batteries are also present on the aircraft to start the APU and provide backup power for critical cockpit equipment and essential functions like emergency lighting [53], [54].

Over time, the AC power generation system in aircraft has evolved to adapt to technological advancements in areas such as power generation efficiency and address specific challenges. Initially, constant frequency (CF) systems with fixed-frequency integrated drive generators (IDGs) were used. These generators were mechanically coupled to the engine, maintaining a constant mechanical speed and electrical frequency on the aircraft's electric bus [55]. In the 1990s, variable frequency (VF) generation systems were introduced to simplify the mechanical gearbox and provide more flexibility. Aircraft like the A380 and A350 adopted variable-frequency generators with a doubled voltage standard of 230/400 VAC to meet increased electrical power demands [56]. Further advancements led to the emergence of variable-speed constant-frequency (VSCF) systems in the 2000s [57]. These systems incorporated power electronic converters (PECs), allowing for variable speeds and frequencies. However, the introduction of power electronics introduced a range of harmonics, which had to be managed using passive and active power filters [58]. This evolution in power generation systems enabled the replacement of fixed-frequency power loads, such as induction motor-driven pumps, with power electronics-controlled loads compatible with variable frequency standards (ranging from 360 to 900 Hz). This transition was evident in systems like the A380's flight control actuation systems, which employed electro-hydrostatic actuators (EHAs) as a hydraulic network backup.

Table 2-1 Recent Advances in Aircraft Power Generation Systems [21]

Power generation type	Civil aircrafts	Power ratings
Constant frequency	A340	4×90 kVA
	B777	2×120 kVA
Variable frequency	A380	4×150 kVA
	B787	4×250 kVA
VSCF (115V at 400 Hz)	MD-90	2×75 kVA

The power generation system in aircraft has undergone a gradual evolution, transitioning from a 115 VAC 400Hz constant frequency system to variable speed constant frequency, and finally to variable speed variable frequency. Table 2-1 provides an overview of the power generation

solutions employed in recent aircraft. In the following subsections, the architectures of these power generation systems will be looked into, exploring their operating principles and examining the core equipment involved, namely the starter/generator.

2.1.1.1 Constant Speed Constant Frequency

Traditional aircraft power generation systems rely on a mechanical coupling between the engine and generator shafts through a gearbox known as a constant speed drive (CSD). The CSD converts a variable speed input into a constant output speed required to drive the AC generator. This hydromechanical CSD maintains a constant output frequency of 400 Hz, resulting in a steady supply of electrical power. In addition, this approach ensures a stable output speed, while allowing for variations in the input speed, such as the engine shaft speed. However, the use of the CSD necessitates maintenance and adds weight and size to the power generation system. Moreover, the gearbox itself is costly, challenging to maintain, and compromises system reliability, highlighting the need for improvements [55].

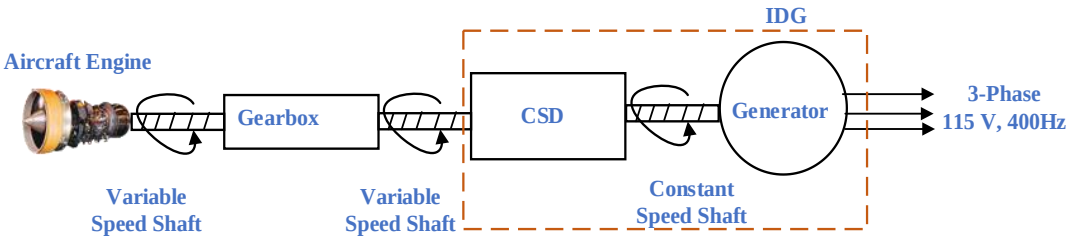


Figure 2.1 Constant frequency constant speed using IDG.

To address these concerns, in the 1970s, the generator and CSD were integrated into a single unit called an integrated drive generator (IDG) [12], [59]. This integration marked a significant advancement, resulting in improved power density, enhanced system reliability, and weight reduction. The IDG system has been implemented in various aircraft models such as the A340, B717, B737NG, B747, B767-400, B777, and the MD-12 [46], [60]. Figure 2.1 illustrates the block diagram of the IDG system. Despite the introduction of IDG, these power generation system components still need to be located near the engine and cannot be distributed throughout the aircraft, presenting a limitation in design flexibility. As a result, alternative topologies are being explored to address these limitations and improve overall aircraft's power generation system performance.

2.1.1.2 Variable Speed Constant Frequency (VGSCF)

The Variable Generator Speed Constant Frequency (VGSCF) system is an advanced power generation solution that has emerged as an alternative to traditional constant speed drive (CSD) architectures. Unlike the CSD system, which relies on a mechanical gearbox to maintain a constant speed, the VGSCF system utilises a direct connection between the generator and the engine to achieve a constant frequency output, as shown in Figure 2.2. However, since the engine speed can vary during different flight phases, the generator produces an output frequency that fluctuates accordingly [57]. To rectify this, a cyclo-converter or matrix power converter, along with a filter, is employed to convert the variable frequency output into a fixed frequency (typically 400 Hz) and voltage supply for the aircraft [61], [62], [63].

One of the main advantages of the VGSCF system is its ability to simplify the mechanical drive system. Through the elimination of the need for complex gearboxes and constant speed drives, the system becomes more streamlined, reducing weight, size, and maintenance requirements. Additionally, the introduction of PECs enables finer control over the electrical frequency, improving the overall performance and flexibility of the aircraft's power generation system. However, a notable drawback of this system is that the power converter must handle the entire power generated by the generator. As a result, the power converter must exhibit high reliability to ensure the required level of safety in the aircraft's operation. Presently, power electronics technology still faces reliability challenges, which limit the widespread adoption of this configuration, making it a less commonly chosen option [61].

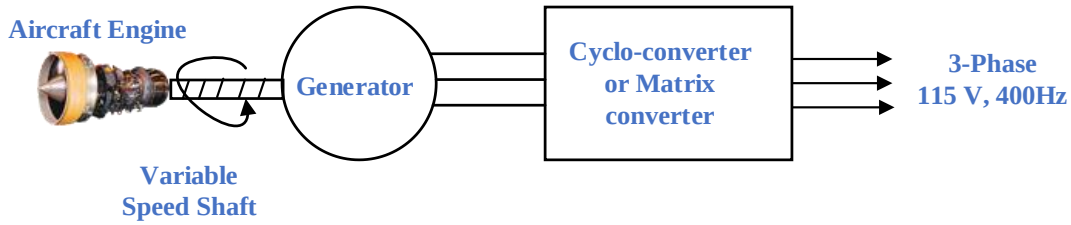


Figure 2.2 VGSCF system with a power converter.

2.1.1.3 Variable Speed Variable Frequency (VSVF)

The Variable Speed Variable Frequency (VSVF) generation system offers a new configuration for aircraft power generation, addressing some of the challenges faced by the VGSCF system. In this new configuration, the generator is directly connected to the gas turbine engine, as

illustrated in Figure 2.3 [64]. As a result, the generated electrical frequency varies according to the engine speed, typically ranging from 320 to 800 Hz, while maintaining a controlled voltage [65].

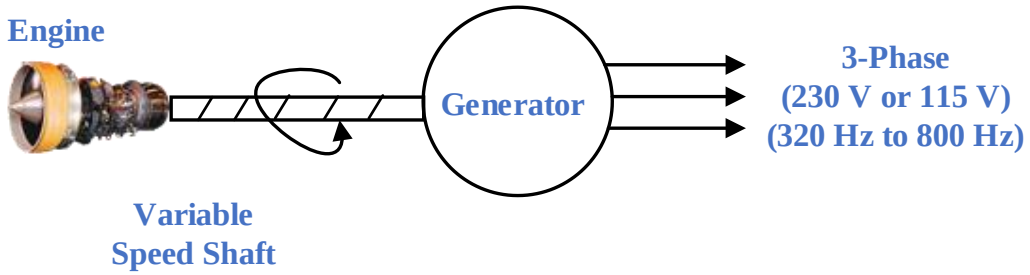


Figure 2.3 Variable speed variable frequency generation system.

The key advantage of this system is the direct connection between the generator and the power bus, which simplifies the overall electrical generation setup and reduces costs. However, one drawback is that the variable frequency output from the generator is not suitable for most onboard loads, necessitating the use of power converters for control purposes and to ensure compatibility with variable frequency power [9], [61]. This architecture has been successfully implemented in aircraft such as the Boeing 787 and Airbus A380. In these aircraft, the voltage is adjusted to 115V AC (A380) or 230V AC (B787).

The variable frequency range of the VSVF system can present challenges for aircraft loads that are sensitive to frequency, particularly AC motors. When these motors are directly powered by the AC grid, their speed is influenced by the frequency of the grid, which can lead to inconsistent performance. To address this issue, local power converters can be employed to ensure the appropriate frequency and control of these motors. Additionally, advanced control techniques can be implemented to optimise the performance of these motors [46].

2.1.1.4 DC Power Generation

The DC power generation system in aircraft relies on DC generators to supply the necessary voltage for powering onboard loads. Typically, there are two DC buses: a 28 VDC bus for low-power loads and a higher voltage bus, such as 270 VDC or 540 VDC, for high-power loads [12]. The DC generator is carefully controlled to maintain a constant DC voltage, regardless of changes in engine speed or load power. This control mechanism is important for meeting

aerospace standards, including the stringent MIL-STD-704F [49], which ensures compatibility between the aircraft power system and other electrical loads.

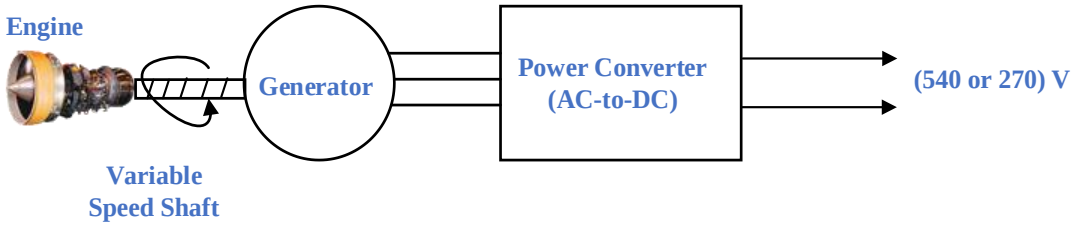


Figure 2.4 AC generator with AC-DC converter.

The DC power generation system has already been adopted in military aircraft like the F35 and is also a part of the electric power system in the B787. Figure 2.4 illustrates a DC power generation system featuring a variable frequency generator that supplies power to an AC-DC converter. The AC electrical power generated by the generator is rectified to produce a DC power output of either 270 V or 540 V [9]. The architecture shown in Figure 2.4 offers several advantages, including reduced corona effect, elimination of the need for reactive power compensation, decreased skin effect, and ultimately reduced power loss in the transmission cable [66]. Some DC power generation systems incorporate conversion mechanisms to meet the specific requirements of various loads. These systems involve the transformation of high-voltage DC into either 115VAC at a frequency of 400Hz or 28VDC. Lockheed Martin's F-22 and F-35 aircraft employ these DC power generation configurations that offer enhanced efficiency compared to traditional methods. These configurations have fewer power conversion stages, resulting in a more streamlined and efficient power generation process [46].

2.1.1.5 Electrical Machines for Starter/Generator Applications

Electrical machines play a vital role in providing power generation and starting functions, thus, contributing to the overall performance and efficiency of the aircraft's electrical power system. In starter/generator (SG) applications, the electrical machines are designed to serve dual purposes. During the starting phase, they act as motor-like devices, providing the necessary torque to initiate the rotation of the engine. Once the engine is running, these machines transition seamlessly into generators, converting mechanical energy from the engine into electrical energy to power various onboard systems and charge the aircraft's battery [67], [68].

The SG scheme offers a simplified connection between the engine and the electrical machine, eliminating the need for accessory gearboxes, power take-off shafts, and engine tower shafts in future aircraft designs. Instead, a power converter is employed to serve as an interface between the aircraft's main bus and the electrical machine, resulting in a reduction in the complexity of the power system [67]. With this arrangement, the power converter controls the flow of power into and out of the electrical machine, allowing it to function as either a starter or a generator. The power flow and a visual representation of the SG system can be observed in Figure 2.5.

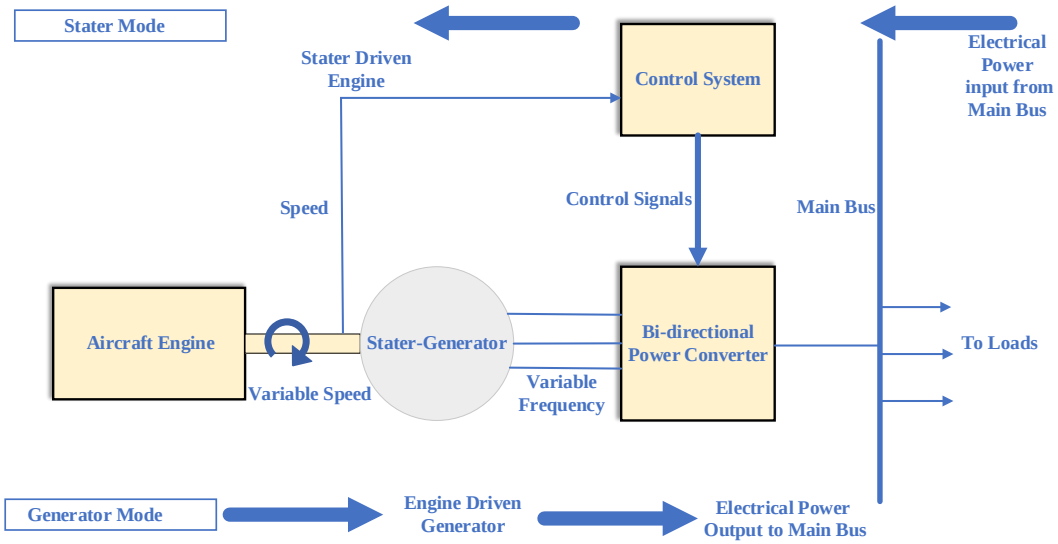


Figure 2.5 Overall Architecture of the Starter-Generator System.

As shown in Figure 2.5, the SG system utilises a bi-directional power converter to drive the electrical machine in two modes: motoring and generating. In the motoring mode, the machine is driven by the power converter using power from the main bus, enabling it to accelerate the aircraft's engine. The control system regulates the speed of the machine to match a reference value, ensuring efficient operation. Alternatively, in the generating mode, the engine acts as a source of mechanical power. This mechanical power is then converted into electrical power by the electrical machine and power converter. The generated electrical power is subsequently utilised to supply power to various loads onboard the aircraft [28].

One of the key objectives in the development of electrical machines for SG applications is to achieve high efficiency and power density. This involves designing machines that can deliver a high output power while minimising energy losses and size constraints. Additionally, these

machines should exhibit reliable performance, withstand the demanding operating conditions of aircraft environments, and ensure a smooth transition between motor and generator modes. Different types of electrical machines have been explored for SG applications, including induction machines (IM), permanent magnet machines (PMM), and switched reluctance machines (SRM). Each type offers distinct advantages and challenges, and researchers continue to investigate and optimise their performance for different applications [69].

Wound Field Synchronous Machine (WFSM)

The Wound Field Synchronous Machine (WFSM) is a synchronous machine that employs a wound field rotor and stator windings. The WFSM consists of a rotor, which includes a field winding, and a stator, which contains armature windings. The field winding is connected to a direct current (DC) power source and creates a magnetic field when energized. The armature windings, on the other hand, are connected to the aircraft's electrical system and interact with the magnetic field to generate electrical power.

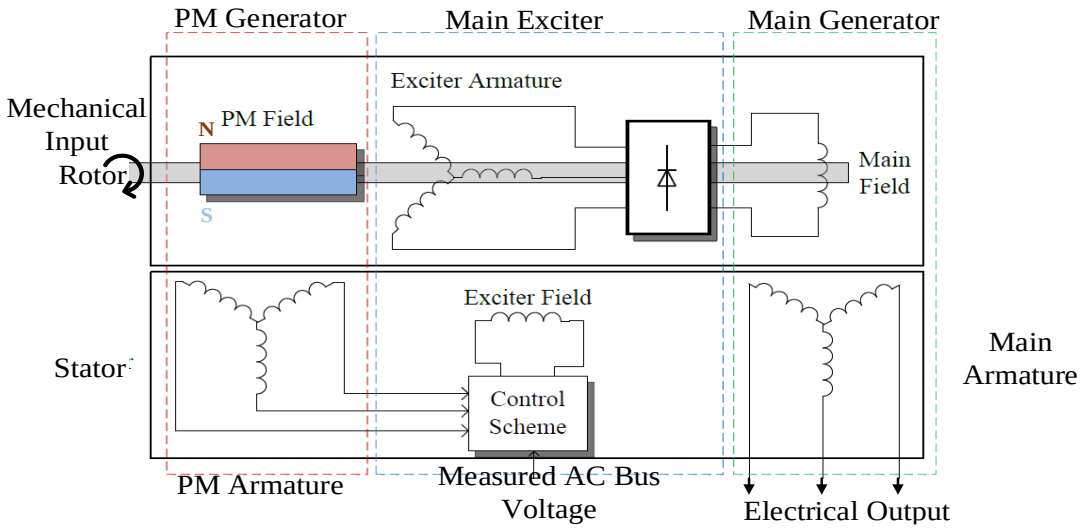


Figure 2.6 Diagram of the three-stage wound-field synchronous machine [70].

Figure 2.6 shows the equivalent electrical structure of a typical three-stage WFSM, which consists of three distinct electric machines integrated into a single housing. The left side of the circuit represents a Permanent Magnet (PM) generator, which produces a variable frequency voltage based on the speed of the engine. The control system of the WFSM detects the voltage levels at the PM generator armature and adjusts the exciter field accordingly by providing a suitable DC reference. The exciter, located in the middle of the circuit, consists of an armature

and windings. The control scheme ensures that the exciter armature voltage is controlled in response to the exciter field. This voltage is then rectified into DC form using a rotating diode rectifier. The rectified DC creates a main excitation field, which induces AC voltage through the main armature windings. This AC voltage is utilised for various aircraft applications [70]. In addition to its excitation control, the WFSM's control scheme also monitors and regulates the output AC voltage. This ensures that the generated AC voltage remains stable and within the desired range.

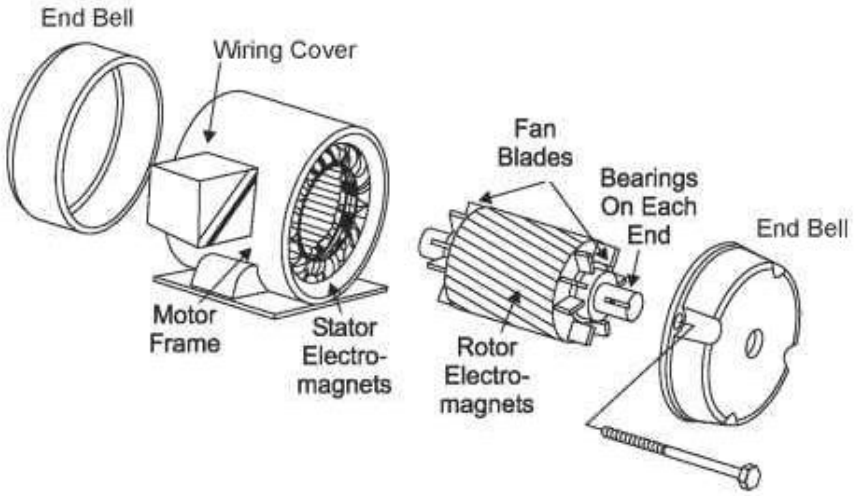


Figure 2.7 Induction motor construction [74].

The WFSM is a potential choice for future More Electric Aircraft (MEA) applications due to its advantages in field regulation, mature technology, and potential direct connection to the distribution network. However, this machine topology has certain limitations. The presence of multiple windings and electronic components on the rotor contributes to its complexity. To achieve higher power density, additional windings and larger diodes are necessary, which increases the overall complexity and weight of the system. The heavier rotor imposes constraints on the achievable operating speed of the machine [71], [72]. Furthermore, if the three-stage WFSM is intended to support electrical engine start operations, additional windings are required, further increasing the complexity [73]. Considering these drawbacks, the three-stage WFSM may not be suitable for meeting the power rating improvement demands of the MEA. Thus, it is necessary to explore alternative machines that offer improved efficiency and performance for MEA SG systems.

Induction Machine (IM)

The induction machine (IM), also known as an asynchronous machine, is a widely used type of electrical machine in various industries and applications. It is known for its simplicity, robustness, and cost-effectiveness [75]. The construction of an IM consists of two main components: the stator and the rotor as shown in Figure 2.7. The stator consists of a laminated core with slots that hold insulated copper windings. These windings are arranged in a specific pattern to create a rotating magnetic field when an alternating current (AC) is applied. The rotor, on the other hand, can be either a wound rotor or a squirrel cage rotor.

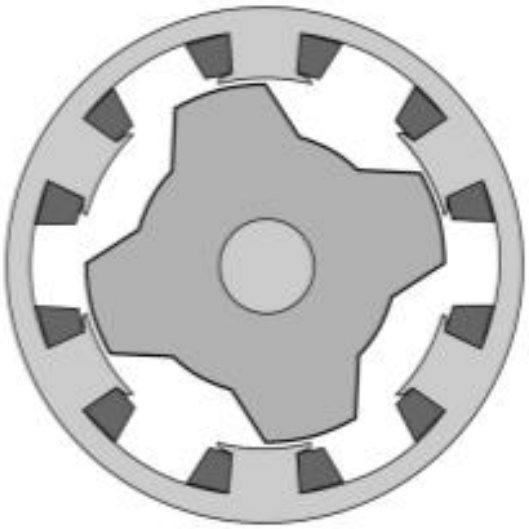


Figure 2.8 Structure of stator and rotor of the switched reluctance machine [77].

The IM exhibits notable characteristics that make it suitable for MEA applications. These include its high robustness, fault tolerance, low cost, and tolerance to high operating temperatures. However, despite its advantages, the IM does encounter certain challenges that need to be addressed for MEA applications. These challenges include low power density [71], the presence of large end windings, and excitation problems at high speeds [76]. In MEA applications, where weight reduction is a priority, the IM's relatively larger size and weight may also pose a challenge [76]. These issues require further research and development efforts to optimise the performance and overcome the limitations of the IM in MEA applications.

Switched Reluctance Machines (SRM)

Switched Reluctance Machines (SRM) are a type of electrical machine that offer unique characteristics and advantages for various applications, including MEA systems. These machines operate based on the principle of magnetic reluctance, utilising the tendency of

magnetic flux to flow through the path of least reluctance. The SRM consists of a stator with salient poles and a rotor with salient teeth as shown in Figure 2.8. The stator poles are energized sequentially by switching the current flow, creating a magnetic field that interacts with the rotor teeth [78]. The absence of permanent magnets or field windings on the rotor is a distinguishing feature of SRMs.

One of the key advantages of SRMs is their simplicity in design and construction. With a reduced number of parts, such as the absence of permanent magnets and brushes, SRMs offer a more robust and reliable solution. The simplicity also contributes to easier maintenance and lower manufacturing costs compared to other machine types. SRMs are highly suitable for variable speed applications due to their inherent ability to operate over a wide range of speeds. They exhibit excellent performance in high-speed regimes and can maintain efficiency even at low speeds. This flexibility makes SRMs well-suited for the varying power demands of aircraft systems during different flight phases. Furthermore, SRMs offer advantages in terms of fault tolerance and reliability [73].

Although SRMs have many benefits, they also present some challenges. One major challenge is the generation of acoustic noise and vibration due to the nature of the operating principle. Mitigation techniques, such as proper mechanical design and control algorithms, are necessary to minimise these effects. Another drawback is the presence of a high torque ripple, which can impact system efficiency and smooth operation. These drawbacks restrict the usage of the SRM for MEA applications [77], [73]. Thus, addressing these challenges associated with torque ripple reduction, and noise reduction will enhance the applicability of SRMs in aerospace applications and contribute to their wider adoption in the industry.

Permanent Magnet Machine (PMM)

The PMM (Permanent Magnet Machine) utilises permanent magnets in the rotor to provide excitation. These magnets can be either surface-mounted or interior-mounted. The structure of the stator in a PMM is like that of an IM as shown in Figure 2.9. However, the rotor of the PMM differs, as it incorporates permanent magnets that generate a constant magnetic field [77]. Unlike the IM, the PMM experiences higher efficiency and power density, making it suitable for a wide speed range with superior torque and power capabilities. PMMs have gained significant popularity in recent years, particularly in electric vehicle (EV) and hybrid electric

vehicle (HEV) applications [79]. They offer advantages such as a wide torque-speed range, superior torque and power density, and high efficiency.

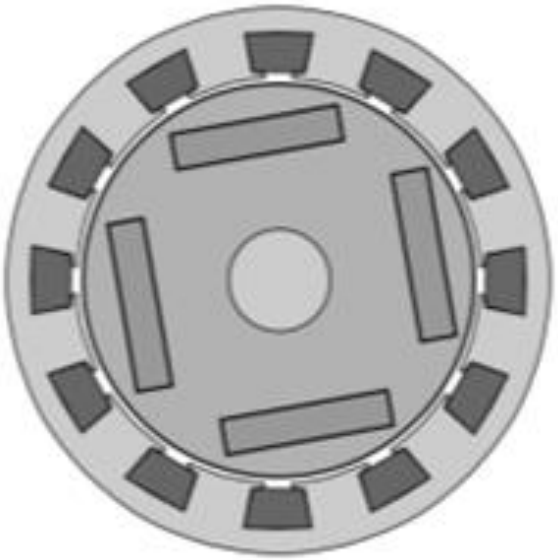


Figure 2.9 Structure of a permanent Magnet Machine [77].

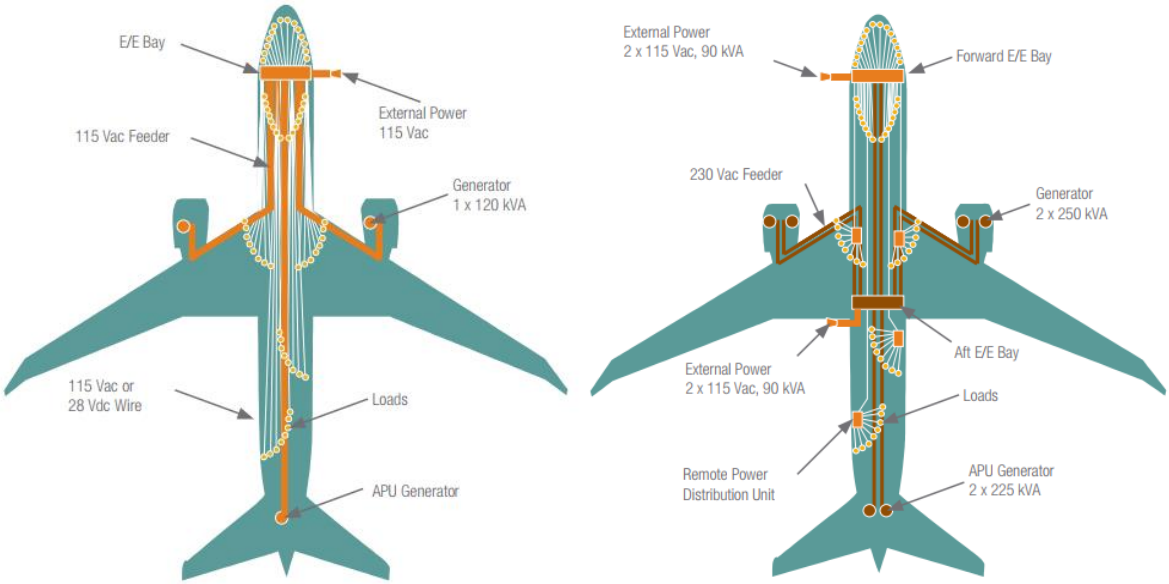
In a study [80], a surface mounted PMM machine with a power rating of 45 kVA and a rotational speed of 32 krpm was used for an SG application. It was connected to the DC bus through a neutral point clamped (NPC) three-level converter, and experimental results demonstrated excellent power generation and control performance. Another research [81] employed an interior PM (IPM) synchronous motor as a SG, and a field-weakening strategy was developed to enhance its power generation capability in the high-speed range. The PMM offers advantages such as higher efficiency, power density, and a wide speed range. However, considerations for temperature management, fault tolerance, and cooling systems must be addressed for their application in aerospace and other industries [28]. In summary, each of the three machine types has its advantages when used as a SG:

- ✓ SRMs are preferred for their robustness.
- ✓ IMs are chosen for their mature technology and cost-effectiveness.
- ✓ PMM offers high power density and superior performance. Due to their high efficiency, power density, and well-established control strategies, the PMM-based SG system will be utilised in this thesis.

2.1.2 Overview of Power Distribution Architectures

In aircraft power distribution systems, both AC and DC topologies are commonly used. AC power at 115V/400Hz is supplied to large electrical loads such as galleys, while 28V DC power is used for avionics, flight control, and essential services powered by the battery [16]. The DC power in the conventional aircraft is obtained by converting the AC power through transformer rectifier units (TRUs). However, the operation of TRUs can introduce harmonic distortions into the AC side of the aircraft's EPS. This harmonic distortion can have negative effects on the performance of sensitive instruments and circuits within the aircraft. TRUs, being the primary source of harmonics in the EPS, have the potential to increase voltage distortion and the presence of harmonic content. This can result in malfunctions and disruptions in the operation of sensitive equipment and circuits onboard the aircraft. Also, in conventional aircraft, the distribution system is centralised, requiring power to be sent to the front of the aircraft, resulting in increased line losses and inefficiency [82].

However, with the shift towards MEA, power generation and distribution are now located closer to the point of consumption. This is made possible by advanced solid-state power controllers and contactors with improved communication capabilities, enabling remote distribution. This approach reduces line losses, increases efficiency, and allows for significant reductions in the volume and weight of the aircraft. Consequently, lower-rated equipment can be used, leading to cost savings in maintenance and improved fuel efficiency. Figure 2.10 (a) shows the power distribution system of a traditional aircraft, while Figure 2.10 (b) shows the power distribution system of a MEA. Figure 2.10 (b) showcases the modern network configuration implemented in the Boeing 787 aircraft as an example.



(a) (b)

Figure 2.10 Power distribution system in conventional aircraft and B787 [15].

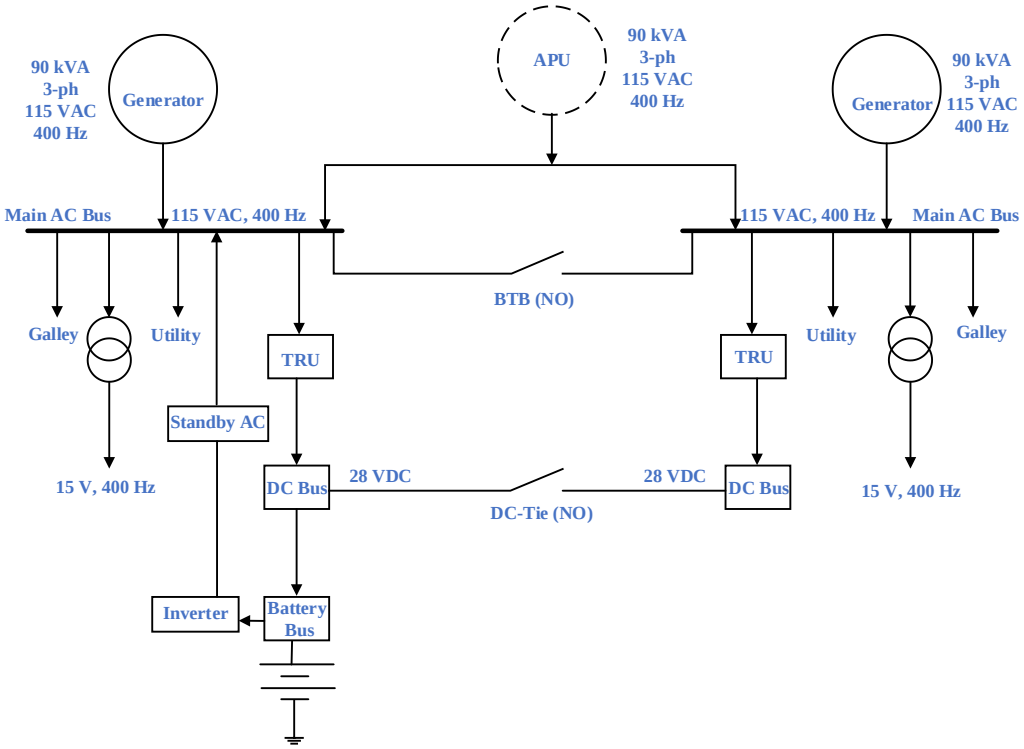


Figure 2.11 Conventional B767 aircraft power distribution system [83].

2.1.2.1 Power Distribution System Architecture in Conventional Aircraft

The power system configuration in a conventional aircraft involves the generation of electrical power from engine-driven generators to supply both AC and DC loads. In most aircraft, the engine-driven generators are connected in parallel, with each generator responsible for powering a specific set of distribution buses. These generators are interconnected through a Bus-Tie Breaker (BTB) arrangement [83].

If one generator fails, it is isolated from its respective busbar, and the loads on that busbar are transferred to the functioning generator. If both generators fail, essential services in the aircraft are powered by the onboard batteries for a predetermined duration based on the battery's state of charge (SOC) and the power requirements of the loads. The simplified power distribution system of a conventional aircraft, such as the Boeing 767, is shown in Figure 2.11 (excluding the external power system) [46]. The generators supply AC loads with a constant-frequency AC voltage of 115V at 400 Hz [84], [46]. The TRU's main function is to convert the 115V AC voltage into 28V DC voltage, which is then supplied to the DC buses. This conversion enables the DC buses to receive the appropriate voltage level required to power the respective DC loads. The DC-tie system is employed to interconnect the two DC buses in case of a failure in either the main AC bus or the TRU [83]. Moreover, autotransformers facilitate the supply of 115V AC voltage at a constant frequency of 400 Hz from both main AC buses to specific loads. In situations where both generators are non-functional, the batteries supply power to essential loads and feed the main bus through an inverter [83].

2.1.2.2 Power Distribution System Architectures in MEA

MEA EPS architectures represent the latest advancements in aircraft EPS evolution [7], [85]. It is worth noting that state-of-the-art technology emphasizes two main approaches: high-voltage variable frequency (ranging from 360 Hz to 900 Hz) AC primary distribution or high-voltage DC distribution (at 270 V, ±270 V, or 540 V).

One example of a hybrid AC-DC MEA EPS architecture can be found in the European Union (EU) FP6 project MOET [86], [87]. This architecture, as shown in Figure 2.12 (a detailed description can be found in [88]), follows an islanded structure during normal operating

conditions. Each generator is responsible for its own loads and distribution layers. Only in the event of a fault, specific inter-tie contactors can transfer load to a healthy primary source.

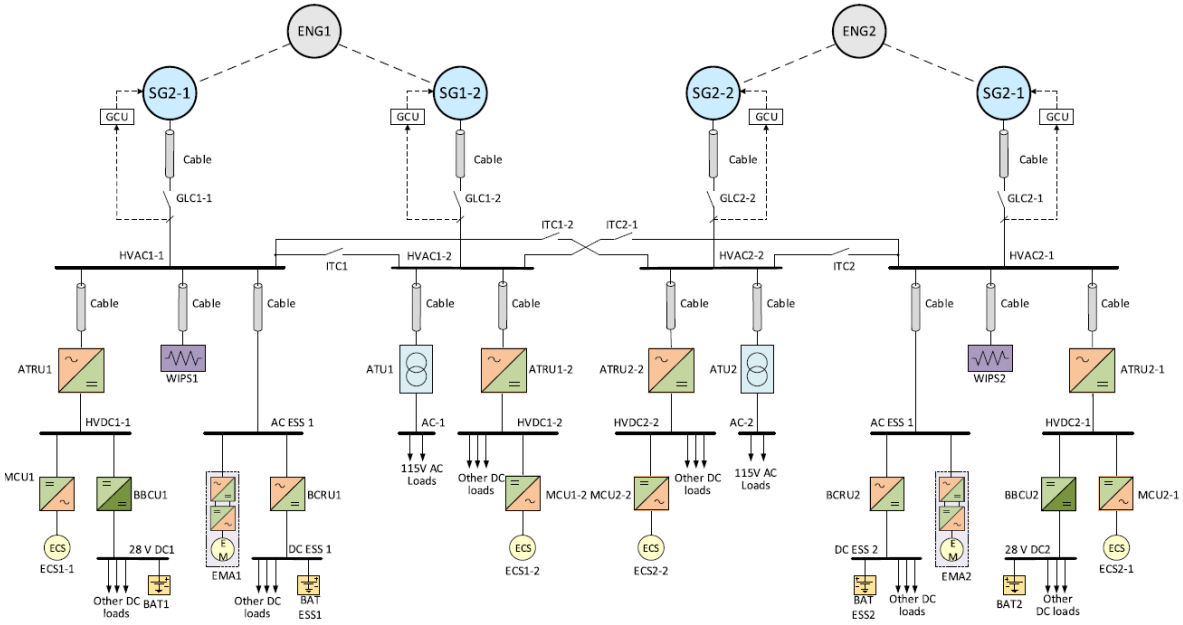


Figure 2.12 Electrical Power Distribution Architecture for MEA in the MOET Project [89].

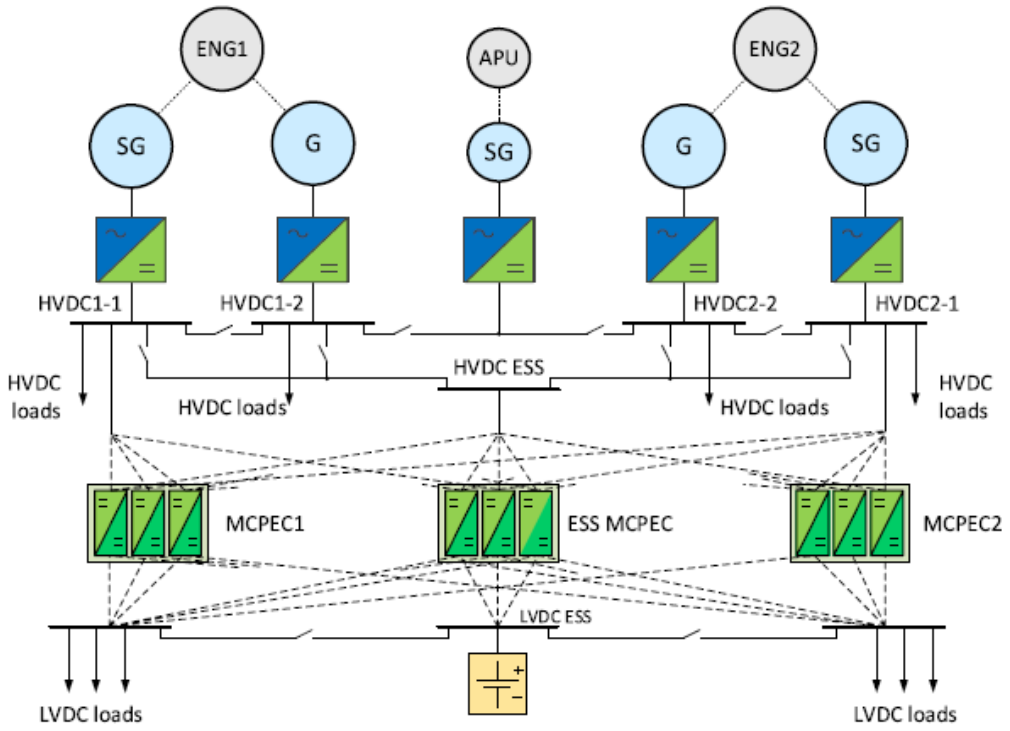


Figure 2.13 Flexible power distribution architecture with modular and identical PECs [89].

A notable characteristic of this topology is its extensive use of power electronic converters, resulting in a high reliance on power electronic components. However, since many onboard loads are only required for short durations during flight missions, the utilisation rate of power electronics in this EPS architecture is relatively low. Enhancing this utilisation rate would lead to significant reductions in the overall weight and cost of the EPS system [89].

The use of modular PECs in the MEA EPS allows for flexible architecture and improved power availability. The architecture as shown in Figure 2.13 consists of smaller PECs called "cells" that can connect primary buses to secondary buses without causing power interruptions. These cells can operate in parallel with others, providing redundancy and allowing for increased power availability [87]. Also included in the architecture are an energy storage system (ESS) and modular cell power electronic converter (MCPEC). The modular design of the cells also offers benefits in terms of weight and volume reduction, as they can be easily replaced as individual units. The EPS with this architecture functions as a smart MG, with the supervision logic responsible for energy management and optimising the system configuration. Recent research has focused on developing optimised control logic for these architectures, aiming to improve overall EPS performance in terms of reliability, safety, power availability, weight reduction, and component count reduction [90].

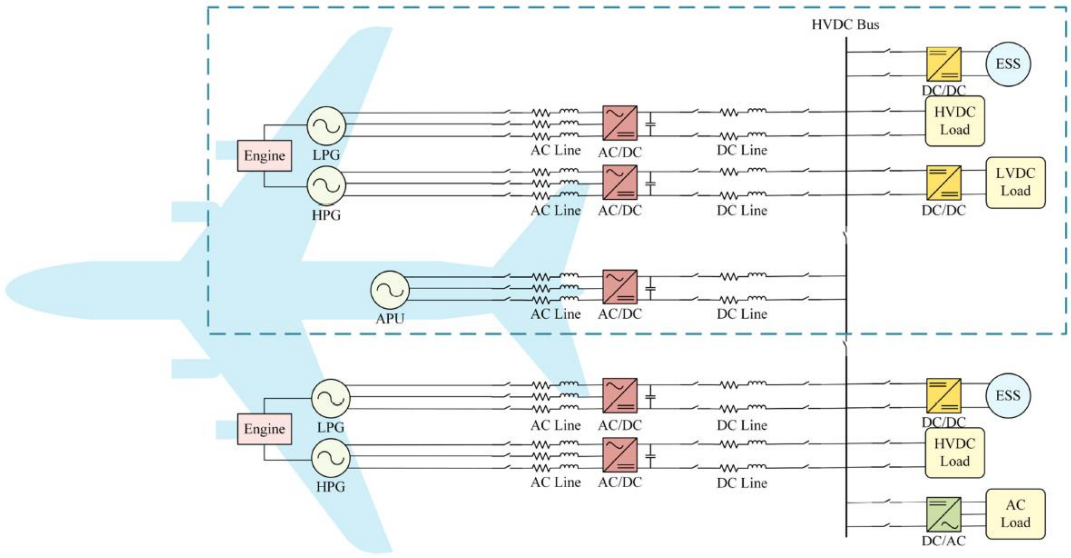


Figure 2.14 Single bus electrical power distribution system [91].

A recent development in the MEA power distribution system is the adoption of a "single-bus" concept, where all or most of the system is connected to a single bus that interfaces with all the loads and power sources as shown in Figure 2.14 [35], [92], [91], [93]. This configuration is enabled by using active PECs to control and regulate the primary sources. The HVDC bus allows for the connection of various power management equipment. The use of a single DC bus configuration offers several advantages compared to an AC network. It improves system efficiency, reduces costs, and results in smaller system sizes. This is mainly because fewer PECs are required, leading to higher overall efficiency. Additionally, the absence of transformers in AC/DC converters significantly reduces the size of the DC network. Another benefit of the single-bus topology is the ease of establishing optimal power allocations through decentralised droop control. This can result in significant weight reduction by reducing the design ratings of the main power sources. These advancements in the MEA power distribution system enhance efficiency and contribute to a more compact and effective power system [94].

2.1.3 Power Consumption and Electric Loads on Aircraft

The power consumption on aircraft involves various electrical services and loads that serve different functions. These services include lighting, heating, motors and actuation, subsystem controllers, and avionics systems [83]. Nevertheless, in the EPS of MEAs, various types of physical loads can be categorised into constant impedance loads (CIL), constant current loads (CCL), and constant power loads (CPL). These load types are used to analytically represent the behaviour of different electrical loads on the aircraft. Constant impedance loads (CIL) are characterised by their impedance remaining constant regardless of the operating conditions. Examples of CILs include resistive loads and other devices such as the wing ice protection system, galley ovens, and cargo heaters [95]. These loads exhibit a consistent impedance value during operation. Constant current loads (CCL) draw a constant current from the power supply. They include devices like transducers that require a consistent current input for their operation. Most loads connected to the high-voltage DC (HVDC) bus in MEA systems, which are supplied by PECs or inverters, behave as constant power loads (CPL). These loads, such as DC/DC converters for resistive loads and DC/AC inverters for motor drives, consume power at a constant rate regardless of voltage or current fluctuations [95].

The heating load is necessary for anti-icing or de-icing systems (WIPS) and can consume a significant amount of power, often in the tens of kilovolt-amperes (kVA) [83]. Motors are

employed in various applications on board the aircraft. These include linear actuation for engine control and trim actuators, and engine starters for initiating engine and APU operation [83]. These electrical services and loads are essential for the proper functioning of the aircraft, ensuring safety, comfort, and operational efficiency. Proper management and allocation of power to these systems are significantly important to meet the diverse power requirements and maintain reliable operation throughout the flight.

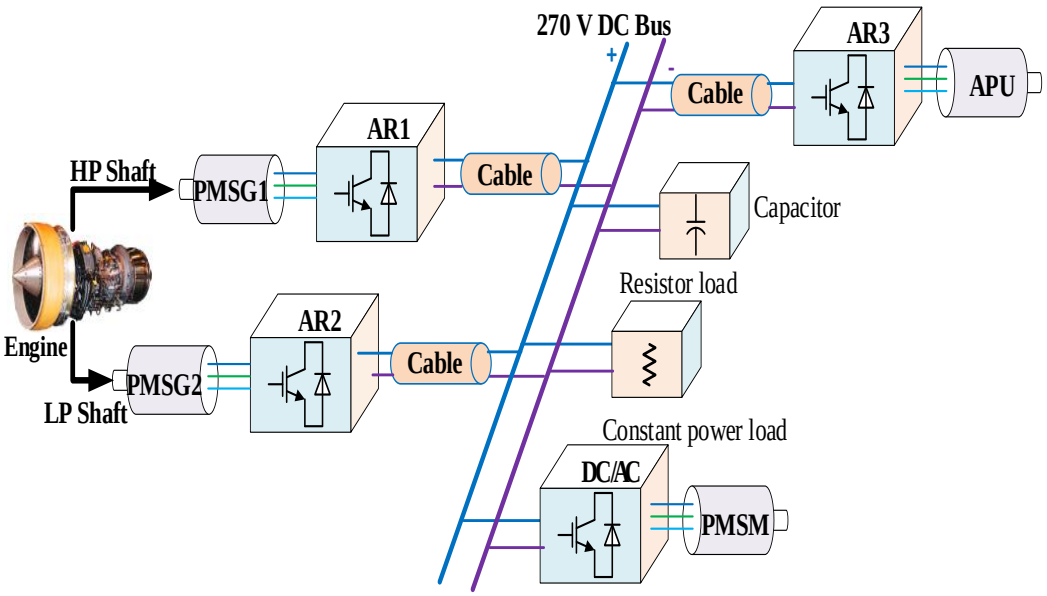


Figure 2.15 A single bus EPS architecture for future MEA applications.

2.1.4 Single Bus-based Multi-Generator Electrical Power System

After analysing the power generation, distribution, and utilisation system in the MEA, this thesis focuses on the study of a single-bus electrical power system (EPS) architecture with multiple generators feeding power to the same bus. The architecture, depicted in Figure 2.15, serves as the basis for the research conducted in this thesis. As shown in Figure 2.15, two permanent magnet synchronous generators (PMSGs) are connected directly to the turbine shafts through active rectifiers (ARs). These generators can operate at variable speeds. The two generators extract power from the main engine through the high-pressure (HP) and low-pressure (LP) shafts, ensuring efficient utilisation of the engine's generated power. They operate in parallel to transfer the power to the DC bus, typically providing a 270V DC output. This DC power can be obtained either from the main engine-driven generators or through active rectification. Additionally, during the ground starting of the engine, the 270V DC power can

also be sourced from a ground-based auxiliary power unit (APU). Utilising parallel generation with a single bus offers several anticipated advantages, such as enhanced power system redundancy. This means that in the event of a generator failure, the parallel system can ensure an uninterrupted power supply. Furthermore, the parallel operation of multiple generators can be effectively managed, providing potential benefits in terms of weight reduction, improved efficiency, increased availability, and cost savings [89]. The on-board loads consist of a combination of conventional resistive loads and Controlled Power Loads (CPLs) that are typically driven by tightly controlled power electronics.

As mentioned in Chapter 1, Section 1.3, there are challenges associated with coordinating the control of multiple power sources and ensuring proper power management within this architecture. One of the key motivations for this PhD research lies in exploring and addressing these challenges in achieving efficient load sharing and optimal power management within the studied single-bus EPS architecture. Nevertheless, a comprehensive understanding of the electrical power system (EPS) requires an introduction to the characteristics of each component within the system. This enables a holistic view of how the system operates and interacts.

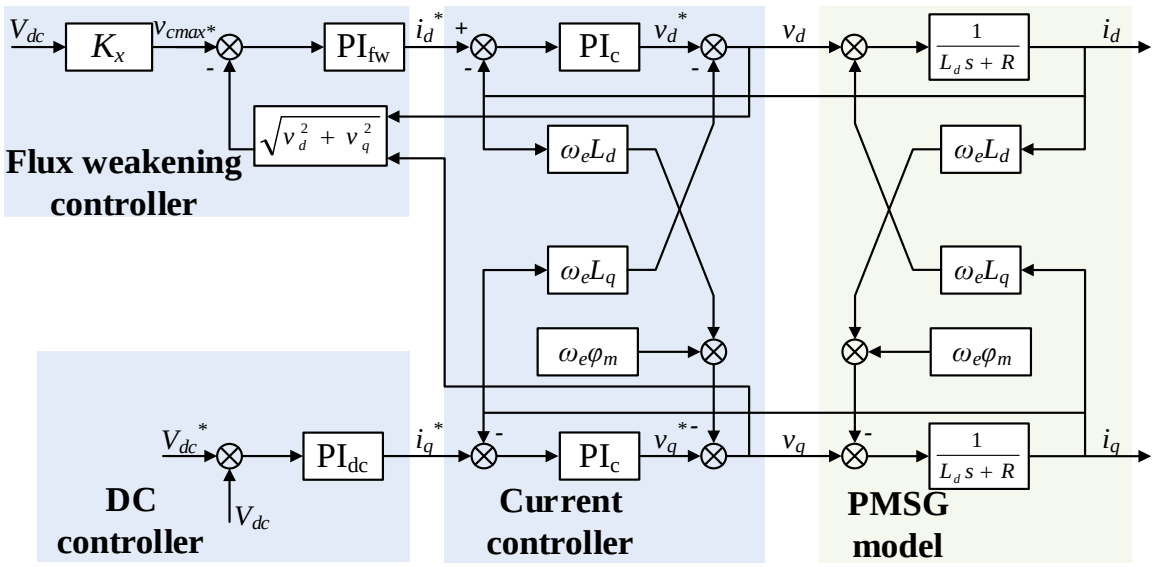


Figure 2.16 Control block diagram of PMSM.

2.1.4.1 PMSG Model

Three-phase Permanent Magnet Synchronous Generators (PMSGs) have gained widespread use in power generation over the past decades. To simplify the calculations and avoid the

complexity of dealing with three phases, PMSGs are often modelled using synchronous and rotating reference frames, such as the dq frame [96]. The frame transformation from three-phase to *dq* is presented in Appendix B.

$$\begin{cases} v_d = R_s i_d + L_d \dfrac{di_d}{dt} - \omega_e L_q i_q \\ v_q = R_s i_q + L_q \dfrac{di_q}{dt} + \omega_e L_d i_d + \omega_e \varphi_m \end{cases} \tag{2-1}$$

The dynamic equations for the PMSG in the dq frame (in (2-1)) are given by the following variables: v_d (d-axis stator voltage), v_q (q-axis stator voltage), i_d (d-axis current), i_q (q-axis current), L_d (d-axis inductance), L_q (q-axis inductance), R_s (stator resistance), φ_m (flux linkage of the permanent magnet), and ω_e (electrical rotor angular velocity). The PMSG model diagram, represented in olive green, is depicted in Figure 2.16, based on the equation (2-1). The derivation process for equation (2-1) is detailed in Appendix C.

The maximum allowable phase currents are governed by the ratings of both the inverter and the machine. Additionally, the maximum voltage is contingent on the available DC-link voltage and the modulation method used. These voltage and current limitations can be represented as follows, neglecting the stator resistance and transient terms [97]:

$$\begin{cases} \omega_e \sqrt{(L_s i_q)^2 + (L_s i_d + \varphi_m)^2} \le v_c^{max} \\ \sqrt{i_d^2 + i_q^2} \le i_c^{max} \end{cases} \tag{2-2}$$

The parameters v_c^{max} and i_c^{max} represent the maximum phase voltage amplitude at the fundamental frequency and the maximum phase current, respectively.

2.1.4.2 Control of the PMSG system

A. Flux weakening and DC Link control.

The flux weakening (FW) control is important to ensure the machine operates within the voltage limit circle and enables high-speed operation, particularly in the context of MEA. This control strategy involves injecting a demagnetizing current to weaken the PMSG's flux, reducing the back-emf generated. By effectively managing the demagnetizing current, the

stator voltage can be regulated [98]. The use of the flux weakening controller impacts (i_d), and it remains active during generator mode to maintain the stator voltage ($v_c = \sqrt{v_d^2 + v_q^2}$) at the required level and prevent converter overmodulation. As the machine rotates beyond the base speed, the flux-weakening operation activates, injecting a negative d-axis current (i_d^*) based on the error between the reference voltage and the converter's voltage limit. The FW controller equation is as expressed in (2-3).

$$i_d^* = \frac{k_{iFW}}{s}(v_c^{\max} - v_c) \tag{2-3}$$

where the integral gain of the FW controller is represented as k_{iFW}. It is essential to note that if the PMSG operates in a region where flux weakening is not necessary, $i_d^* = 0$.

During generation mode, the outer DC power loop sets the q-axis current reference (i_q^*). In flight, the system operates in generation mode, and the q-axis current reference (i_q^*) is determined by the dc-link current or voltage demands, which are dictated by the specific power sharing method. For example, if the power sharing method is voltage feedback-based droop control (current-mode droop control method), the current reference should be implemented. Conversely, if the power sharing method is current feedback-based droop control (voltage-mode droop control method), a voltage reference should be used.

B. Current control

The current control loop regulates the dq-currents (i_d and i_q) based on their reference values (i_d^* and i_q^*). Figure 2.16 illustrates the dq current loops along with their corresponding control plant. The flux-weakening controller and DC controller generate the dq-current references, which are then supplied to the current controller. The feedforward terms within the current control plant are utilised to compensate for the coupling effect in the dq frame. Consequently, the control plant can be simplified to first-order transfer functions, expressed as (2-4) for the d-axis current and (2-5) for the q-axis current.

$$\frac{i_d}{v_d^*} = \frac{1}{L_s s + R} \tag{2-4}$$

$$\frac{i_q}{v_q^*} = \frac{1}{L_s s + R} \tag{2-5}$$

A block diagram showing the current PI controller and plant is shown in Figure 2.17.

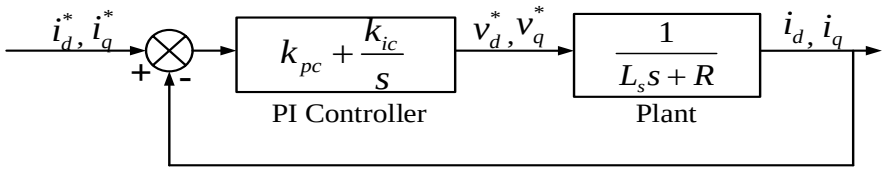


Figure 2.17 Current Controller Transfer Function

By incorporating a PI controller with feedforward elements, a closed-loop transfer function can be derived as follows:

$$\frac{i_d}{i_d^*} = \frac{k_{pc} s + k_{ic}}{L_s s^2 + \left(R + k_{pc}\right) s + k_{ic}} \tag{2-6}$$

$$\frac{i_q}{i_q^*} = \frac{k_{pc} s + k_{ic}}{L_s s^2 + \left(R + k_{pc}\right) s + k_{ic}} \tag{2-7}$$

The transfer function, resembling an ideal second-order response, with k_{pc} and k_{ic} representing the proportional and integral gains of the current regulator can be expressed as in (2-8). The denominator terms in equations (2-6) and (2-7) are the determinants of the current controller dynamic response. In order to obtain the PI controller gain parameters, they are compared with the standard second-order response equation shown in (2-8).

$$\frac{\omega_n^2}{s^2 + 2\xi\omega_n s + \omega_n^2} \tag{2-8}$$

The damping ratio (ζ) and natural bandwidth (ω_n) for the current regulator can be expressed as follows, using equations (2-9) and (2-10), respectively:

$$\omega_n = \sqrt{\frac{k_{ic}}{k_{pc}}} \tag{2-9}$$

$$\xi = \frac{R + k_{pc}}{2L_s\omega_n} \tag{2-10}$$

To achieve the desired dynamic and static response, the values of ζ and ω_n are typically set based on the fundamental frequency and switching frequency. With these values, the proportional and integral gains of the current regulator can be calculated accordingly. While the tuning method is straightforward to apply, it may come with drawbacks due to the presence of a zero in the closed-loop transfer function, as shown in equations (2-6) and (2-7). An examination of the impact of this zero on control performance reveals that it can enhance dynamic performance and will not pose a significant challenge to the system stability.

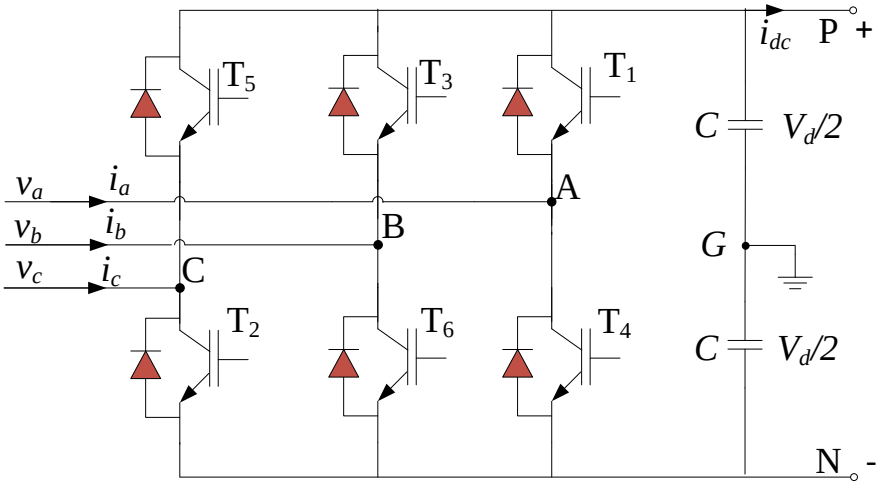


Figure 2.18 Two-level three-phase active front end (AFE) rectifier.

2.1.4.3 Converter Model

The need for high power quality in MEA systems has led to the adoption of active-front-end converters (AFE) as a potential replacement for traditional transformer rectifiers. AFE converters offer improved electrical behaviour while maintaining robustness and safety requirements. Two-level and three-level converters, especially the neutral point clamped topology, are considered suitable for aircraft applications [99]. In this thesis, a two-level converter (shown in Figure 2.18) is chosen over a three-level converter for its simplicity and intrinsic reliability due to the minimal number of devices. Besides, the focus of this research is on designing and testing the control scheme, and the two-level converter serves this purpose effectively.

The converter, like the PMSG, is modelled in the dq rotating frame. In this frame, the AC voltage of the power converter is expressed as

$$v_c = \sqrt{v_d^2 + v_q^2} \tag{2-11}$$

where v_d and v_q are peak voltages. As depicted in Figure 2.19, the d-axis and q-axis components of the AC-side terminal voltage can be represented as follows:

$$v_d = \frac{1}{2} m_d v_{dci} \tag{2-12}$$

$$v_q = \frac{1}{2} m_q v_{dci} \tag{2-13}$$

where m_d and m_q represent the modulation indices in their respective directions.

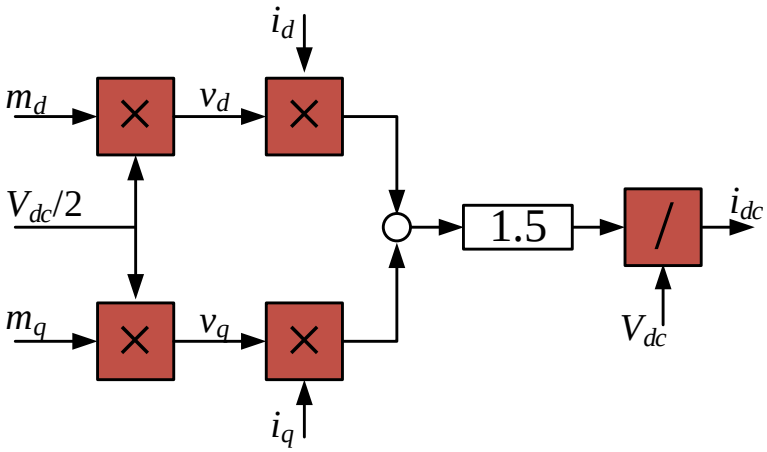


Figure 2.19 Model of a two-level active front-end (AFE) power converter in dq frame.

The real power at the AC-side terminal of the two-level AFE can be represented as in (2-14).

$$P = \frac{3}{2}\left(v_d i_d + v_q i_q\right) \tag{2-14}$$

Assuming negligible power loss in the converter, the power balance between the DC and AC sides can be expressed as

$$V_{dc} i_{dc} = \frac{3}{2}\left(v_d i_d + v_q i_q\right) \tag{2-15}$$

where i_{dc} represents the output DC current flowing into the capacitor.

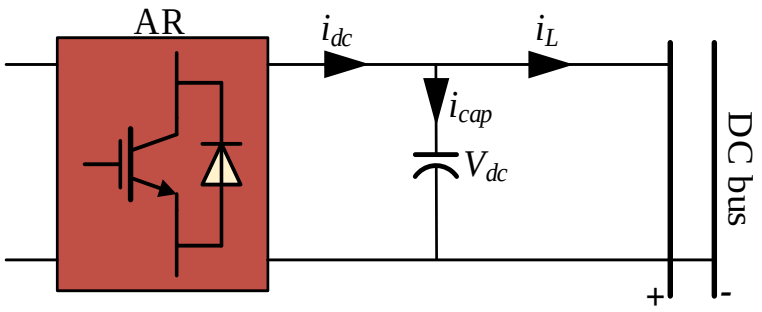


Figure 2.20 DC-link model

2.1.4.4 DC-link Model

In the DC-link model shown in Figure 2.20, the magnitude of the current passing through the DC-link capacitor (i.e., i_{cap}) is dependent on the current supplied to the DC-link by the AC-DC converter. The dynamics of the DC-link can be expressed using equation (2-16).

$$\frac{dV_{dc}}{dt} = \frac{i_{dc} - i_L}{C_b} \tag{2-16}$$

In (2-16), i_{dc} represents the current generated from sources, i_L is the output current for loads, and C_b is the capacitance of the DC-link. Assuming that the interconnecting cable impedance can be neglected, the DC link voltage (V_{dc}) will be equal to the main bus voltage (V_{bus}). The nominal voltage of the main bus is typically defined based on specific standards, such as MIL-STD-704F for MEA. For instance, a nominal voltage of 270V is specified, and a voltage range between 250V and 280V is considered acceptable for MEA applications [49].

2.1.4.5 Load Model

Conventional aircraft primarily rely on electric power to energize avionics, lighting, entertainment systems, and galleys. However, the evolution of power electronics has paved the way for MEAs to incorporate additional electric loads, such as air conditioning, pressurisation, flight controls, fuel pumps, and wing ice protection [99]. In general, the electric aircraft DC

grid experiences a mix of constant impedance loads (e.g., wing ice protection) and constant power loads (CPLs), as indicated in equation (2-17).

$$P_L = P_{res} + P_{cpl} = \frac{v_{dc}^2}{R_{res}} + P_{cpl} \tag{2-17}$$

where P_{cpl} and P_{res} represent the total power of the CPL and resistive load, respectively, and R_{res} denotes the resistance of the resistive load. The voltage-current relationship can be expressed as in (2-18)

$$i_L = \frac{V_{bus}}{R_{\text{res}}} + \frac{P_{\text{cpl}}}{V_{bus}} \tag{2-18}$$

In simulation studies, the constant power load (CPL) can be effectively represented as a controllable current source. The model diagram depicting the load combination is illustrated in Figure 2.21.

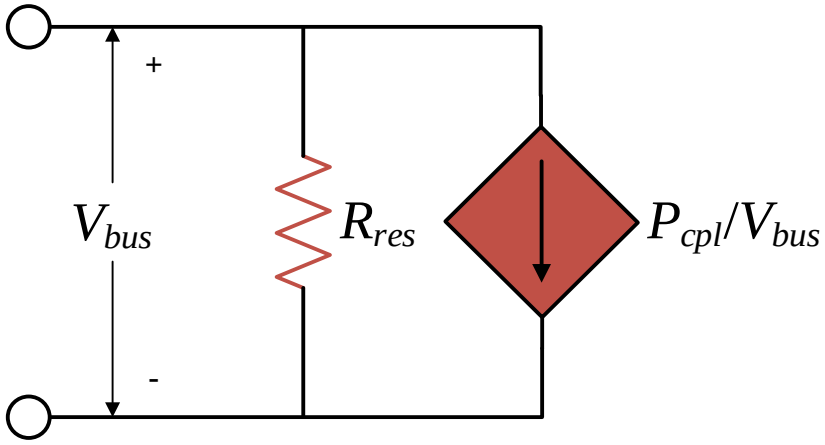


Figure 2.21 Load model combining constant impedance load (CIL) and constant power load (CPL).

The subsequent subsections will present a detailed review of load sharing among the parallel sources.

2.2 Power Sharing Control Methods

After examining the existing electrical loads in the MEA, it is important to address the issue of load power sharing within the multiple generator-based single-bus architecture. The studied

architecture shown in Figure 2.15 can be considered a challenging case of islanded DC MG [94]. Therefore, the power sharing methods utilised in DC MGs can be extended to the EPS examined in this thesis. Implementing power sharing control enables system-level optimisation, including improvements in efficiency and power management. From a communication perspective, power sharing control can be categorised into three methods: centralised control, distributed control, and decentralised control [100]. These methods will be further explained and illustrated in the subsequent sections.

2.2.1 Centralised control

The centralised control method is commonly employed in distributed generation (DG) based DC grids, as shown in Figure 2.22 [101]. In this approach, a centralised controller is utilised to regulate the DC bus and coordinate the operation of various power modules, such as PMSGs. The DG data is collected and processed by a centralised aggregator, and feedback commands are then transmitted through a digital communication network to the individual DG units and their corresponding local controller (LC), as illustrated by the dashed lines (in blue colour).

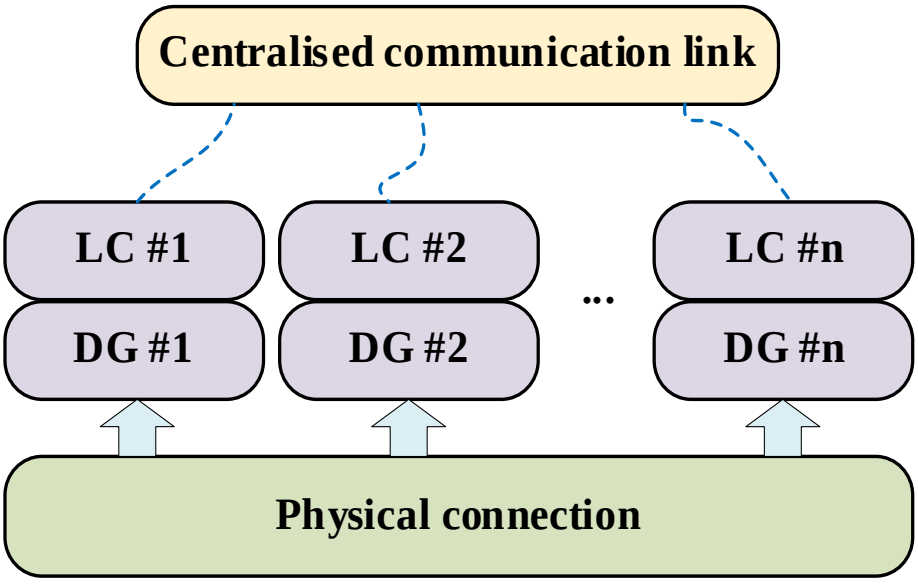


Figure 2.22 Centralised control operating principle in DC EPS.

In small-scale grid systems, centralised control is relatively straightforward to implement, as depicted in Figure 2.23. The central controller manages the voltage regulation of the DC bus and determines the current references for each power module by dividing the total current reference based on the rated power ratio of the sources [28], [102]. The splitting of the total

current reference is based on the rated power ratio of the sources and can be achieved through average splitting [102] or unequal splitting algorithms [103]. Examples of applications where centralised controllers are used in MGs can be found in [104], [105].

Alternatively, master-slave control can be implemented as a substitute for centralised control. This configuration involves designating one module as the "master" and the remaining modules as "slaves" [106], [107], [108]. The master module takes charge of regulating the DC-link voltage and generating current references for the slave modules as shown in Figure 2.24. The advantage of master-slave control is that it eliminates the need for an additional central controller, resulting in cost reduction. However, it is worth noting that master-slave control presents greater challenges in implementation compared to centralised control.

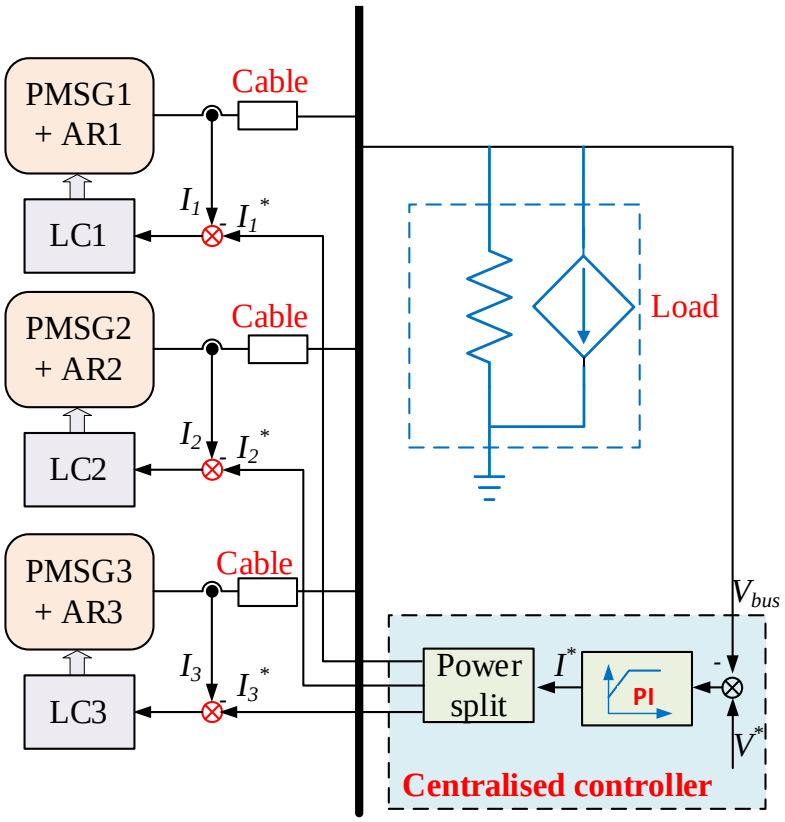


Figure 2.23 Control scheme of centralised control.

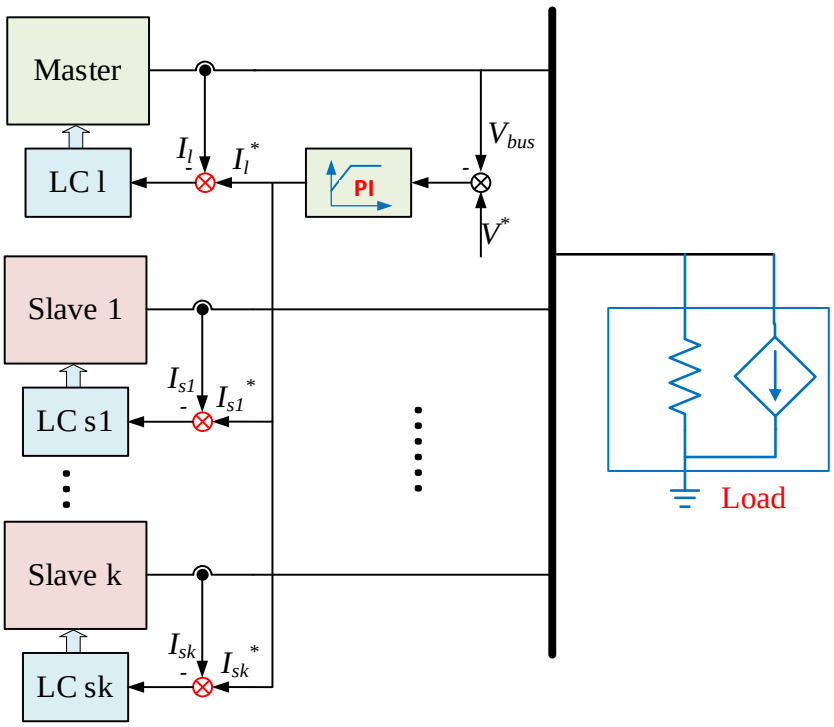


Figure 2.24 Control scheme of master-slave control.

Centralised control offers notable advantages in terms of voltage regulation and current-sharing performance. It provides a robust framework for achieving the desired objectives of the entire system under the management of a single operator [109]. However, the major drawbacks of the centralised control strategy are that it has a single point of failure, needs high speed communication, and provides less reliability [110]. If the central controller fails (a single point of failure), it can result in the shutdown of the entire MG, impacting its operation and functionality. In addition, the dependence on communication networks for data exchange limits its application to smaller-scale grid systems, as large-scale systems may experience constraints in communication bandwidth [109]. In such cases, hierarchical control, which combines local converters and coordinated control through digital communication links (DCL), becomes a preferred choice [111], [36]. Hierarchical control provides a certain level of independence between control levels, ensuring system reliability even in the event of centralised control failure [112], [113], [114], [115].

2.2.2 Distributed control

The distributed control method operates without a central control unit, relying instead on communication between local controllers through dedicated DCL, as shown in Figure 2.25.

One key advantage of this approach is its ability to maintain full functionality even in the event of communication link failures, as it is not reliant on a single point of control [116]. This resilience to single-component failures makes distributed control a robust and reliable solution.

In the distributed control strategy, local controllers exchange information that is limited to locally available variables. This means that if two local controllers are not directly connected by a DCL, they do not have direct access to each other's data and their system observation is constrained. However, this limitation can be mitigated by employing consensus algorithms, as described in [117]. These algorithms enable local controllers to achieve a level of awareness comparable to that of a centralised controller, facilitating the seamless achievement of objectives such as voltage restoration, output current sharing, and overall system efficiency improvement [118], [119]. Furthermore, the distributed control architecture offers greater flexibility and reliability when compared to the centralised control method [100], [120].

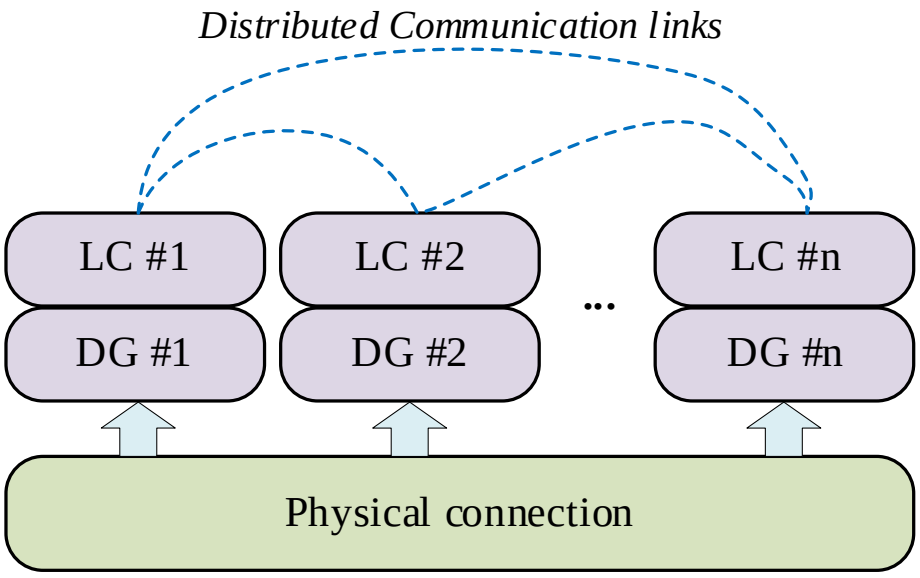


Figure 2.25 Operating principles of distributed control in DC EPS.

Despite the many benefits of the distributed control method, analysing the performance of distributed control in MGs can be complex due to its decentralised nature. Additionally, the interconnections required between individual units in the distributed control scheme may reduce system redundancy and flexibility [121]. It is important to note that distributed control in MGs has been studied extensively in the literature, with various implementations and investigations found in references [119], [40], [122]. The work presented in references [119]

utilises a distributed control model to establish a primary/secondary control structure for DC MGs. Each converter within the system is equipped with both current and voltage regulators. The proposed cooperative control scheme ensures accurate global voltage regulation and facilitates load sharing among the converters. In [40], droop control is described as the primary control method for achieving load current sharing in DC EPS applications. The average DC voltage and current are controlled using two PI controllers, which are guided by a low-bandwidth communication-based consensus algorithm. However, the approach employed in [40] only utilises static averaging, assuming that all units can communicate with each other. Alternatively, [122] demonstrates the application of a consensus algorithm in a modular DC-DC converter system, where each converter serves as a node in the communication graph. The communication graph layout can be randomly selected. In comparison to [40], the methods proposed in [119] and [122] require only neighbour information and utilise a sparse communication graph across the DC EPS, resulting in a reduced number of communication lines. Additional studies that utilise the distributed control approach, specifically for AC MGs, can be found in references [123, 124, 125].

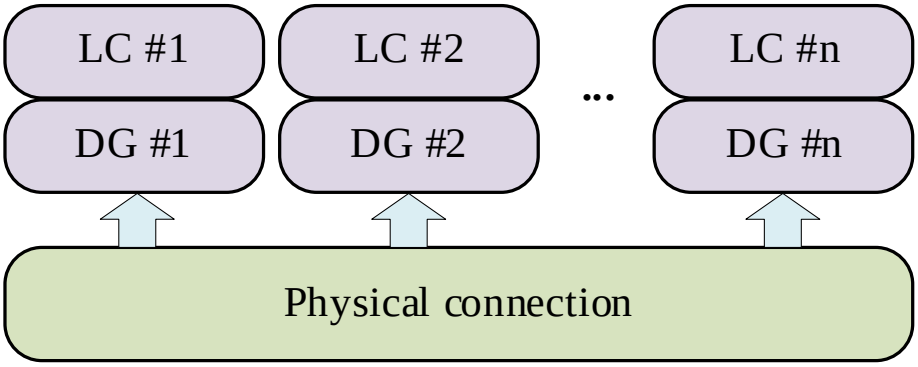


Figure 2.26 Operating principles of decentralised control in DC MGs.

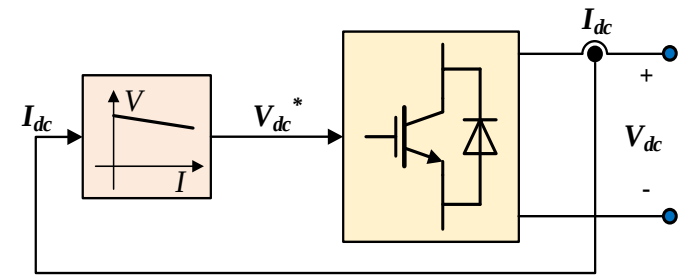
2.2.3 Decentralised control

Decentralised control employs local measurements and local controllers to regulate individual components without the need for communication between units, as shown in Figure 2.26. In the event of a module failure, the remaining modules can still contribute to power sharing by following their droop settings, thereby enhancing system reliability [111]. This control principle offers the advantage of easy control implementation and independence from digital communication networks. Additionally, each parallel module can operate independently using

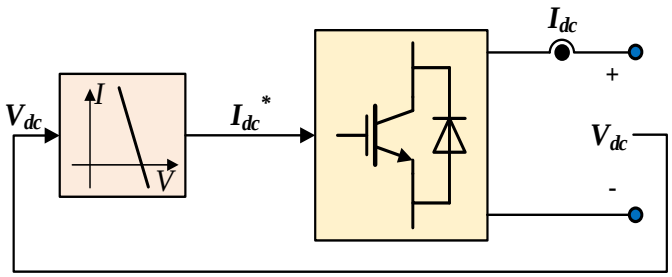
only LCs and measurements, eliminating the need for costly communication networks [121]. However, the absence of a communication network results in limited information exchange between units, which can restrict the performance of the system.

Droop control is considered a decentralised control method that operates independently of a communication network. It is used to achieve parallel operation and current sharing among multiple sources in a power system. The droop control is realised by adding a "virtual resistance" to the local voltage controllers of the sources to regulate their power sharing. This virtual resistance limits the flow of circulating current and helps prevent excessive power flow between sources. The "virtual resistance," also known as the droop gain, droop constant, or droop coefficient, differs from a "real resistance" in that it remains constant regardless of working conditions such as temperature. Unlike real resistance, virtual resistance does not produce actual power losses and does not vary with environmental factors. A virtual resistance is an ideal value used in the context of control systems. Therefore, by operating independently and without the need for a communication link, droop control provides reliable and cost-effective control.

The droop control method has been extensively used in traditional AC electrical power system grids [111, 126, 127]. Its reliability, simplicity, and modularity have made it a successful choice for power sharing among parallel sources and converters in DC systems [40]. Unlike AC systems, where "reactive power" is applicable, DC systems transfer only active power. The amount of active power transferred in the DC network can be determined by the voltage. Thus, a similar droop control mechanism can be implemented in DC systems by establishing a relationship between active power (P) and voltage (V) to achieve the desired load sharing through voltage adjustments. In some cases, the P-V droop can be expressed as an I-V droop, which is also a common type of DC droop [128]. The voltage mode (i.e., V-I strategy) and current mode (i.e., I-V strategy) droop control strategies can be illustrated using Figure 2.27 (a) and (b) respectively [128].



(a)



(b)

Figure 2.27 Droop characteristics (a) V-I droop (b) I-V droop.

In the voltage-mode droop control method, the output current is measured and then fed into the V-I droop characteristics, as shown in Figure 2.27 (a). Subsequently, the calculated reference voltage, V_{dc}^*, is provided to the inner voltage controller. The DC voltage is then regulated based on the V-I droop characteristics. Conversely, the current-mode droop control method is implemented by measuring the output DC voltage, which is then input to the I-V droop characteristics, as illustrated in Figure 2.27 (b). Additionally, the calculated reference current, I_{dc}^*, is supplied to the inner current controller, and the injected current is controlled in accordance with the I-V droop characteristics. The voltage controller references for the voltage mode drop control strategy and the output current reference for the current mode droop control strategy can be calculated as shown in (2-19) and (2-20) respectively.

$$V_{dci}^* = V_{dc}^* - k_{di} I_{dci} \tag{2-19}$$

$$I_{dci}^* = \frac{V_{dc}^* - V_{dci}}{k_{di}} \tag{2-20}$$

In the context of the droop controller, let's denote i as the number of subsystems, V_{dci}^* as the output, which represents the reference value of the DC output voltage of the ith converter. V_{dc}^*

corresponds to the rated value of the DC voltage. I_{dci}^{*} is the generated reference DC current of the *i*th converter. The coefficients k_{di} is the droop gain associated with voltage-mode and current-mode droop control startegies. Additionally, I_{dci} represent the output current of the *i*th converter.

As a decentralised control method, droop control can enhance power sharing while promoting system modularity and reliability. However, the presence of impedance in the interconnecting cable can impact droop control performance, and the cable resistance is susceptible to changes like temperature variations. To address the influence of cable resistance, the droop gain needs to be adjusted accordingly, but this adjustment involves a trade-off in the droop gain design. Illustrating the effect of mismatched cable resistances on droop control, we can take the example of the two parallel-connected DC sources depicted in Figure 2.28. Figure 2.29 illustrates the V-I droop characteristics curve for the two parallel connected DC sources, highlighting the unequal load sharing caused by the impact of mismatched line resistances within the system. Observing Figure 2.29, it can be observed that when the droop gain for the converters is set small, identical, or comparable to the mismatched line resistance R_{ci}, the current sharing error (I_{dc1} - I_{dc2}) becomes significantly high. Conversely, setting a high droop gain larger than the line resistance ($k_{di} \gg R_{ci}$) can mitigate the impact of unequal line resistance on current sharing, reducing the current sharing error. However, this approach may result in poor bus voltage regulation (as shown in Figure 2.29), which is unacceptable for many practical applications due to threats to system stability and power quality.

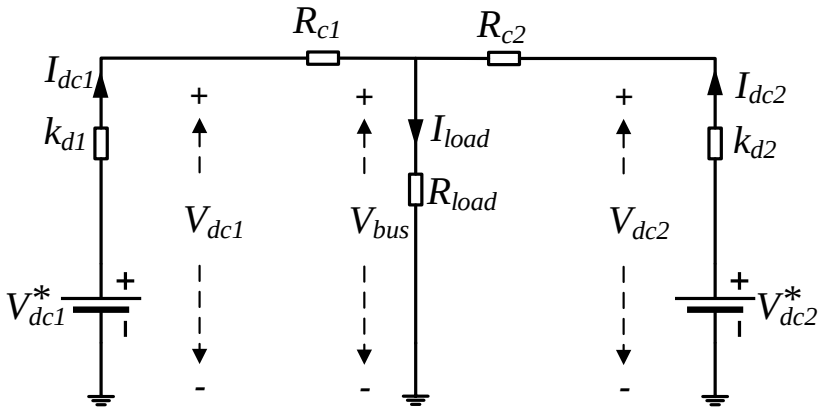


Figure 2.28 Two-source single load DC MG

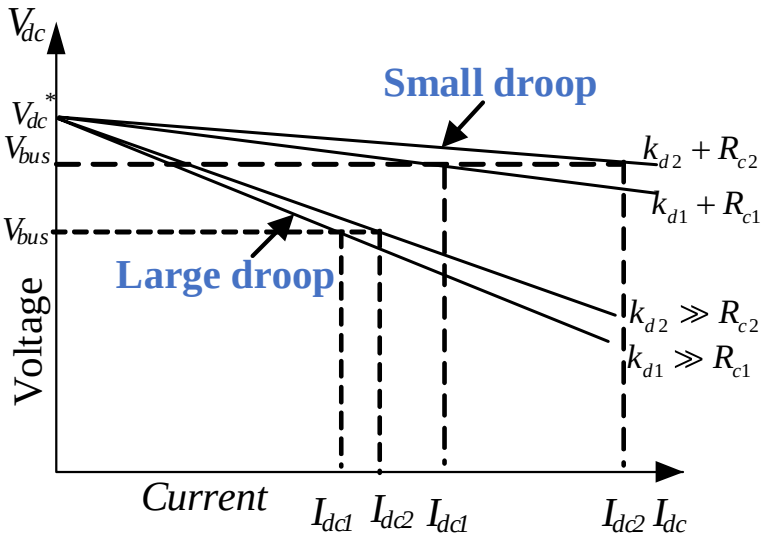


Figure 2.29 Trade-off between power sharing accuracy and voltage regulation.

Table 2-2 Comparison of Various Control Principles

	Centralised control	Distributed control	Decentralised control
Communication medium	DCL	DCL	Power Line
Modularity	Low	High	High
Centralised controller	Yes	No	No
Reliability	Low	Medium	High
Single point of failure	Yes	No	No
Advantages	Flexible and serves as the best foundation for the use of advanced control functionalities.	Not affected by a single point of failure.	Local measurement and regulation
Disadvantages	Single point of failure and limited to small-scale DC EPS.	Complex analytical performance analysis.	Depends only on local variables, hence, the lack of global information.

Despite the inherent trade-off, droop control remains a viable and competitive solution for distributed DC EPS, suitable for both small and large-scale systems, as it offers advantages such as independence from communication channels, increased system reliability, and modularity. Therefore, the design and optimisation of converters' droop coefficients play an important role in striking the right balance between accurate current sharing and satisfactory DC bus voltage regulation. In [129], a novel droop method is introduced for converter parallel operation to enhance load-sharing performance by regulating the nominal voltage. However, this method has limitations as it only considers equal sharing conditions. In [130], the impact of DC interconnecting cable impedance on DC MG balancing power distribution under droop control is investigated, and an analytical expression for estimating the balancing power distribution accounting for DC line voltage drops is derived. In [131], an adaptive droop control approach is applied for effective power sharing in multi-terminal DC (MTDC) grids, ensuring self-sustaining power sharing, tight DC link voltage control, and prevention of overload during the outage of a power converter. Additionally, [132] proposes a novel voltage control technique for DC-DC converters with an energy storage system (ESS) that combines fuzzy control with gain-scheduling techniques to achieve energy management and power sharing objectives. The approach establishes the relationship between load state and droop gain, enabling simultaneous DC voltage regulation and stored energy balancing without a trade-off between high droop gain and voltage regulation. In [111], a three-level control hierarchy (primary, secondary, and tertiary) inspired by the ISA-95 and electrical dispatching standard is proposed to address the challenges associated with droop control in DC MG systems. This hierarchical structure offers improved load sharing, voltage regulation, flexibility, and intelligence. The primary control level employs droop control with an output-impedance virtual loop for DC output current sharing, while the secondary control level handles voltage restoration and frequency synchronisation by compensating for deviations caused by the primary control. Additionally, the tertiary control level is responsible for energy management, allowing the MG to achieve various objectives such as reduced energy cost and increased efficiency. A summary of the various control principles is provided in Table 2-2.

To summarise, droop control, as a decentralised method, can achieve balanced power sharing among parallel sources by utilising local variable information. Its improved modularity and system reliability make droop control a suitable choice to address power sharing challenges in DC systems.

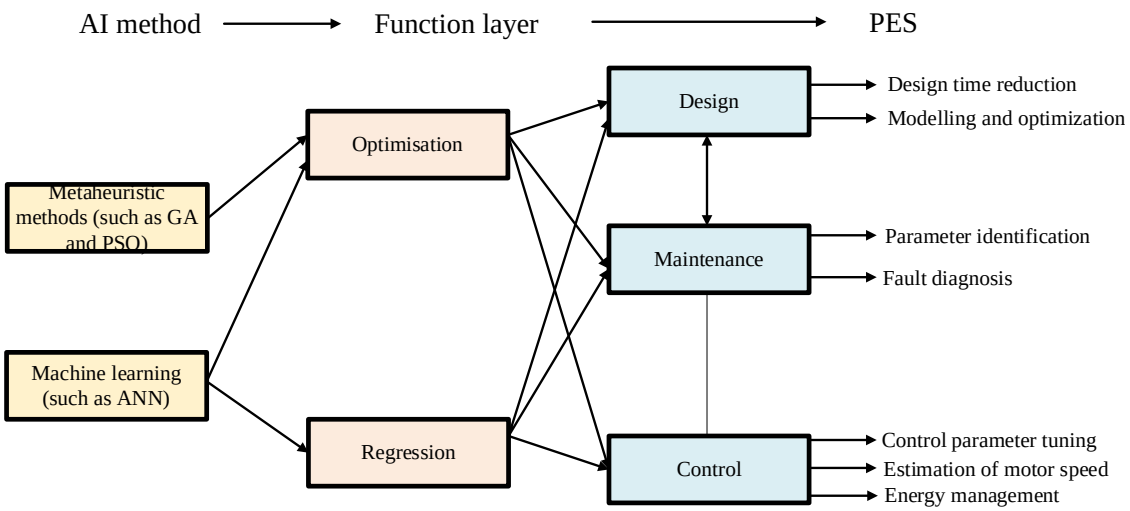


Figure 2.30 Application of some AI methods in power electronic systems (PES).

2.3 Artificial intelligence techniques in power electronics and control

The implementation of AI techniques in EPS enables them to learn and reason similarly to human beings, leading to improved system performance [133]. AI has found widespread use in various industrial applications, including computer vision, autonomous vehicles, image classification, and speech recognition, due to its numerous advantages. In the field of power electronics, AI has been extensively applied for tasks such as design optimisation, system health estimation, and intelligent control, spanning over the last three decades. A comprehensive review of AI applications in power electronics is available in [133], covering design [134], control [135], and maintenance phases [136], with AI often utilised for optimisation tasks in the design phase of PES [137]. The important functions of AI, serving as an intermediary layer between AI and power electronic applications as shown in Figure 2.30, can be classified into optimisation, classification, regression, and data structure exploration. However, this thesis solely focuses on optimisation and regression aspects.

Optimisation: Optimisation using AI involves finding the best solution for a given problem, aiming to either maximise or minimise the objective functions while considering user-defined constraints and conditions. This technique is extensively used in system parameter design tasks to identify the optimal set of parameters that lead to desired system performance. In essence, optimisation helps explore and determine the most suitable parameters that fulfil design goals within specified constraints [133].

Regression: Regression in AI involves establishing a relationship between input and output variables through training. Once trained, the AI technique can predict output variables based on given input variables. This is particularly useful in control applications, where a regression model can establish a functional relationship between input signals and control output variables, enabling intelligent controllers to predict control variable values based on input electrical signals [133].

The field of power electronics extensively utilises AI methods, including expert systems, fuzzy logic, metaheuristic methods, and machine learning techniques. A comprehensive review [133] emphasizes the widespread application of AI in power electronics, with a focus on regression and optimisation tasks using machine learning techniques. In the following subsection, we will explore metaheuristic methods and machine learning techniques, which are particularly relevant and extensively applied in power electronics.

2.3.1 Metaheuristic methods

Metaheuristic methods serve as efficient and scalable tools for optimisation tasks in power electronics, avoiding the need for complex calculations of gradient and Hessian matrices. These methods, inspired by biological evolution, include trajectory-based (e.g., tabu search and simulated annealing) and population-based methods (e.g., genetic algorithm (GA), particle swarm optimisation (PSO), and ant colony optimisation (ACO).

In [138] and [139], the PSO technique is utilised to tune the parameters of the PI controller and determine the optimal droop coefficient. In [138], the objective functions for optimisation involve minimising the error in measured power and improving damping characteristics in both autonomous and grid-connected modes. In the autonomous mode, the power sharing coefficients and controller parameters are optimised. In addition, the design parameters in [138] are optimised to enhance the damping characteristics in both autonomous and grid-connected modes to enhance its stability and minimise the error in the measured power. However, the constraint used for searching the optimal design parameter settings requires the need to carry out a small-signal model analysis. On the other hand, [139] focuses on achieving stable coordination of multiple DGs interfaced with inverters for effective active and reactive power sharing, while also enhancing the control of the inverters against disturbances like voltage and frequency. In [140], a novel enhanced droop control method is introduced, incorporating virtual

impedance, and coupling compensation into the basic droop control for AC MG applications. The virtual impedance parameters are optimised using an improved particle swarm optimisation (IPSO) algorithm, eliminating the need to calculate the line resistance. However, the accuracy of current sharing relies heavily on the proper tuning of the virtual impedance. Meanwhile, [141] proposes an approach to determine the optimal droop settings of dispatchable DG units in an islanded DC MG, aiming to minimise total operational cost and emissions. This bi-objective optimisation problem is solved using the fuzzy membership function and PSO. The harmony search (HS) algorithm is employed in [142] to search for the optimal droop resistance that will minimise the current sharing error.

Population-based methods are commonly used due to their superior convergence speed and global searching capability, with GA and PSO being the most popular. However, they are heuristic and have an intensive computational burden [133]. In addition, for every design objective, a new set of simulations are required [39] to find the optimal droop gain. Another drawback includes the possibility of being stuck in the local optimum due to the premature convergence of the results of the optimisation [143, 144]. Thus, there is no guarantee that their solutions are globally optimal.

2.3.2 Machine Learning

Machine learning (ML) is a subset of AI that allows computer algorithms to recognise patterns and behaviours in power electronics systems by learning from collected data. Machine learning algorithms have gained significant popularity in power electronics applications owing to their ability to learn non-linear system behaviours rapidly and efficiently. Their advantage lies in not relying on explicit knowledge of the physical system model, allowing them to accurately map and establish relationships between desired system parameters [145]. This capability presents a significant advantage for electrical power system parameter design and optimisation. ML can be categorised into supervised learning, unsupervised learning, and reinforcement learning. These data-driven algorithms can work with both structured and unstructured data to make decisions based on previous experiences and collected information [133], [146].

2.3.2.1 Supervised learning

Supervised learning involves establishing implicit mappings and functional relationships between input and output data pairs in a training dataset [145]. This approach is particularly

beneficial in power electronics, where formulating system models can be complex. Supervised learning encompasses tasks like classification, which deals with labelling discrete categories, and regression, which predicts continuous variables [133], [147]. Once the model is trained, it can evaluate new data points from a testing dataset, and its generalisation on new inputs is important for its performance. Supervised learning methods in power electronics can be classified into connectionism-based methods (e.g., neural networks), probabilistic graphical methods, and memory-based methods (e.g., kernel methods) [133]. Neural network (NN) methods utilise connection weights and structures to learn from training data, with fuzzy neural networks (FNN) and recurrent neural networks (RNN) improving robustness and dynamic performance, respectively. Probabilistic graphical methods use diagrams to represent conditional dependence relationships and are well-suited for handling uncertainty and incomplete knowledge. Kernel methods, such as support vector machine (SVM) and relevance vector machine (RVM), utilise a subset of the training dataset for testing and are more efficient for smaller datasets [133].

2.3.2.2 Unsupervised learning

Unsupervised learning operates without labelled data, allowing it to autonomously detect patterns from unlabelled datasets. It is used for tasks such as clustering, compression, and analysis of data [145]. For example, it can be applied in medical imaging, fault diagnosis, and computer vision. While it offers the advantage of not requiring labelled data, it often necessitates longer training times and larger datasets, leading to increased computational complexity and a higher risk of generating inaccurate results. Nonetheless, unsupervised learning serves as valuable data preprocessing for subsequent analytics, aiding in reducing the computational burden and improving accuracy [133], [148].

2.3.2.3 Reinforcement learning

Reinforcement learning (RL) stands apart from supervised and unsupervised learning as it does not rely on a training dataset [145]. Instead, RL aims to find an action strategy that maximises rewards for a specific task through trial-and-error interactions with systems or simulation models, allowing it to progressively accumulate experience and learn a strategy that achieves predefined goals [133], [149]. This dynamic programming approach is advantageous in cases

where existing datasets are limited, or the system model is difficult to formulate. One practical application of RL is maximum power point tracking (MPPT) [150].

Among the machine learning methods, supervised learning takes the lead in its application to power electronics. This dominance stems from the versatility of supervised learning, making it a central and widely used tool in various machine learning-related applications within power electronic systems [133].

2.3.3 Artificial Neural Networks (ANN)

Artificial Neural Networks (ANNs) are a class of machine learning models inspired by the structure and function of biological neural networks found in the human brain [151]. They are powerful tools used for various tasks, including pattern recognition, classification, regression, and optimisation. The structure of an ANN is shown in Figure 2.31. The feedforward neural network (FFNN) is the most frequently employed type of ANN in power electronics applications [133]. The choice of FFNN is driven by its simple structure. In an FFNN, data flows in a forward direction, starting from the input layer and progressing through the hidden layer(s) before reaching the output layer [152]. In various applications, the FFNN is utilised to take advantage of its static nonlinear mapping property [133]. In [153], an FFNN is used for waveform processing and delay less filtering. The FFNN is capable of converting m-phase waveforms with different shapes, frequencies, and magnitudes into n-phase waveforms with various characteristics. This approach simplifies hardware implementation and allows for easy embedding of additional single processing functions due to its flexible structure. Also, in [154], an FFNN is used to implement Space Vector PWM (SVPWM) for a three-level voltage-fed inverter. The NN takes sampled command phase voltages as input and generates pulse width patterns for SVPWM as output. The training data are generated through simulation using an SVPWM algorithm. The performance of the FFNN-based SVPWM is compared with a conventional DSP-based solution, demonstrating its flexibility in implementation on a dedicated IC chip.

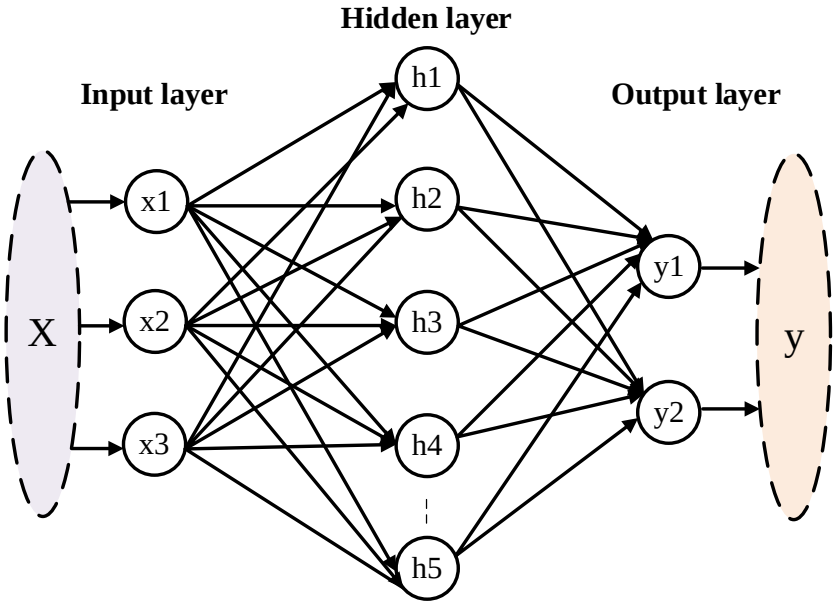


Figure 2.31 Artificial neural network representation.

As the name implies, data is feedforward from the input to the output (as shown in Figure 2.31) and there is no feedback from the output to the input. The basic FFNN structure consists of an input layer which receives the data or features that are fed into the network for processing, a hidden layer and an output layer which produces the final result or prediction of the ANN's task. Depending on the problem's complexity, the FFNN structure can be expanded to contain more than one hidden layer as shown in Figure 2.31. The hidden layers, if present, process the input data through a series of weighted connections. Each neuron in the hidden layers applies a transformation to the data based on its corresponding weights and biases. These hidden layers help the network learn complex patterns and representations from the data [151].

There exists a certain number of neurons in each of these layers. The neurons present in each layer process the information coming from the neurons in the layer before it. The training dataset is usually divided into two: input and output data. The number of parameters in the input and output data used for training determines the number of neurons in the input and output layers respectively. However, for the hidden layer, the number of neurons is determined by the system designer. Each neuron applies an activation function, which introduces non-linearity to the model. Common activation functions include sigmoid, tanh, and ReLU (Rectified Linear Unit) [151]. During training, the network adjusts the weights and biases associated with each connection to minimise the error or loss function between the predicted output and the actual

target output. The training process in ANNs typically involves backpropagation, where the error signal from the output layer is propagated backwards through the network to update the weights and biases. This iterative process helps the network improve its predictions over time [151].

Assuming the inputs supplied to the input layer are x_1 to x_N, where N denotes the number of inputs. These inputs are multiplied with their respective weights w_{ik}^l and then added to the bias value b_k^l. The weight and bias values are updated during the training iteration. The results are processed with the aid of an activation function σ. The sigmoid symmetric transfer function (i.e., tansig) shown in (2-21) is considered in this thesis as the activation function. The generated neuron output in layer l becomes h_i^l. The same procedure is repeated to compute the output of other neurons in the other layers. The expression for the signal flow of the ANN for each layer and the output of the FFNN is expressed in (2-22)-(2-24).

$$\left(\sigma(\gamma) = \left(2 \middle/ (1+e^{-2\gamma})\right) - 1\right) \tag{2-21}$$

- Layer 1 (input):

$$h_i^1 = x_i, \qquad i = 1,\ldots,N_l \tag{2-22}$$

where x_i represents the inputs.

- Layers (hidden):

$$h_i^1 = \sigma\left(\sum_{k=1}^{N_{l-1}} w_{ik}^l h_k^{l-1} + b_k^l\right), \qquad i = 1,\ldots,N_l \tag{2-23}$$

where $k = 1,\ldots,N_{l-1}$

- Layer (output):

$$y_i = w_i^l h_i^L, \qquad i = 1,\ldots,N_l \tag{2-24}$$

where y_i represents the outputs.

AI methods offer a solution to improve the formulation of design objectives in power electronics system (PES) design. By employing surrogate models, computational efforts are significantly reduced, as these models mimic the behaviour of complex system dynamics that are difficult to characterise or computationally intensive. The conventional design process in PES design involves time-consuming iterative steps and may rely on expert intuition without sufficient data for reference. ANN-based surrogate models act as efficient replacements, reducing design time and enabling more reliable and efficient design processes. These surrogate models are excellent alternatives for solving power electronics problems that require complex computer simulations or physical experiments, accurately predicting outputs across the entire design space while replacing detailed simulation models [133, 155, 156]. To that end, in this thesis, ANNs are chosen as a fundamental tool for parameter identification and control design in the MEA HVDC distribution network aiming to contribute towards advancements in power system control and optimisation. ANN's flexibility allows them to handle complex functions and intricate data patterns, making them suitable for addressing the challenges in the power system [151]. However, overfitting, where the model performs well on training data but poorly on unseen data, is a common challenge in training ANNs. Despite this challenge, ANNs have achieved remarkable success in various domains, such as image and speech recognition, natural language processing, and control systems.

2.4 Summary

Considering the emphasis on weight reduction for MEA, the Permanent Magnet Synchronous Generator (PMSG) is chosen for power generation due to its high efficiency and power density compared to other electrical machines. HVDC power distribution technology is adopted due to its popularity, high reliability, efficiency, and ease of interconnecting different power sources. Three control approaches are presented: centralised, distributed, and decentralised control, with a comparison of their pros and cons. The decentralised control is favoured for its high reliability, modularity, and dependence on local variables, making it effective for mitigating source contingencies and communication breakdown. The chapter identifies ANN as the suitable AI and ML algorithm for parameter identification and control design in the thesis, owing to its flexibility in dealing with complex power systems.

Chapter 3 Optimal Droop Control Design using ANN.

The design of the droop coefficient is one of the challenges for the droop control of converters, as it plays a key role in enhancing the performance of the droop control method. This chapter presents an ANN optimisation-based technique for the design of optimal droop control of parallel-connected converters in a fast and accurate manner, without imposing an additional computational burden on the system. The developed ANN-based design strategy of droop coefficients is used for load sharing and DC bus voltage regulation for MEA application. In the design process, the optimal droop coefficient setting is obtained by evaluating a user-defined fitness function with the aid of a trained ANN-based surrogate model. The system performance metrics predicted by the surrogate model are compared with that obtained from the simulation model.

3.1 Introduction

As described in Chapter 2, this thesis focuses on studying a promising single-bus HVDC EPS architecture for the future more electric aircraft (MEA) electrical power system (EPS). This architecture consists of multiple parallel-connected sources and multiple loads (see Figure 2.15). In this setup, PECs act as essential elements connecting electrical sources and loads [38, 155]. One of the most widely used PECs topologies is the voltage source converter (VSC). The control of these PECs' interfacing sources to the MG is a key issue in the MG's operation especially concerning the sharing of the load power demand among the sources and voltage regulation [38, 39].

The droop control method is widely adopted for load sharing and voltage regulation in DC MGs due to its independence from communication networks, high reliability, and modularity [111, 157]. This control technique involves introducing a virtual resistance, known as the droop coefficient or droop gain, in series with the converter on the DC bus side to dynamically adjust power sharing. The droop gains are usually predetermined and fixed for each PEC, determined based on the converter's current ratings to achieve proportional current sharing. However, the

conventional droop control has limitations in achieving accurate load sharing and voltage regulation due to practical factors such as mismatched interconnecting cable impedance and nominal voltage reference offset.

As a rule of thumb, when the droop gains of the converters are selected to be large, there is almost a guaranteed accurate power sharing among the sources [111]. This is because the influence of cable resistance on power sharing becomes negligible. However, this results in poor regulation of the DC bus voltage, due to the unequal voltage drops across the transmission cables connecting the paralleled converters to the DC bus, particularly under heavy load conditions. Also, the use of a large droop coefficient has the potential of affecting the system's stability [40]. On the other hand, when the droop coefficient selected for the converters is small, the regulation of the DC bus voltage is enhanced while the power sharing accuracy is degraded [158]. Hence, a trade-off exists between power sharing accuracy and voltage regulation when using the droop control method [159]. Therefore, finding an optimal droop coefficient becomes important in striking the right balance between accurate load sharing and acceptable voltage regulation.

Over time, several approaches have been proposed to enhance the droop control method's performance. Some strategies suggest using a large droop coefficient for improved load sharing [36, 160, 161], but they are only suitable for small-scale MGs where interconnecting cable resistance is negligible [162]. A communication network is required in [161] to compensate for the huge deviation in the DC bus voltage due to the large droop coefficient. The use of a communication link will reduce the reliability and modularity of the droop control method and increase the cost. Other methods, like the general piecewise droop (GPD) design in [163], offer improved load sharing and voltage compensation but involve complex strategies based on different load regions. Adaptive droop control is another option [164, 165, 166, 167], adjusting the droop gain based on the system's loading condition, but it requires online parameter estimation and communication links [168]. An enhanced droop control strategy [158, 169, 170], independent of communication networks, adjusts the droop coefficient using estimated cable resistances. The line resistance is estimated by actively injecting a pulse disturbance into the system [169, 170]. The injection of disturbance has the potential of affecting the power quality of the system.

It can be observed that the existing proposed approaches have limitations, such as reliance on communication, computational complexity, or the need for accurate subsystem parameters. Therefore, some of these approaches may not be robust and reliable in ensuring optimal performance for different MGs, especially when the system parameters are difficult to obtain. To overcome these challenges, an alternative solution is to explore intelligent and efficient computing techniques for determining the optimal droop coefficient of the converters, ensuring robust and reliable performance in various MG scenarios.

This chapter proposes a possible solution to improve the performance of the traditional droop control method by employing the ANN-based optimisation for the design and selection of the optimal droop coefficient of power converters without incurring an extra computational burden on the EPS and reducing the design time. To carry out an efficient and reliable design process, the usual procedure used in the design of a power electronics system (PES) parameter involves performing optimisations to find the optimum design parameter that will yield the best performance. This design process involves running many simulations by using different combinations of the design parameter as input. These are usually time-consuming and computationally expensive. In this regard, the AI method can be employed as a surrogate model to serve as a replacement for the original PES to reduce the design time [133, 156]. Surrogate models are excellent alternatives for solving power electronics problems that require carrying out complex computer simulations of physical experiments. The main purpose of the surrogate model is to accurately predict the output of a detailed simulation model or experiment across the whole design space while replacing the original detailed simulation model. By exploring different combinations of the droop coefficients in the design space, the desired ANN can be trained efficiently after data generation. Based on the design criteria, the ANN can be used to quickly find the optimal droop coefficient. Moreover, it mitigates the risk of getting stuck in local optima, a common issue with other intelligent optimisation techniques like Genetic Algorithm (GA) and Particle Swarm Optimisation (PSO). Unlike other methods, the proposed approach directly provides the best design for any additional sub-design space, eliminating the need for further data collection and training. Additionally, the power system designer is not required to define the relationship between training data and a pre-defined function, simplifying the process. Furthermore, the modularity and reliability of the traditional droop control method are maintained as no additional communication links are necessary.

The main research contributions of this chapter are as follows:

- Introducing an ANN-based optimisation approach for selecting the optimal droop coefficient of the converter, which is a new technique that has not been explored in previous works.
- Achieving quick and accurate determination of the optimal droop coefficient after training significantly reduces the design time. The approach requires only a small amount of data collected from simulations.
- Implementing the NN offline and utilising the optimal droop coefficient online during HIL experiments, ensures no additional computational burden on the EPS during implementation.
- Validating the effectiveness of the proposed approach through simulations and HIL experiments.

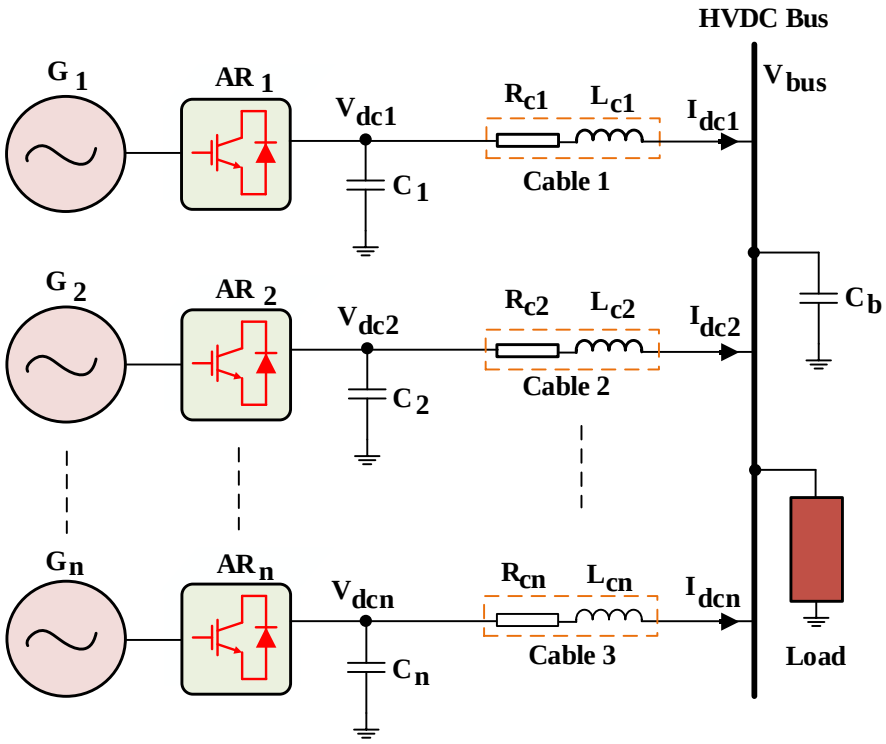


Figure 3.1 Typical Single bus Multi-source HVDC architecture for future MEA EPS.

3.2 System Description

Figure 3.1 illustrates a potential multi-source DC grid architecture for the future MEA EPS distribution network. The power sources ($G_1 \ldots G_n$) are assumed to be permanent magnet synchronous generators (PMSGs), drawing power from the aircraft engine. These sources are connected to the main HVDC bus (operating at 270V or 540V) through pulse-width-modulated

active front-end controlled rectifier units (AR_1-AR_n) and transmission cables. Each source is regulated and controlled by its corresponding AR unit. The main DC bus is equipped with a capacitor bank denoted as C_b, while the local converters have output capacitors C_1-C_n. The electrical loads on the MEA include constant power loads (CPLs) and resistive loads.

The MEA EPS, referred to as the PMSG-AR systems, can be operated as either current sources or voltage sources, depending on the chosen control strategy. In this thesis, the voltage-mode droop control scheme, based on the approach proposed in [94], is adopted for achieving current sharing among the sources. Figure 3.2 depicts the voltage-mode droop control scheme implemented for a single PMSG-AR system.

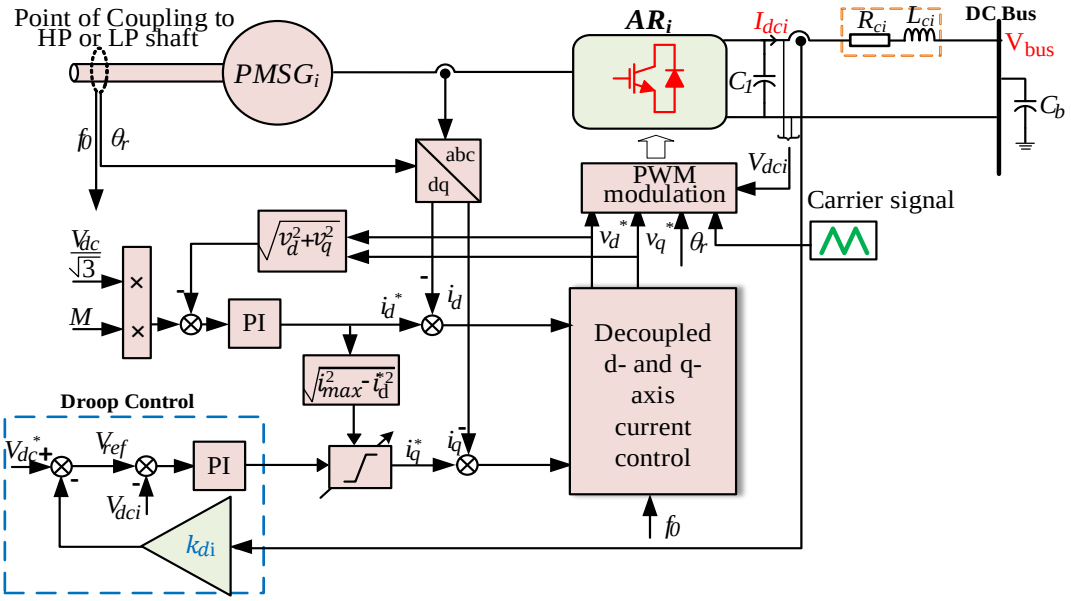


Figure 3.2 Control diagram of the PMSG-AR system controlled using the voltage-mode droop control scheme.

The control structure is designed in a cascaded manner, with the inner loop responsible for regulating the d- and q-axis currents. To accommodate the high-speed operation of the PMSG in the MEA application, flux-weakening control is usually applied at the outer loop, involving injecting a negative component of the flux current i_d into the machine. Additionally, the PMSG operates as a generator, and the DC link current I_{dc} is regulated by the droop characteristics within the outer loop. The modulation index M (represented as "M" in Figure 3.2) plays a crucial role in the control process. While Figure 3.2 shows the control structure for a single

PMSG-AR system, it's important to note that the thesis considers three parallel-connected PMSG-AR systems. The control structure remains the same for each of these multiple systems.

3.3 Problem Formulation

To achieve load sharing and voltage regulation in the DC MG, a droop control mechanism is widely employed. For simplified analysis, Figure 3.3 presents the steady-state equivalent circuit model of a two-source system. The droop-controlled parallel-connected sources with the interfaced converters (i.e., the PMSG-AR systems) are represented as an ideal voltage source followed by a virtual resistance, as depicted in Figure 3.3. Additionally, the interconnecting cable impedance connecting the parallel-connected converters to the DC bus is approximated as resistance for the analysis of the steady-state operation.

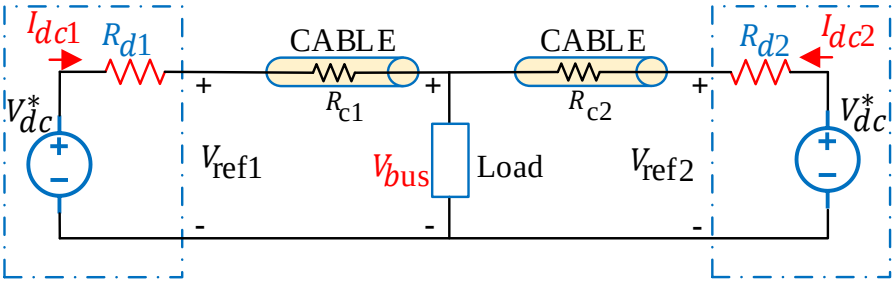


Figure 3.3 Steady-state equivalent circuit model of a droop-controlled DC MG formed by two (PMSG-AR) systems and one resistive load.

In the droop control mechanism, to realise load sharing, the output voltage reference of each converter drops when the output current increases [40]. The terminal voltage is regulated based on the measured branch output DC current, I_{dci}. The output voltage reference of the converters, derived using the droop control method, is expressed in (3-1).

$$V_{ref\,i} = V_{dc}^* - R_{di} I_{dci} \tag{3-1}$$

where the fixed virtual droop coefficient and the nominal bus voltage (270 V) are denoted as R_{di} and V_{dc}^* respectively. The value of the droop coefficient for each converter is typically limited and determined based on the current ratings of the converters, as shown in (3-2).

$$R_{di} \leq \frac{\delta V_{\max}}{I_{d\,ci\,\max}} \tag{3-2}$$

where I_{dcimax} is the maximum/full-load output current of the *i*th converter and the maximum allowable deviation of the DC bus voltage is δV_{max}. The expression (3-2) sets the value of the droop coefficient for each converter, ensuring that the voltage deviation at their output, caused by the droop control mechanism, remains within the maximum allowable value δV_{max}. δV_{max} is typically set at around 5% of the nominal voltage [171]. It ensures that the voltage variation is limited and helps maintain stable operation within acceptable margins, even during load variations.

Neglecting the interconnecting cable resistance, expression (3-3) provides the current sharing ratio between the sources in a steady state. This ratio determines how the load current is distributed among the parallel-connected sources.

$$I_{d\,ci} I_{dc1} : I_{dc2} = \frac{1}{k_{d1}} : \frac{1}{k_{d\,2}} \tag{3-3}$$

where $k_{d1}=R_{d1}$ and $k_{d2}=R_{d2}$ are the droop gain of the converters. The droop gain for each PEC is typically chosen to enable proportional current sharing based on their power ratings. As shown in equation (3-3), the droop coefficients are inversely proportional to the current ratings of the converters. This design ensures accurate current sharing among the sources when applying the same nominal voltage to each droop characteristic, assuming the interconnecting cable resistance can be neglected. However, in larger and low-voltage DC MGs, neglecting the transmission cable impedance becomes impractical, as it has a predominantly resistive nature and impacts the droop controller's performance. The limitations of the traditional droop control method, including the effects of transmission cable impedance, are further discussed in detail in the following subsections.

3.3.1 Degradation of the DC Bus Voltage

As shown in equation (3-1), the droop control function causes the converter's output voltage to decrease as the output current increases. However, these deviations can be controlled within an acceptable range by appropriately selecting the droop gains of the PECs, as indicated in the conventional droop gain design expressed in (3-2). Nevertheless, these deviations in the output

voltage of the converters can lead to the degradation of the DC bus voltage. Moreover, when considering the voltage drop across the distribution cable impedance, the deviation in the bus voltage becomes more pronounced. As a result, if the voltage drop on the cables is taken into consideration and voltage control dynamics are neglected, the steady-state bus voltage V_{bus} is determined as follows:

$$V_{bus} = V_{refi} - R_{ci} I_{dci} = V_{dc}^{*} - (k_{di} + R_{ci}) I_{dci} \tag{3-4}$$

where R_{ci} is the resistance of the cables.

3.3.2 Degradation in the Current Sharing Accuracy

Similarly, due to the voltage drop across the unequal interconnecting cable resistance, the output DC voltage at the terminal of each of the parallel-connected PECs will be different. Thus, leading to poor load sharing among the sources.

From (3-4), it can be derived that,

$$(k_{di} + R_{ci}) I_{dci} = (k_{dj} + R_{cj}) I_{dcj} \qquad \forall i, j = 1, ..., N \tag{3-5}$$

Therefore, based on the expression in (3-5), the sources will share the load current demand between them according to the ratio expressed in (3-6).

$$I_{dc1} : I_{dc2} = \frac{1}{k_{d1} + R_{c1}} : \frac{1}{k_{d2} + R_{c2}} \Leftrightarrow \frac{I_{dc1}}{I_{dc2}} = \frac{k_{d2} + R_{c2}}{k_{d1} + R_{c1}} \tag{3-6}$$

It is obvious from (3-6) that the current sharing ratio between the converters will be affected by the unequal interconnecting cable resistance and the droop gain of the converters in steady states. In this chapter, we expand the two-source system depicted in Figure 3.3 to include three sources. By doing so, we can calculate the current sharing ratio between the converters using the equations in (3-7) and (3-8), where the current of converter 1 serves as the reference value.

$$n_1 = \frac{I_{dc2}}{I_{dc1}} = \frac{k_{d1} + R_{c1}}{k_{d2} + R_{c2}} \tag{3-7}$$

$$n_2 = \frac{I_{dc3}}{I_{dc1}} = \frac{k_{d1} + R_{c1}}{k_{d3} + R_{c3}} \tag{3-8}$$

where n_1 and n_2 are the current sharing ratio between converter 1 and 2, and converter 1 and 3 respectively. These current sharing ratios will not be as desired when using the traditional fixed and identical droop coefficient obtained using the expression in (3-2). This can be attributed to the influence of the unequal cable resistance on the current sharing performance of the conventional droop control method. Also, the DC bus voltage regulation expressed in (3-4) can be normalised as expressed in (3-9).

$$V_{bn} = \frac{V_{bus}}{270} \tag{3-9}$$

From (3-7) and (3-8), the line impedance between generator connected ARs and the main DC bus has a significant impact on power sharing between different sources. This is extremely true for aerospace applications, where two main generators and converters (assuming AR1 and AR2) are located within the engine nacelle and another generator set (assuming to be AR3) is within the auxiliary power unit located at the tail of the aircraft. These 3 ARs are connected to DC bus bars located at the power distribution centre at the centre of an aircraft fuselage with long cables. Achieving equal power sharing and maintaining DC bus voltage regulation poses a significant challenge for the droop control method. One approach to ensure accurate power sharing is by setting the droop gains to values much larger than the line resistances (i.e., $k_{di} >> R_{ci}$). By doing so, the power sharing accuracy improves as the influence of line impedance is mitigated. However, the application of large droop gain will compromise the bus voltage regulation as well as load current will result in a large voltage drop. This thesis thus proposes a better approach to achieve accurate power sharing and acceptable voltage regulation while mitigating the impact of the line impedance.

3.4 Proposed ANN-based Droop Coefficient Design Approach

This section introduces the utilisation of ANNs to optimise the droop coefficient of the converters, aiming to minimise errors in the current sharing ratio between the converters and achieve acceptable DC bus voltage regulation. The methodology for the proposed droop coefficient design and selection process will be thoroughly discussed in this section. Additionally, the structure and training of the ANN will be presented.

3.4.1 Methodology

The overall flowchart of the proposed design approach is shown in Figure 3.4. As shown in Figure 3.4, the design methodology involves three stages (i.e., A, B and C). These stages are efficiently carried out offline. In stage A, the studied MEA EPS's detailed simulation model is run in a loop for every combination of the droop gains: k_{d1}, k_{d2}, and k_{d3} (used as input to the simulation) within a design range. The output DC currents of the converters (i.e., I_{dc1}, I_{dc2}, and I_{dc3}), and bus voltage regulation V_{bus} are extracted at the end of each simulation. Thereafter, the extracted data is automatically processed to compute the corresponding current sharing ratios between the converters n_1 and n_2 and the normalised bus voltage V_{bn}. The sweep range of the droop coefficient should be pre-defined and selected in such a way that it covers a feasible design space and with high fidelity for the desired control objectives.

In stage B, the processed data is used to train the ANN to become a dedicated fast surrogate model mapping the relationship between the droop gains of the converters (i.e., k_{d1}, k_{d2}, and k_{d3}) and the current sharing ratios between the converters (n_1 and n_2) and normalised bus voltage regulation (V_{bn}). The ANN-based surrogate model will be trained with the droop coefficient combinations as input and n_1, n_2, and V_{bn} as the targeted output following a similar pattern as in the simulation. The trained surrogate model can then be used to predict the current sharing ratio between the converters and normalised bus voltage regulation for any combination of the droop coefficients. An interesting fact about this approach is that the processes involved in stages A and B are required to be executed just once for a particular system configuration and working conditions [39, 172].

In stage C, in the first instance, the design space of (k_{d1}, k_{d2}, and k_{d3}) is sampled with very small steps to generate many design points which are then used as input to the surrogate model. Consequently, the corresponding outputs (n_1, n_2, V_{bn}) can be quickly generated using the surrogate model. Using the surrogate model, it becomes much faster to generate results when compared to the detailed simulation model which is a huge advantage. With a detailed mapping between the droop coefficients (k_{d1}, k_{d2}, and k_{d3}) and control objectives (n_1, n_2, V_{bn}), a user-defined fitness function f_{ann} thus can be utilised to identify the optimal droop gain settings to achieve the desired control objectives. This will be detailed in the following sections.

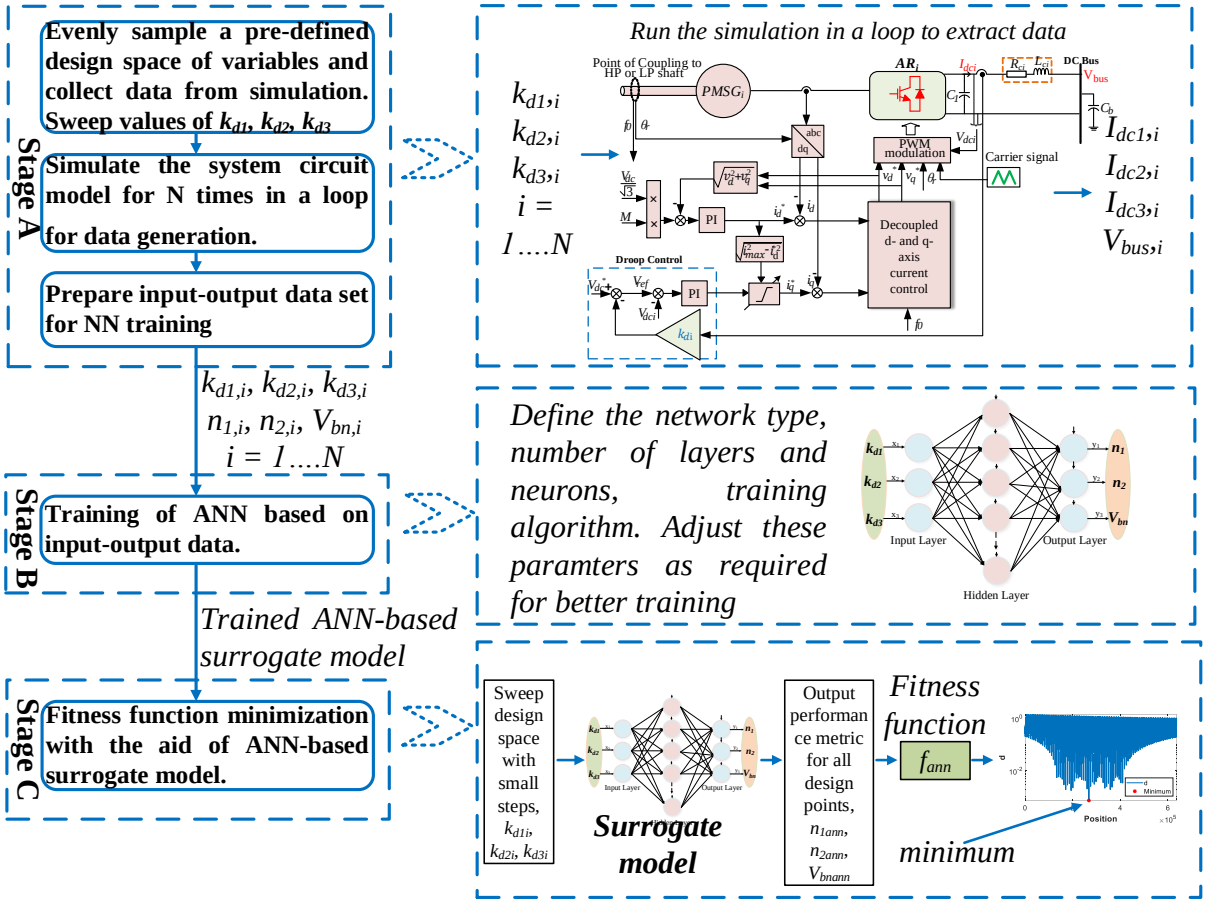


Figure 3.4 Flowchart of the proposed ANN-based design of the droop coefficient in droop control of power converters.

3.4.2 ANN Structure and Training

Various kinds of ANN structures exist in the literature [173], however, the feed-forward neural network (FFNN) is chosen to train the surrogate model. It is an enhanced structure of the ANN that has the capability of solving both linear and non-linear problems due to the introduction of a hidden layer. It has an excellent generalisation capability and can efficiently map the design parameter (i.e., k_{d1}, k_{d2} and k_{d3}) and the performance metrics (i.e., n_1, n_2 and V_{bn}). Details about the FFNN are provided in Chapter 2, Section 2.3.3. The relationship between the design parameter and the performance indicators as represented by the FFNN can be expressed as in (3-10).

$$y = F(x) \Leftrightarrow (n_1, n_2, V_{bn}) = F(k_{d1}, k_{d2}, k_{d3}) \tag{3-10}$$

where x denotes the input to the ANN and y is the output.

Figure 3.5 shows the FFNN model structure used in training the surrogate model. The structure consists of 3 neurons in the input layer, 11 neurons in the hidden layer and 3 neurons in the output layer. It can be observed that the input parameters at the input layer are the droop coefficient combinations $x_1 = k_{d1}$, $x_2 = k_{d2}$ and $x_3 = k_{d3}$. Hence, the number of neurons in the input layer is 3. Also, the output layer contains 3 neurons since the three-performance metrics $y_1 = n_1$, $y_2 = n_2$, and $y_3 = V_{bn}$ are the targeted output. The droop coefficient is the design variable. The surrogate model is trained offline using the Levenberg-Marquardt backpropagation algorithm. The training is executed using the neural network (NN) fitting toolbox available in MATLAB.

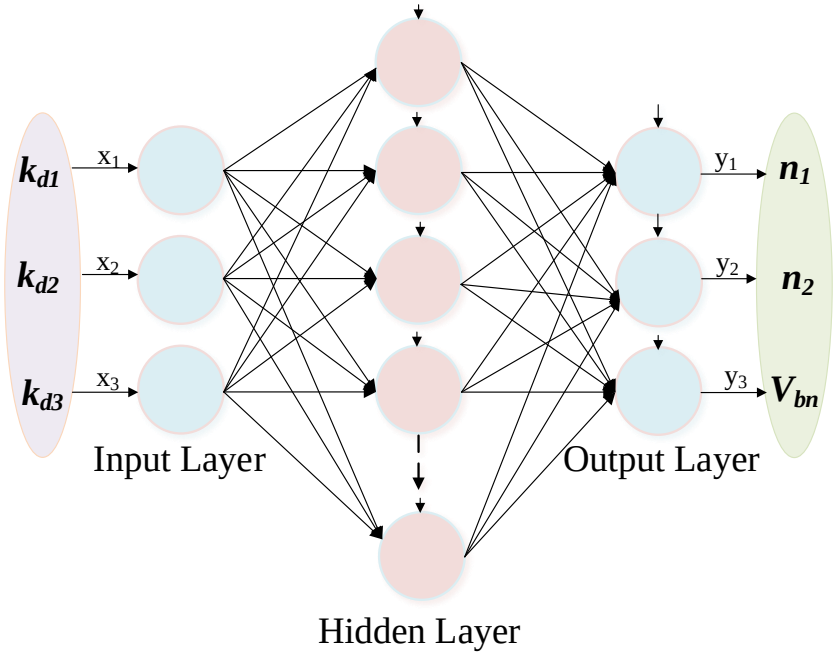


Figure 3.5 Structure of the three-layer FFNN-based surrogate model.

3.5 Application of the Proposed Approach in the Droop Coefficient Design for the MEA EPS

In this section, stages A and B of the proposed design methodology are verified on the single-bus HVDC grid architecture for the future MEA EPS. Furthermore, after training, two design examples will be demonstrated using stage C.

3.5.1 Data generation

The data used for training the ANN-based surrogate model is generated from the detailed MEA EPS control model (shown in Figure 3.2) which is developed in MATLAB SIMULINK©. The parameters used for the simulation are provided in Table 3-1. The data is extracted for a CPL of 40 kW which is considered the maximum load. To ensure a feasible design space with good fidelity, the choice of the design range for the design variables must be selected such that the stability of the system is not affected. To that end, the upper and lower limits of the droop coefficients design range are selected as +10% and -10% respectively of the traditional identical and fixed droop coefficients (shown in Table 3-1) obtained using the conventional droop gain design. The sweep range and sampling step selected for k_{d1}, k_{d2}, and k_{d3} are given in Table 3-2.

Based on the detailed comparative stability analysis of the droop control methods carried out in [174], the maximum value of the droop gain for stable operation is expressed as

$$k_{di} < \frac{V_{dc}^{*2}}{4P_{cpl}} - R_{ci} \tag{3-11}$$

where P_{cpl} is the power of constant power loads connected to the DC bus. By substituting the MEA EPS parameters shown in Table 3-1 in (3-11), the maximum droop gain would be 0.4256. It can therefore be said that the design range selected is within the acceptable limit to ensure stable operation.

As shown in Table 3-2, 11 settings of each of the droop gains are tested, thus, making 1331 droop gain combinations used in the simulation for data generation. The performance indicators n_1, n_2 and V_{bn} are automatically computed at the end of each simulation. The multiple simulations are automated using MATLAB programmed codes. Each simulation run costs around 6 s. The simulation is conducted on a standard computer with 4-core processors. It takes around 35 minutes to collect the data samples. The collected data is utilised for training the ANN-based surrogate model.

Table 3-1 Parameters of the system used as a case study in simulations and HIL experiments.

Category	Parameters	Values
PMSG parameters	Nominal power	45 kW
	Base speed	8000 rpm
	Switching frequency	100 kHz
	Maximum modulation index	0.9
	Pole pair	3
	Stator winding resistance R_s	1.058 mΩ
	Winding inductance L_d=L_q	99 µH
	Flux linkage	0.03644 Wb
Converter, cable, and load parameters	DC-link capacitance C_b	1.2 mF
	Converter dead time T_d	3 µs
	DC link-rated voltage	270 V
	Traditional droop coefficients k_{di}	1/4.25, 1/4.25, 1/4.25
	Cable resistances R_{ci}	3 mΩ, 30 mΩ, 15 mΩ
	Cable inductances L_{ci}	1 µH, 10 µH, 5 µH
	Load power used during data generation	40 kW

Table 3-2 Range and sampling step used in data generation.

Parameter	Range	Sampling Step	Number of Samples
$1/k_{d1}$	[3.825, 4.675]	0.085	11 x 11 x 11 = 1331
$1/k_{d2}$	[3.825, 4.675]	0.085	
$1/k_{d3}$	[3.825, 4.675]	0.085	

3.5.2 ANN-based Surrogate Model Development

The structure chosen for training the surrogate model is illustrated in Figure 3.5. To avoid underfitting or overfitting in the trained surrogate model's performance, it is very important to choose a suitable number of neurons for the hidden layer(s). However, since, this is assigned by the system designer, it is generally advisable to start with a small number of neurons and then gradually adjust this based on the observed training performance [133]. In this chapter, a hidden layer with 11 neurons is utilised, resulting in an excellent match between the training data and the surrogate model's predicted output. The trial-and-error process for adjusting the number of neurons is fast, typically completed within a few seconds [39].

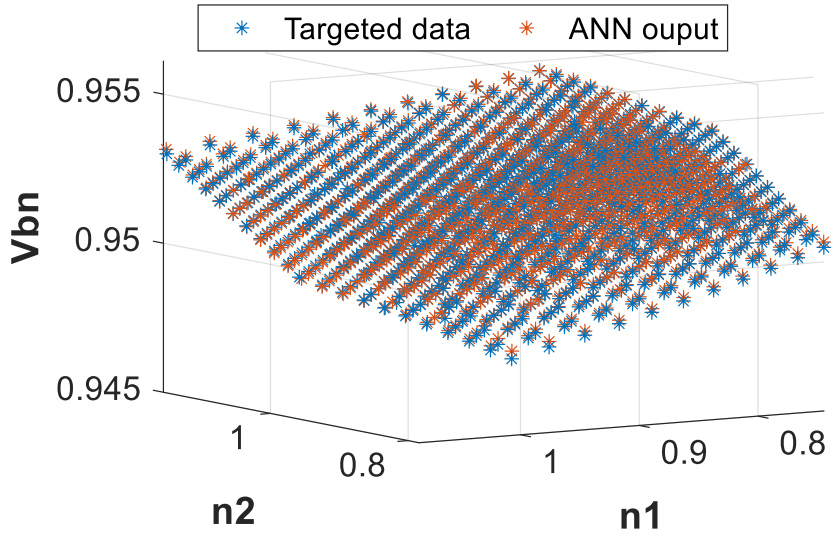


Figure 3.6 Comparison between the 1,331 targeted data obtained from the detailed simulation model shown in Figure 3.2 and the predicted output of the trained ANN model shown in Figure 3.5.

The collected dataset is divided into three parts for training, validation, and testing, comprising 70%, 15%, and 15%, respectively. The training performance is evaluated using the root mean square error (RMSE) between the surrogate model's output and the targeted data used during training. A well-trained surrogate model will have an RMSE close to zero. For n_1, n_2, and V_{bn}, the computed RMSE values are 0.00085733, 0.0012517, and 0.000045932, respectively. Figure 3.6 displays a comparison between the surrogate model's predictions and the target data used for training, demonstrating a very close match between the ANN predictions and the targeted data.

Table 3-3 Range and sampling step used in optimisation.

Parameter	Range	Sampling Step	Number of Samples
$1/k_{d1}$	[3.825, 4.675]	0.01	86 x 86 x 86 = 636056
$1/k_{d2}$	[3.825, 4.675]	0.01	
$1/k_{d3}$	[3.825, 4.675]	0.01	

3.5.3 Design Examples with Different Fitness Functions

The objectives of the optimisation are to minimise the error in the current sharing ratio between the converters and achieve good regulation of the DC bus voltage. Therefore, in this section, the trained surrogate model will be used to find the optimal droop coefficient settings k_{d1}^{opt}, k_{d2}^{opt}, and k_{d3}^{opt} for realizing the desired control performance such as equal power sharing among the generators. At the beginning of the optimisation stage, the droop coefficients are sampled evenly with a small step of 0.01 within the design space as shown in Table 3-3. Thereafter, the trained surrogate model was used to evaluate 636,056 droop gain combinations by predicting their corresponding current sharing ratios between the converters (n_{1ann} and n_{2ann}) and normalised bus voltage (V_{bnann}). It took the surrogate model about 0.16 s to make the evaluation. In order words, it takes the surrogate model approximately about 0.252 µs to output one result. This speed makes it convenient to use an exhaustive search algorithm to find the optimal droop gain settings that minimise the fitness function.

Furthermore, when the data generation and training time is considered, it will only cost the proposed approach approximately about 1 hour to optimise the droop coefficient. However, when compared to the detailed simulation model, it takes about 6s to generate the corresponding current sharing among the converters and DC bus voltage for only one combination of the droop coefficient. Therefore, for the considered 636,056 droop coefficient combinations (i.e., design points), it will take the detailed simulation model 1,060.1 hours or 6.31 weeks to evaluate the whole design points. Hence, the CPU time is reduced by more than 1,058 hours compared to the direct optimisation using the simulation software. This level of speed and accuracy is the motivation behind the use of the ANN design approach. Though it takes time to run detailed simulations to get the required ANN training data, this is justified by

a much faster optimisation of droop coefficient designs in the ANN execution stage. In addition, we do not need to apply any traditional optimisation techniques (e.g., convex optimisation, heuristic algorithms) and have no risk of getting stuck on the local optimum. The randomness introduced during training, such as random weight initialization, helps ANNs avoid convergence to local optima [151].

Even for search algorithm-based optimisation (such as GA and PSO), usually, thousands of samples are needed which would still cost much longer computational time than the proposed approach (which only costs 0.16 s to evaluate 636,056 design points). This is because the computation burden of such optimisation algorithms depends entirely on the simulation model time. However, there are many factors in both approaches which can affect the total computational time. For example, data collection and training in our approach and parameter tuning in search algorithms-based optimisation. The two design examples considered in this chapter are presented in the following subsections.

3.5.3.1 Minimisation of error in current sharing ratios

The first objective (i.e., the first design example) is to find the optimal droop setting to minimise the error in the current sharing ratio between the converters. For a desired equal current sharing among the converters, the current sharing ratios between the converters should be equal to 1 (i.e., $n_{1desired} = 1$, and $n_{2desired} = 1$). The fitness function to achieve this is defined in (3-12). To generate the best design point that will yield this objective, an integrated function d is employed. Using d, the fitness function in (3-12) can be combined as one as shown in (3-13).

$$f_{ann1i} = \begin{cases} f_{ann1_1i} = |n_{1ann} - 1| \\ f_{ann1_2i} = |n_{2ann} - 1| \end{cases} \tag{3-12}$$

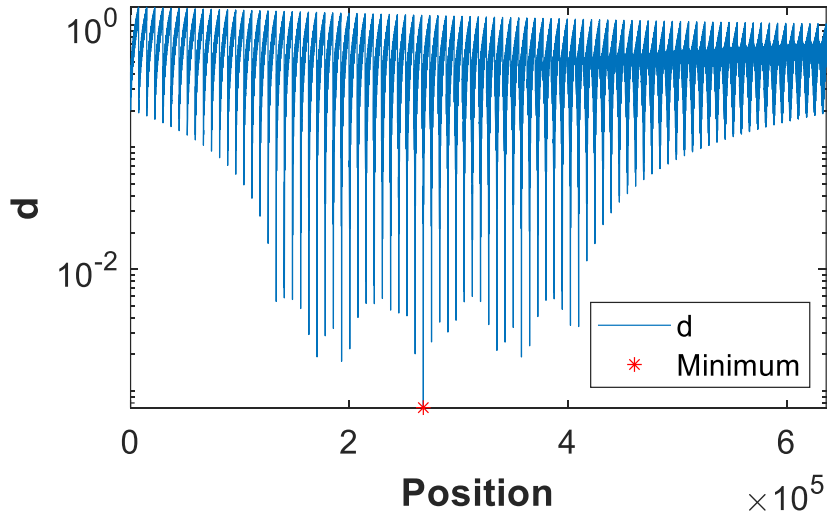
$$d_i = \sqrt{\left(\frac{f_{ann1_1i}}{f_{ann1_1\max}}\right)^2 + \left(\frac{f_{ann1_2i}}{f_{ann1_2\max}}\right)^2} \tag{3-13}$$

where f_{ann1_1i} represents the error in the difference between the ith current sharing ratio between converters 1 and 2 predicted by the surrogate model and the desired current sharing ratio between converter 1 and 2, and f_{ann1_2i} denotes the error in the difference between the ith current

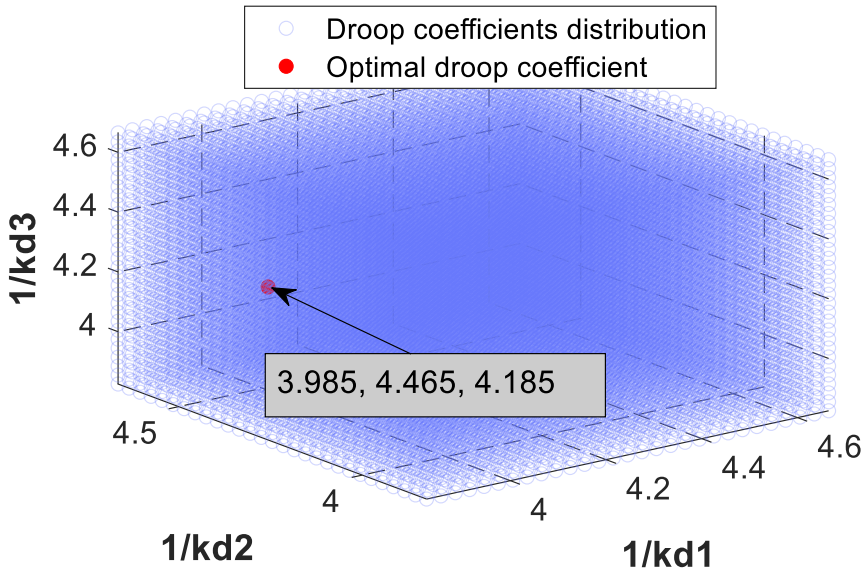
sharing ratio between converters 1 and 3 predicted by the surrogate model and the desired current sharing ratio between converter 1 and 3. The optimal solution can be obtained by finding the index of the minimum value of *d*. This can be realised by simply using the *min* function in MATLAB as an exhaustive search algorithm, as expressed in (3-14).

$$[\min_d, index] = \min(d_i) \tag{3-14}$$

As shown in (3-14), the *min* function can provide the minimum value of *d* and the index (i.e., position) where this value occurs. Therefore, the position of the minimum value of *d* that will correspond to the optimal droop coefficient setting (k_{di}^{opt}) can be found. The plot of the integrated function *d* and the position of its minimum value is shown in Figure 3.7 (a). Consequently, the optimal droop setting at this position was found to be k_{d1}^{opt} = 1/3.985, k_{d2}^{opt} = 1/4.465 and k_{d3}^{opt} = 1/4.185 as shown in Figure 3.7 (b). The corresponding current sharing ratios and normalised bus voltage predicted by the surrogate model are n_{1ann} = 1.0000, n_{2ann} = 1.0000 and V_{bnann} = 0.9511.



(a)



(b)

Figure 3.7 Optimal droop coefficient setting for the fitness function in (3-12) (a) The plot of the integrated function *d* and position of its minimum value at 267,697. (b) Optimal droop coefficient settings that minimise *d* are indicated with a red dot.

3.5.3.2 Minimisation of error in current sharing ratios with good bus voltage regulation

The second objective (i.e., second design example) has to do with finding the optimal droop setting that will provide the best possible current sharing ratios between the converters and acceptable normalised bus voltage. The fitness function for the second design example is expressed in (3-15).

$$f_{ann2i} = \begin{cases} f_{ann1_1i} = |n_{1ann} - 1| \\ f_{ann1_2i} = |n_{2ann} - 1| \\ f_{ann2_1i} = |V_{bnann} - 1| \end{cases} \tag{3-15}$$

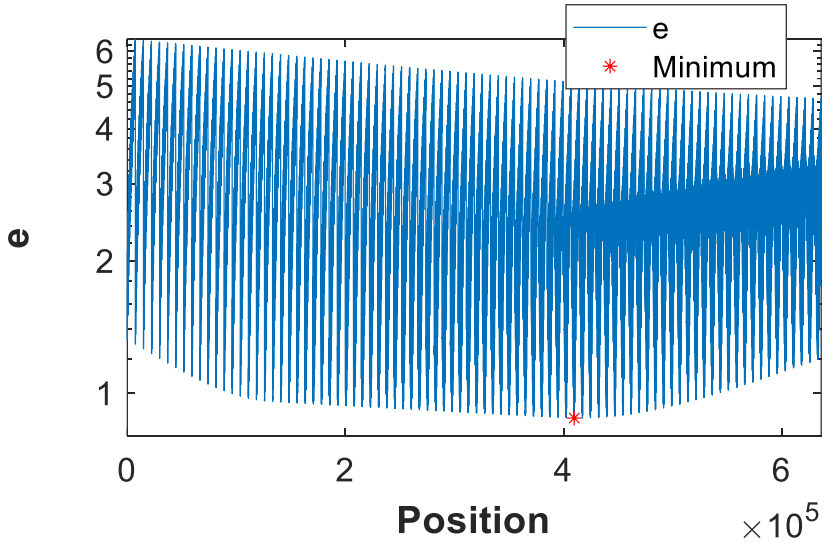
where f_{ann2_1i} represents the error in the difference between the *i*th normalised bus voltage (V_{bnann}) predicted by the surrogate model and the normalised desired system nominal voltage of 1 (i.e., 270 V). Using the integrated function *e*, the fitness function in (3-15) can be combined as one as expressed in (3-16).

$$e_i = \sqrt{20.\left(d_i\right) + \left(\frac{f_{ann2_1i}}{f_{ann2\max}}\right)^2} \tag{3-16}$$

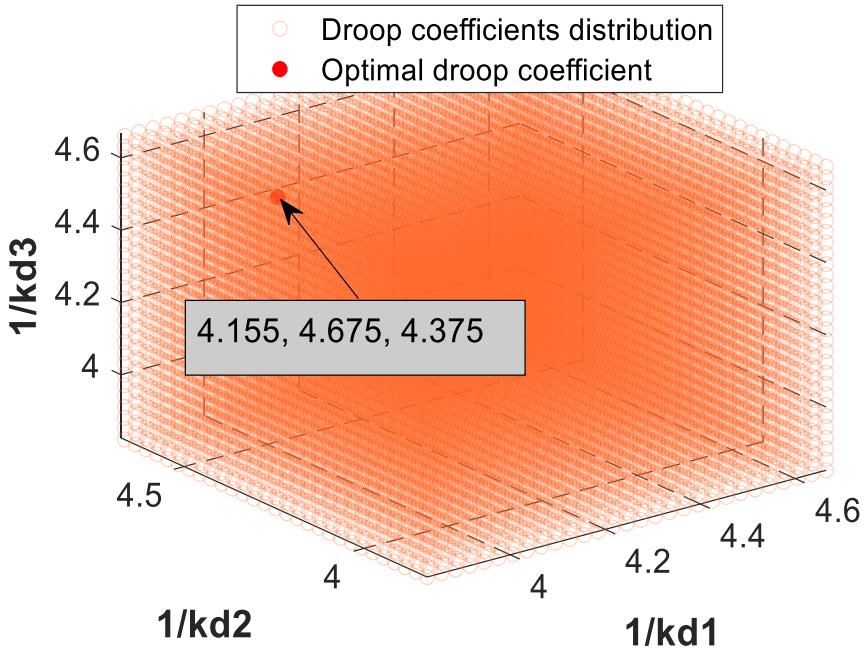
Coefficient 20 was selected in (3-16) to give priority to the minimisation of the error in the current sharing ratios. A value of 1 can be selected when the control objectives have the same priority. The value can be adjusted depending on which of the control objectives has higher priority. However, current sharing is usually accorded higher priority in the operation of the MG [171]. It is important to mention that choosing any other value in (3-16) would provide the optimal droop gain settings that will give the compromise solution (i.e., trade-off) between the control objectives, but the results will be different. The weighting coefficient selection process involves a trial-and-error process. The optimal droop coefficient setting that would guarantee the optimal trade-off between the current sharing and bus voltage regulation can be obtained using the expression in (3-17).

$$[\min_e, index] = \min\left(e_i\right) \tag{3-17}$$

The plot of the integrated function e and the position of its minimum value is shown in Figure 3.8 (a). Consequently, the optimal droop setting at this position was found to be $k_{d1}{}^{opt}$ = 1/4.1550, $k_{d2}{}^{opt}$ = 1/4.6750 and $k_{d3}{}^{opt}$ = 1/4.3750 as shown in Figure 3.8 (b). The corresponding current sharing ratios and normalised bus voltage predicted by the surrogate model at this position are n_{1ann} = 0.9994, n_{2ann} = 1.0005 and V_{bnann} = 0.9532.



(a)



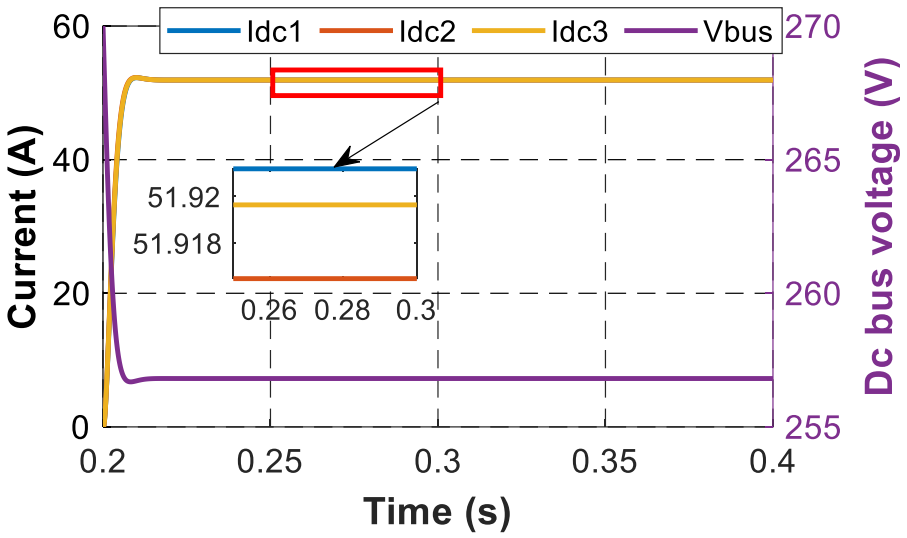
(b)

Figure 3.8 Optimal droop coefficient setting for the fitness function (3-15) (a) The plot of the integrated function *e* and position of its minimum value at 409,704. (b) Optimal droop coefficient setting that minimizes e is indicated with a red dot.

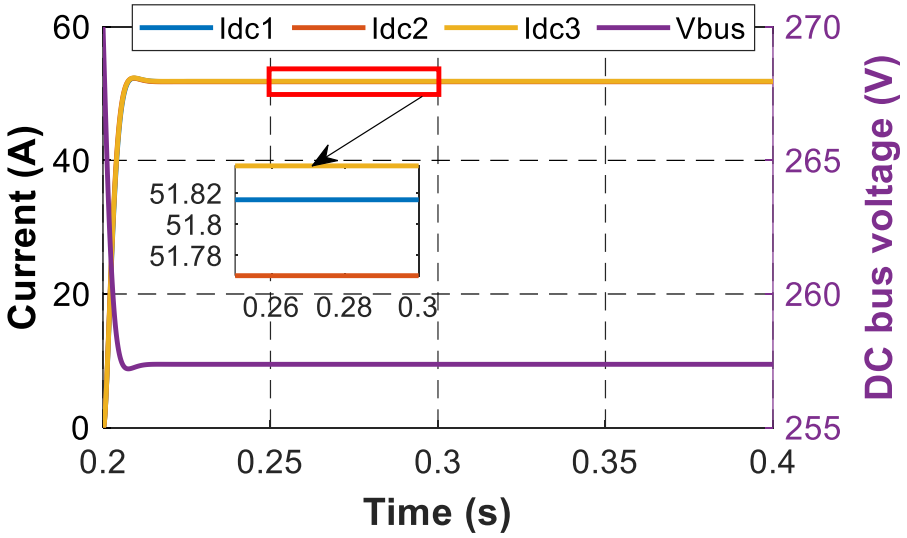
3.6 Simulation Results

To validate these results, simulations of the detailed MEA EPS model, as shown in Figure 3.1, were conducted in MATLAB Simulink. These simulations utilized the optimal droop settings obtained in both design examples. The simulation parameters are as shown in Table 3-1. A CPL of 40 kW was applied at 0.2 s during the simulation. The results obtained are shown in Figure 3.9 (a) and (b) respectively. As shown in Figure 3.9 (a), when the optimal droop coefficient setting from the first design example (shown in Figure 3.7 (b)) is used, the output currents shared among the converters in steady states were I_{dc1} = 51.920 A, I_{dc2} = 51.920 A and I_{dc3} = 51.920 A. Consequently, the calculated current sharing ratios between the converters are n_1 = 1 and n_2 = 1. Similarly, when the optimal droop coefficient setting from the second design example (shown in Figure 3.8 (b)) is used, the output currents shared among the converters in steady states were I_{dc1} = 51.820 A, I_{dc2} = 51.770 A and I_{dc3} = 51.840 A as shown in Figure 3.9 (b). Thus, the calculated current sharing ratios between the converters are n_1 = 0.9990 and n_2 = 1.0004. The result of the bus voltage regulation V_{bus} obtained when using the optimal droop settings from the first and second design examples are 256.8 V and 257.4 V respectively as

shown in Figure 3.9 (a) and (b) respectively. Accordingly, the calculated normalised bus voltages V_{bn} are 0.9511 and 0.9533 respectively. It can be observed that the voltage regulation performance is within the acceptable range (i.e., > $0.950V_{dc}^{*}$). Furthermore, there is an excellent match between the calculated current sharing ratios and normalised bus voltage from the simulation results using the optimal droop settings from the two design examples (n_1 and n_2) and the result obtained using the trained ANN model (n_{1ann} and n_{2ann}).



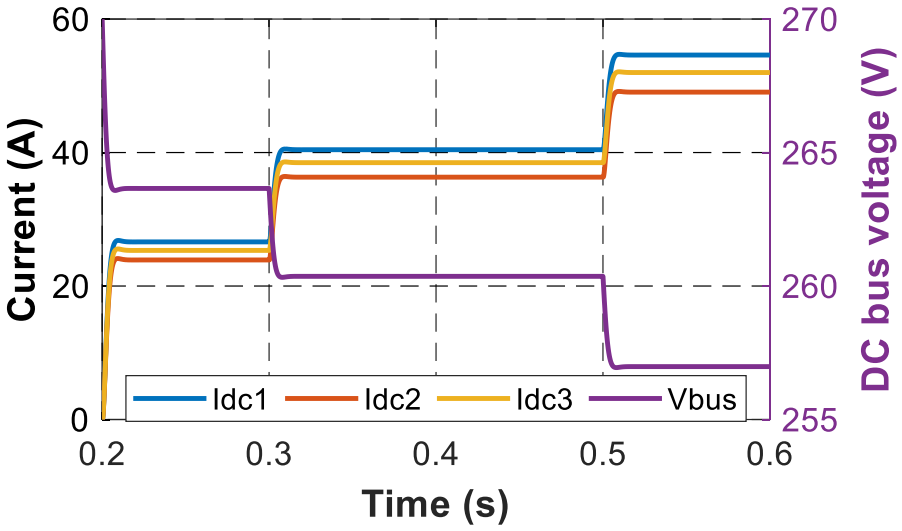
(a)



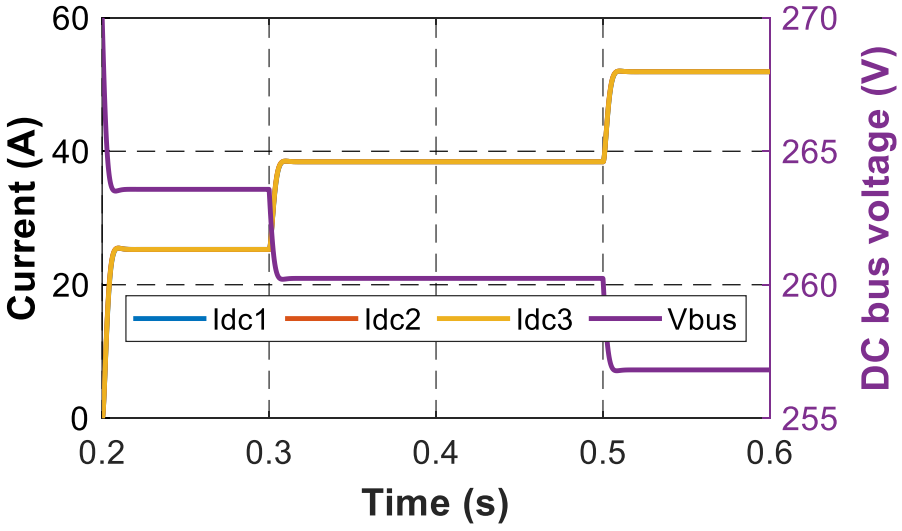
(b)

Figure 3.9 Simulation results for current sharing and voltage regulation using the optimal droop coefficient from (a) the first design example and (b) the second design example.

For clarity and to further show that the proposed approach works well under load changes, a comparison with the traditional fixed and identical droop gains obtained using the conventional droop gain design is carried out using simulation studies. The simulation parameters are the same as those shown in Table 3-1. The traditional droop gains are also shown in Table 3-1. The optimal droop gain settings from the first design example are used for the comparison. CPLs of 20 kW, 30 kW and 40 kW are applied during the simulation at times 0.2 s, 0.3 s and 0.5 s respectively. The results obtained are shown in Figure 3.10.



(a)



(b)

Figure 3.10 Current sharing and bus voltage regulation using (a) Traditional fixed and identical droop gains. (b) Optimal droop gain settings from the first design example.

As shown in Figure 3.10 (a), the traditional droop gains cannot yield accurate load sharing due to the influence of the unequal interconnecting cable resistance on the droop control method. At time t = 0.5 s, the output DC currents flowing through the three converters are I_{dc1} = 54.610 A, I_{dc2} = 49.060 A and I_{dc3} = 51.990 A respectively and the DC bus voltage regulation is V_{bus} = 257 V. Hence, the calculated current sharing ratios between the converters and normalised bus voltage regulation in steady state are n_1 = 0.8984, n_2 = 0.9520 and V_{bn} = 0.9519. As expected, the bus voltage regulation increases with an increase in load demand due to the droop action. However, the drop in the bus voltage is less than 5% of the nominal voltage value for the maximum load demand considered. Conversely, the optimal droop gain settings obtained using the proposed approach can maintain equal and accurate current sharing among the converters as desired despite the load fluctuations (as shown in Figure 3.10 (b)). At time t = 0.5 s, the output DC currents flowing through the three converters are I_{dc1} = 51.92 A, I_{dc2} = 51.92 A and I_{dc3} = 51.92 A respectively and the DC bus voltage regulation is V_{bus} = 256.80 V as shown in Figure 3.10 (b). Hence, the calculated current sharing ratios between the converters and normalised bus voltage regulation are n_1 = 1, n_2 = 1 and V_{bn} = 0.9519. Similarly, the drop in the bus voltage is less than 5% of the nominal bus voltage value for the maximum load demand considered. Besides, a voltage range of between 250 V to 280 V is acceptable for the MEA EPS application in steady states [49]. Hence, these results show that, compared to the conventional droop gain design, the proposed optimal droop gain design strategy can enhance the performance of the droop control method by mitigating the influence of unequal line resistance.

A simulation was conducted to assess the robustness of the optimal droop coefficient setting in maintaining accurate current sharing in the event of a fault in one of the generators. The optimal droop gain settings from the second design example are used in the simulation. Figure 3.11 illustrates the results obtained. During the simulation, a CPL of 40 kW was applied. The results depicted in Figure 3.11 demonstrate that before the disconnection of PMSG2, all three converters operated in parallel, effectively sharing the load current demand with a ratio of n_1 = 0.9990 and n_2 = 1.0004. Subsequently, upon the disconnection of the second PMSG2, converters 1 and 3 took on the responsibility of sharing the load current demand, with current sharing values of I_{dc1} = 79.1 A and I_{dc3} = 79.84 A, respectively. Despite the loss of converter 2, the bus voltage remained adequately regulated within the permissible limits for MEA applications. Notably, the bus voltage declined from 257.40 V (when all three sources were

active) to 250.50 V following the disconnection of PMSG2, as depicted in Figure 3.11. Considering these outcomes, it is evident that the optimal droop coefficient setting exhibits commendable performance even under fault conditions, with a notably stable transient response.

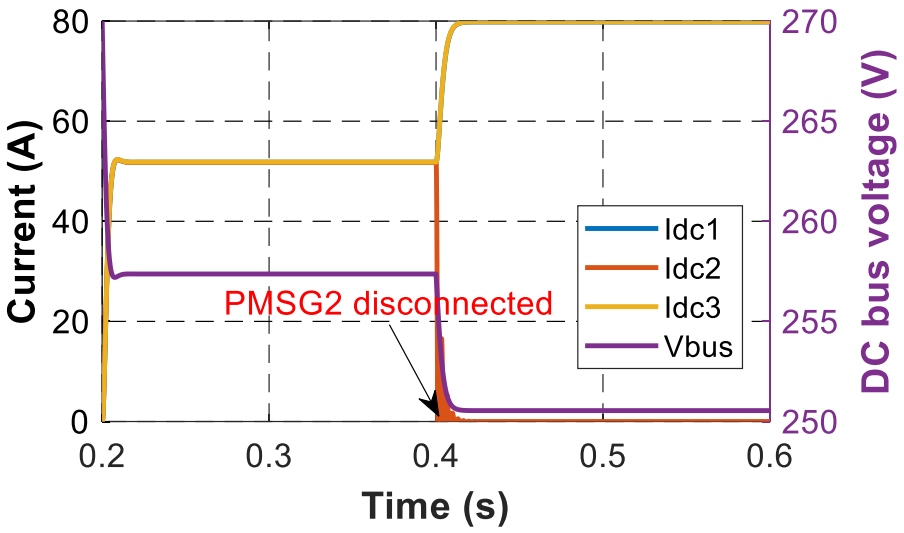
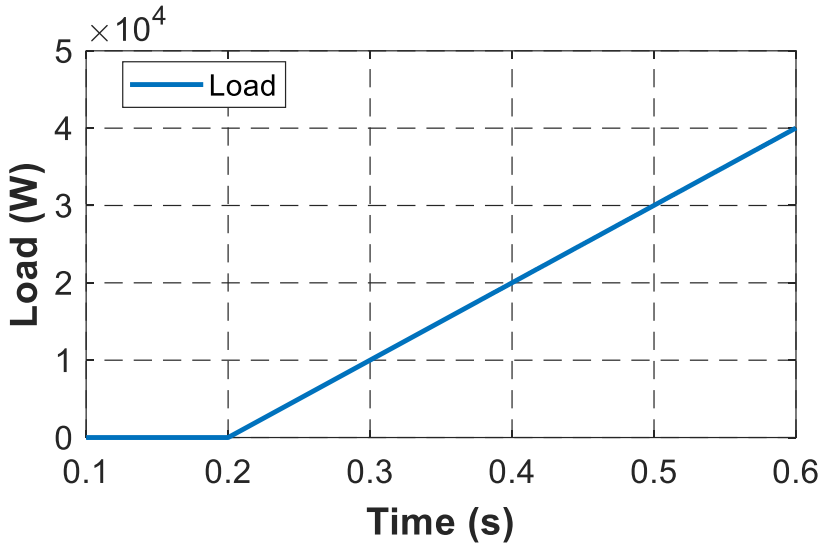


Figure 3.11 Simulation results for current sharing and bus voltage regulation using the optimal droop coefficient from the second design example under source fault conditions.

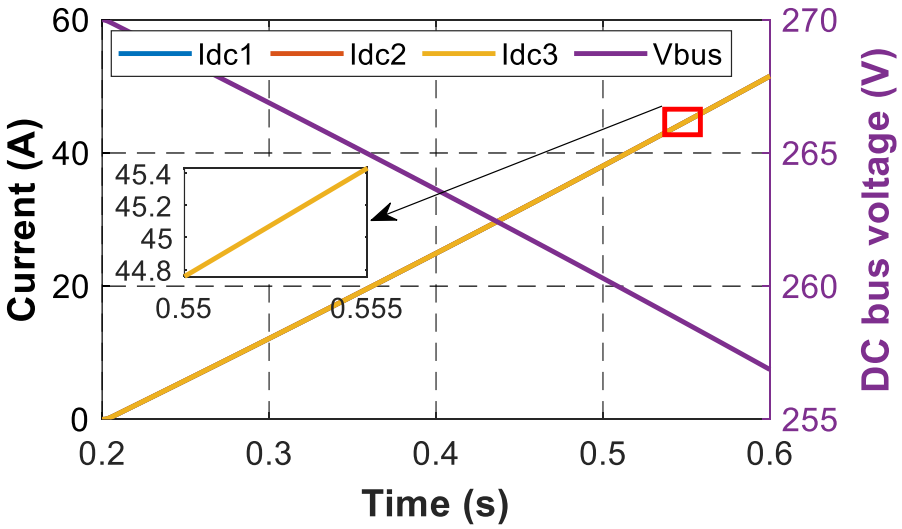
While the simulation results presented in Figure 3.10 depict the MEA EPS's response to instantaneous load changes, it is essential to account for more realistic scenarios, such as ramped loads. Ramped load variations better emulate actual operating conditions within practical systems, notably in aircraft electrical power systems. To address this, we conducted simulations of the detailed MEA EPS model, illustrated in Figure 3.1, using MATLAB Simulink. These simulations employed the optimal droop settings obtained from the first design example, with the simulation parameters outlined in Table 3-1. At 0.2 s into the simulation, a ramped load was introduced, as illustrated in Figure 3.12 (a). The results concerning current sharing and bus voltage regulation are presented in Figure 3.12 (b).

Figure 3.12 (b) reveals that when applying the optimal droop coefficient setting from the first design example, the load current demand is equally distributed among the converters. This achievement aligns with the desired sharing ratios of $n_1 = 1$ and $n_2 = 1$. Furthermore, the bus voltage exhibits a reduction of less than 5% from the nominal bus voltage value, even under the maximum load demand (i.e., 40 kW, as shown in Figure 3.12 (b)). These results emphasize

that, compared to conventional droop gain design, the proposed optimal droop gain design strategy enhances the performance of the droop control method by mitigating the influence of mismatched cable resistances. In addition, the results obtained provide insights into how the proposed approach responds to gradual load variations, which is important for ensuring the stability and reliability of the MEA EPS.



(a)



(b)

Figure 3.12 (a) Ramp load (b) Current sharing and bus voltage regulation using optimal droop gain settings from the first design example under a ramped load.

Since the line resistance is the main factor that influences the current sharing and voltage deviation, additional simulation studies are carried out to test the robustness of the proposed

approach to a variation in the interconnecting cable resistance. The cable inductance is not included in the robustness study because it does not have an impact on the steady-state performance of the system [161]. To that end, each of the cable's parasitic resistance is varied by ± 20% and ± 50% from their initial values shown in Table 3-1. Other system parameters remain unchanged. The optimal droop gain settings obtained from the first design example are used for the simulation studies. Also, a CPL of 40 kW is applied during the simulations. The results obtained are summarised in Figure 3.13.

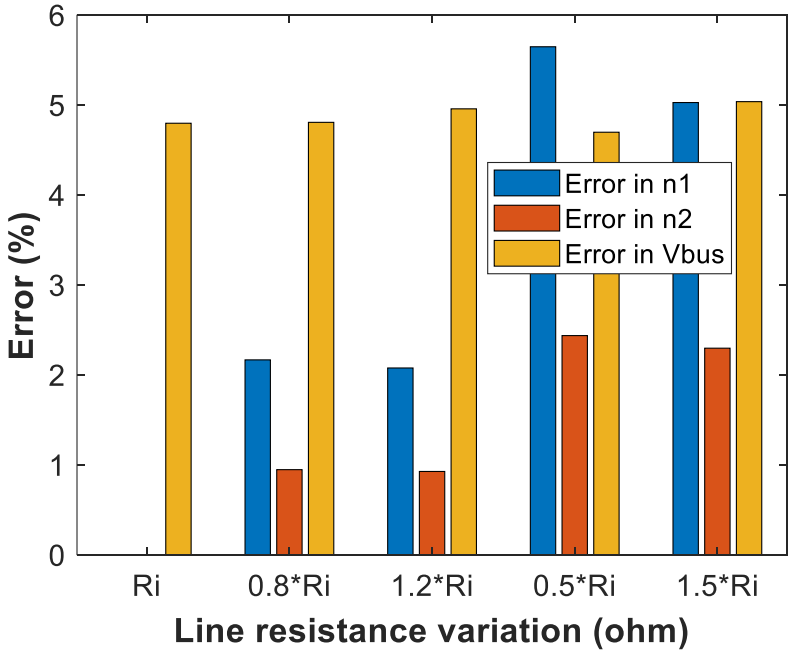


Figure 3.13 Summary of the optimal droop coefficient settings performance against different line resistance variations.

As shown in Figure 3.13, the percentage error in the current sharing ratios (n_1 and n_2) from their ideal values is mostly around or less than 5% for n_1, and less than 3% for n_2. Similarly, the bus voltage deviation from its nominal value is mostly around 5% for the various line resistance variation. This demonstrates the good steady-state performance and robustness of the obtained optimal droop coefficient settings using the proposed design strategy. Therefore, though the cable resistance affects the current sharing, the optimal droop gain settings can significantly reduce the error in the current sharing ratios and maintain the bus voltage within an acceptable range.

3.7 Summary

In this chapter a new method is proposed for optimising droop gain design in the control of parallel-connected converters. It has been demonstrated that the ANN optimisation-based design can be used for selecting optimal droop gains in controlling power converters within the MEA multi-source EPS. The method involves offline training of a surrogate model using data obtained from the traditional droop control. The trained ANN acts as a surrogate model, enabling quick determination of the optimal droop coefficient combination based on any user-defined fitness function. This ANN-based surrogate model substantially reduces computational demands, thereby expediting the design process without compromising accuracy. Notably, the performance metrics predicted by the surrogate model closely align with those obtained from the simulation model. The simulation results highlight that the chosen optimal droop coefficient settings significantly enhance the performance of the traditional droop control method under both steady-state and transient conditions.

Chapter 4 Real-Time Tuning of Optimal Droop Gain Using ANN.

Building on the research presented in Chapter 3, this chapter introduces a new approach for real-time tuning of optimal droop gain parameters using ANNs. The chapter explains the development of an ANN-based approach for real-time tuning and its integration into the hardware control platform. In contrast to conventional data mapping where ANNs relate control variables to system responses as described in chapter 3, this method employs "reversed data training." Here, the ANN uses system responses as inputs and control variables as outputs. For instance, in an aircraft DC MG scenario, where multiple generation systems share power through droop control, the ANN is trained in reverse. Power sharing ratios are input, and the ANN provides the corresponding droop coefficients as output. This chapter illustrates the effectiveness and simplicity of this approach for determining optimal droop gains based on desired power sharing requirements.

4.1 Introduction

Designing the optimal droop gain to achieve accurate load sharing and effective voltage regulation poses a multi-objective optimisation challenge, as these control objectives often conflict with each other. Different AI multi-objective optimisation techniques have been employed to compute the optimal droop gains of the converters to achieve the desired control objectives [175, 171, 176, 142, 138, 177, 178, 179, 139]. In [175, 171, 176, 138], the MOOP is tackled by converting these multiple-objective optimisation problems into a single objective (SO) one using a weighted sum method [180]. The PSO technique is employed in [175, 171, 176] for the computation of the optimal droop settings to realise two control objectives of current sharing error minimisation and enhanced voltage regulations for various loading conditions of a DC MG. In the weighted sum approach, the objective functions are added together with different weights for optimisation. However, when one objective is realised, the other objective is degraded due to its conflicting nature. Thus, this requires the knowledge of the optimum weighting factor design to obtain the optimal solution. The tuning of the weighting

coefficients is not trivial and is a time-consuming task. In addition, a slight change in the weighing coefficient may result in a large change in the control objectives [177, 179]. Besides, this approach only provides a single solution and is highly dependent on the assigned weights, thus, not providing flexibility to the power system designer [181]. In contrast, authors in [177, 179] solved this MOOP by using an extra compromising step called the fuzzy membership function after deriving Pareto optimal front solutions. For example, to obtain the optimal droop gains for distributed generators (DGs) in an islanded DC MG, the nondominated sorting genetic algorithm (NSGA II) was used to generate the Pareto optimal front of the formulated multi-objective optimisation (MOO) in [177]. The proposed MOO approach considers the system voltage regulation, improved current sharing among the DGs and minimisation of the total loss in the system. The fuzzy membership function is employed to obtain the best-compromised solution from the Pareto optimal front.

Though the population-based methods (especially the GA and PSO) are the most widely used to solve optimisation problems in power electronics and allow the user to find good optimal design variables (i.e., have good search capability) [133], however, they are heuristic and have an intensive computational burden [133]. In addition, for every design objective, a new set of simulations are required [39] to find the optimal droop gain. Another drawback includes the possibility of being stuck in the local optimum due to the premature convergence of the results of the optimisation [143, 144]. Thus, there is no guarantee that their solutions are globally optimal. Besides, since optimisation involves different control objectives, there is a need to formulate the objective function. Furthermore, when a wide operating range is considered, the heuristic methods will need to run many simulations and experimental results which are time-consuming. Thus, limiting their practical implementation in industrial applications that require speed and efficiency [133].

An approach can be considered good for optimal droop gain design if it provides the power system designer with a simple way to obtain the optimum system performance for any design criteria without incurring a huge computational burden in the implementation of the algorithm. The ANN can offer the optimal solution by automatically learning the underlying relationship between the model inputs and outputs by using its inherent decision-making feature. The use of ANN for optimal droop gain design offers several advantages. It provides a simple way to obtain the optimum system performance without a significant computational burden. The ANN can approximate non-linear functions accurately, making it applicable to problems with

unknown or difficult-to-formulate fitness functions, generating optimal solutions without trade-offs [151]. Additionally, data collection is only required once, unlike heuristic methods [182] that need multiple data collections for different design objectives, making ANN a powerful tool for Multi-Objective Optimisation Problems (MOOPs).

In recent years, conventional ANN optimisation-based design has been employed for the design and automated selection of some power electronics parameters such as the weighting factor in the cost function of the finite control set model predictive control (FCS-MPC) [39, 172, 183]. In [144], it was used to design and select the parameter of the active disturbance rejection control controller for the dual active bridge converter. In [155], an ANN-aided automated design for the reliability of power electronics systems is proposed. The design and optimisation of the DC filter for the MEA distribution system using search and surrogate algorithms are carried out in [184]. In [185], it is used for the design and selection of the optimal weighting factors used for predictive torque control in a motor drive. Similarly, [186] employs it to facilitate the design of optimal droop gain for droop control of parallel-connected PECs in the MEA (as presented in Chapter 3). The conventional ANN optimisation-based design involves training an offline surrogate model using data from experiments or detailed simulations of the EPS. Thereafter, the surrogate model is used to replace the original detailed simulation model in performing optimisation and selection of the desired optimal system parameter. Compared to the met-heuristic optimisation techniques, the surrogate model can be used in future studies without running the original system model, saving time, and eliminating the need for new simulations for different control objectives within a sub-design space [39]. However, despite the benefits of conventional ANN optimisation-based design, it exhibits some drawbacks that are undesirable in practical implementation including increased computational burden due to probing numerous design points and complexity in converting MOOP to a single-objective using the weighted sum method for optimal droop gain design.

AI techniques can provide adaptive and robust power systems control variables that can respond to changes in system conditions in real-time [133]. In this regard, for ease of implementation, methods are required that have low complexity and computational burden. Due to the drawbacks associated with the meta-heuristic approach and conventional ANN optimisation-based design, they not only make the offline design of control parameter complex and computationally intensive, but none of these methods also allow control parameters to be tuned in real-time [187]. Based on the literature reviewed, it is identified that it has become

imperative to analyse ANN for droop gain parameters design and computation from the practical implementation perspective.

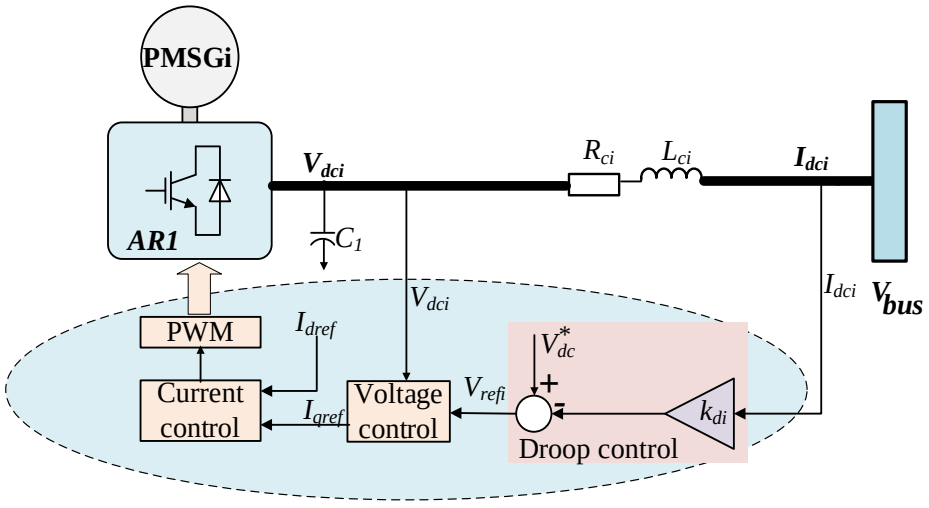
Motivated by the above discussions, this chapter builds upon the research presented in Chapter 3, where the conventional ANN optimisation-based design is used for offline computation of optimal droop gains of converters. Unlike the work presented in Chapter 3, the proposed approach eliminates the need for intermediate optimisations by utilising reverse data training of the ANN to directly predict the optimal droop gain settings. Thus, reducing computational burden and complexity, and enabling real-time tuning of droop gain parameters. The proposed approach represents a significant improvement over the method presented in Chapter 3 and offers several advantages: (1) It is a self-contained application that does not depend on external hardware to set the optimal droop gain of converters in local controllers. This advantage stems from the fact that the ANN is implemented directly within a hardware control platform. (2) Facilitates automatic updates of optimal droop gain settings in local controllers, and ensures quick adaptation to reference changes, thereby achieving the desired control performance.

The trained ANN model can be used offline or implemented in a digital control platform for real-time computation of the optimal droop gains. In the proposed approach, once the training is completed, the power system designer can input the desired control objectives (i.e., a specific design point). The surrogate model can then quickly calculate the optimal droop gains based on these specified objectives. This allows for immediate determination of the optimal droop gains using the surrogate model. The main research contributions in this chapter are highlighted as follows.

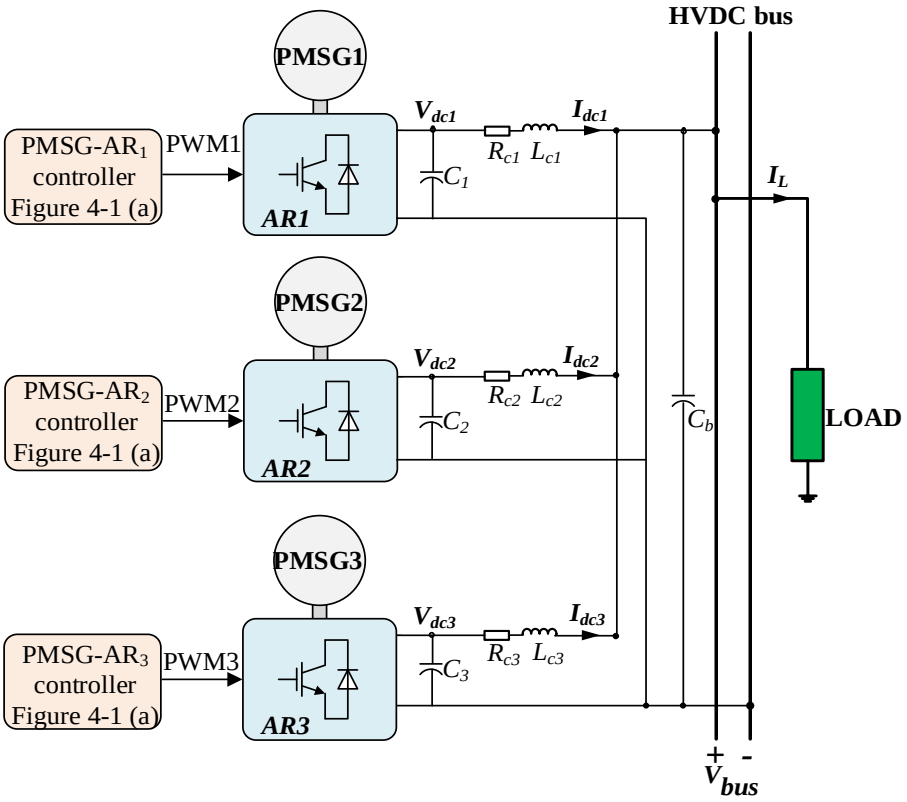
- ✓ The design and validation of a real-time method for the online tuning of the optimal droop gains of parallel-connected converters based on the desired power sharing ratios and voltage regulation references. This approach effectively regulates power-sharing and bus voltage control for droop-controlled converters. To the author's best knowledge, this work represents the first attempt to address the real-time tuning of optimal droop gain settings for droop control of parallel connected converters.
- ✓ A detailed comparison between the proposed design strategy and conventional ANN optimisation-based design has been performed.

4.2 System Description

Figure 4.1 illustrates the architecture of a 270 V single DC bus power system. This architecture is recognised as a highly prospective choice for the EPS of future more electric aircraft (MEA) [94]. Therefore, it serves as a relevant case study in this chapter. As shown in Figure 4.1, the power system configuration consists of multiple parallel-connected generators (specifically, permanent magnet generators, denoted as PMSGi) that supply electrical power to a high-voltage direct current (HVDC) bus. Each generator is connected to the bus through its respective AC/DC converter (ARi). The control structure of the system typically follows a cascaded design, consisting of outer voltage and inner current control loops, as depicted in Figure 4.1 (a). The outer loop is responsible for regulating the DC-link voltage, which is achieved through the implementation of droop characteristics during the generation mode. On the other hand, the inner current control loop is dedicated to controlling the d- and q-axis currents. The FW controller generates the I_{dref}, while the I_{qref} is produced by the DC-link voltage controller. However, to simplify the control structure and given the focus of this thesis on the design of droop gains for power sharing among various power generation sources in an onboard HVDC power network for MEA applications, only the droop control structure is presented in Figure 4.1 (a). Within an islanded DC MG, the primary controller is used for current loop and voltage loop control within a single PMSG-AR system. The droop control is generally implemented to define the voltage reference within the primary level voltage control, as shown in Figure 4.1 (a).



(a)



(b)

Figure 4.1 (a) Local PMSG-AR primary controller (b) MEA EPS HVDC grid

The converters are pulse-width modulated and controlled via their respective primary local controllers shown in Figure 4.1 (a). The capacitor C_b is the capacitor bank of the main DC bus, and the local capacitors for each of the converter modules are represented as C_1, C_2 and C_3. The load power in the MEA DC grid is composed of a combination of constant impedance load and constant power load. Additionally, to represent the generators on the left-wing engine, right-wing engine, and auxiliary power unit (APU) of the aircraft, three Permanent Magnet Synchronous Generator (PMSG)-Active Rectifier (AR) systems are considered.

4.3 Proposed Droop Gain Design Approach and Comparison with Conventional ANN Optimisation-Based Design

This section presents a detailed description of the procedures involved in the droop gain design using both the proposed design approach and the conventional ANN optimisation-based design. Additionally, a comprehensive overview of the ANN structure and training process is provided, highlighting the key aspects of the network architecture and the training procedure.

4.3.1 Procedure

The design process for both approaches is carried out in three stages, (i.e., Stages A, B and C) as illustrated in the flowchart shown in Figure 4.2. Stage A is data generation, and the process is the same for both approaches. The data can be generated from either a detailed simulation or experiments. The data generated from high-fidelity simulation models of a multi-generator system (Figure 4.1 (a)) can be carried out on a standard multi-core computer. In this thesis, the data generation is carried out on a computer with processor specification as Intel (R) Core (TM) i3-8100 CPU @ 3.60GHz (3.60 GHz). Stage B involves ANN training with the data obtained from stage A in both approaches. The training process varies between the two approaches. With the surrogate model from stage B, the required droop gains can be derived immediately for the defined power sharing ratio and DC bus voltage in stage C using the proposed approach. However, the selection of the optimal droop gain with the aid of the surrogate model from stage B requires extra effort when using the conventional ANN optimisation-based design. Hence, the method of obtaining the optimal droop gain settings differs between the two approaches. These three stages are further elaborated as follows.

In stage A, data is extracted by running the detailed simulation model of the MEA EPS shown in Figure 4.1 (a) for different combinations of the droop gains (i.e., k_{d1}, k_{d2}, and k_{d3}) within a design range. The corresponding current sharing ratios (i.e., n_1 and n_2) and the normalised bus voltage (V_{bn}) are computed automatically at the end of each simulation and stored. The relationship between the input (x) and the processed output (y) of the simulation during data is expressed in (3-10) [186].

In stage B, for the proposed approach, the surrogate model is trained with the system performance indicators (i.e., n_1, n_2 and V_{bn}) as inputs and the droop coefficients (i.e., k_{d1}, k_{d2} and k_{d3}) as outputs. This way, the surrogate model can be used to predict its output quickly and accurately when provided with a suitable input. For clarity, the surrogate model represents the relationship in (4-1).

$$y = F(x) \Leftrightarrow (k_{d1}, k_{d2}, k_{d3}) = F(n_1, n_2, V_{bn}) \tag{4-1}$$

Alternatively, for the conventional ANN optimisation-based design, the surrogate model is trained by following the same input-output pattern used in data generation (i.e., the relationship in (3-10)) to train the surrogate model.

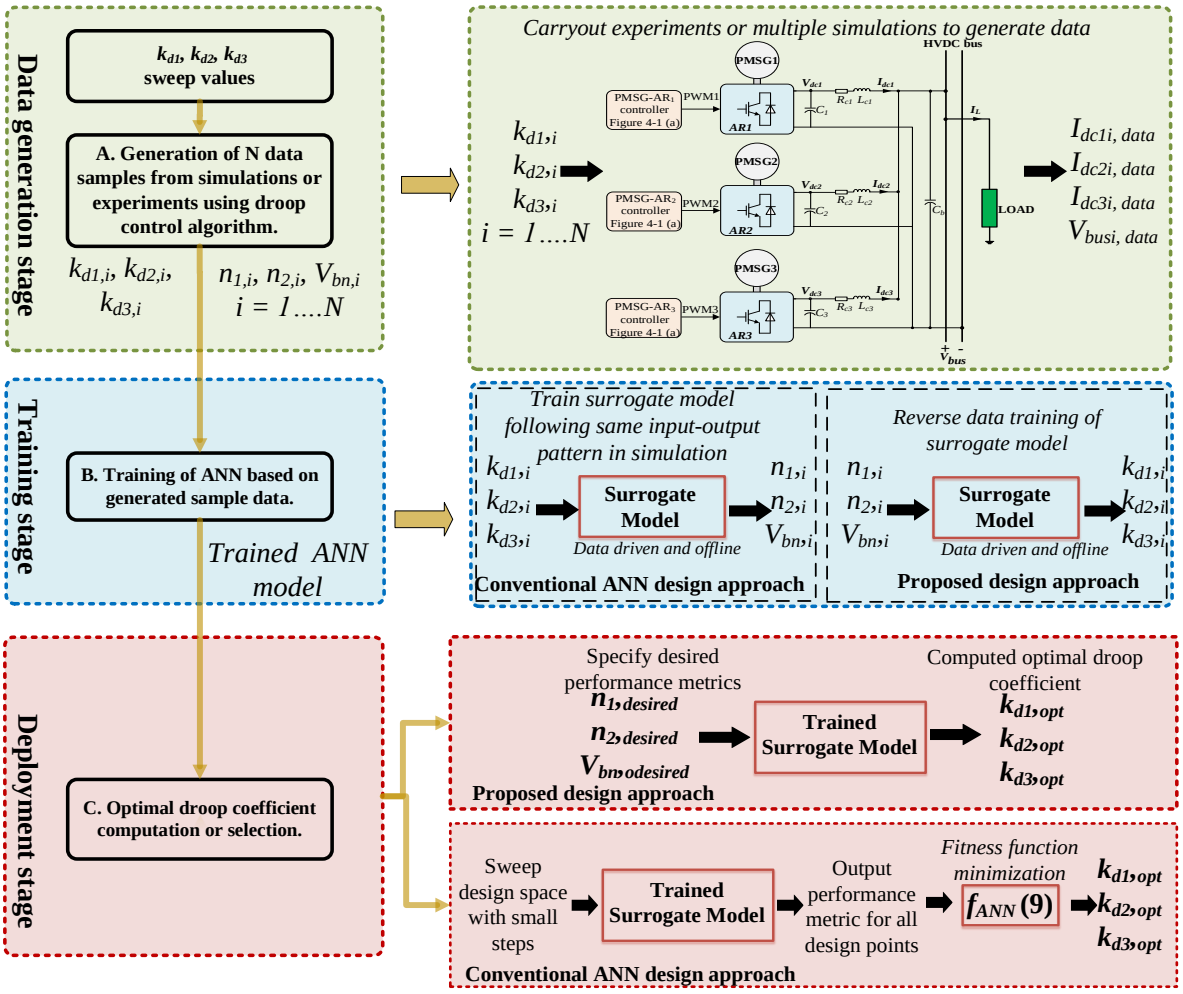


Figure 4.2 Flowchart of the comparison of the proposed design approach and conventional ANN optimisation-based design of the droop coefficient in droop control of power converters.

Finally, in stage C, for the proposed approach, the power system designer can specify the desired performance metrics (i.e., one design point) as input for the surrogate model to compute the optimal droop coefficient that will yield such performance as shown in Figure 4.2. This approach is expected to significantly reduce the prediction time and simplify the optimal droop coefficient design and computation process. In contrast, the conventional ANN optimisation-based design involves stage C which consists of sampling the design space using small steps, resulting in numerous design points. These design points are then fed into a surrogate model, which predicts the corresponding system performance metrics. Subsequently, a user-defined

fitness function, denoted as f_{ann}, is formulated, and evaluated using the surrogate model predictions. By minimising the fitness function f_{ann}, the optimal droop coefficient setting that satisfies the desired control objectives can be determined instantly [186]. It can therefore be seen that there are some fundamental differences between the proposed method in this chapter and the ANN-optimisation-based design presented in Chapter 3, including the ANN training dataset selection, design philosophy and the way to identify the optimal droop gains as clarified in Table 4-1.

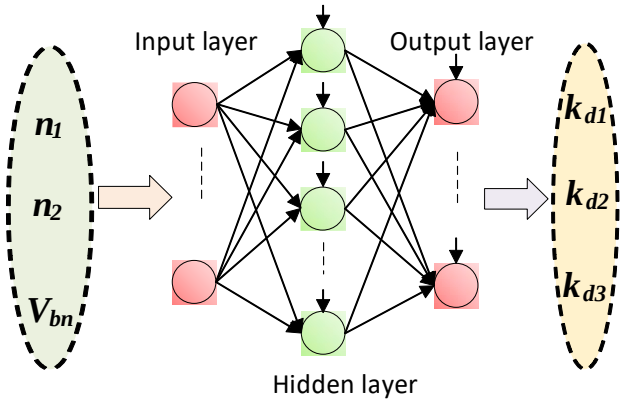
Table 4-1 Fundamental differences between the proposed approach and the ANN optimisation-based design.

Items	**ANN optimisation-based design (chapter 3)**	**Proposed approach**	**Different / Same**
Data generation	Using different droop gains in the DC generation systems and collecting DC currents, calculate power sharing.	Using different droop gains in the DC generation systems and collecting DC currents, calculate power sharing.	Same
ANN training	Input dataset [different droop gains] Output dataset [DC currents, bus voltage].	Input dataset [DC currents, bus voltage] Output dataset [different droop gain].	Different
Optimisation	Using ANN derived to generate a further large amount of data. Extra search algorithm to find droop gain sets with the minimum cost function.	Directly use derived ANN.	Different

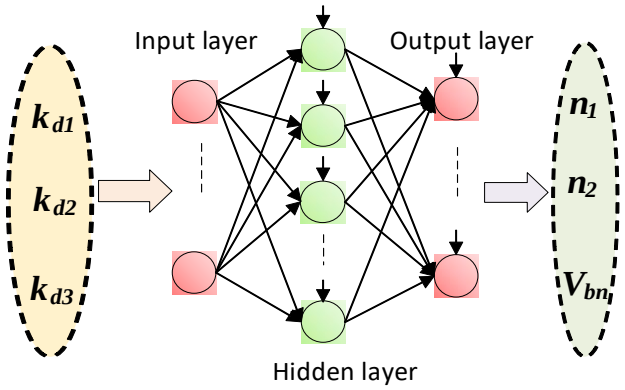
4.3.2 ANN Structure and Training

Theoretical analysis suggests that an ANN has the potential to approximate any input-output relationship with high precision, given the appropriate structure, including the number of neurons and layers, is selected for training [133]. In this chapter, the surrogate models are trained offline using FFNN with a Levenberg-Marquardt-based backpropagation training algorithm [39]. Figure 4.3 (a) and (b) illustrate the structure of the surrogate models for the

proposed approach and the ANN optimisation-based design, respectively. Both surrogate models consist of three layers. To ensure a fair comparison, both approaches employ hidden layers with 11 neurons each.



(a)



(b)

Figure 4.3 Schematics of the FFNN (a) Proposed design approach (b) Convectional ANN optimisation-based design [186].

The data sample is divided into three sets—training samples, validation samples, and testing samples—prior to training the surrogate model. The percentage for each set is randomly allocated with the training data having the largest share. Thereafter the weight and biases of the ANN are also randomly selected for the initial iteration. However, the weight and biases are updated in subsequent iterations based on the error observed in the previous iteration. The validation set of data is used to evaluate the ANN training by computing the error between the ANN-predicted output and the training data set [188]. The root mean square error (RMSE) is commonly employed as a metric to assess the training performance of the regression ANN. If the computed RMSE indicates overfitting or underfitting, the training can be halted. However,

if the training performance is unsatisfactory, adjustments can be made to the surrogate model structure, particularly regarding the number of neurons in the hidden layer.

4.4 Optimal Droop Gain Design for the MEA EPS

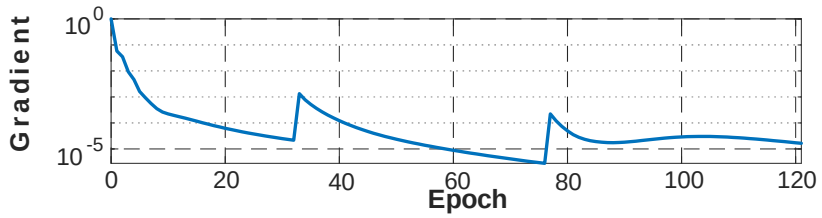
This section aims to validate the procedures of the proposed design strategy in the context of droop control for the system depicted in Figure 4.1 (a). Furthermore, the verification will include the demonstration of Stage C using a design example for comparison of both the proposed approach and the ANN optimisation-based design (presented in Chapter 3). Additionally, the flexibility of the proposed approach will be showcased through two other design examples. It is worth noting that the proposed design strategy can be applied to other bus systems without any loss of generality, highlighting its broad applicability.

4.4.1 Data generation

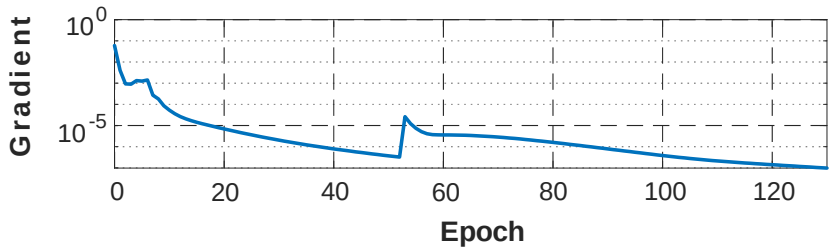
Prior to data generation, it is important to establish a defined range, known as the design space, for the droop gains. Table 3-2 presents the range of droop gains used for data generation, along with the corresponding sampling step. The design space is carefully chosen to align with practical considerations, taking into account the desired control objectives while ensuring system stability. In the case of conventional droop gain design, the determination of droop gains is typically based on the power rating of the converters, aiming to achieve effective voltage regulation and stable operation. To maintain consistency, the upper and lower boundaries of the design range for each design parameter are set at +10% and -10% respectively, relative to the conventional droop gains specified in Table 3-1. In addition, extensive stability analysis of droop control approaches in voltage source converter-based DC MGs, along with the investigation of the effects of droop gains on stability [174], confirms that the selected design range falls within the acceptable limits for stable operation. As indicated in Table 3-2, a total of 1331 droop gain combinations are systematically explored as inputs in the simulation model depicted in Figure 4.1 (a). Random combinations of these inputs are utilised to generate the dataset used for training the ANN. Following each simulation, the values of n_1, n_2, and V_{bn} are automatically calculated and stored for further analysis.

The simulation utilises the system parameters and equivalent DC cable parameters listed in Table 3-1. The PMSG parameter values in Table 3-1 are based on the specifications of the AEGART (Aircraft Electrical Starter-Generation System with Active Rectification

Technology) machine, designed for the next-generation business Jet application [189]. These PMSGs have identical power ratings and are designed to transmit power in a 1:1:1 ratio. The AC-DC converter's switching frequency, f_c, is set at 100 kHz. To simulate real-world conditions, a dead time T_d and a computational delay of one sampling time are included in the simulation model. The simulations were performed on a standard PC equipped with a quad-core processor, with each simulation taking approximately 6 seconds to execute. Therefore, the total time required for data collection amounts to approximately 35 minutes. The data generation process is automated through MATLAB codes. Data was extracted specifically for a 40-kW load connected to a CPL. The extracted data was subsequently utilised to train the FFNN structures illustrated in Figure 4.3 (a) and (b).

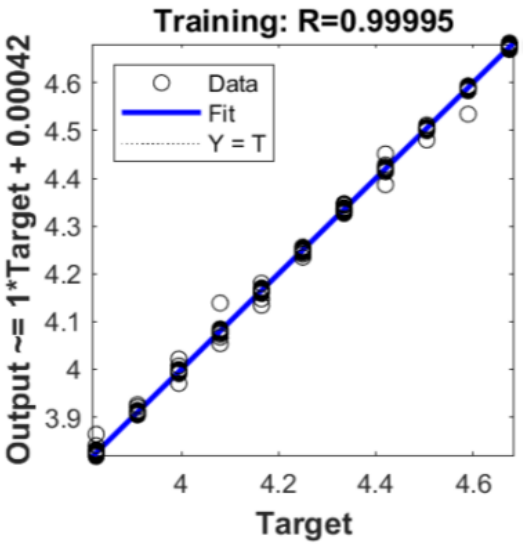


(a)

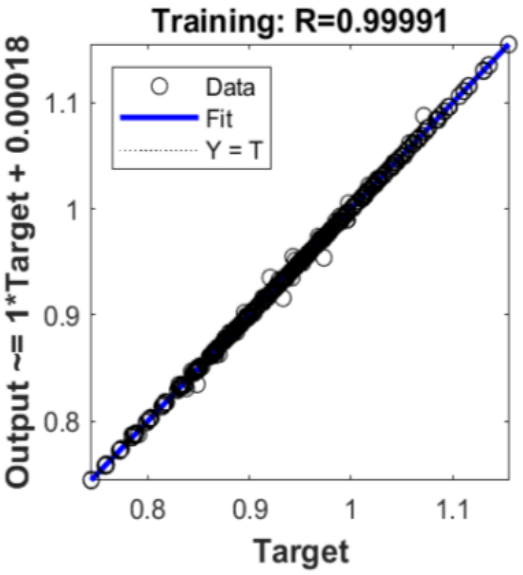


(b)

Figure 4.4 ANN model training profile for (a) Proposed design approach and (b) ANN optimisation-based design approach.



(a)



(b)

Figure 4.5 Comparison of the regression plot of the trained ANN showing the relationship between the targeted data (o) and the surrogate model prediction (blue line) for (a) Proposed design approach and (b) ANN optimisation-based design approach.

4.4.2 Development of the Surrogate Models

Prior to training the surrogate models, the generated data is divided into three sets: 70% for training, 15% for validation, and the remaining 15% for testing. The training process is successfully conducted using the NN fitting toolbox in MATLAB. The weights and biases of both surrogate models are optimised using the Levenberg-Marquardt backpropagation

algorithm, ensuring a fair comparison between the two approaches. Since the ANNs in the proposed approach and the conventional ANN optimisation-based design are trained differently, it is crucial to compare the performance of the ANN models.

The training state of the selected ANN structure (shown in Figure 4.3 (a) and (b)) are depicted in Figure 4.4 (a) and (b) for the proposed design approach and the ANN optimisation-based design respectively. Figure 4.4 illustrates the change in the gradient coefficient over the course of multiple epochs in ANN training. During each epoch, the ANN processes all the training data samples once to update its weights and reduce the error. The lower the gradient coefficient value, the more effective the training and testing of ANN model [190]. In Figure 4.4 (a) and (b), it is evident that the gradient curve of the ANN models reaches exceptionally low values across all epochs. In addition, the final gradient coefficient for each of these approaches is almost zero. Thus indicating, improved training and testing of the ANN models. The ANN model for the proposed design approach has stopped training at 121 epochs as shown in Figure 4.4 (a), as it attained the best validation set, while the ANN model used for the ANN optimisation-based design has stopped training at 130 epochs Figure 4.4 (b). It is important to note that the maximum allowable training epoch was set at 1000. Figure 4.5 (a) and (b) illustrate the performance comparison for the two models, where evaluation metrics such as root mean square error (RMSE) and correlation coefficient (regression R-value) are employed. A lower RMSE value and a higher R-value indicate higher accuracy in the trained network predictions. Thus, the closer the RMSE value is to 0 and the R-value is to 1, the better the accuracy of the trained network predictions.

The proposed approach demonstrates calculated root mean square error (RMSE) values of 0.0032956, 0.002183, and 0.0031714 for k_{d1}, k_{d2}, and k_{d3}, respectively. On the other hand, the conventional ANN optimisation-based design approach yields calculated RMSE values of 0.00085733, 0.0012517, and 0.000045932 for n_1, n_2, and V_{bn}, respectively. These RMSE values indicate that the surrogate models are effectively trained, and the selected FFNN structures deliver exceptional results. The regression plots depicted in Figure 4.5, generated by the NN fitting toolbox, display a strong alignment of data points with the linear regression lines for both approaches. Moreover, the R-values exhibited in Figure 4.5 (a) and (b) confirm the satisfactory training of the surrogate models in both approaches.

4.4.3 Design Examples

4.4.3.1 First design example

As the benchmark method, the conventional ANN optimisation-based design is initially employed to identify the optimal droop coefficient setting (i.e., k_{d1}^{opt}, k_{d2}^{opt}, and k_{d3}^{opt}) that achieves a well-balanced solution between the current sharing ratios among the converters and normalised bus voltage regulation. Subsequently, the proposed approach is utilised to obtain the same results efficiently and effectively.

a) ANN-optimisation-based design

In the initial stage of the conventional ANN optimisation-based design, the design range of the droop coefficient is evenly sampled with a small step size of 0.01 (see Table 3-3). This sampling process results in approximately 636,056 design points, representing various droop gains, which are utilised as input for the surrogate model. Subsequently, the surrogate model is employed to predict the corresponding performance metrics, namely n_{1ann}, n_{2ann}, and V_{bnann}, for each of the 636,056 droop gain combinations. These predictions are then utilised to evaluate a user-defined fitness function, facilitating the assessment of the performance of each droop gain setting. The detailed design procedures for the ANN optimisation-based design (shown in Figure 3.4 and included in Figure 4.2 for comparison with the proposed approach in this chapter). Considering the second design example presented in Chapter 3, Section 3.5.3.2, the optimal droop gain design point is selected as k_{d1}^{opt} = 1/4.1550, k_{d2}^{opt} = 1/4.6750 and k_{d3}^{opt} = 1/4.3750. In addition, the corresponding current sharing ratios and normalised bus voltage predicted by the ANN are n_{1ann} = 0.9994, n_{2ann} = 1.0005 and V_{bnann} = 0.9532, respectively.

b) Proposed approach

In the approach proposed in this chapter, the power system designer needs to specify the desired system performance metrics within the design space, representing a single design point. These desired metrics serve as inputs to the surrogate model, which computes the optimal droop gain settings necessary to achieve the specified control objectives. To facilitate direct comparison, the predicted performance metrics obtained from the surrogate model in the conventional ANN optimisation-based design approach are utilised as inputs for the surrogate model in the proposed approach. Specifically, the desired performance metrics are set as $n_{1desired}$ = 0.9994,

$n_{2desired}$ = 1.0005, and $V_{bndesired}$ = 0.9532. As a result, the surrogate model in the proposed approach calculates the optimal droop coefficients as $k_{d1}^{computed}$ = 1/4.1509, $k_{d2}^{computed}$ = 1/4.6718, and $k_{d3}^{computed}$ = 1/4.3710.

Table 4-2 Other design examples

Case	Desired performance metrics	Computed optimal droop gains		
		$k_{d1}^{computated}$	$k_{d2}^{computated}$	$k_{d3}^{computated}$
1	$n_{1desired}$ = 1, $n_{2desired}$ = 1, $V_{bndesired}$ = 0.9532	1/4.1508	1/4.6749	1/4.3685
2	$n_{1desired}$ = 0.8, $n_{2desired}$ = 1, $V_{bndesired}$ = 0.9600	1/5.0684	1/4.5701	1/5.4082

4.4.3.2 Other Design Examples

For the three-source system studied in this thesis, there are multiple possibilities for meeting the load power demand. This chapter focuses on two specific approaches, which are outlined in Table 4-2. In Case 1, all three sources are assumed to have identical ratings and are expected to cooperate in sharing the load power demand equally. Additionally, the bus voltage should be regulated within an acceptable range for the maximum electrical load considered in this study (i.e., 40-kW). As shown in Table 4-2, for equal load sharing among the sources, the desired sharing ratio is defined as $n_{1desired}$ = 1 and $n_{2desired}$ = 1. Moreover, the desired bus voltage regulation is around 95% of its nominal value (i.e., $V_{bndesired}$ = 0.9532 = 257.364 V). Using the proposed approach, by inputting these desired performance metrics into the trained surrogate model, the surrogate model predicts the optimal droop gain settings required to achieve such performance objectives, as shown in Table 4-2. In Case 2, generators 1 and 3 are tasked with sharing an equal load (assumed to have the same ratings), which is higher than the load assigned to generator 2 (assumed to have 80% of the rating of generator 1). To accomplish the desired load sharing and bus voltage regulation, the performance metrics presented in Table 4-2 are used as inputs to the surrogate model of the proposed approach. The surrogate model predicts

the optimal droop gain settings necessary to achieve the desired performance objectives, as shown in Table 4-2.

This demonstrates that the same surrogate model can be utilised to compute different optimal droop gain settings to accomplish various control objectives within the design space, eliminating the need for additional simulations. Consequently, our proposed approach offers flexibility and time-saving advantages compared to other optimisation techniques such as PSO and GA. The predicted optimal droop settings for Cases 1 and 2, as shown in Table 4-2, will be validated in the HIL experiment.

4.4.4 Computational Burden

Both approaches share the same computational burden (offline) in data generation. For the three design variables considered in this study (i.e., k_{d1}, k_{d2} and k_{d3}), it took approximately 35 minutes to generate the required data. However, if the number of design variables is increased to four (e.g., for a system with four PMSG-AR systems) and each variable has 11 settings to be tested, a total of 11^4 = 14,641 data samples would be needed for training. With each simulation taking 6 seconds to run on a standard computer with processor specification as Intel (R) Core (TM) i3-8100 CPU @ 3.60GHz (3.60 GHz), it would take around 6 hours to generate the data. Therefore, the offline computational burden in stage A increases exponentially as the number of design variables increases. To mitigate this, one option is to increase the sampling step. Instead of testing 11 combinations for each design variable, a smaller number, such as 10, could be tested. This would reduce the total number of data samples generated to 10^3 = 1000 instead of 1331 for a system with three design variables. However, increasing the sampling step may impact the learning and performance of the neural network model [172]. A better solution is to utilise the parallel computing toolbox in MATLAB. This toolbox enables efficient utilisation of the computer's multicore processors. By incorporating a few lines of code, simulations that would typically take days to run can be completed in just a few hours. Furthermore, by employing a PC with a higher number of processors, such as 24-core processors, the data generation process can be significantly accelerated. For instance, the 1331 data samples used in this study could be obtained within approximately 6 minutes on a PC with 24-core processors.

Table 4-3 Comparison between the conventional droop gain design, conventional ANN optimisation-based design and proposed design approach for the design of three control variables, k_{d1}, k_{d2} and k_{d3}.

Method	Accuracy of power sharing	Complexity of implementation	Code execution time	Potential for online tuning of droop gain parameter
Conventional droop gain design	Low	Low	-	-
Conventional ANN optimisation-based design [186]	High	High	-High - Around 0.16 s - Increases with an increase in the number of design variables and may become impractically long.	Not possible [187].
Proposed design approach	High	Low	-Low -Around 0.000135 s - Low prediction time irrespective of the number of design variables.	Good [191, 192, 193, 194].

While the NN model itself is computationally lightweight, the computational burden in stage C of the conventional ANN optimisation-based design increases with the number of design variables. However, the burden is not as significant as in stage A. For example, for the three design variables considered in this study, the surrogate model can output one design point in approximately 0.252 μs, resulting in the evaluation of all 636,056 design points taking around 0.16 s. The optimal solution is then obtained by simply finding the minimum value of the fitness function plot using the *min* function in MATLAB. However, when the number of design variables increases to four, and the same sampling step of 0.01 is used, approximately 55 million fitness functions need to be evaluated using the surrogate model. This evaluation process takes around 14 s. As a result, the computational burden for fitness function evaluation

becomes more intensive. Furthermore, evaluating such large fitness functions using the *min* function in MATLAB may become impractically long, and MATLAB's maximum array size preference could be exceeded due to memory and processing limitations. Consequently, the conventional ANN optimisation-based design may impose restrictions on the number of design variables that can be effectively handled. To mitigate the computational burden and overcome the limitation on the number of design variables, the fitness function can be evaluated sequentially, or gradient descent optimisation can be employed [39]. However, the ANN optimisation-based design approach may be prone to getting trapped in local minima in such a scenario. On the other hand, stage C of the proposed approach only requires a single user-defined desired design point as input to predict the optimal droop coefficients. Thus, it maintains a low computational burden regardless of the number of design variables, which is a significant advantage.

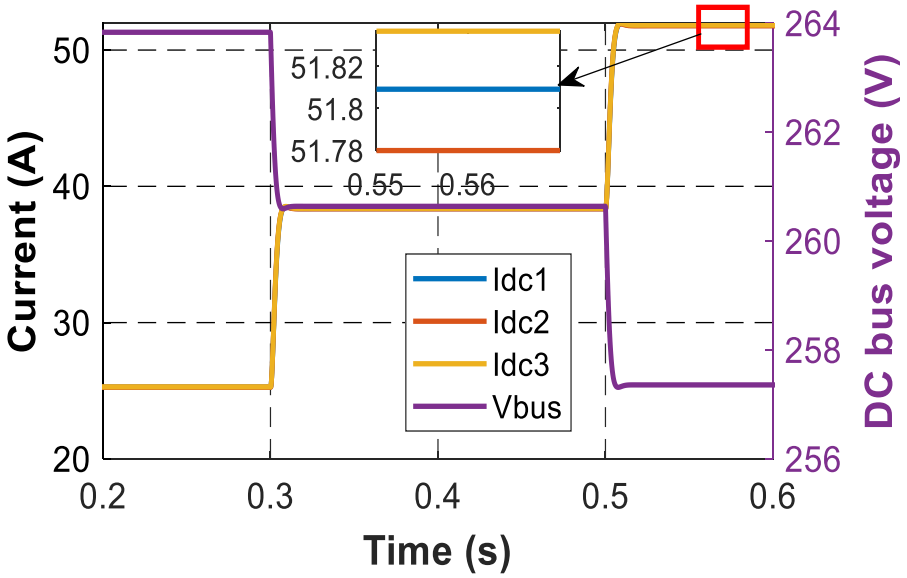
Table 4-3 provides a summarised comparison between the conventional ANN optimisation-based design and the proposed design approach. The proposed approach offers additional advantages, including its potential for real-time tuning of droop gain parameters.

4.5 Simulation Results

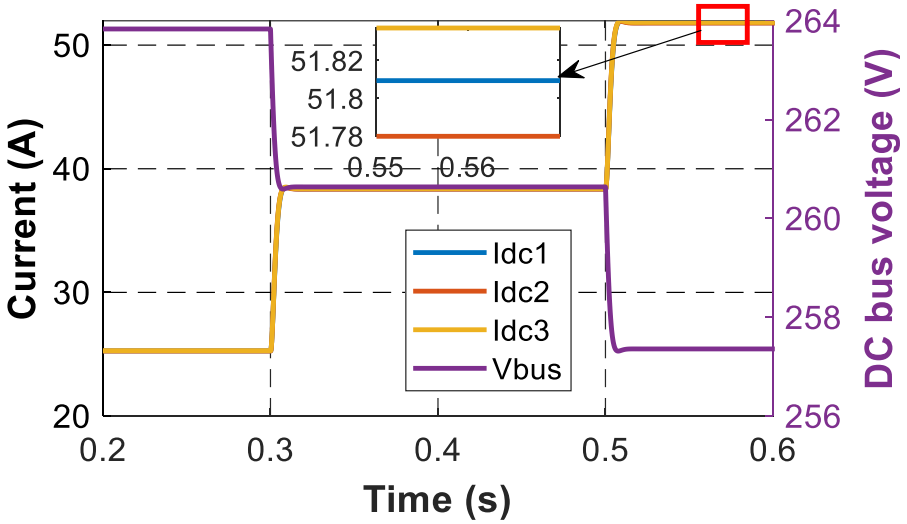
The detailed MEA EPS model (shown in Figure 4.1) used as case study is built in MATLAB Simulink environment. The simulation parameters are as shown in Table 3-1.

4.5.1 Equal Power Sharing with Three Generators

For comparison and to validate the optimal droop gain settings obtained using both design approaches (presented in Section 4.3.3), the optimal droop coefficient settings are utilised as inputs in the detailed simulation model of the studied system. Simulations are conducted with different constant power loads (CPLs) of 20 kW, 30 kW, and 40 kW at different time intervals, and the corresponding results are presented in Figure 4.6. The simulation parameters remain consistent with those provided in Table 3-1.



(a)



(b)

Figure 4.6 Simulation results of a comparison of the current sharing and bus voltage regulation performance using droop gain settings from the (a) Conventional ANN optimisation-based design and (b) Proposed design approach.

In Figure 4.6 (a), the current sharing and bus voltage regulation obtained using the optimal droop coefficient settings obtained from the conventional ANN optimisation-based design approach are recorded as I_{dc1} = 51.82 A, I_{dc2} = 51.77 A, I_{dc3} = 51.84 A, and V_{bus} = 257.4 V at t = 0.5 s. Consequently, the computed current sharing ratios between the converters and normalised bus voltage regulation are determined as n_1 = 0.9990, n_2 = 1.0004, and V_{bn} = 0.9533. Similarly, in Figure 4.6 (b), the current sharing and bus voltage regulation using the computed

optimal droop coefficient settings from the proposed approach yield I_{dc1} = 51.81 A, I_{dc2} = 51.78 A, I_{dc3} = 51.84 A, and V_{bus} = 257.4 V, respectively. Consequently, the calculated current sharing ratios between the converters and normalised bus voltage regulation are determined as n_1 = 0.9994, n_2 = 1.0006, and V_{bn} = 0.9533.

Based on the obtained results, it is evident that both approaches can achieve the desired control objectives. Additionally, it is observed that under the same design criteria, similar optimal droop gain settings can be obtained from both approaches, resulting in similar control performance as shown in Figure 4.6. However, the proposed approach in this chapter offers notable advantages over the conventional ANN optimisation-based design (presented in Chapter 3). With the proposed approach, only a single desired design point is required as input to the surrogate model for computing the optimal droop parameters. In contrast, the conventional ANN optimisation-based design necessitates processing and feeding the surrogate model with approximately 636,056 design points to determine the optimal droop gain parameter. Moreover, the proposed approach eliminates the need for formulating objective functions and assigning weighting factors to trade off control objectives, which is required in the conventional approach. As a result, the proposed design approach offers the power system designer a simple, flexible, and efficient method for generating optimal droop gain settings with low complexity and computational burden. These advantages are significant when compared to other optimisation techniques.

Furthermore, the proposed approach shows potential for online computation of droop gain parameters due to its low complexity and computational burden, as indicated by existing literature [191, 192, 193, 194]. Previous works that share similarities with the proposed design approach demonstrate reduced iterations for identifying optimal control variables [191], decreased computational burden [192], absence of weighting factor tuning, and short execution time [193, 194]. These features serve as the primary motivations behind the proposed approach. In general, ANN models trained offline can be employed either offline or implemented in a digital microprocessor for online applications [194].

4.5.2 Equal Power Sharing with Four Generators

To assess the performance of the proposed design approach in scenarios involving more than three control variables, a case study is conducted with four PMSG-AR systems aiming for

equal power sharing. In this setup, an additional PMSG-AR system is connected in parallel to the system depicted in Figure 4.1 (a). To establish the connection, an extra DC cable with resistance and inductance values of 20 mΩ and 6.67 μH, respectively, is utilised.

To accommodate the additional PMSG-AR system, a new dataset is generated for training the surrogate model. This process involves generating a total of 14,641 data samples, which requires approximately 6 hours to complete. For achieving equal power sharing among the generators and ensuring good bus voltage regulation, the desired inputs provided to the trained surrogate model are specified as $n_{1desired}$ = 1, $n_{2desired}$ = 1, $n_{3desired}$ = 1, and $V_{bndesired}$ = 0.964. Furthermore, the desired current sharing ratio between converter 1 and 4 is denoted as $n_{3desired}$. The surrogate model executes the code and computes the optimal droop gain settings to achieve the desired control performance within 0.000176 seconds.

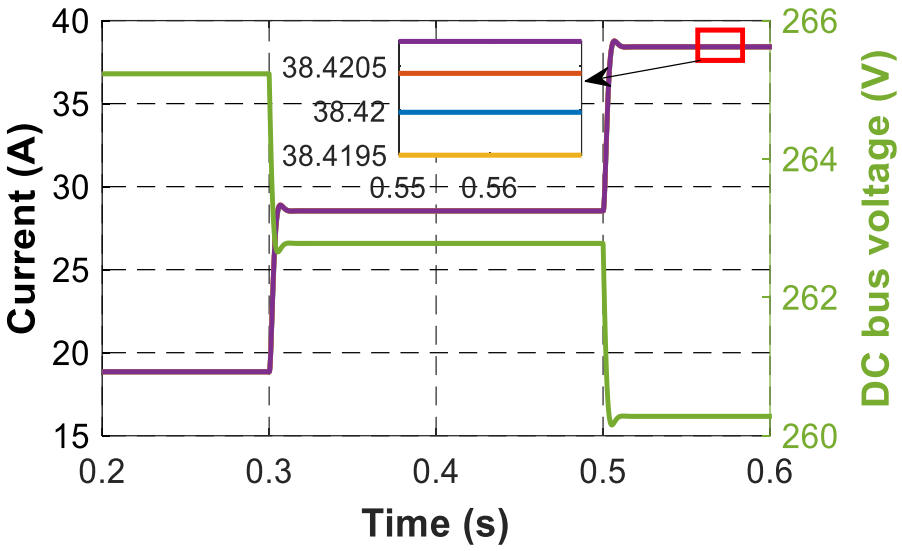


Figure 4.7 Simulation results for current sharing and bus voltage regulation using the proposed design approach for equal power sharing among four generators.

The computed optimal droop gain settings for the four PMSG-AR systems are determined as $k_{d1}^{computed}$ = 4.0017, $k_{d2}^{computed}$ = 4.4865, $k_{d3}^{computed}$ = 4.2035, and $k_{d4}^{computed}$ = 4.2939. These settings are utilised as inputs in the simulation, where CPLs of 20 kW, 30 kW, and 40 kW are applied at different time intervals. The resulting outcomes are presented in Figure 4.7. At t = 0.5 s, the obtained current sharing and bus voltage regulation values are I_{dc1} = 38.42 A, I_{dc2} = 38.42 A, I_{dc3} = 38.42 A, I_{dc4} = 38.42 A, and V_{bus} = 260.30 V. Consequently, the computed current sharing ratios between the converters and normalised bus voltage regulation are

determined as n_1 = 1.000, n_2 = 1.000, n_3 = 1.000, and V_{bn} = 0.964. These results demonstrate the capability of the proposed approach to handle complex networks and promptly compute the optimal droop gain settings immediately after the training process.

The primary objective of the study in the chapter is to achieve real-time computation of the optimal droop gain settings (k_{d1}^{opt}, k_{d2}^{opt}, and k_{d3}^{opt}) for the converters to enable the controller to adapt quickly to reference changes. The block diagram of the proposed control strategy for the PMSG-ARi systems in the MEA EPS distribution network is shown in Figure 4.8.

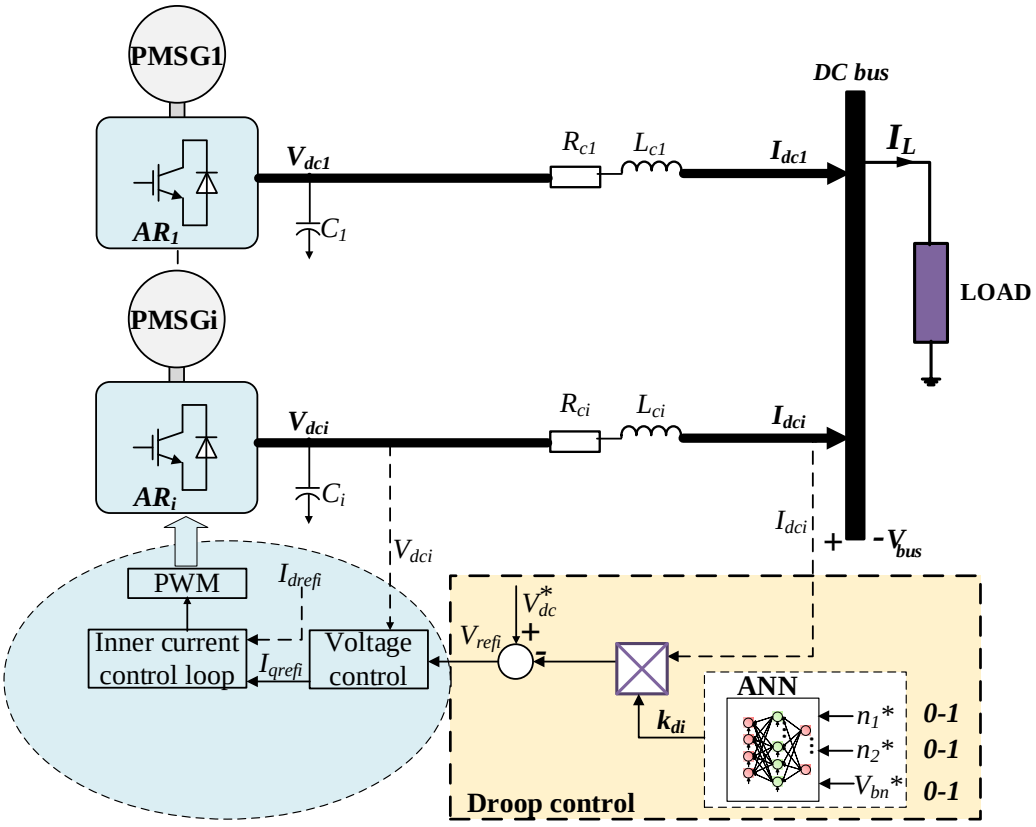
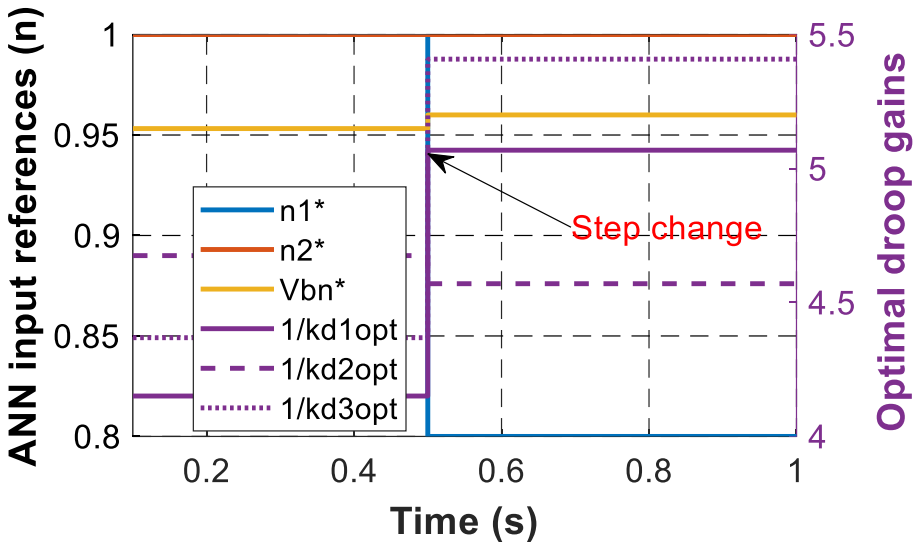


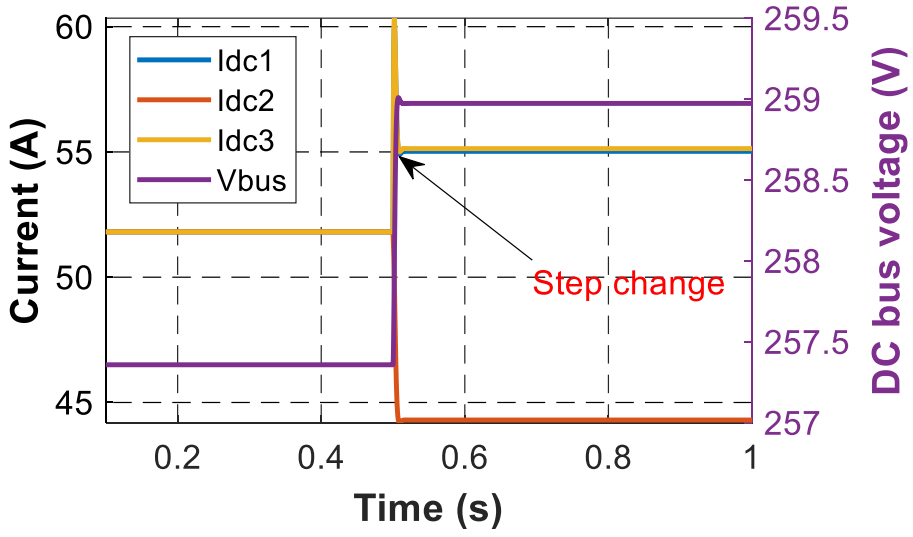
Figure 4.8 Block diagram of the proposed control strategy for the PMSG-ARi systems in the MEA EPS distribution network.

To exhibit the dynamic capabilities of the proposed methodology, a step change in the desired system responses is demonstrated, transitioning from n_1^* = 1.0, n_2^* = 1.0, V_{bn}^* = 0.9532 to n_1^* = 0.8, n_2^* = 1.0, V_{bn}^* = 0.96, as depicted in Figure 4.9. The response of the ANN, depicted in Figure 4.9 (a), showcases the immediate adjustment of computed optimal droop gain settings following the transient. Meanwhile, Figure 4.9 (b) illustrates the response of the local controllers, adapting current sharing and voltage regulation to align with the desired system

response. Importantly, the ANN's response is nearly instantaneous, a distinguishing advantage of the proposed approach over alternative methods based on the heuristic or ANN optimisation techniques.



(a)



(b)

Figure 4.9 Step response: (a) Desired system response (ANN model's input) and computed optimal droop gain settings by ANN model (b) Current sharing and bus voltage regulation.

4.6 Summary

This chapter introduced an innovative method for designing optimal droop gains in converters, emphasizing reduced computational complexity, and enhanced real-time tuning. The proposed approach simplifies the derivation of optimal droop gains based on power sharing requirements. It enables rapid computation of optimal droop gains using a single desired design point, significantly reducing execution time. The approach eliminates the need for complex objective functions and weighting factors, streamlining the design process. It allows adaptive adjustments of droop gains to meet specific performance needs, enhancing flexibility in dynamic conditions. Extensive simulations confirmed the method's effectiveness in regulating power sharing among parallel-connected converters and improving real-time control performance. Compared to conventional methods, this approach offers simplicity, lower computational burden, and avoids the need for explicit fitness functions, making it a promising solution for practical implementation in MEA EPS applications.

Chapter 5 Artificial Intelligence-Based Hierarchical Control Design

In the conventional droop control method employed in the primary control layer, there is an inherent trade-off between current-sharing accuracy and voltage regulation. Consequently, to achieve both accurate current sharing and maintain the bus voltage at its nominal value, secondary control schemes are implemented. Nevertheless, a proper design of control parameters of an electrical power system (EPS) is important as it has a huge impact on its stability and dynamic features. To that end, this chapter proposes a new artificial intelligent-based design strategy for the optimal design of the power sharing and bus voltage compensation coefficients for the islanded more electric aircraft (MEA) EPS DC MG. The effectiveness of the proposed approach is validated in both simulations and HIL experiments.

5.1 Introduction

The MEA EPS distribution network used as a case study is a typical DC MG operating in the islanding mode as shown in Figure 5.1. Figure 5.1 depicts the connection of two electrical generators (i.e., permanent magnet synchronous generators (PMSGs) to separate engine shafts: a high-pressure (HP) shaft and a low-pressure (LP) shaft. Alongside the generators, an auxiliary power unit (APU) is also present in the aircraft, serving as a backup power source in the event of engine or generator failure. These generators are feeding power to a common DC bus through their dedicated AC-DC converters. The generators operate in parallel, collectively supplying power to the DC bus. The generation systems, each with one PMSG and one AC/DC converter (referred to as *PMSG-AR* system), are connected to the DC bus with cables represented by resistive-inductive models. Within this MEA EPS, *PMSGs* extract power from aircraft engines or APUs. In aerospace applications, permanent magnet generators (PMGs) are favoured over other electrical machines such as switched reluctance starter/generators (SRSGs), wound-field synchronous machines (WFSMs), or induction generators (IG). This preference is attributed to the advantages in power density, volume, and weight [92]. Furthermore, achieving controlled power sharing among the generators holds the potential to

decrease the required generator capacity and enable operation at maximum efficiency levels [92].

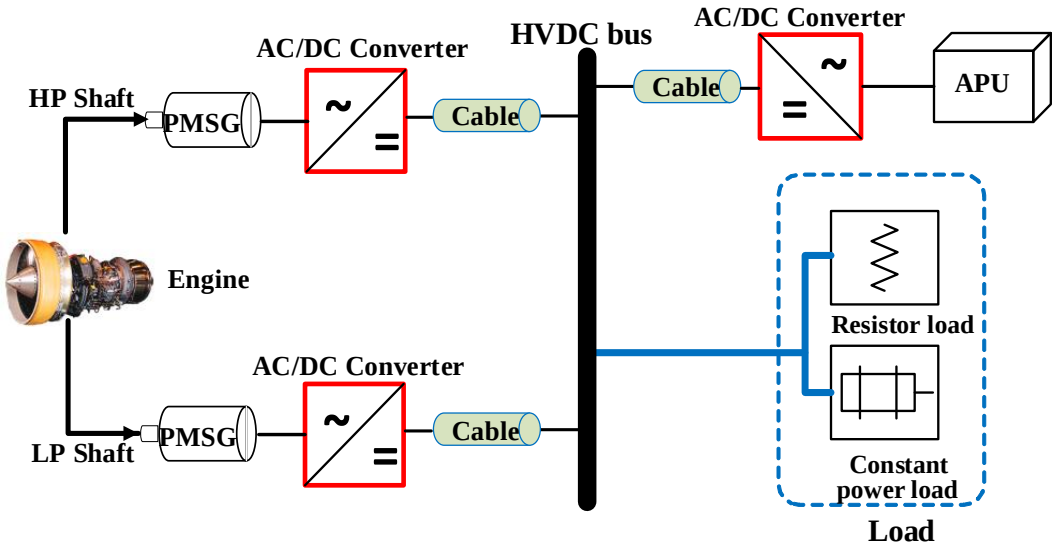


Figure 5.1 Single-bus HVDC distribution network utilised in the MEA EPS

However, a major concern in such a system operating in the islanded mode is the problem of power sharing and bus voltage regulation [111] which if not properly handled may result in power quality and stability issues in the EPS. In addition, the EPS could experience a huge disturbance when there is a sudden load change or one of the sources is under fault conditions. For example, the transition from standby mode to full operational mode, such as turning on various avionics systems, can result in an instantaneous increase in load. This disturbance may cause a significant drop in the bus voltage which can be harmful to loads, incur additional losses, affect the power quality, and make the EPS less stable. In this regard, there is a need for a robust control technique that will guarantee stable operation in different conditions of the EPS by restricting the bus voltage variation within an acceptable range while enhancing the current sharing dynamic performance. These are crucial issues that need to be addressed and are the focus of this chapter. Besides, a safety-critical application [195] such as the MEA requires a great control performance over the bus voltage in most conditions of the aircraft operations to power the electrical loads onboard and to meet MIL-STD-704F [49] and DO-160E [196] voltage standards.

The most suitable control strategy to tackle such concerns to realise both bus voltage compensation and improved load sharing simultaneously is the implementation of a secondary control (SC) [197, 198]. The SC level is used for voltage restoration due to the deviations

generated by the primary control (PC). The distributed control scheme is the most used secondary control scheme and is regarded as a trade-off between centralised and decentralised control schemes. In this control method [119], [161], [40, 199-205] [40, 199, 200, 201, 202, 203, 204, 205], the SC is implemented in local controllers that share information among themselves through a low bandwidth digital communication (LBC) link, without depending on a central controller. The use of large droop gains is recommended in [161], [40, 203, 204, 205] to minimise the error in load sharing at the PC level which is due to the potential inequality in nominal voltages and feeder resistance. Consequently, in [161], the product of the average current calculated by each local controller and a constant shift coefficient is used to shift up the droop characteristics line in each module in a proportionate manner as the load increases for compensation of the bus voltage deviation. In [199], the poor voltage regulation and load-sharing errors are compensated separately with the aid of a proportional (P) controller and a proportional-integral (PI) controller respectively. However, just as in [161], the principle of selecting the compensation coefficient is also difficult. A voltage drop of about 12% was recorded in [199] and to almost zero in [204] when one of the sources were disconnected due to a fault condition. Hence, their bus voltage regulation performance during the transient period can be regarded as poor. In [168, 206], adaptive droop control algorithms with secondary controllers to suppress the circulating current and the effect of line resistance on current sharing in a low-voltage DC MG are proposed. In these proposed methods, the droop parameters of the converters are adaptively adjusted following the estimated line resistance of the corresponding subsystem. However, their control performance is highly dependent on the accurate estimation of the feeder resistance. Moreover, since the distributed secondary control relies on a digital communication link, the availability, expandability, and reliability of the whole system will reduce. This will also increase the cost of the system and possibly its weight [160]. In addition, it may suffer from communication latency, traffic, and cyber-attacks [207, 208], which are not desirable in a safety-critical application such as the MEA EPS.

To improve the system reliability, a decentralised secondary control scheme that is independent of a communication link is proposed in [158, 209, 169, 210, 211]. In [158], a proportional (P) controller is implemented at the secondary control level to mitigate the influence of interconnecting cable resistance on load sharing. The proposed control method relies only on the local controllers and all the control variables are measured locally. Although independent of a communication link, however, it requires accurate knowledge of the line resistance to

determine the gain of the P-controller to adjust the droop gain of each converter module for better load sharing and DC bus voltage regulation. Besides, it is difficult to estimate the line resistance in practical situations. Also, its bus voltage regulation performance is poor under heavy load conditions and a source outage. The SC approaches presented thus far for voltage restoration rely either on online parameter estimation, communication medium and/or an extra PI controller. Hence, making the control system complex and unreliable.

In sharp contrast to the conventional voltage compensation methods, an improved bus voltage compensation approach to eliminate the deviation of the bus voltage and improve power sharing performance is proposed in [94]. In the proposed method, the droop gains of the converters are set to be larger than the cable resistance to achieve accurate power sharing at the PC level. Compared with existing approaches, although the approach in [94] has the advantage of not requiring a digital communication link and extra controllers, it can only provide good bus voltage regulation performance when the participating converters are contributing to the load current. Therefore, making the voltage regulation performance depend on the EPS condition.

Despite the good progress made in previous SC methods, high droop gains are commonly set for the converters to achieve accurate power sharing at the PC level. It is observed that this makes the control system less robust and reliable in the event of a source fault and/or failure of the SC [199]. This is of great concern and makes it important for further investigation into the design of the control parameters. It is expected that by the optimal design of the control parameters, the EPS should be able to maintain operation with good bus voltage performance in different conditions of the EPS. A safety-critical application such as the MEA EPS could benefit from such an optimal design.

Motivated by the challenges enumerated above, this chapter focuses on the optimal design of the control parameters used for power sharing and bus voltage compensation at the PC and SC levels respectively by developing a new AI-based design methodology. The proposed optimal design of the droop and bus voltage compensation coefficients is to maintain a good power quality within an acceptable range and ensure robust control performance during load changes, source failure and even in a situation of the failure of the SC [212]. The main contribution of this chapter is the development of a new neural network-based design strategy for the computation of the optimal droop and compensation coefficients based on desired power

sharing ratio and bus voltage regulation. Furthermore, a comparative assessment of the proposed approach with the control method used in [94] shows that the proposed method performs well in terms of power sharing and bus voltage regulation under a source outage even when the compensation coefficient is not updated in real-time and in the event of the failure of the SC.

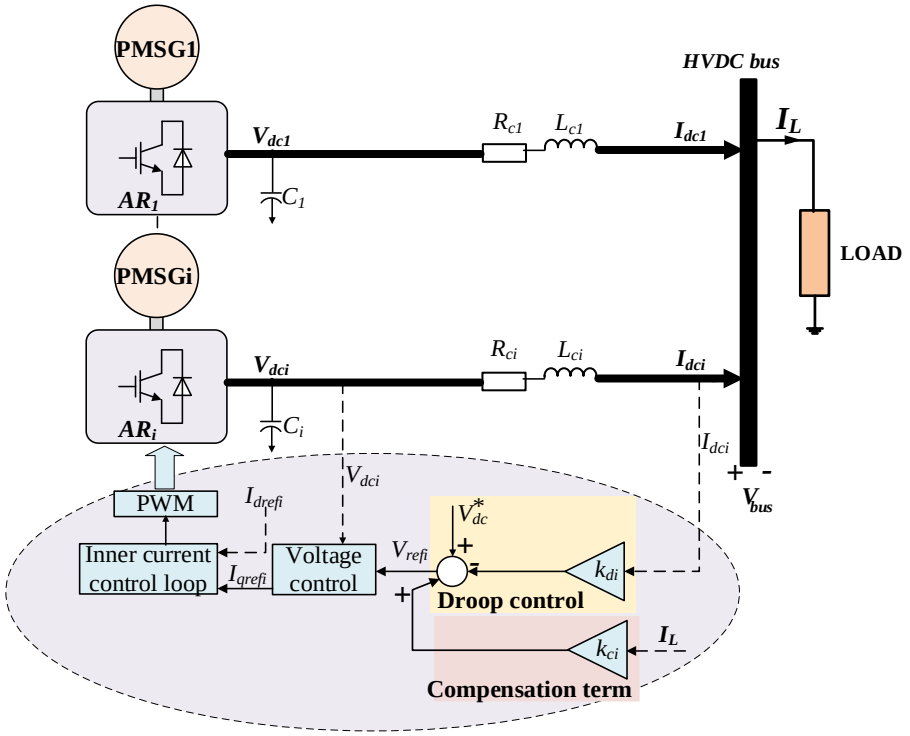


Figure 5.2 Proposed Hierarchical Control scheme for the MEA EPS DC grid.

5.2 Proposed Bus Voltage Compensation

It can be observed from (3-4) that due to the droop control, the bus voltage V_{bus} will not be equal to its nominal value V_{dc}^*, except if $I_{dci} = 0$. Moreover, the deviation will be more pronounced when a fault occurs on one of the generators and is disconnected from the system and under load changes. Therefore, there is a need to compensate for the bus voltage deviation and maintain it at or near its nominal value. One way to maintain the DC bus voltage at its nominal value is by adjusting the converter references. Hence, this thesis proposes the bus voltage restoration using a feedforward compensation technique as shown in Figure 5.2. In the proposed technique, a secondary compensation term ΔV is designed and added as feedforward into the primary controller.

Based on the addition of the compensation term, the expression in (3-1) becomes

$$V_{ref\,i} = V_{dc}^{*} - k_{di} I_{dci} + \Delta V \tag{5-1}$$

Consequently, the HVDC bus voltage V_{bus} after compensation becomes.

$$V_{bus} = V_{dc}^{*} - (k_{di} + R_{ci}) I_{dci} + \Delta V \tag{5-2}$$

It can be observed from (5-1), that the droop characteristics can be shifted (i.e., adjusted) along the voltage axis by adding a correction term ΔV. As the ultimate control goal is to achieve V_{bus} to be 270V, thus the total load current on the HVDC bus is critical and is used in the compensation term as

$$\Delta V = k_c I_L \tag{5-3}$$

where the total load current I_L is given as

$$I_L = I_{dc1} + I_{dc2} + I_{dc3} = (V_{dc}^{*} - V_{bus}) \sum_{i=1}^{n} \frac{1}{(k_{di} + R_{ci})} \tag{5-4}$$

From (5-3) and (5-4), we can see that the voltage reference of each power source in the system can be adjusted using the compensation term via a feedforward link as shown in Figure 5.2. As shown in Figure 5.2, each local dc-link voltage reference V_{refi} (i=1,2,3) is now added with a common compensation term ΔV associated with the total load currents (i.e., k_cI$_L$). No extra communication link or voltage controller is needed. The total load current I_L is transmitted to the local controllers via power line communication [198]. To achieve expected compensation and power sharing, the coefficient k_c and local droop k_{di} need to be properly selected and will be discussed in the next Section 5.3.

To facilitate the development of our proposed optimal control parameters design and computation strategy in Section 5.3, the way the droop and compensation coefficients are selected in [94] will be presented first since the feedforward technique is also used for the voltage compensation. In the first instance, the individual droop gains k_{di} are selected for the converters to be larger than the line resistance R_{ci} (i.e., $k_{di} \gg R_{ci}$) to mitigate the effect of cable resistance on power sharing. Also, the voltage compensation coefficient referred to as the

global droop gain k_c is selected as follows. From (5-4), the droop characteristics of the DC bus are defined by the expression (5-5) [94].

$$k_c = \frac{1}{\sum_{i=1}^{n} \frac{1}{(k_{di} + R_{ci})}} \tag{5-5}$$

where k_c is the global droop gain. By selecting the individual droop gain to be large, the effect of line resistance in (5-5) can be ignored. Hence, the expression in (5-5) can be re-written as

$$k_c = \frac{1}{\sum_{i=1}^{n} \frac{1}{k_{di}}} \tag{5-6}$$

It can be observed from (5-6) that the global droop gain k_c is closely related to the individual high droop gains k_{di}. This coefficient selection process has the following drawbacks.

- In a situation where not all the participating converters are contributing to the load current due to for example a source failure, then, the bus voltage regulation becomes poor [201]. To solve this problem and restore the bus voltage to its nominal value, the global droop gain will need to be updated in real-time according to the new EPS condition. Thus, requiring extra effort.
- If the SC fails and only the primary droop control is working, the high individual local droop gain selected for the converters will lead to a huge drop in the bus voltage. Such a huge drop in the bus voltage is not ideal for the electrical loads onboard the aircraft and it will degrade the system performance, causing power quality and system stability issues.

Therefore, the way the droop and compensation coefficients are selected in [94] makes the control approach highly dependent on the EPS condition and less robust. Motivated by these challenging issues, a novel and intelligent design strategy for the optimal design of the control parameters to safeguard a safety-critical application such as the MEA EPS from such vulnerabilities and ensure acceptable voltage regulations in different conditions of the EPS will be developed. The control problem is considered an optimisation problem in which an ANN-based surrogate model is used for the computation of the optimal settings of the droop and

compensation coefficients. A detailed comparison between the proposed approach and the method used [94] is provided in Section 5.4.

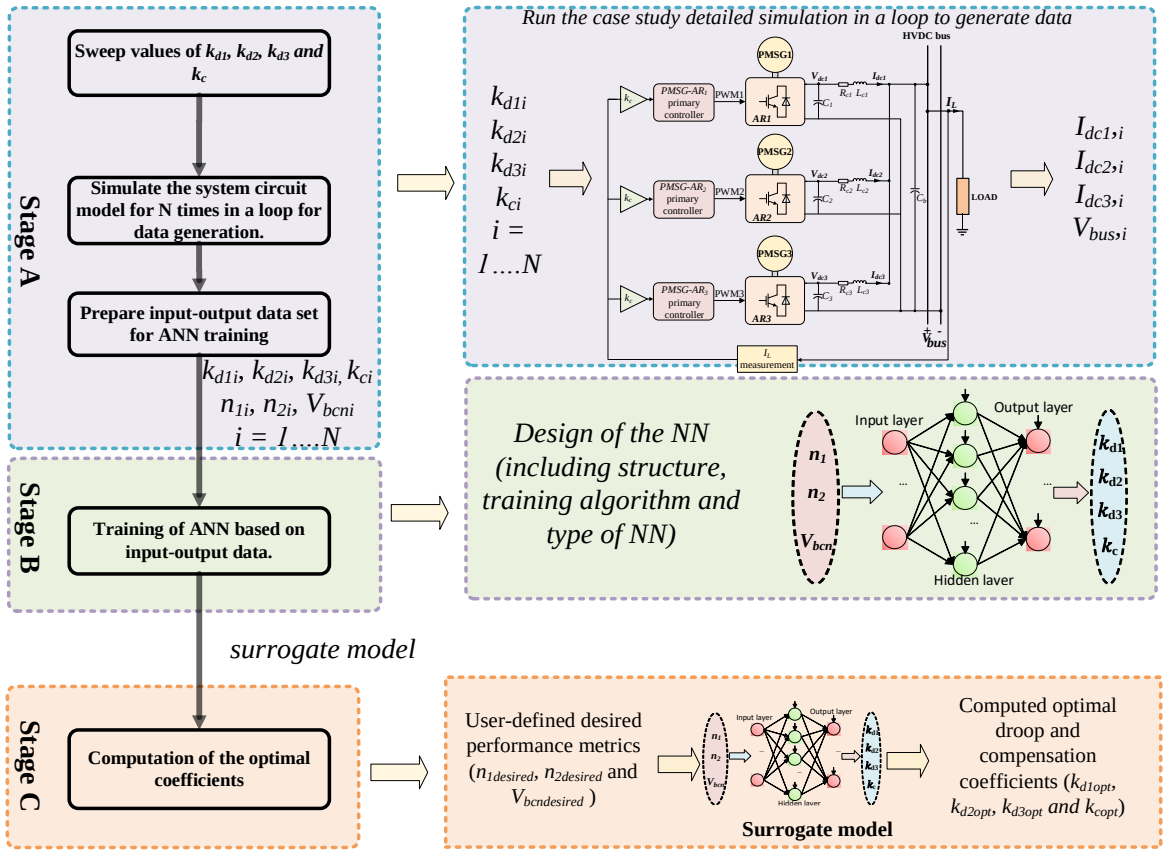


Figure 5.3 Flowchart for the design of the droop and compensation coefficients using the ANN approach.

5.3 Proposed ANN-based Hierarchical Control Design Approach

The main objective of this section is to introduce the design process of the optimal droop gain of each power source, k_{di}, and compensation coefficient, k_c, to achieve accurate power sharing and bus voltage restoration. A neural network-based design strategy for the computation of the optimal droop and compensation coefficients that will yield a user-defined desired power sharing ratio and bus voltage compensation at the PC and SC levels simultaneously will be developed.

5.3.1 Methodology

Figure 5.3 shows the flowchart of the design steps to be followed. As shown in Figure 5.3, there are three stages (i.e., stages A, B and C) in the process of obtaining the optimal control coefficients. Each of the stages is discussed as follows.

5.3.1.1 Stage A: Data generation

To generate data to train the ANN, the detailed model of the case study shown in Figure 5.4 is built in MATLAB Simulink and is simulated with different combinations of the droop gains, k_{d1}, k_{d2}, and k_{d3}, and the compensation coefficient, k_c within a design space shown in Table 5-1. The corresponding current sharing ratios, n_1 and n_2, and normalised bus voltage $V_{bcn} = V_{\text{bus}}/270$ are thus derived and stored after each simulation cycle. A total of 14,641 data samples were obtained from the simulation exercise. The multiple simulations were run in a loop with the aid of MATLAB codes on a standard computer with quad-core processors. Each simulation run takes around 6 s, thus, it takes approximately 6 hours to generate the entire data samples. The system parameters used in the simulation for data generation are shown in Table 3-1.

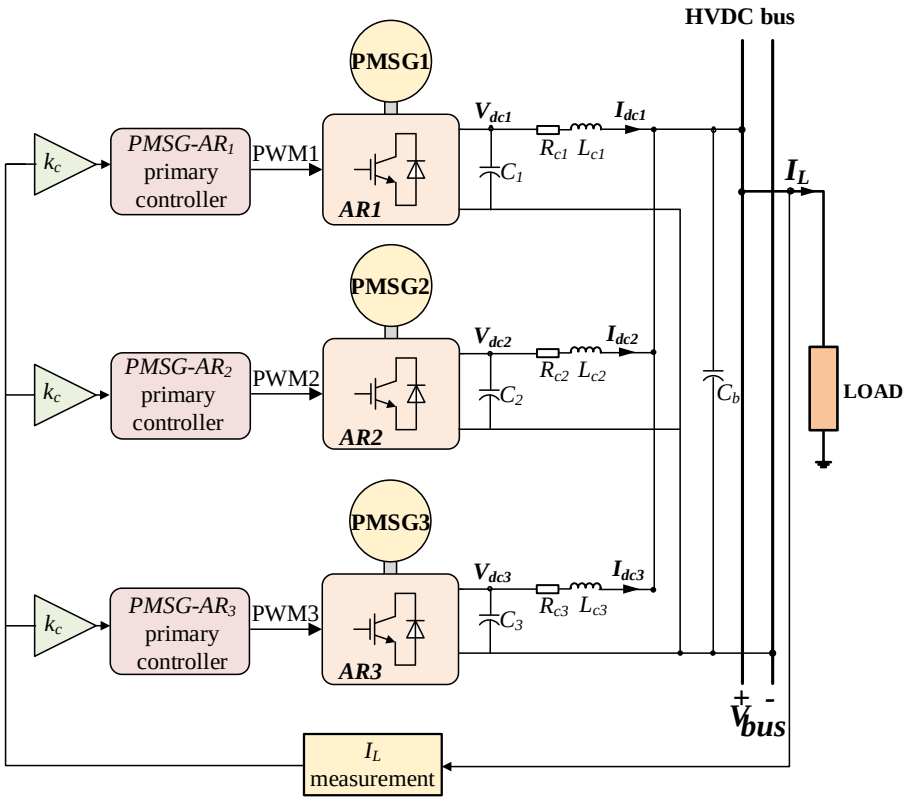


Figure 5.4 Case study setup

Table 5-1 Simulation Input Variables Ranges for Data Generation

Parameter	Range	Sampling Step	Number of Samples
$1/k_{d1}$	[3.825, 4.675]	0.085	11 x 11 x 11 x 11 = 14,641
$1/k_{d2}$	[3.825, 4.675]	0.085	
$1/k_{d3}$	[3.825, 4.675]	0.085	
$1/k_c$	[11.475, 14.025]	0.255	

In stage A, the relationship between the inputs (x) to the simulation model and processed outputs (y) can be represented as

$$y = F(x) \Leftrightarrow (n_1, n_2, V_{bcn}) = F(k_{d1}, k_{d2}, k_{d3}, k_c) \tag{5-7}$$

5.3.1.2 Stage B: Training and Development of the Surrogate Model

The data generated from stage A is used to train an ANN-based surrogate model in stage B. The ANN is trained with the current sharing ratios (n_1 and n_2), and the normalised bus voltage (V_{bcn}) as inputs and the droop and compensation coefficients (k_{d1}, k_{d2}, k_{d3}, and k_c) as outputs to derive a fast surrogate model to allow quick computation of the optimal control coefficients. The FFNN structure shown in Figure 5.5 with the backpropagation training algorithm is used for the training and development of the surrogate model.

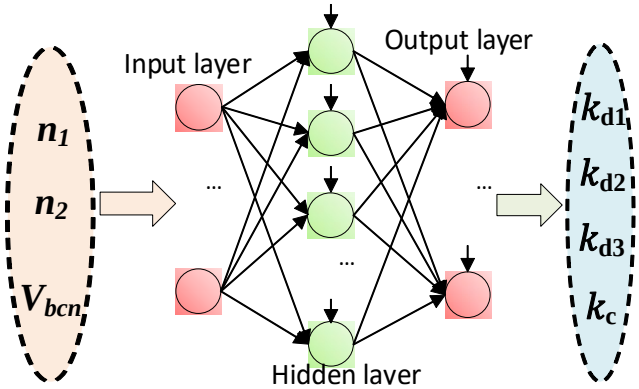


Figure 5.5 Schematic of the NN-based surrogate model.

The FFNN structure is made up of 3 neurons in the input layer which are equivalent to the three system outputs n_1, n_2 and V_{bcn}, 11 neurons in the hidden layer and 4 neurons in the output layer which are equivalent to the four design variables (k_{d1}, k_{d2}, k_{d3} and k_c). The surrogate model represents the input-output data mapping relationship in (5-8).

$$y = F(x) \Leftrightarrow (k_{d1}, k_{d2}, k_{d3}, k_c) = F(n_1, n_2, V_{bcn}) \tag{5-8}$$

The ANN-based surrogate model is usually employed to establish the relationship between input data and output data through mapping in situations where the relationship between the two is unknown or computationally intensive to assess. It can approximate non-linear functions to a high degree of accuracy with little knowledge about the system [133]. The training was implemented using the built-in NN fitting toolbox in MATLAB. Further details about the NN fundamental working principle, structure selection and training process can be found in [145], [188].

5.3.1.3 Stage C: Deployment of the surrogate model

Finally, after training, the surrogate model can be used in stage C and power system designers can define the desired current sharing ratios (i.e., $n_{1desired}$ and $n_{2desired}$) and normalised bus voltage regulation ($V_{bcndesired}$) that are within the design space as input to the surrogate model to compute the optimal droop and compensation coefficients (k_{d1opt}, k_{d2opt}, k_{d3opt} and k_{copt}) to yield such control performance. The computed optimal droop and compensation coefficients can then be used to control the load sharing and bus voltage regulation as desired in both simulations and HIL experiments. The proposed design strategy only requires specific input-output data measurement and does not need detailed information and knowledge of the system under study. Hence, making it robust when compared with existing design approaches.

5.3.2 Design Consideration and Stability Concerns

Before carrying out the proposed design approach, the design range of the design variables (i.e., k_{di} and k_c) should be pre-defined. It is important to choose a proper design range for the design variables in such a manner that the stability of the system will not be compromised and based on the desired control objectives. To that end, the upper and lower bounds (i.e., design range) of each of the droop gains are defined to be +10% and -10% respectively of the traditional fixed droop gains. Furthermore, a detailed comparative stability analysis of droop

control approaches in voltage source converter-based DC MGs carried out in [174], found that the maximum droop gain for stable operation should not exceed the expression in (3-11). For the compensation coefficient k_c, its range is selected as shown in Table 5-1 to maintain the droop control function and guarantee system stability [161].

5.3.3 Computational Burden

The data generation stage (i.e., stage A) costs time (i.e., computational burden) and this may increase exponentially with an increasing number of design variables. Quantitatively speaking, the time taken (offline) for the data generation was estimated by using the duration it takes to run one single simulation as a benchmark. Therefore, for the 14,641 design variable combinations and simulation runs, the computational burden for the data generation amounted to about 6 hours on a standard computer with quad-core processors. However, it would have only cost around 1 hour or less to run the simulations for the same design variable combinations on a computer with a 24-core processor by running the simulations in parallel with the aid of the parallel computing toolbox in MATLAB and a few lines of codes. It is important to note that, although, this stage A comes with some computational costs (offline), however, it is only required to be executed once and not for every coefficient design that is within the design space.

The training stage B is straightforward and can be accomplished quickly using the NN fitting toolbox in MATLAB. The usual challenge in this stage is the selection of a suitable number of neurons for the hidden layers. Although the selection is done using a trial-and-error process, the process can be executed quite fast (less than 1 minute). Besides, the NN fitting toolbox generates results quickly. Thus, the power system designer can arrive at a suitable number of neurons within a short time.

The trained surrogate model can output results with just a click of a button after being provided with appropriate inputs. Thus, making this stage several orders of magnitude faster than stages A and B.

5.4 Design Examples and Validation Using Simulation

5.4.1 Design Examples

In this section, the trained surrogate model is used to compute the optimal droop and compensation coefficients to realise two (2) exemplary control goals for the MEA EPS. The two (2) design cases considered in this chapter are explained as follows.

5.4.1.1 Design example 1: Equal load sharing and bus voltage compensation

In this design example, the sources ($PMSG_{1\text{-}3}$) are assumed to have equal ratings (i.e., $I_{dc1}^{rated} = I_{dc2}^{rated} = I_{dc3}^{rated}$) and thus expected to share the load current demand equally while maintaining the bus voltage regulation at its nominal value in steady states. To achieve this control performance, the desired current sharing ratios and normalised bus voltage which are used as inputs to the surrogate model are defined as $n_{1desired} = 1$, $n_{2desired} = 1$, and $V_{bcndesired} = 1$. Consequently, the computed optimal droop and compensation coefficients by the surrogate model are obtained as $k_{d1opt} = 1/4.0305$, $k_{d2opt} = 1/4.5211$, $k_{d3opt} = 1/4.2342$, and $k_{copt} = 1/11.9501$.

5.4.1.2 Design example 2: Unequal load sharing and bus voltage compensation

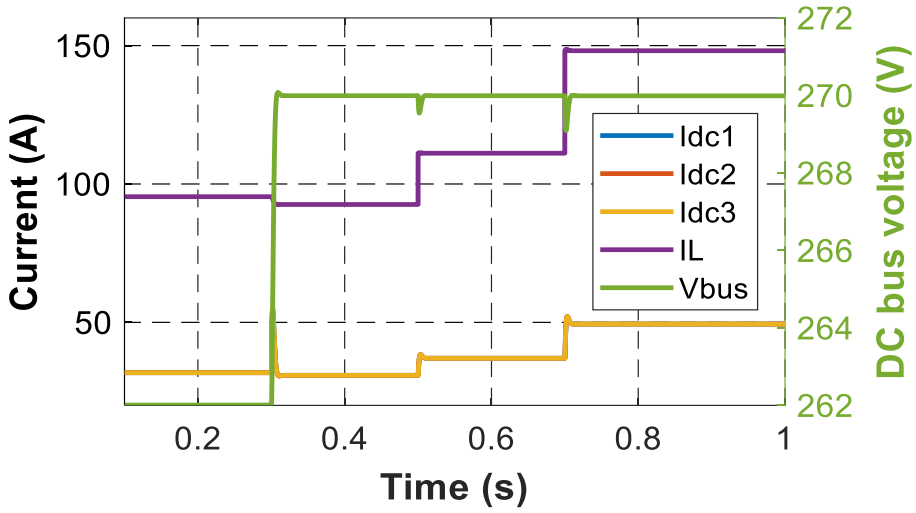
In this design example and within the design space considered (see Table 5-1), $PMSG_1$ and $PMSG_3$ are assumed to have equal ratings but 10% higher than that of $PMSG_2$ (i.e., $0.9I_{dc1}^{rated} = I_{dc2}^{rated} = 0.9I_{dc3}^{rated}$). Therefore, $PMSG_{1,3}$ is expected to share the load demand equally and more than $PMSG_2$. In addition, the bus voltage regulation is desired to be maintained at its nominal value in steady states. To achieve this control objective, the desired current sharing ratios and normalised bus voltage which are inputs to the surrogate model are defined as $n_{1desired} = 0.9$, $n_{2desired} = 1$, and $V_{bcndesired} = 1$. Thus, the computed optimal droop and compensation coefficients by the surrogate model are $k_{d1opt} = 1/4.2434$, $k_{d2opt} = 1/4.2540$, $k_{d3opt} = 1/4.4698$, and $k_{copt} = 1/12.1502$. The validity of these computed optimal coefficients from the two design examples will be tested first in simulation.

5.4.2 Simulation Results

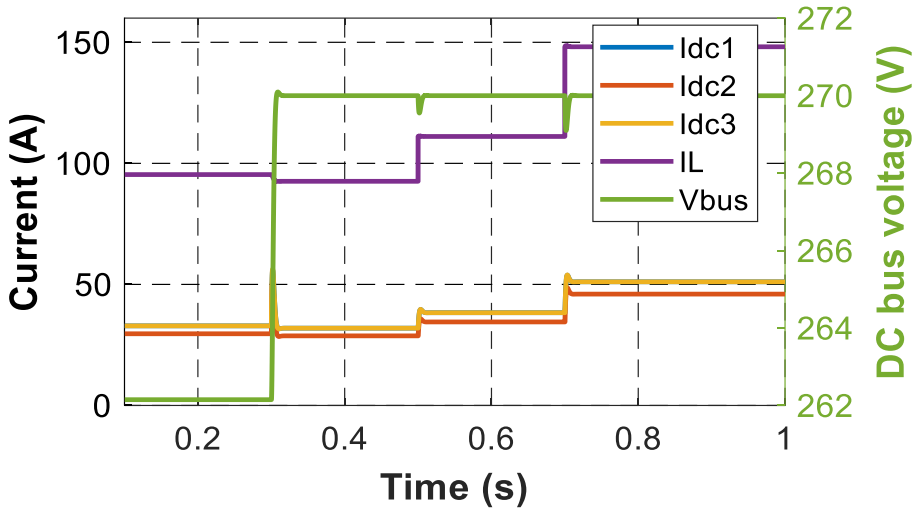
In this section, the performance of the proposed approach with the optimal control coefficient settings is validated and compared with the conventional droop control method and the approach proposed in [94] using simulation case studies. In this regard, the MEA EPS distribution network case study (shown in Figure 5.4) with three *PMSG-AR* systems working in parallel is modelled in MATLAB/Simulink. The simulation parameters are the same as those shown in Table 3-1.

5.4.2.1 Case 1: Normal scenario

Figure 5.6 (a) and (b) show the simulation results of the case study based on using the optimal coefficient settings obtained from design examples 1 and 2 respectively. CPLs of 25 kW, 30 kW and 40 kW are applied at times 0.1 s, 0.5 s and 0.7 s respectively during the simulation. As shown in Figure 5.6 (a), from time t = 0.1 s to t = 0.3 s only the PC (i.e., droop control) is activated, hence, the bus voltage drops to around 262 V which represents a 2.96% deviation of the bus voltage from its nominal value. This is an advantage of using the optimal droop gain settings at the PC level. Though it cannot maintain the bus voltage at its nominal value at this control level due to the droop control action. However, it can mitigate the tradeoff between the current sharing accuracy and bus voltage regulation. Besides, a voltage range of between 250 V to 280 V is acceptable for the MEA application in steady states [49]. Immediately the SC is activated at t = 0.3 s, the voltage drop at the PC level is compensated and the bus voltage is restored to its nominal value as desired (i.e., $V_{bcndesired}$ = 1). Furthermore, the bus voltage is maintained at its nominal value despite the load changes. Also, equal current sharing in the desired ratio ($n_{1desired}$ = 1 and $n_{2desired}$ = 1) is achieved at both PC and SC levels irrespective of the load fluctuations. The result of this case study shows that the proposed approach can guarantee both proportional current sharing and bus voltage restoration simultaneously as desired.



(a)

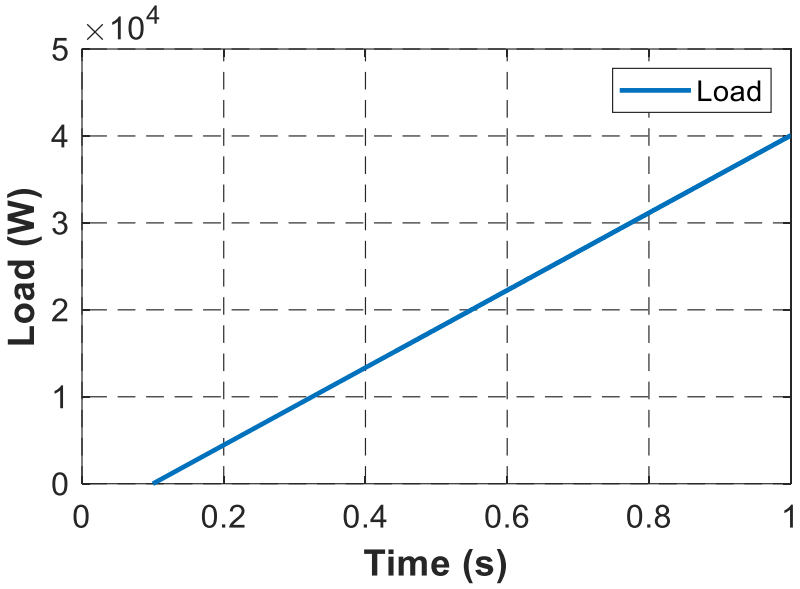


(b)

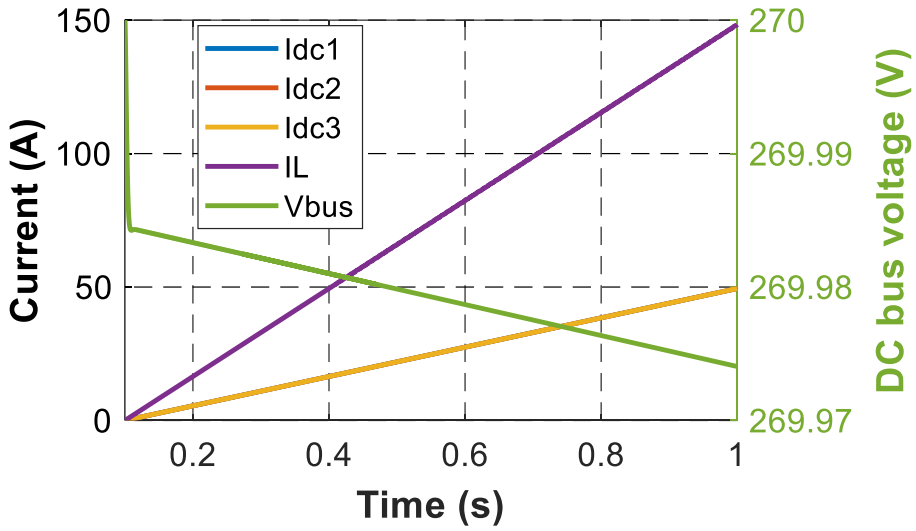
Figure 5.6 Simulation results of the case study for load sharing and bus voltage regulation using Optimal control coefficient from (a) Design example 1 (b) Design example 2.

Similarly, as shown in Figure 5.6 (b), from t = 0.1 s to t = 0.3 s only the PC is activated, hence, the bus voltage drops to around 262.15 V which represents a 2.91% deviation of the bus voltage from its nominal value. However, immediately the secondary control is activated at t = 0.3 s, the voltage drop at the primary control level is compensated and the bus voltage is restored to its nominal value as desired (i.e., $V_{bcndesired}$ = 1). Furthermore, the bus voltage is maintained at its nominal value despite the load changes. Also, proportional current sharing in the desired ratio ($n_{1desired}$ = 0.9 and $n_{2desired}$ = 1) is achieved at both PC and SC levels irrespective of the

load changes. This result demonstrates that the proposed approach can yield proportional current sharing and bus voltage restoration simultaneously as desired.



(a)



(b)

Figure 5.7 (a) ramp load (b) Simulation results of the case study for load sharing and bus voltage regulation using optimal control coefficient from design example 1.

The performance of the proposed approach is tested under a ramp load. A ramp load is applied at 0.1 s as shown in Figure 5.7 (a). Figure 5.7 (b) show the simulation results of the case study based on using the optimal coefficient settings obtained from design examples 1. As shown in Figure 5.7 (b), using the proposed control strategy and with the SC activated, the bus voltage

is maintained at or near its nominal value despite the gradual load changes. Also, equal current sharing in the desired ratio ($n_{1desired}$ = 1 and $n_{2desired}$ = 1) is achieved irrespective of the load changes. The result of this case study shows that the proposed approach can guarantee both proportional current sharing and bus voltage restoration simultaneously as desired.

5.4.2.2 Case 2: Comparison with an existing method

Here, the proposed control approach is compared with the one presented in [94]. The control parameters for the proposed method are k_{d1opt} = 1/4.0305, k_{d2opt} = 1/4.5211, k_{d3opt} = 1/4.2342, and k_{copt} = 1/11.9501 as obtained from design example 1. The parameters for [94] are $k_{d1} = k_{d2} = k_{d3}$ = 2, and k_c = 2/3 to meet the condition $k_{di} \gg R_{ci}$. The simulation parameters are the same as in Case 1. The system goes through the following four stages:

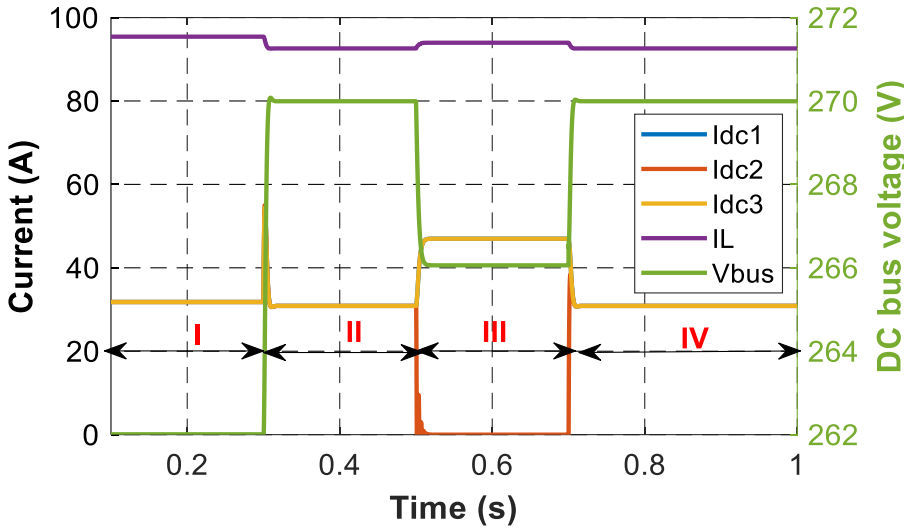
Stage I (0.1 – 0.3 s): A CPL of 25 kW is applied in the simulation and only the primary control (i.e., droop control is activated) at t = 0.1 s.

Stage II (0.3 – 0.5 s): Secondary control is implemented at t = 0.3 s.

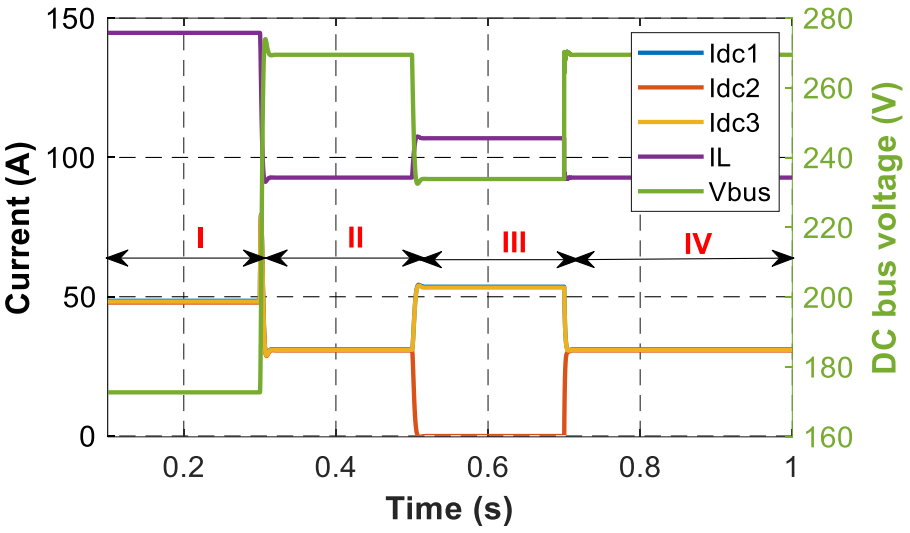
Stage III (0.5 – 0.7 s): PMSG-AR$_2$ is disconnected from the system (assumed to be under fault condition).

Stage IV (0.7 – 1 s): The fault is cleared and the *PMSG-AR$_2$* is re-connected back to the system.

The simulation result for this case study is shown in Figure 5.8 (a) and (b) for the proposed method and the approach presented in [94] respectively. In stage I, it is observed that with only the PC activated and using the optimal droop gain settings, both accurate current sharing and a very good bus voltage regulation (the V_{bus} drops to 262 V) can be realised as shown in Figure 5.8 (a). On the other hand, though the method proposed in [94] can achieve accurate current sharing using high drop gains at the PC level, however, the bus voltage drop is very high (the V_{bus} drop to 172.75 V) as shown in Figure 5.8 (b). This voltage drop represents about a 36.19% deviation of the bus voltage from its nominal value. This is not good for loads and may cause instability in the system if the SC fails.



(a)



(b)

Figure 5.8 Simulation results of the case study for load sharing and bus voltage regulation comparison between (a) Proposed method [212] (b) Approach presented in [94].

In stage II, both approaches can achieve accurate power sharing and restore the bus voltage to its nominal value simultaneously when the SC is activated at t = 0.3 s as shown in Figure 5.8 (a) and (b). However, despite the SC being active, the method presented in [94] to have good control over the bus voltage when *PMSG-AR*$_2$ is assumed to be faulty and temporarily disconnected (i.e., under a source outage (SO)) from the system at t = 0.5 s (i.e., stage III). The bus voltage drops to 233.89 V (representing a voltage drop of about 13.37% of the nominal value) under the fault condition as shown in Figure 5.8 (b). In contrast, the proposed control

approach with designed optimal control parameters has excellent control over the bus voltage even under SO (or fault conditions). The bus voltage drops to 266.06 V (representing a voltage drop of only about 1.46% of the nominal value) as shown in Figure 5.8 (a). This clearly shows the superiority of the proposed approach. Therefore, it can be said that the bus voltage regulation performance is significantly affected under the conditions of a source outage (SO) and failure of the SC when using the control parameters from [94], while the control parameter obtained using the proposed approach can guarantee desired power sharing and improved bus voltage compensation in different EPS operation conditions.

Table 5-2 Comparison of branch current and transmission loss of the method in [94] and proposed control approach.

Method		[94]	Proposed approach [212]
Stage I	Branch currents (I_{dc1}/I_{dc2}/I_{dc3})	48.55 A /47.91 A/48.26 A	31.80 A/31.80 A/31.80 A
	Transmission loss	110.90 W	48.54 W
Stage III	Branch currents (I_{dc1}/ I_{dc2}/ I_{dc3})	53.60 A/0.00 A/53.28 A	46.98 A/0.00 A/46.98 A
	Transmission loss	51.20 W	39.73 W
Stages II and IV	Branch currents (I_{dc1}/ I_{dc2}/ I_{dc3})	31.12 A/30.71 A/30.94 A	30.86 A/30.86 A /30.86 A
	Transmission loss	45.71 W	45.56 W

Furthermore, as shown in Table 5-2, the proposed approach can reduce the current in the individual branches compared to the method used in [94]. Consequently, the interconnecting cable losses are also reduced. It can therefore be said that the efficiency of the system will be enhanced due to reduced losses in lines as shown in Table 5-2. This can be attributed to the better voltage regulation of the proposed approach compared to the approach used in [94]. The system's stability and overall efficiency will be increased using the proposed control method. Finally, as shown in Figure 5.8 (a) and (b), the system is restored to its pre-fault condition immediately after the fault is cleared and the *PMSG-AR*$_2$ is reconnected back to the system at t = 0.7 s.

5.4.2.3 Plug-and-Play Capability

This case study demonstrates the plug-and-play capability of the proposed approach. Here, the surrogate model is trained with data samples obtained under different conditions of the EPS (such as one or two generators failure). To enhance the capability of the proposed strategy, the author suggests including abnormal operation scenarios in the ANN training to have more dynamic data sets. The data set should be stored in a lookup table to train the corresponding surrogate model [190]. This way, the training sessions will need to be carried out once or less frequently and not whenever the network changes. The recomputed optimal compensation coefficients are k_{copt} = 1/11.9501 when all three sources are working, k_{copt} = 1/7.9649 when two sources are working, and k_{copt} = 1/3.9798 when only one source is operational. However, irrespective of the number of sources under fault conditions, the other active sources will share the load power demand according to their respective optimal droop gain. Thus, the optimal droop coefficients are unchanged and remain as k_{d1opt} = 1/4.0305, k_{d2opt} = 1/4.5211 and k_{d3opt} = 1/4.2342 for equal load sharing. A CPL of 40 kW is applied at t = 0.1 s during the simulation and the secondary control is also activated.

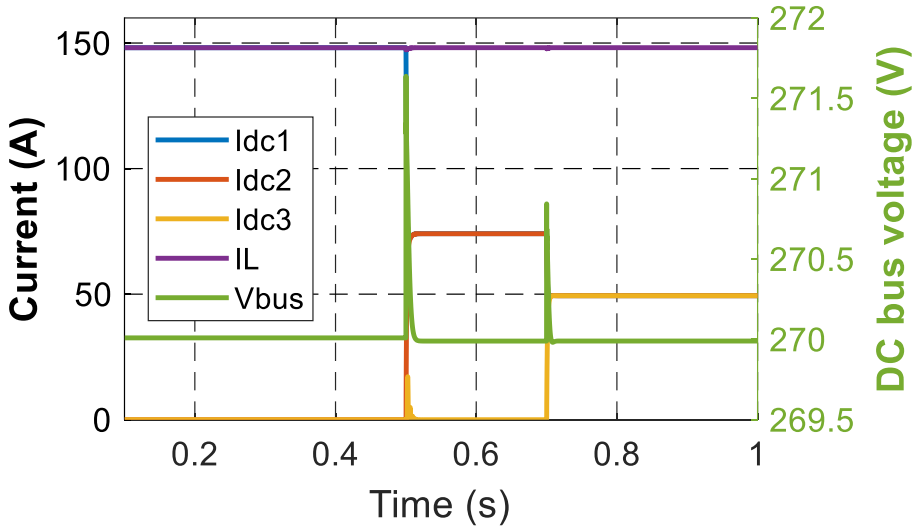


Figure 5.9 Simulation results showing the plug-in and plug-out capability of the proposed approach.

As shown in Figure 5.9, only *PMSG-AR*$_1$ is initially connected to the DC bus, followed by *PMSG-AR*$_2$ and then *PMSG-AR*$_3$. The results obtained show that as the new PMSG-AR system

is connected to the DC bus, both accurate power sharing and bus voltage restoration are realised simultaneously.

5.4.2.4 Impact of Variation in the Cable Resistance

The line resistance is usually unknown in practice and is considered the major factor that influences the current sharing and voltage deviation in the DC MG [213, 206]. Furthermore, it is affected by various factors such as temperature variation, the materials of the transmission cable and their thickness. In this case study, the impact of the variation of the cable resistance on the current sharing and voltage regulation performance of the proposed control method is investigated.

A CPL of 25 kW is applied during the simulation and the optimal droop and compensation coefficients from design example 1 are used. The cable resistances are varied by - 30%, 30%, - 50%, 50% and 200% which corresponds to 0.3, 1.3, 0.5, 1.5 and 2 respectively of their initial values shown in Table 3-1. The results obtained are shown in Figure 5.10. It can be observed from Figure 5.10 that with a variation of -30%, 30%, -50% and 50% in the cable resistance, the error in the current sharing ratios (n_1 and n_2) from their desired values is mostly around 5% or less for n_1 and less than 3% for n_2. Some errors in the current sharing are acceptable, especially under light load conditions and provided the sources are working within their capacity [37], [213, 214]. Also, even when the cable resistance was doubled, the error in the current sharing ratio n_2 is less than 5%, while the error in the current sharing ratio n_1 is 9.61%. However, in all the cable resistance variations investigated, the deviation of the bus voltage from its nominal value is less than 0.5%. This verifies the robustness and good steady-state performance of the proposed control approach.

The cable resistance variation test showed that the proposed control method may not yield acceptable control performance for the sharing ratio between converter 1 and 2 (i.e., n_1) for a 200% variation in the cable resistance. In the event of a significant variation in the line resistance, the ANN model will need to be updated accordingly for better current sharing performance of the proposed control method [190].

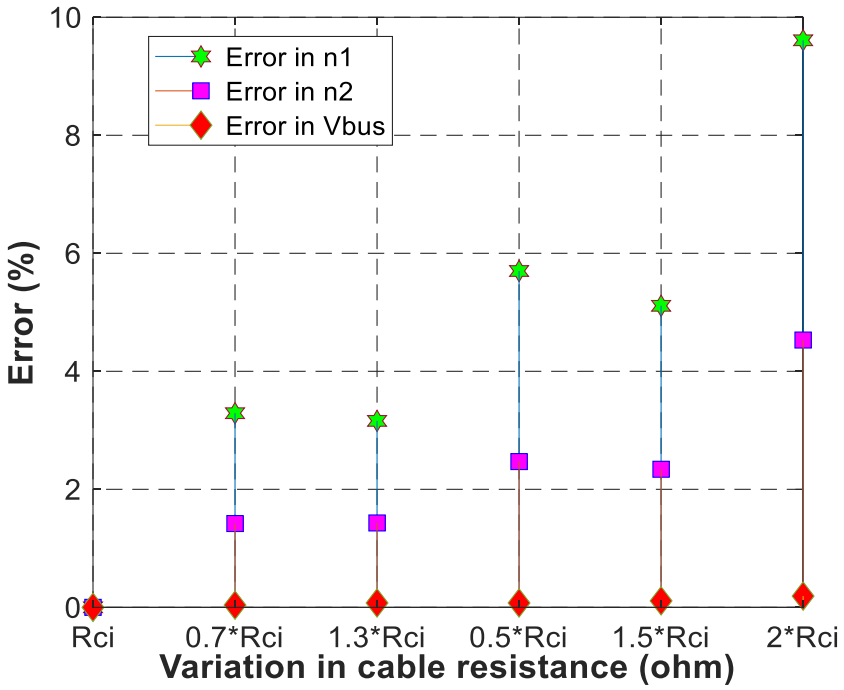


Figure 5.10 Effect of variation in cable resistance on current sharing accuracy and bus voltage regulation of the proposed approach.

5.5 Summary

This chapter presented an innovative strategy to address voltage deviations and enhance overall voltage regulation in the islanded DC MG of the MEA EPS. The proposed design approach incorporates an ANN as a surrogate model to compute the optimal droop and voltage compensation coefficients based on desired power-sharing ratios and bus voltage regulation requirements. The effectiveness of the proposed approach is validated through extensive simulations and HIL experiments, demonstrating its ability to efficiently control and manage the MEA EPS distribution network. Through the proposed approach, the bus voltage regulation and dynamic performance of the MEA EPS improved in different EPS operation conditions while simultaneously achieving optimal load power sharing among power sources when compared with the state-of-art methods. Consequently, the safety and continuous operation of the electrical loads onboard the MEA are guaranteed. Furthermore, the proposed approach substantially reduces the total load current and output currents from each converter. This leads to enhanced EPS efficiency by reducing losses in lines, particularly under fault conditions and in the event of a secondary control failure, when compared to state-of-the-art methods. The

proposed control approach can be conveniently implemented since there is no need for additional controllers and existing communication infrastructure such as power line communication can be utilised.

Chapter 6 Real-time Line Resistance Identification with Artificial Intelligence

This chapter presents a new approach using two ANNs models to address the challenges of accurate current sharing and voltage regulation in DC MGs. The first ANN (ANN1) is employed to compute optimal droop gain settings for converters, aiming to achieve precise current sharing. However, interconnecting cable resistance changes during operation may lead to a deviation of the power sharing ratio when only ANN1 is used. To overcome this, another ANN (ANN2) is used to identify the line impedance during operation. In real-time operation, the ANN2 estimated interconnecting cable resistances are used to compensate for the voltage deviation. Together with ANN1 identified optimal droop gain, a robust power sharing control has been achieved with accurate current sharing and improved regulation of the bus voltage, even in the presence of varying line resistances. The proposed approach is evaluated under different line resistance scenarios to assess its effectiveness. Simulation results demonstrate the superior performance of the proposed control method over conventional droop control approaches, offering promising prospects for enhancing the operation of DC MGs.

6.1 Introduction

Microgrids are becoming increasingly popular in emerging technologies like MEA and hybrid electric vehicles due to their simplified control, higher system reliability, and easier integration of alternative energy sources compared to AC networks [111]. In typical DC MGs, multiple power sources are connected in parallel through power electronic converters to a common DC bus. However, the conventional droop control method used for power sharing faces challenges due to mismatched interconnecting cable resistance and offset in the nominal voltage reference, leading to power imbalances and voltage deviations. To enhance stability and control performance, addressing these practical issues is essential, with the offset issue being manageable through proper sensor calibration, while the mismatched interconnecting cable resistance needs careful consideration in low-voltage DC MGs. In addition, the line resistance can change during the EPS operation due to environmental conditions such as variations in

temperature and other factors [94]. Moreover, such changes may be difficult to predict in advance, therefore, the system control performance is also threatened due to parameter uncertainty.

While maintaining the reliability and modularity of the droop control, the design and computation of the optimal droop gain settings using AI techniques are considered an elegant approach to mitigate the trade-off between power sharing and bus voltage regulation [138], [171], [177], [215], [216]. With the optimised droop gain settings, the controllers are expected to adapt and perform robustly under different conditions of the EPS. However, the desired control performance may not be achieved especially when there is a significant variation in the nominal line resistance during the operation of the EPS [186]. Thus, for improved control performance, the AI technique will need to be updated accordingly (for example by collecting new data samples to re-train the ANN model), which requires extra effort and may become inefficient [186].

An alternative method proposed to improve droop control is the adaptive droop control scheme [217], which involves adjusting the droop gains of the PECs in real-time by incorporating online parameter identification to ensure desired control performance and stability in the face of varying EPS conditions. This approach provides greater flexibility and is more practical than conventional droop control when it comes to current sharing and voltage regulation. The adaptive droop control based on online line impedance identification is the most commonly used approach and can be easily incorporated into the droop controller using a simple feedback control loop [168], [218], [219], [220], [217]. However, its control performance is highly dependent on the accuracy of the line impedance identification. In this regard, the approach used in the estimation of the line impedance is very important as it would have an impact on the accuracy of the identification and the overall control performance of the system. This is one of the main motivations of this research. Besides, the knowledge of line impedance is also beneficial for other purposes including islanding detection [221], controller design [222], and online stability evaluation [223].

The existing line impedance identification techniques are broadly classified into two categories: active, and passive methods [224, 225]. The passive detection method involves identifying line impedance based on inherent system characteristics [226]. Being a non-intrusive technique, it eliminates the need for disturbance injection. The line impedance

identification is performed using voltage and current measurements taken at the point of common coupling (PCC). A passive detection method involving the use of the recursive least squares (RLS) is employed in [206], [220, 227], an extended Kalman filter is used in [228], and the RLS method combined with the Kalman filter is employed in [218] for grid impedance, voltage amplitude and phase angle estimation. Due to the non-injection of perturbation into the system, the passive detection techniques do not affect the stable operation of the system. However, they require complex computation processes, thus making their implementation in practical systems difficult. For example, the RLS algorithm implemented in [220, 229] requires the measurement of the inverter's output voltage, current, and the common bus voltage to estimate each corresponding feeder impedance. Furthermore, since they make use of the existing system noise for impedance identification, their detection accuracy is thus relatively low in a system with an inherent low signal-to-noise ratio (SNR) [226].

Alternatively, active detection techniques require the simultaneous injection of perturbations into the system and the processing of the corresponding voltage and current information at the PCC to estimate the line impedance. Different kinds of perturbations including single harmonic injection [230], wideband pulse injection, frequency injection, current pulse injection [231] and step perturbation are used in this technique. The line resistance is estimated using active pulse injection, information detection (i.e., voltage and current measurements before and after injection) and then calculation in [169, 170]. The injection of disturbance into the system may also affect its stability and power quality [232], leading to a temporary decline in the converter's performance and a significant amount of time may be required to accurately estimate the system parameters [233].

To implement the aforementioned line impedance detection algorithms, it is necessary to measure the voltage and current at the PCC. Thus, additional current and voltage sensors will be required in the system. This will incur additional costs to the system, possibly increase its weight and may also introduce noise into the system. To eliminate the need for additional sensors and the injection of harmonics into the system, the line resistances are estimated using mathematical calculations in [168]. There, only knowledge of the output currents of the converters and DC bus voltage is required in the proposed method. However, when the DC bus is located at a considerable distance from the converters, accurately measuring it can become challenging, potentially resulting in inaccuracies during the estimation of line resistance. Overall, the need to measure two or more system parameters for the estimation of the line

resistance makes the existing identification methods complex and prone to errors. [234] proposes an intelligent and data-driven approach for offline line resistance estimation in the DC MG. However, the proposed method can only be applied under constant load, and no experimental studies were conducted to validate its effectiveness.

To overcome the above-mentioned challenges, this thesis proposes an ANN-based online line resistance identification method. The fundamental concept involves utilising optimal droop gain settings to solve an equation set and determine the nominal or initial line resistance values. The initial line resistance values are then employed to generate data, which is used to create an identification model based on ANN. This model maps the relationship between current sharing ratios between the converters and line resistances within a predefined design range. If there are variations in the nominal line resistance values during EPS operation, the ANN-based identification model can identify the new line resistance. This enables real-time adjustment of the voltage reference of each converter, ensuring accurate current sharing and enhanced voltage regulation. By employing this method, it is possible to achieve a high level of estimation accuracy without compromising system stability or introducing additional computational complexity. In addition, the only parameter that requires measurement is the output current of the PECs that is used for the normal control and operation of the EPS. Thus, no extra sensors are required. The main contributions of this chapter are as follows.

- Development and implementation of an online initial line resistance estimation algorithm in the MG controller which involves solving a simple equation set.
- Development and implementation of an identification model based on ANN in the MG. This model allows for the real-time estimation of line resistance during the EPS operation. To the best of the authors' knowledge, the proposed method has not been previously explored for line resistance estimation.
- The proposed approach can guarantee accurate current sharing and improved voltage regulation in both steady-state and transient conditions.

6.2 Modified Droop Control Algorithm

To address the limitations of the conventional droop control method and improve its control performance, a modified droop control algorithm is proposed [158, 235]. The concept behind this modified algorithm is to adjust the voltage reference of each converter to compensate for

any terminal voltage deviations, resulting in improved power sharing accuracy. Thus, a compensation term/voltage offset ΔV is generated and added to the conventional droop equation in (3-1). Thus,

$$V_{ref\,i} = V_{dc}^{*} - k_{d\,i} I_{d\,ci} + \Delta V \tag{6-1}$$

The compensation term ΔV can be obtained as

$$\Delta V = R_{ciest} I_{dci} \tag{6-2}$$

where R_{ciest} is the estimated line resistances. In summary, estimating the line resistances precisely is crucial for generating the appropriate compensation term for each converter to improve the performance of the droop control method. Furthermore, this knowledge will aid in stabilizing the system by suppressing the circulating current among the PECs [168]. The main challenge is in the accurate estimation of the corresponding subsystem line resistances R_{ci} under varying EPS conditions. In sharp contrast to existing methods, this thesis proposes an artificial intelligence-based online line resistance estimation method, and this will be presented in the next Section.

6.3 Proposed Approach for Enhanced Droop Control

The proposed droop control strategy can be divided into two stages. The first stage involves using AI to estimate line resistance online and the second stage is implementing a modified droop control algorithm.

6.3.1 Rational for Using Artificial Intelligence (AI)

Machine learning (ML) algorithms that are data-driven have attracted significant attention in the estimation of EPS parameters because of their capability in learning about the behaviours of non-linear systems [236, 237, 238, 239]. The machine learning algorithm is usually designed in such a way as to learn and establish the functional relationship between the desired parameter to be estimated and signals that can be easily measured in the system without the need for the power system designer to know the relationship between the input and output data [133]. Thus, saving costs for the system. For practical applications, machine learning-based solutions can be utilised as tools for the estimation of EPS parameters since they are non-invasive and do not

need hardware sensors, unlike the existing line resistance identification methods. The ANN is one of the most powerful and commonly used ML tools for establishing such a functional relationship [133]. In addition, there is no need for knowledge of the system dynamics beforehand. Therefore, a systematic ML-based interconnecting cable resistance estimation methodology will be developed in this chapter.

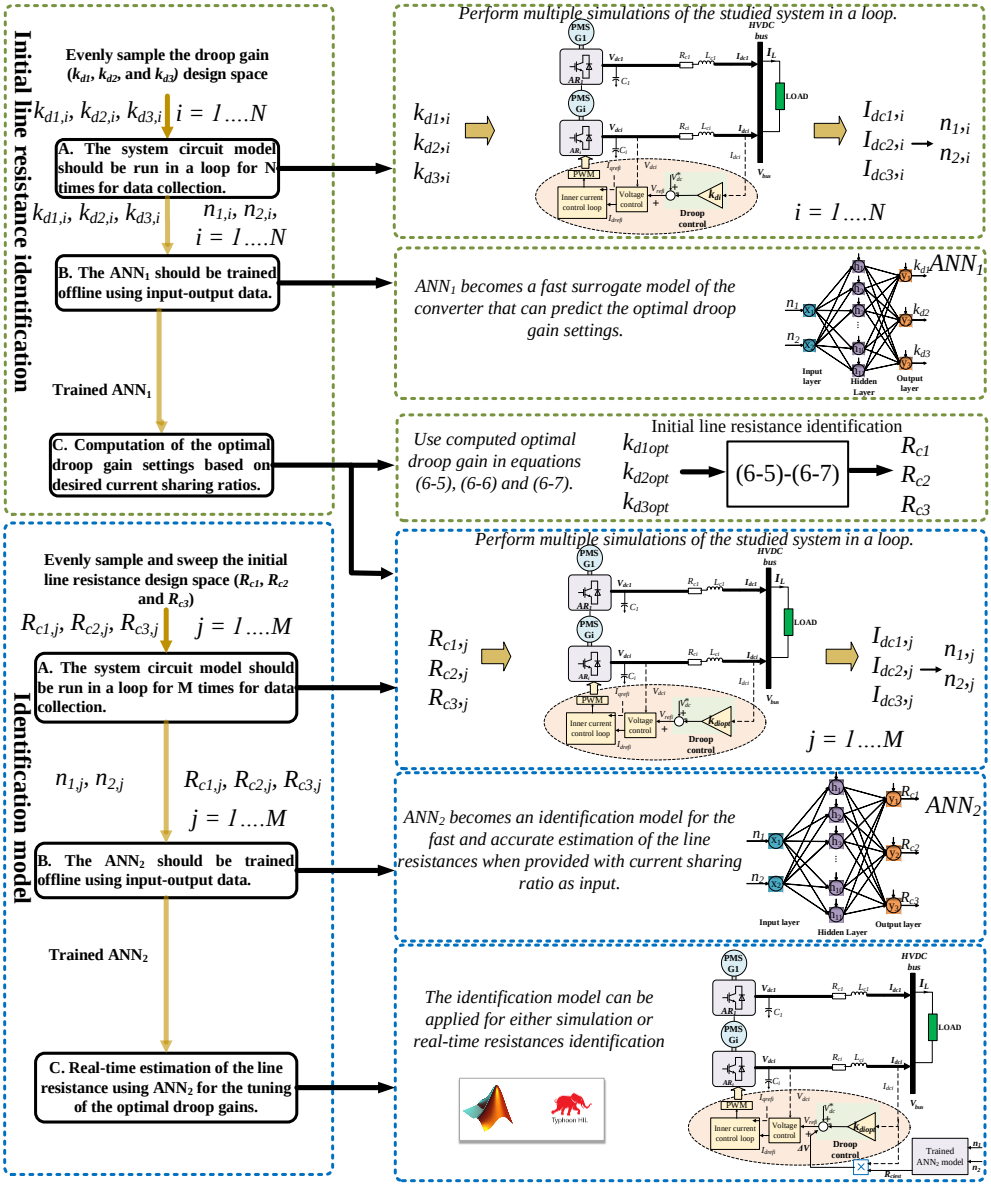


Figure 6.1 Flowchart diagram depicting the proposed methodology for online estimation of interconnecting cable resistances.

6.3.2 Proposed AI-Based Online Line Resistance Estimation

This thesis only considers the line resistance estimation since the line inductance does not affect the steady-state droop control performance of the DC MG [161]. The research utilises a machine learning algorithm to analyse data obtained from a simulation model and identify line resistance by considering the current sharing ratios between the converters.

Figure 6.1 shows the entire flowchart and procedures to follow in the proposed AI-based online line resistance estimation method. The entire process is made up of two parts. The initial part of the process (enclosed in dotted green lines) involves creating a design strategy for computing the optimal droop gain settings using an ANN-based surrogate model (referred to as ANN_1). This approach is used to achieve the desired power sharing ratio between the PECs. After obtaining the optimal droop gain settings, a set of equations is used to estimate the initial line resistance online [240]. The second part (enclosed in dotted blue lines) deals with the development of an identification model (denoted as ANN_2) based on the initially identified line resistance that can be used for the real-time estimation of the line resistance during the EPS operation. Figure 6.1 shows that each part of the process consists of three steps: data collection (step A), development and training of the surrogate model (step B), and deployment of the surrogate model (step C). The goal is to obtain the trained identification model (i.e., ANN_2). The subsequent sections will describe the development of the two ANNs (i.e., ANN_1 and ANN_2) required to achieve this objective.

6.3.2.1 Training of ANN_1: Data Collection, Model Development and Training, and Deployment of the Surrogate Model

Step A: Data Collection

The necessary data can be gathered either from a simulation model or an experimental rig of the studied system. This research gathers data from simulations and verifies the proposed approach using simulations and HIL experiments. Table 6-1 presents the simulation parameters used. The simulation also includes a computational delay equivalent to one sampling time and the model's converter dead times to replicate experimental conditions as closely as possible.

Table 6-1 Parameters of the system used as a case study in simulations and HIL experiments.

Category	Parameters	Values
PMSG parameters	Nominal power	45 kW
	Base speed	8000 rpm
	Switching frequency	100 kHz
	Maximum modulation index	0.9
	Pole pair	3
	Stator winding resistance R_s	1.058 mΩ
	Winding inductance L_d=L_q	99 µH
	Flux linkage	0.03644 Wb
Converter, cable, and load parameters	DC-link capacitance C_b	1.2 mF
	Converter dead time T_d	3 µs
	DC link-rated voltage	270 V
	Traditional droop coefficients k_{di}	1/4.25, 1/4.25, 1/4.25
	Cable resistances R_{ci}	20 mΩ, 40 mΩ, 60 mΩ
	Cable inductances L_{ci}	1 µH, 10 µH, 5 µH
	Load power used during data generation	40 kW

The sweep values of the droop gains used as input to the simulations are k_{d1} = [1/3.825, 1/3.910, 1/3.995, 1/4.080, 1/4.165,... 1/4.675], k_{d2} = [1/3.825, 1/3.910, 1/3.995, 1/4.080, 1/4.165,... 1/4.675], and k_{d3} =[1/3.825, 1/3.910, 1/3.995, 1/4.080, 1/4.165,... 1/4.675]. The sweep range is chosen near the conventional fixed and identical droop gain specified in Table 6-1 to guarantee a realistic design space with good high fidelity and stability of the system [186]. A total of 1331 combinations of droop gains were swept during the simulations to gather data. At the end of each simulation, the current sharing ratios (i.e., n_1 and n_2) for each droop gain combination were computed and saved. The data points were collected in approximately 35 minutes using a standard computer with 4-core processors. MATLAB codes were employed to automate the

simulations, which were run in a loop. The input (x) and the processed output (y) of the simulation during data generation are represented by the relationship expressed in (3-10). The collected data set is randomly split into three subsets for training, validation, and testing, respectively, with a ratio of 70%, 15%, and 15%.

Step B: Model Development and Training

The structure for the ANN_1 needs to be chosen carefully before proceeding with its training. For ANN_1, a FFNN structure is utilised, as illustrated in Figure 6.2, consisting of an input layer, a hidden layer, and an output layer. The input layer contains two neurons, representing the current sharing ratios (i.e., n_1 and n_2), while the hidden layer has 11 neurons. The output layer comprises three neurons, representing the three droop gains (i.e., k_{d1}, k_{d2}, and k_{d3}). The number of neurons in the hidden layer is determined using the trial-and-error method as there is no standard analytical technique for selecting its appropriate number. The number of neurons in the hidden layer has a crucial impact on how well the ANN model is trained [39]. The goal is to train the ANN_1 as a surrogate model that maps the current sharing ratios to the droop gains. The training is done offline using MATLAB's NN fitting toolbox.

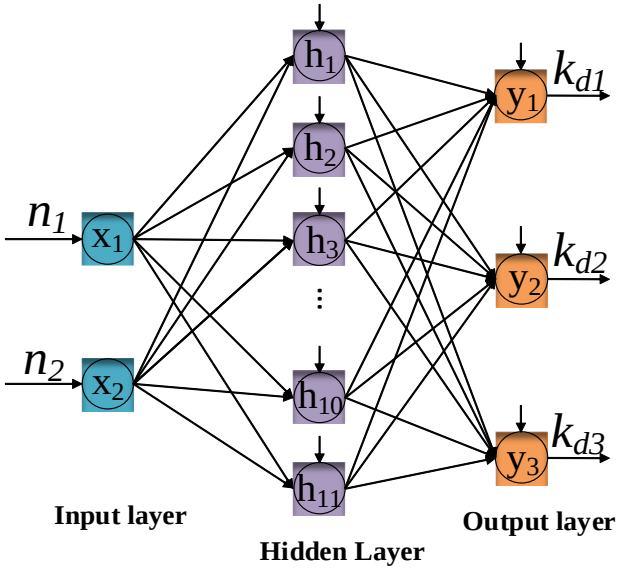
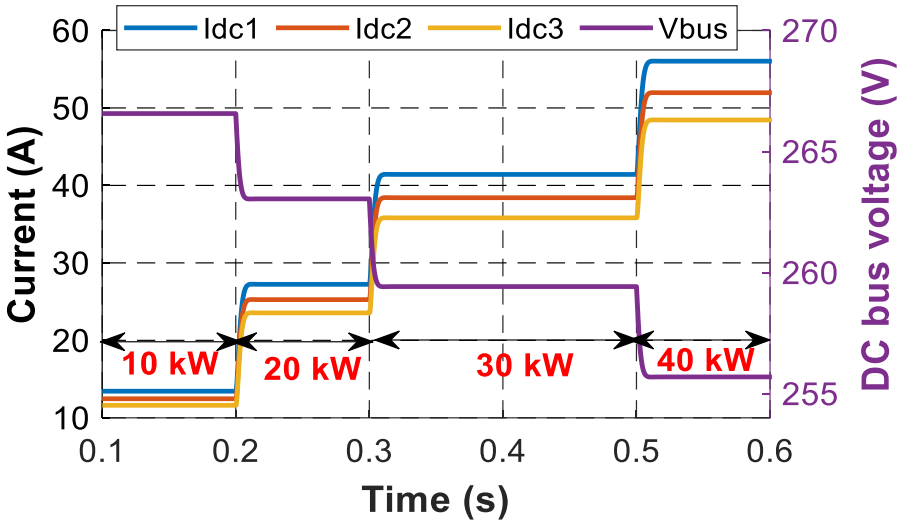


Figure 6.2 FFNN structure of the ANN1-based surrogate model.

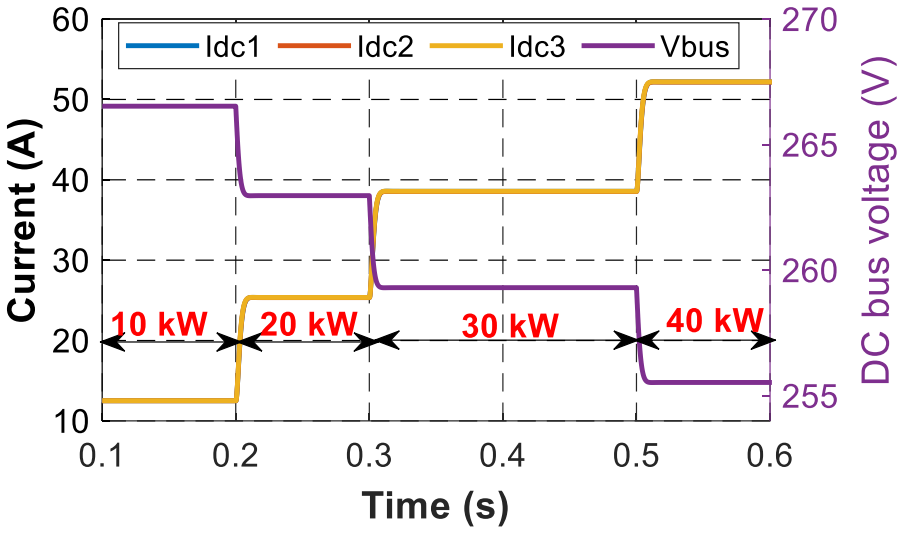
Step C: Deployment

The ANN_1-based surrogate model is deployed after training to calculate the optimal droop gain settings required to achieve the desired user-defined current sharing ratios between the PECs.

To that end, the desired current sharing ratios for equal current sharing among the converters are defined as $n_{1desired}$ = 1 and $n_{2desired}$ = 1 and provided as input to the ANN_1-based surrogate model.



(a)



(b)

Figure 6.3 Simulation results for current sharing and voltage regulation using (a) Traditional fixed and identical droop gains (shown in Table 6-1) (b) Optimal fixed droop gain settings obtained using the proposed approach.

The optimal droop gain settings obtained are k_{d1opt} = 1/3.8884, k_{d2opt} = 1/4.2133, and k_{d3opt} = 1/4.6055. To illustrate the validity of the computed optimal droop gain settings, they are used as input to the simulation model. The simulation parameters are the same as those shown in

Table 6-1. CPLs of 10 kW, 20 kW, 30 kW and 40 kW are applied during the simulation. Figure 6.3 (a) shows the results of the current sharing and bus voltage regulation when the traditional fixed and identical droop gains (shown in Table 6-1) obtained using the conventional droop gain design are used in the simulation. The results are shown in Figure 6.3 (a) with I_{dc1} = 56.03 A, I_{dc2} = 51.96 A, I_{dc3} = 48.44 A, and V_{bus} = 255.7 V at time t = 0.5 s. It can be observed that the current sharing among the converters is not as desired because of the mismatched line resistances. On the other hand, when the optimal droop gain settings are applied in the simulation, both accurate current sharing and good voltage regulation (with I_{dc1} = 52.19 A, I_{dc2} = 52.16 A, I_{dc3} = 52.20 A, and V_{bus} = 255.5 V at time t = 0.5 s) are achieved in the desired sharing ratio as shown in Figure 6.3 (b). Therefore, compared to the traditional fixed and identical droop gains, the computed optimal droop gain settings can mitigate the influence of the mismatched line resistance on the droop control performance [186], [215], [216].

Table 6-2 Error in current sharing ratios and voltage deviation for different variations in line impedance.

	R_{cinew} = 0.5 x R_{ci}	R_{ci}	R_{cinew} = 2 x R_{ci}
L_{cinew}=0.5xL_{ci}	3.80%, 8.10%, 4.96%	0.00%, 0.00%, 5.37%	6.35%, 11.85%, 6.19%
L_{ci}	3.80%, 8.10%, 4.96%	0.00%, 0.00%, 5.37%	6.35%, 11.85%, 6.19%
L_{cinew} = 2x L_{ci}	3.80%, 8.10%, 4.96%	0.00%, 0.00%, 5.37%	6.35%, 11.85%, 6.19%

Since the line impedance parameter can vary during the EPS operation, the robustness of the computed optimal droop gain settings to variations in the interconnecting cable's inductance and resistance are tested using different simulation studies. The results obtained are shown in Table 6-2. As shown in Table 6-2, the simulations are carried out for cases where the initial line's parameters are unchanged (i.e., R_{ci} and L_{ci} as shown in Table 6-1), halved and doubled. The other system parameters remain the same. A CPL of 40 kW is applied during the simulation. The results in Table 6-2 are presented as (x,y,z), where x is the percentage error in the current sharing ratio between PECs 1 and 2, y is the percentage error in the current sharing ratio between PECs 1 and 3, and z the percentage error in the bus voltage deviation.

As expected, the steady-state droop control performance of the studied system is not affected by the variation in the line's inductance [161]. However, the variation in the resistance from their initial values affects the current-sharing ratios and voltage deviation while using the computed optimal droop gain settings. As shown in Table 6-2, it is evident that an increase in the variation of interconnecting cable resistances from their nominal values further deteriorates the control performance. An alternative solution will be to collect new data samples to re-train the ANN_1 model to compute new optimal droop gain settings to adapt the controller to the changing EPS conditions. However, this will make the process complex and inefficient. Based on these results it can therefore be said that there is a need to develop a solution that can adapt the controller to changing EPS operating conditions and improve the current sharing and voltage regulation among PECs simply and efficiently.

The first step towards the development of the proposed approach in this chapter is to use the computed optimal droop gain settings to identify the initial line resistances (R_{ci}) [240]. It may be recalled that by using the traditional fixed and identical droop gain settings in (3-7) and (3-8), the desired equal current sharing ratios between the PECs will not be realised because of the effect of the mismatched line resistance. Now, assuming the computed optimal droop gain settings by ANN_1 can yield equal current sharing among the PECs and in the desired sharing ratio, thus, we can obtain.

$$n_1 = \frac{I_{dc2}}{I_{dc1}} = \frac{k_{d1opt} + R_{c1}}{k_{d2opt} + R_{c2}} = 1 \tag{6-3}$$

$$n_2 = \frac{I_{dc3}}{I_{dc1}} = \frac{k_{d1opt} + R_{c1}}{k_{d3opt} + R_{c3}} = 1 \tag{6-4}$$

Therefore, by considering equations(3-7), (3-8), (6-3), and (6-4), the expressions for the initial line resistances can be obtained as [240]

$$R_{c1} = \frac{\left(\frac{k_{d1}}{n_2} - k_{d3} + k_{d3opt} - k_{d1opt} \right)}{\left(1 - \frac{1}{n_2} \right)} \tag{6-5}$$

$$R_{c2} = \frac{\left(k_{d1} + R_{c1}\right)}{n_1} - k_{d2} \tag{6-6}$$

$$R_{c3} = \frac{\left(k_{d1} + R_{c1}\right)}{n_2} - k_{d3} \tag{6-7}$$

where k_{d1}, k_{d2}, and k_{d3} are the traditional droop gains, n_1 and n_2 are the calculated current sharing ratios based on the traditional droop gain settings, and the computed optimal droop gain settings by the ANN_1-based surrogate model are k_{d1opt}, k_{d2opt}, and k_{d3opt}. As droop gain parameters are set within the controller, implementing the equation set is relatively straightforward [241]. Hence, the initial line resistance can be identified online. The steps undertaken to develop ANN_1 only need to be executed once.

The MATLAB Simulink simulation platform is utilised to validate the proposed approach for estimating the initial line resistances. The simulation involves applying various CPLs, namely 10 kW, 20 kW, 30 kW, and 40 kW. By substituting the traditional fixed and identical droop gains and the computed optimal droop gain settings in (6-5), (6-6) and (6-7), the corresponding estimated line resistances are $R_{c1} = 20.38$ mΩ, $R_{c2} = 40.44$ mΩ and $R_{c3} = 60.42$ mΩ respectively as shown in Figure 6.4. The estimated line resistance matched excellently well with the nominal line resistance values shown in Table 6-1. The percentage error in the estimation is less than 2 %. Thus, showing the accuracy of the proposed initial line resistance estimation method [240]. In addition, the initial line resistance estimation method is robust to changing load conditions.

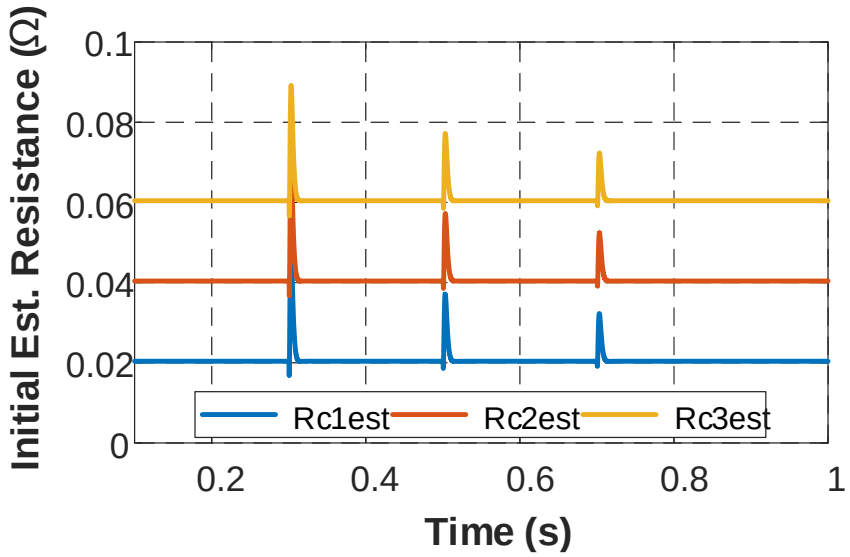


Figure 6.4 Online estimations of the initial line resistances.

It is important to state that, after the initial line resistance identification, if there is a change in the interconnecting cable resistances, the new line resistances cannot be identified by solving the equation set. This can be attributed to the fact that the computed optimal droop gains will not achieve the desired equal current sharing ratio necessary to solve the equation set, considering the assumption made earlier during the formulation of the equation.

Based on the foregoing, there is a need to develop a comprehensive methodology for the identification of the interconnecting cable resistance even when it changes during the system operation. This way, the voltage reference of each of the converters can be tuned adaptively to enhance the droop control performance. The next section will discuss the development of an ANN_2-based identification model.

Table 6-3 Design range based on initially estimated line resistance.

Parameter	Range (mΩ)	Step (mΩ)	Samples
R_{c1}	[18, 22]	0.4	11 x 22 x 31 = 7,161
R_{c2}	[36, 44]	0.4	
R_{c3}	[54, 66]	0.4	

6.3.2.2 ANN_2: Data Collection, Model Development and Training, and Deployment of the Surrogate Model

Although it is challenging to estimate the line resistance in practical scenarios, a change in the interconnecting cable resistance will lead to a change in its conducted current, thus, the corresponding output current of the PECs will also change. Therefore, a functional relationship between the current sharing ratio between the PECs (i.e., n_1, and n_2) and the line resistance within a design range (i.e., R_{ci}) can be established by an offline trained ANN_2 model. Subsequently, the trained ANN_2 model can act as an efficient computational surrogate model for mapping line resistances to current sharing ratios. The proposed model can help in identifying the line resistance accurately within the predefined range. This enables seamless online implementation of the method. The design range for the line resistance is defined as +/- 10% of the initially estimated line resistance, as shown in Table 6-3. This range is chosen to

generate data and to account for any error in the initial line resistance estimation. It should be noted that the power system designer has the freedom to choose the design range for data generation.

Data Collection (Step A): Data is collected by running the simulation model of the studied system in a loop for different combinations of the line resistances. A total of 7,161 data samples are generated based on the line resistance combinations simulated as shown in Table 6-3. The optimal droop gain settings computed using ANN_1 are used for the converters during the data generation and kept constant. At the end of each round of simulation, the current sharing ratios (i.e., n_1 and n_2) are automatically computed and stored. The overall data samples were collected in approximately 2 hours. The data generation process can be fast-tracked with the aid of the parallel computing toolbox in MATLAB [39]. The simulation parameters used for data generation are shown in Table 6-1. The input (x) and the processed output (y) of the simulation during data generation are represented by the relationship expressed in (6-8).

$$y = F(x) \Leftrightarrow (n_1, n_2) = F(R_{c1}, R_{c2}, R_{c3}) \tag{6-8}$$

The dataset is split into three sets randomly: 70% of the data is used for training the ANN_2-based identification model, while 15% is used for validation and another 15% for testing.

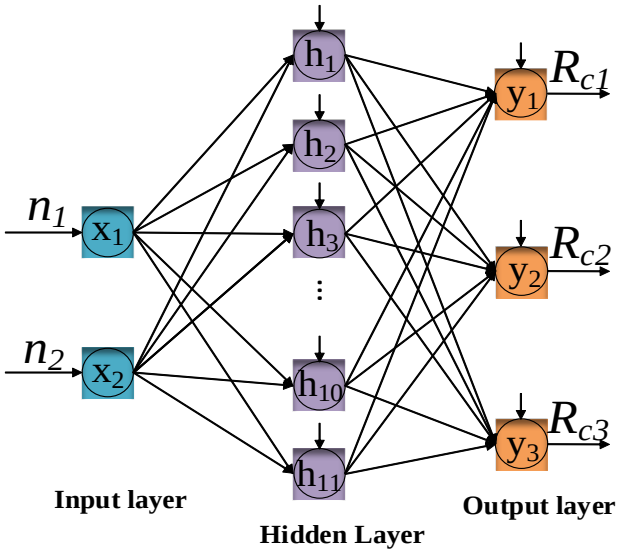


Figure 6.5 FFNN structure of the ANN2-based surrogate model.

Model Development and Training (Step B): The ANN_2 consists of three layers as well. The input layer has two neurons that correspond to the current sharing ratios, namely n_1 and n_2. The

hidden layer has 11 neurons, while the output layer has three neurons corresponding to the line resistances. The architecture of the ANN_2 is depicted in Figure 6.5. The ANN_2 is trained offline using the NN fitting toolbox in MATLAB to establish a functional relationship between the current sharing ratio between the converters (as inputs) and the line resistances (as outputs) within a specified design range.

To verify the performance of the surrogate model, a comparison is made between the original training data and the predictions made by the ANN_2-based identification model. The results of this comparison are presented in Figure 6.6. Based on the comparison between the simulation data and the predictions obtained from the identification model, as depicted in Figure 6.5, it can be concluded that there is a strong agreement between the two sets of data. Hence, the identification model can be considered to be well-trained.

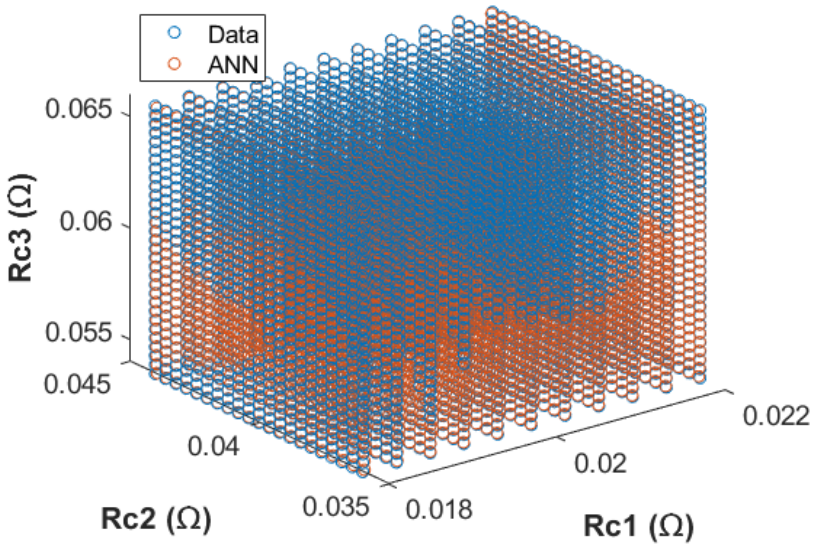


Figure 6.6 Comparison between the simulation data and the surrogate model prediction.

Deployment (Step C): The trained ANN_2-based identification model can then be used for the real-time estimation of line resistances during the EPS operation when provided with the corresponding current sharing rations (i.e., n_1, and n_2) as inputs. Since the identification model is trained offline based on data obtained from parallel simulation, a low computation burden can be achieved in the controller and the HIL device. In this regard, the trained ANN_2-based identification model is compiled into the MATLAB Simulink model. This way the identification model can be used in Simulink or imported into the typhoon HIL control platform

as a standalone Functional Mock-up Unit (FMU) along with its C source code using the Functional Mock-up Interface (FMI) for real-time identification of the line resistances and control [242]. The integration of the offline trained ANN_2 surrogate model into the Typhoon HIL toolchain enables real-time identification of interconnecting cable resistances using current sharing ratios. This approach allows for efficient adjustment of the voltage reference of each converter, allowing the controller to adapt to changing operating conditions while minimising computational load. Moreover, the identification model just serves as an additional block for the conventional droop controller.

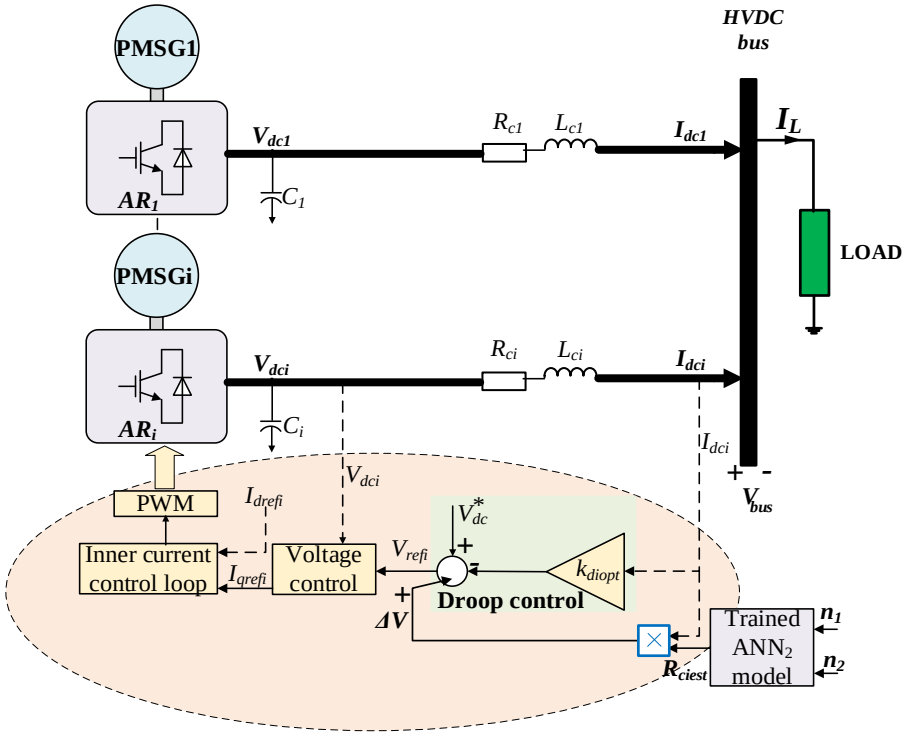


Figure 6.7 Proposed approach implementation on the studied MEA EPS HVDC architecture.

6.3.3 Implementation of the Proposed Online Line Resistance Estimation

Figure 6.7 depicts the implementation of the proposed control approach for improved voltage regulation and accurate power sharing in the more-electric aircraft (MEA) EPS architecture, which serves as the case study for this research. After data collection and training, the identification model is integrated with the droop controller (as shown in Figure 6.7). An ANN-based identification model for real-time estimation of the line resistances (R_{ciest}) is implemented for compensation. Thus, the estimated line resistances R_{ciest} in real-time by the ANN_2-based

identification model are assigned to each of the corresponding converter's primary controllers. The modified output voltage reference value for each can be obtained from (6-1) as

$$V_{refi} = V_{dc}^{*} - k_{diopt} I_{dci} + R_{ciest} I_{dci} \tag{6-9}$$

Similarly, the modified bus voltage becomes.

$$V_{bus} = V_{dc}^{*} - (k_{diopt} + R_{ci}) I_{dci} + (R_{ciest} I_{dci}) \tag{6-10}$$

From (6-10), it can be observed that the effective droop gain becomes.

$$k_{diopt} + (R_{ci} - R_{ciest}) \tag{6-11}$$

Consequently, after the addition of the compensation term in the droop controller in (6-10), the droop characteristics will be modified and restored to their desired designed value as shown in (6-11). In this way, the voltage drops across the mismatched line resistances will be compensated and equalised. Therefore, the impact of the mismatched line resistances on the droop control method's performance is mitigated, leading to precise current sharing and enhanced voltage regulation.

It is important to state that the identification model is only required for the accurate estimation of the line resistances, hence, can be disabled after the estimation and the estimated parameters can be stored and utilised in (6-9). Furthermore, the identification model is configured to re-estimate the line resistances only in a situation where there is an error in the power sharing among the PECs, this is important to prevent the ANN model from the continuous monitoring of the system operation and estimation of the line resistances.

6.4 Simulation Results

To demonstrate the efficacy of the proposed control method, the MEA EPS islanded DC MG depicted in Figure 6.7 is considered. The simulation of the system is performed using MATLAB/Simulink platform. The relevant parameters for the simulation including the DC cable are presented in Table 6-1.

6.4.1 Cable Resistance identification

To confirm the viability of the proposed AI-based method for identifying interconnecting cable resistance, tests are conducted on the MATLAB/Simulink simulation platform. Table 6-4 illustrates the variations in the interconnecting cable resistances examined during the simulations, with the corresponding results presented in Figure 6.8. The results affirm the accuracy of the proposed method in identifying the interconnecting cable resistances.

Table 6-4 Changes in the interconnecting cable resistances

Time (s)	Changes in R_{c1} (mΩ)	Changes in R_{c2} (mΩ)	Changes in R_{c3} (mΩ)
0.0	20.0	40.0	60.0
0.1	18.3	37.6	65.2
0.2	18.5	43.3	63.3
0.3	19.6	42.4	58.4
0.4	19.6	42.4	58
0.5	20.4	40.8	56.4
0.6	20.6	38.2	60.9
0.7	21.4	36.4	65.4
0.8	21.8	35.9	56.5
0.9	22.0	41.2	54.0

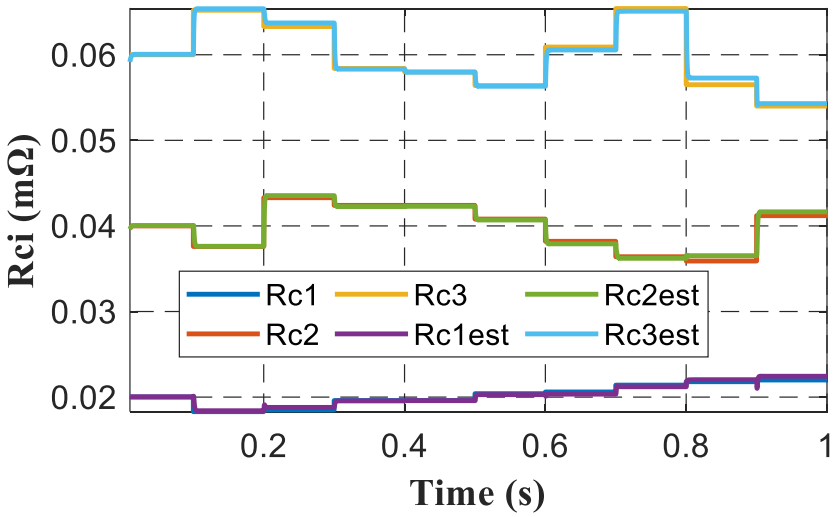


Figure 6.8 The results of interconnecting cable resistances identification

6.4.2 Equal Current Sharing

In this scenario, the optimal droop gain settings obtained from ANN_1 are set for the converters and the initial line resistances (shown in Table 6-1) are assumed to have varied during the EPS operation. Thus, DC line parameters used in the simulation model are R_{c1} = 19 mΩ, R_{c2} = 44 mΩ and R_{c3} = 63 mΩ, while all other system parameters remain unchanged. Under normal operation, the current sharing among the converters is expected to be equal and the ideal current sharing ratio should be 1:1 (i.e., n_1 =1 and n_2 = 1). CPLs of 20 kW and 30 kW are applied at 0.1 s and 0.7 s respectively during the simulation.

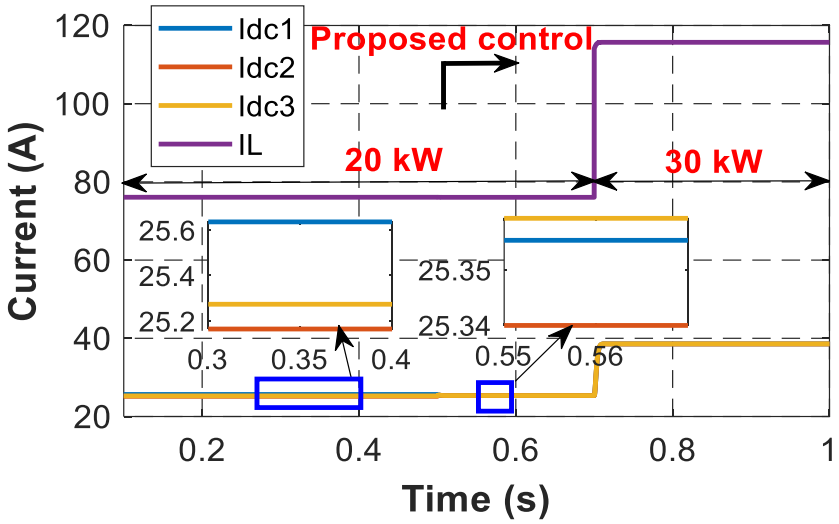


Figure 6.9 Output currents of the three PECs and the total load current using optimal droop gain settings and the proposed control algorithm under a variation in the initial line resistances.

Figure 6.9 illustrates that during the period of $0.1 \leq t < 0.5$ s, the optimal droop gain settings fail to achieve accurate current sharing, which is attributed to the variation in the initial line resistances. For the 20-kW load, the current distribution among the converters and the regulation of bus voltage are as follows: I_{dc1} = 25.63 A, I_{dc2} = 25.16 A, I_{dc3} = 25.27 A, and V_{bus} = 262.9 V. Consequently, the current sharing ratios are calculated as n_1 = 0.9816 and n_2 = 0.9860. These ratios indicate errors of 1.84% and 1.4%, respectively, in the current distribution. While these percentage errors may seem small, it should be noted that this is primarily due to the minimal variation in the initial line resistances considered in this specific case study. However, as illustrated in Table 6-2, significant variations in the initial line resistances would

result in higher percentage errors in the current sharing ratios while using the optimal droop gain settings.

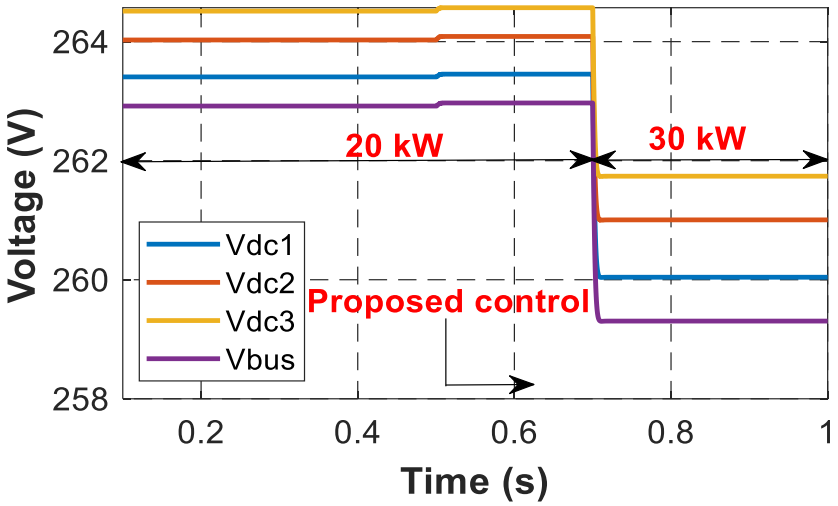


Figure 6.10 Output voltages of the three PECs and the main bus voltage using optimal droop gain settings and the proposed control algorithm under a variation in the initial line. resistances.

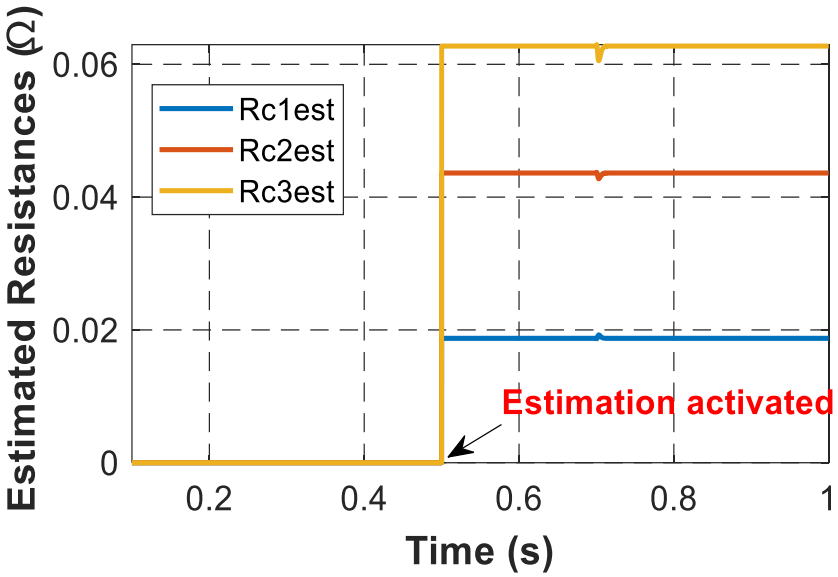


Figure 6.11 Online estimation of the line resistances using the ANN2-based identification model.

In contrast, once the proposed control algorithm is implemented at $t \geq 0.5$ s, the load current is evenly distributed among all converters. In the case of a 20-kW load, the current distribution among the converters and the regulation of bus voltage are as follows: I_{dc1} = 25.36 A, I_{dc2} =

25.34 A, I_{dc3} = 25.36 A, and V_{bus} = 263 V. These outcomes demonstrate the effectiveness of the proposed control approach in mitigating the impact of initial line resistance variations on current sharing within the droop control method. Specifically, the control method accomplishes this by generating voltage offsets that modify the voltage reference of each power electronic converter (PEC). As a result, the load current requirement is evenly divided among the converters, as evidenced by the current profiles after activating the proposed control algorithm. Additionally, the proposed control method proves to be robust in the face of load changes, as it maintains equal load current sharing even when the load power demand is increased from 20 kW to 30 kW as shown in Figure 6.9.

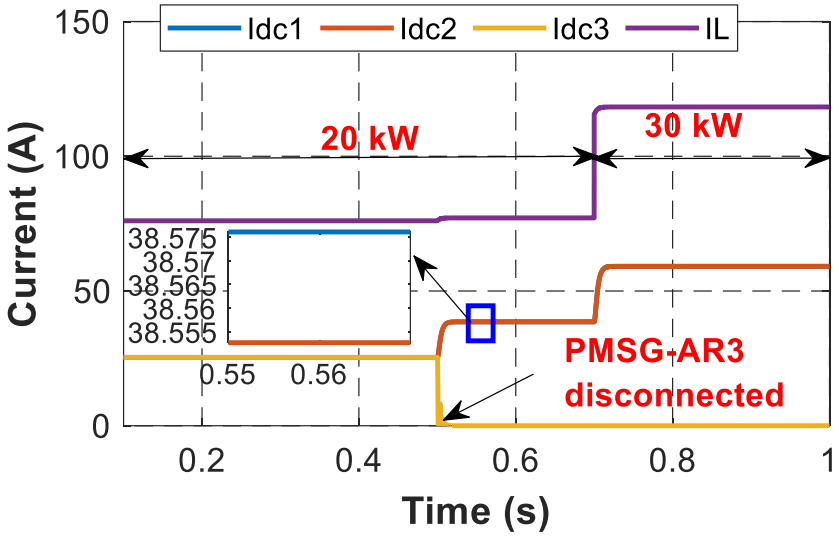
Figure 6.10 illustrates that, under the same load power condition of 20 kW, the proposed control method enhances the regulation of the bus voltage. This is achieved by compensating for voltage drops by generating voltage offsets to the reference voltage of each converter. Converter 3, with a larger line resistance value, has a higher output voltage (i.e., V_{dc3}) than the other converters. Hence, the larger the line resistance value, the greater the voltage offset generated in the reference voltage of the corresponding converter. Furthermore, the bus voltage remains well-regulated and falls within the acceptable steady-state range ($250 \leq V_{bus} \leq 280$) for the MEA application, even during load changes.

In Figure 6.11, the estimated line resistances by the identification model are presented. The results indicate that the identification model performs an accurate estimation of the line resistances once it is activated at 0.5 s. It should be emphasized that the identification model is exclusively utilised for the estimation of the line resistances. Subsequently, the estimated line resistances are employed in the droop controller.

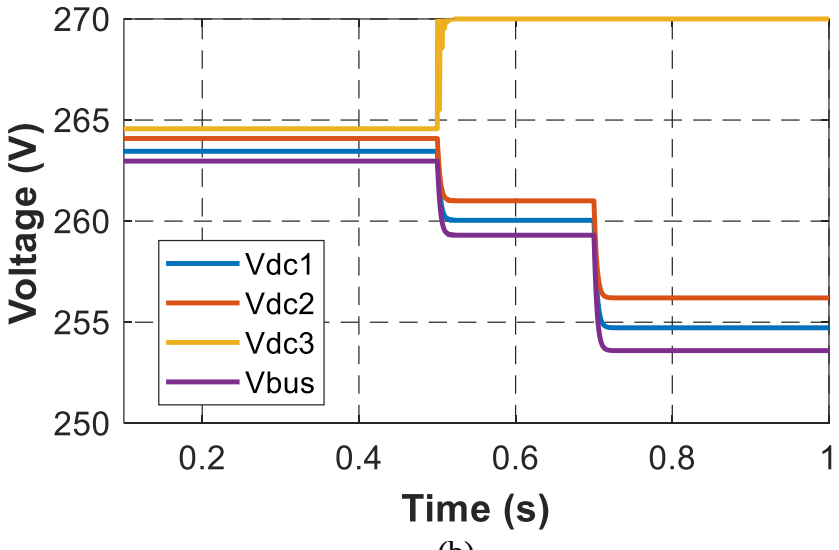
6.4.3 Performance Under Fault Condition

The proposed method's robustness was assessed through a simulated source fault scenario. Initially, three converters operated in parallel to distribute the desired load power of 20 kW. However, at t = 0.5 s, PMSG-AR3 was disconnected, resulting in converters 1 and 2 assuming sole responsibility for meeting the load demand, as observed in Figure 6.12. As shown in Figure 6.12 (a), under the proposed control strategy, converters 1 and 2 can share the load current demand equally between themselves after the loss of the *PMSG-AR3* (i.e., disconnected due to being under fault) at t = 0.5 s. Furthermore, accurate current sharing is maintained between

converters 1 and 2 despite the load change at t = 0.7 s and with *PMSG-AR3* under the fault condition. Also, the bus voltage is well maintained within the acceptable range for the MEA application in different conditions of the system operation as shown in Figure 6.12 (b). These control performances validate the robustness of the proposed control strategy under faulty operating conditions.



(a)



(b)

Figure 6.12 Simulation results using the proposed control algorithm under fault condition (a) output currents of the three PECs and the total load current (b) output voltages of the three PECs and the main bus voltage.

6.5 Summary

This chapter investigated a new approach to address the challenges of line resistance variations in the islanded DC MG of the more electric aircraft (MEA) electrical power system (EPS). The proposed method utilises ANNs for the online estimation of interconnecting cable resistances, enabling accurate current sharing and enhanced voltage regulation among parallel-connected converters. By continuously monitoring and adjusting the voltage reference of each converter based on the estimated line resistances, the proposed control strategy effectively compensates for terminal voltage deviations caused by line resistance mismatches. The effectiveness of the approach is validated through extensive simulations, demonstrating a remarkable accuracy of 99% in identifying interconnecting cable resistance parameters. This real-time line resistance identification technique offers a data-driven solution to eliminate the need for perturbations in the system and paves the way for improved control performance and stability in the MEA EPS distribution network.

Chapter 7 Controller Hardware-In-the-Loop (C-HIL) Setup and validation

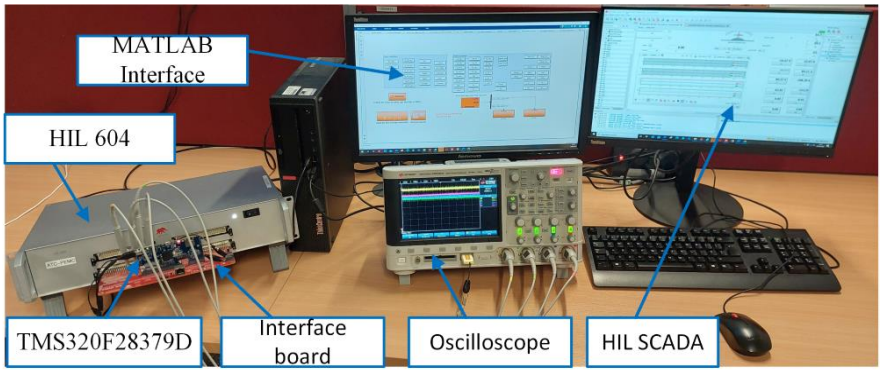
This chapter focuses on the hardware-in-the-loop (HIL) platform used for conducting experiments to validate the proposed AI-based control methodologies introduced in the previous chapter. It provides a detailed description of the HIL setup and presents the experimental results obtained from the validation process.

7.1 Hardware-in-the-loop (HIL) Experimental Setup

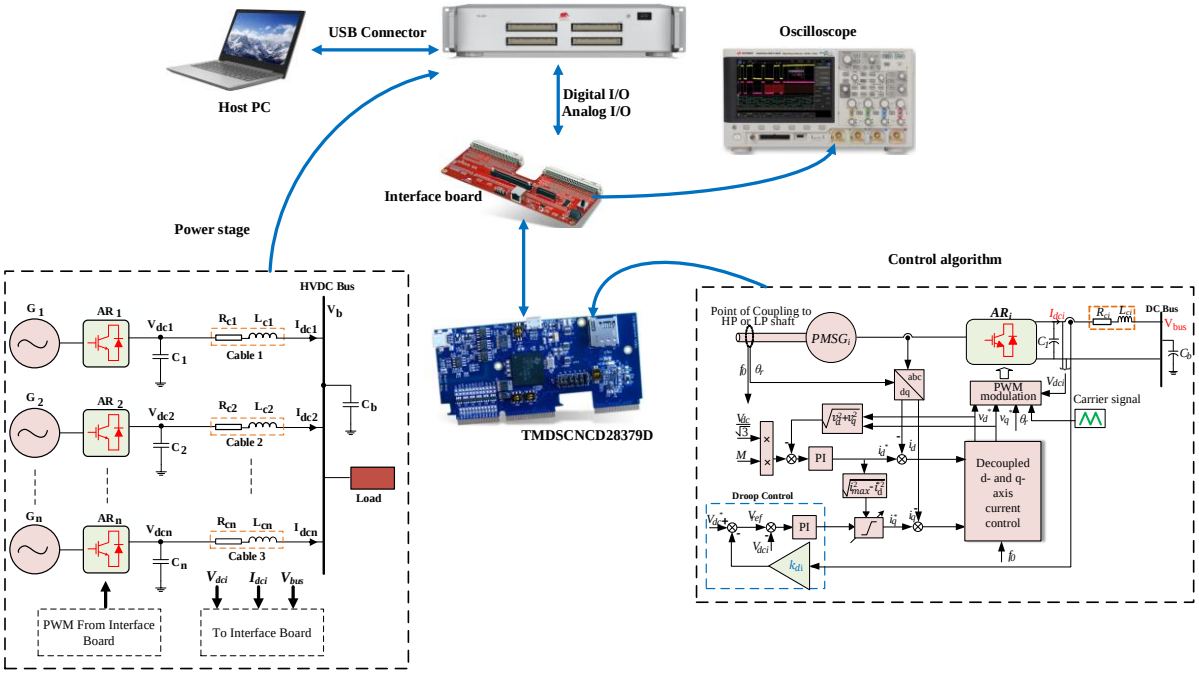
A Hardware-in-the-Loop (HIL) setup consists of a Real-Time Simulator (RTS) and a control system, often using a microcontroller or Digital Signal Processor (DSP). They are connected directly or through an interface board, depending on voltage compatibility. The RTS operates in real-time, generating waveforms to simulate the modelled system. The control system receives these waveforms, processes its algorithm, and sends an actuator signal back to the RTS, forming a closed-loop system. The Controller Hardware-in-the-Loop (C-HIL) setup is a valuable experimental approach used for testing and validating the performance of a controller in a realistic environment before its actual deployment in the field. With C-HIL, an assessment of the controller's effectiveness under diverse case studies and dynamic conditions can be carried out, including full-power scenarios [243]. In addition, using HIL experiments instead of real experimental rig is cost-effective and safe for testing complex setups with multiple generators and converters, and eliminating the risks associated with high-voltage systems [243].

In this thesis, the C-HIL experimental setup is shown in Figure 7.1. It involves modelling the PMSGs, converters, and interconnecting cable impedances in the studied system in real-time and with high fidelity using the typhoon (HIL-604) device real-time emulator. Meanwhile, the control algorithms are implemented on the TI F28379D DSP control card using the Embedded Coder Support Package in MATLAB. The developed codes are debugged and transferred to the DSP through the Code Composer Studio (CCS) software. The gating signal for driving the converter switches is derived from the control card, while communication between the control

card and the typhoon software is established through an interface board as shown in Figure 7.1. The HIL DSP 180 Interface board offers a pin-to-pin compatible connection between the HIL 604 device and the DSP control card. Due to the high-fidelity emulation of the power stage by the Typhoon HIL-604 device, the real DSP controller can effectively control the machines and power converters as it would in a physical power stage. This successful integration validates the proposed methodologies from the controller's perspective. Results collection during the HIL experiments was performed using an oscilloscope.



(a)



(b)

Figure 7.1 (a) C-HIL experimental setup; (b) Simplified block diagram of the C-HIL setup.

7.1.1 DSP Control card

The Texas Instruments F28379D control card shown in Figure 7.2 serves as the control platform, featuring a 32-bit floating-point dual-core microcontroller chip. This chip comes equipped with various useful peripherals, including the ADC module and ePWM module. Additionally, the control card includes the xds100v2 emulator, enabling a convenient interface to the Code Composer Studio Software (CCS) without the need for additional hardware. In addition, it is designed specifically for advanced closed-loop control applications. It offers optimisation for signal processing, sensing, and actuation, making it a strong candidate for real-time control applications. Among its numerous features include dual-core architecture, four 12-Bit Analog-to-Digital Converters (ADC), and four Pulse Width Modulator (PWM) Channels with enhanced features.

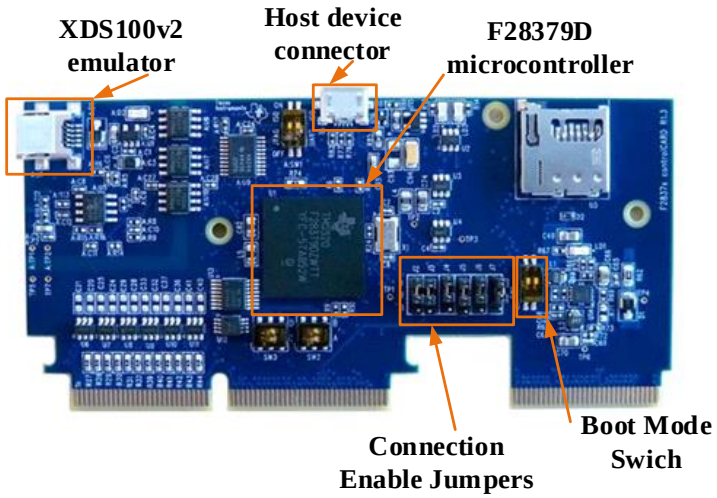


Figure 7.2 Texas Instruments F28379D control card

The control card chosen for the setup offers easy access to nearly all pins of the microcontroller, making it highly convenient to work with. Additionally, it features a fully functioning universal asynchronous receiver-transmitter (UART) emulation onboard, enabling seamless connection to the host computer. This eliminates the need for special JTAG programmer/debugger units and allows simple programming of the microcontroller using just a USB-Cable. A significant factor in selecting this control card is its compatibility with MATLAB/Simulink support package. This package empowers users to effortlessly translate control structures implemented in Simulink into C-Code, streamlining the development and implementation process.

7.1.2 Interface board

The HIL DSP 180 Interface board is a specialised interface designed to establish seamless connectivity between the 180-pin DSP control card and Typhoon HIL 604 device. This interface board enables efficient data exchange and communication between the control card and the HIL emulator, facilitating HIL simulations for controller testing and validation. The interface board layout is shown in Figure 7.3. Within the interface board, all HIL and DSP signals are made available through measurement terminals, ensuring convenient access to the required data for testing and analysis. It is equipped with a High-Speed Electrical Connector (HSEC) 180-pin socket, designed to accommodate the F28379D DSP control card. This ensures a perfect fit and reliable connection. In addition, the interface board provides a total of 24 HIL digital inputs (DI), including 16 DSP PWM signals, and 16 HIL digital outputs (DO), including DSP 3 encoder signals. Additionally, it offers 24 HIL analogue outputs (AO), clamped to 3.3V on the control card, providing a versatile range of input and output options for various simulation scenarios as shown in Figure 7.3 [244].

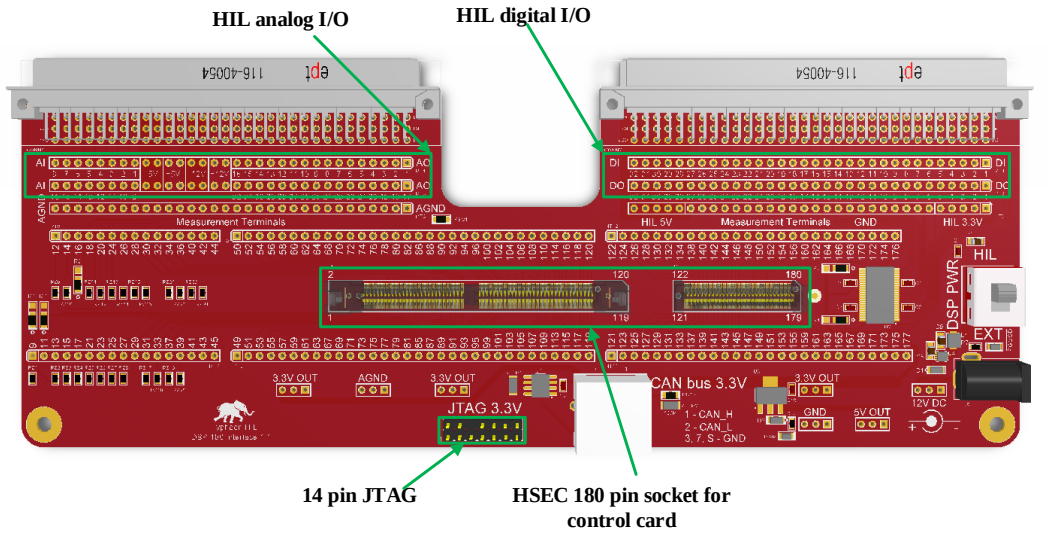


Figure 7.3 HIL DSP 180 Interface board layout.

In the HIL setup, analogue signals from the Typhoon HIL 604 device are connected to the HIL DSP 180 Interface board through measurement terminals. These terminals provide easy access to the analogue signals, and the board ensures proper interfacing and compatibility with the DSP control card. Similarly, the DSP control card generates PWM signals, which are sent back

to the Typhoon HIL 604 device through the HIL DSP 180 Interface board for the control of the emulated power stage.

7.1.3 Embedded Coder Support Package for Texas Instruments C2000 Processors

The Embedded Coder Support Package for Texas Instruments C2000 processors serves as a powerful tool for control algorithm development and deployment. Its integration with MATLAB/Simulink and compatibility with C2000 processors provide an efficient and effective solution for implementing control applications in real-time environments. Furthermore, it comprises various modules and blocks that enable seamless control algorithm development and simulation within the MATLAB/Simulink environment. Some of these modules include the ADC (Analog-to-Digital Converter) block, which is essential for the processing and controlling of analogue data using the DSP control card. A Space Vector Pulse Width Modulation (SVPWM) module facilitates the simulation of SVPWM techniques, for efficient control of the three-phase inverters. Another important block is the ePWM (Enhanced Pulse Width Modulator), which is required for generating pulse width modulated signals used to control emulated power stage. The implementation of some of these modules is further elaborated on as follows.

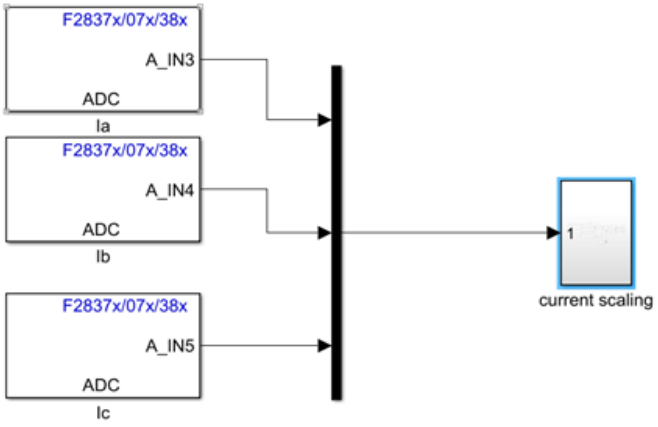


Figure 7.4 ADC module in Simulink.

7.1.3.1 ADC Module

The ADC module plays a very important role in the measurement and processing of controlled analogue quantities. Since the DSP controller operates with digital values, the ADC module is responsible for converting the analogue signals from the HIL device into digital values that can be further processed by the DSP as shown in Figure 7.4.

To achieve good conversion, the analogue outputs from the HIL device, which represent signals like current measurements, are calibrated to be within the same voltage range as the ADC of the DSP, typically 3.3V or 3V. For example, if the maximum peak value of the current (sinusoidal waveform) in the simulation is 50A, the scaling factor in the HIL analogue output settings should be set to 33.33 (i.e., 2 x 50(range +-50) / 3.00 = 33.33), and an offset of 1.5V (3.00/2 = 1.50) to achieve the desired conversion range. Figure 7.5 shows the HIL device output settings.

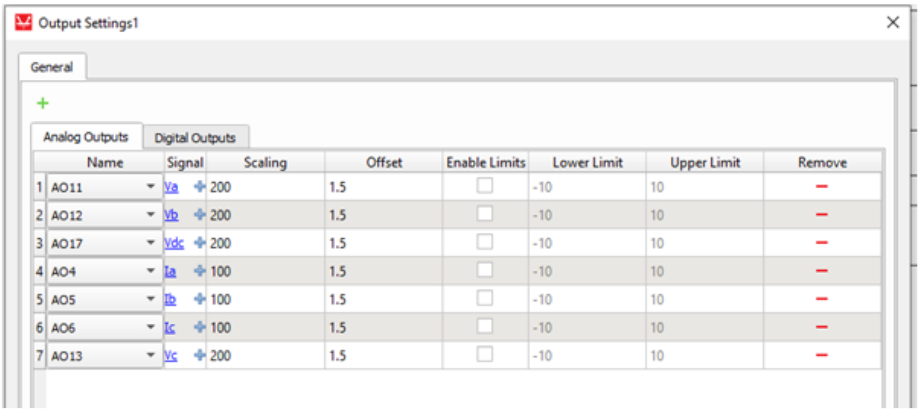
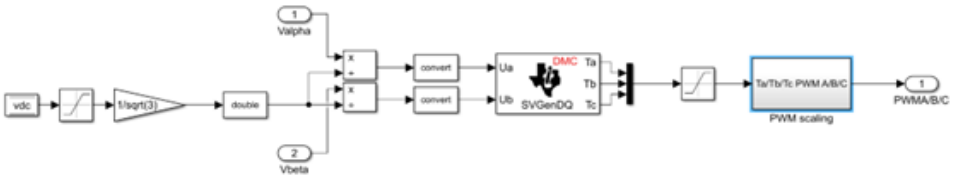


Figure 7.5 HIL device output settings.

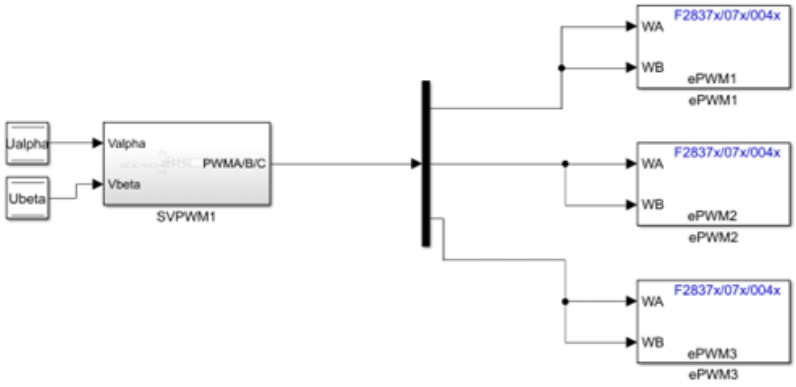
7.1.3.2 SWPWM Module

The next module utilised from the C2000 Simulink library is the Space Vector Pulse Width Modulation (SVPWM). This module receives the alpha and beta components of the desired inverter output voltage as inputs and employs the space vector PWM technique to compute the required duty ratios for the inverter legs. The outputs of the SVPWM module are the three dwell times (Ta, Tb, Tc) as shown in Figure 7.6 (a), which are subsequently fed into the ePWM modules for further processing and control of the inverter as shown in Figure 7.6 (b). The

SVPWM module plays a vital role in generating the appropriate pulse width modulation signals for the inverter, ensuring efficient and accurate control of the power output.



(a)



(b)

Figure 7.6 SVPWM Simulink implementation for code generation.

7.1.3.3 ePWM Module

The ePWM module can generate PWM signals that control the gate driver of the inverter. Each ePWM module represents one complete PWM channel, consisting of two PWM outputs: ePWMxA and ePWMxB as shown in Figure 7.6 (b). These outputs are directly linked to two different pins on the DSP. One advantageous feature of the ePWM module is the ability to generate ePWMxB as an exact inverted version of ePWMxA, while also providing a controlled Dead-Band (DB) between these two outputs. The Dead-Band is a time delay introduced between the activation of the ePWMxA and ePWMxB signals. This feature is employed to prevent the forbidden switching state, where both phase-legs of the inverter have the same switching state simultaneously, which could lead to a short circuit and cause damage to the system.

7.1.4 HIL 604 device

Typhoon offers comprehensive HIL control software that consists of a schematic editor and a control centre. The schematic editor allows users to model the power stage of the system being studied, enabling real-time simulation. In Figure 7.7, we can observe a schematic representation of the three-phase inverter and Permanent Magnet Synchronous Motor (PMSM) used in the study. The three-phase inverter components are directly obtained from the converter library, while the PMSM is obtained from the machine's library. As depicted in Figure 7.7, the model focuses solely on the electrical components, and all the components are externally controlled by adjusting their properties. For the three-phase inverter, the operation mode is set to "Digital input per switch," and for the PMSM, the load is configured as "SCADA / external," as illustrated in Figure 7.8 (a) and (b) respectively.

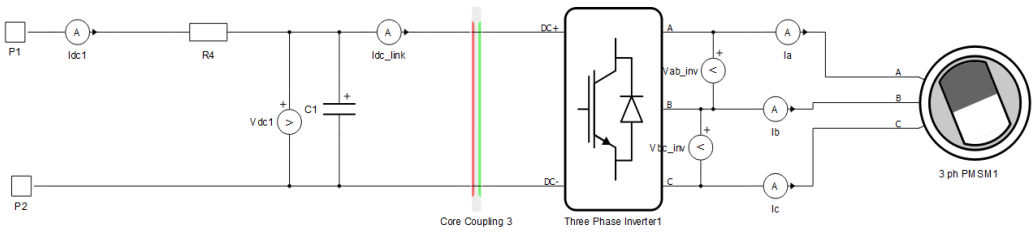
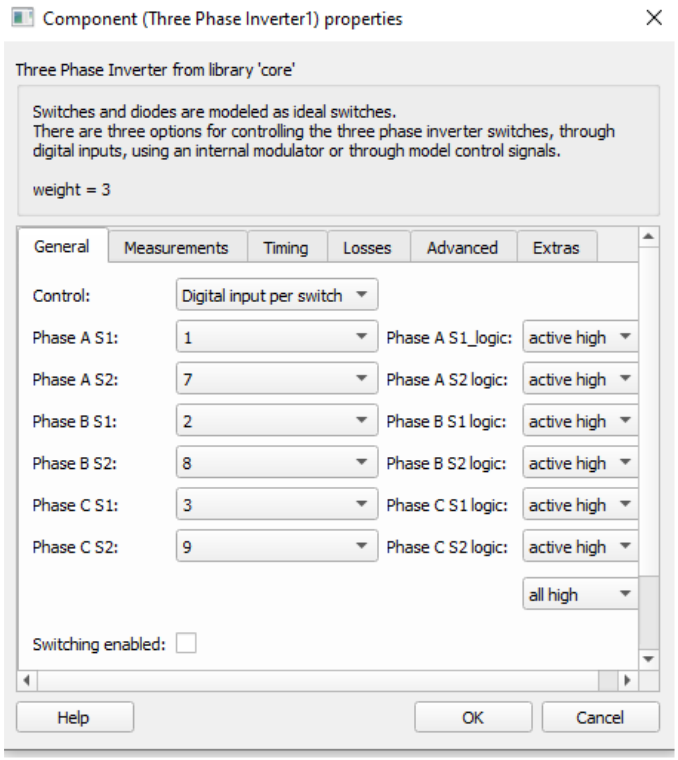
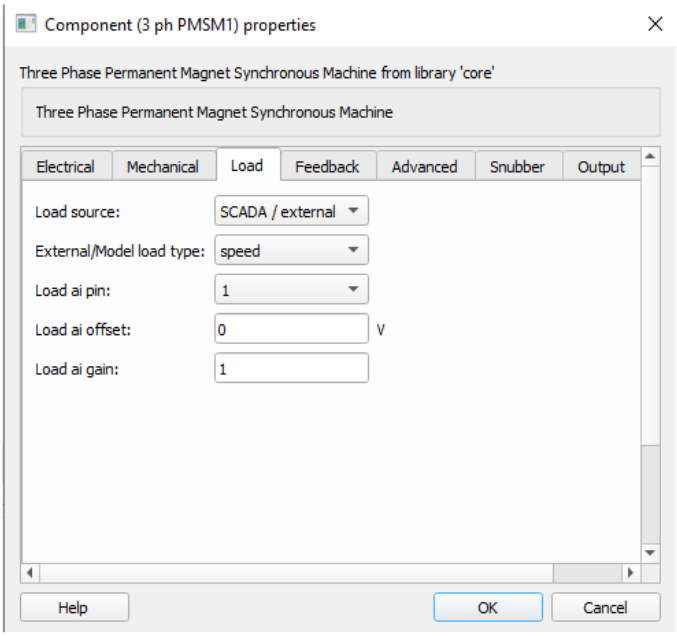


Figure 7.7 Model of the Inverter and PMSM implemented in Typhoon HIL schematic editor.

After configuring all settings in the schematic editor, the plant system is compiled and executed in real-time using the FPGA solver within the HIL604 device. Prior to compilation, the control algorithm program code which is developed with the aid of the Embedded Coder Support Package in MATLAB is debugged and transferred to the DSP through the Code Composer Studio (CCS) software. Once the automated C-Code is running on the DSP, it takes control of the plant system through the interface board, enabling seamless interaction and control of the system.



(a)



(b)

Figure 7.8 Externally controlled properties (a) Three-phase inverter (b) PMSM

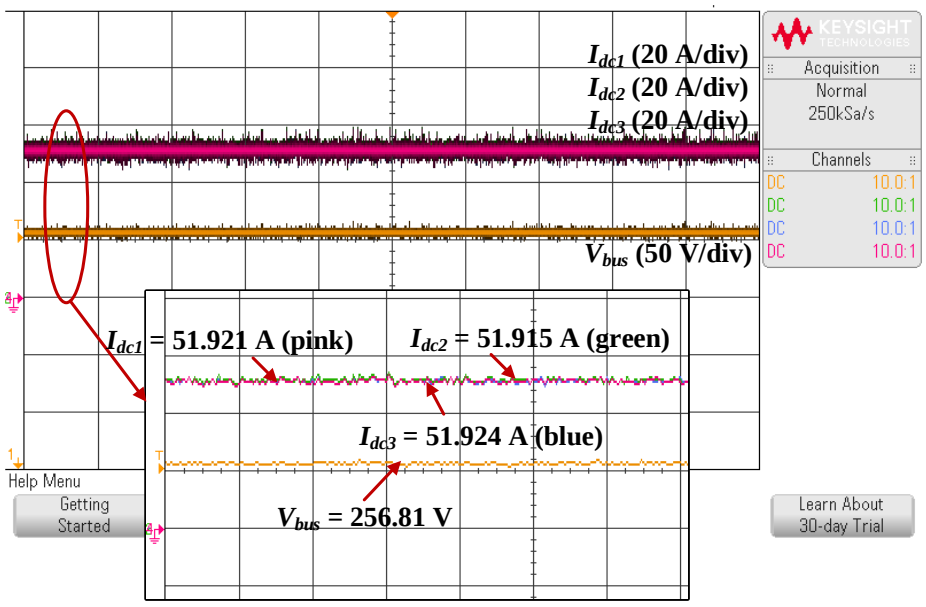
Following the thorough examination of the HIL experimental setup, the subsequent section will present the findings and outcomes obtained from the conducted HIL experiments.

7.2 HIL Experimental Results for Optimal Droop Control Design using ANN.

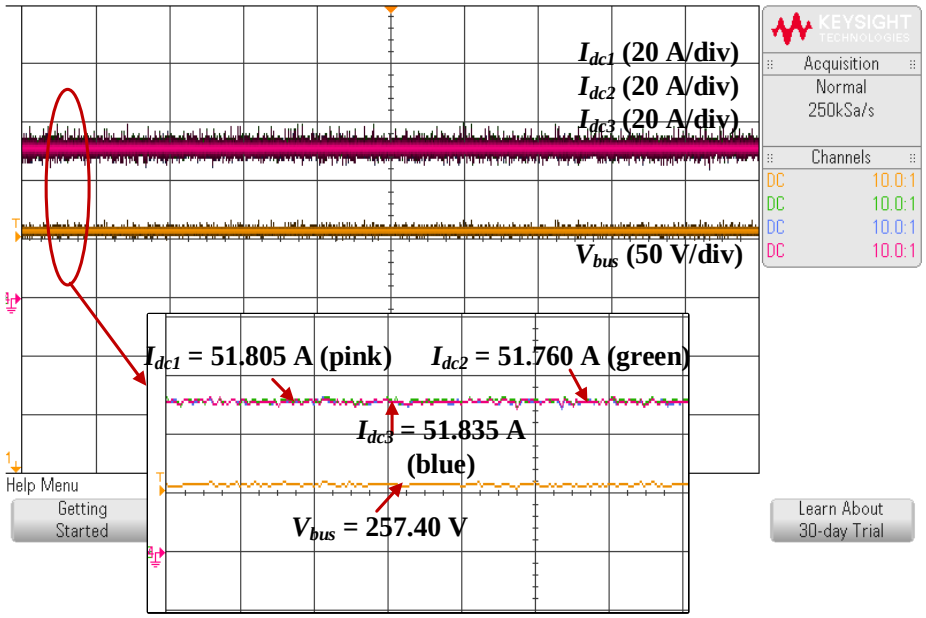
The optimal droop coefficient settings obtained using the proposed design strategy are validated in the TI DSP TMS320F28379D control card using the controller hardware-in-the-loop (C-HIL) experiment shown in Figure 7.1 (a). The PMSGs, converters and interconnecting cable impedance as shown in Figure 3.1 are emulated using the typhoon HIL (HIL604) real-time emulator. The control algorithms shown in Figure 3.2 are implemented in the control card. Results are obtained via an oscilloscope connected to the interface board. The HIL experimental setup works in such a manner that the DSP controller receives voltage and current signals from the HIL-604 device via the interface board. Consequently, the generated PWM signals from the DSP are sent to the converter switches via the interface board. This way, the accurate modelling and control of the system power structure are realized in real-time and with high fidelity. The parameters used in the HIL experimental setup are shown in Table 3-1.

7.2.1 Validation of Optimal Droop Setting Design

The optimal droop coefficient settings from the first and second design examples are validated here in steady states and the results obtained are shown in Figure 7.9 (a) and (b). As shown in Figure 7.9 (a), the output currents shared among the converters and bus voltage regulation using the optimal droop setting from the first design example were I_{dc1} = 51.921 A, I_{dc2} = 51.915 A, I_{dc3} = 51.924 A and V_{bus} = 256.81 V. Hence, the calculated current sharing ratios and normalised bus voltage are n_1 = 0.9999, n_1 = 1.0004, and V_{bn} = 0.9511. Similarly, as shown in Figure 7.9 (b), the output currents shared among the converters and bus voltage regulation using the optimal droop setting from the second design example were I_{dc1} = 51.805 A, I_{dc2} = 51.760 A, I_{dc3} = 51.835 A and V_{bus} = 257.40 V. Hence, the calculated current sharing ratios and normalised bus voltage are n_1 = 0.9991, n_1 = 1.0006, and V_{bn} = 0.9533. Based on the results obtained, it can be said that the optimal droop coefficient settings can yield the desired control objectives. Also, the results obtained from the ANN prediction, detailed MEA EPS simulation model and C-HIL experimental setup (see Figure 7.1 (a)) matched excellently well as shown in Table 7-1. The little differences between the C-HIL experimental results and the ANN predictions might be because the ANN is trained using data obtained from the MEA EPS simulation model. Moreover, the components used in the simulation are modelled ideally.



(a)



(b)

Figure 7.9 HIL Experimental results for steady-state current sharing and bus voltage regulation using the optimal droop coefficient from (a) the first design example and (b) the second design example.

Table 7-1 Comparison of performance metrics.

Design example	First			Second		
Metrics	n_1	n_2	V_{bn}	n_1	n_2	V_{bn}
ANN	1.0000	1.0000	0.9511	0.9994	1.0005	0.9532
Simulation	1.0000	1.0000	0.9511	0.9990	1.0004	0.9533
HIL experiment	0.9999	1.0004	0.9511	0.9991	1.0005	0.9533

7.2.2 Comparison with traditional droop coefficient

To show the superiority of the proposed design strategy, the HIL experimental result of the droop control method which uses the conventional identical fixed droop coefficient (shown in Table 3-1) is shown in Figure 7.10. The output currents shared among the converters and bus voltage regulation in steady states were I_{dc1} = 54.610 A, I_{dc2} = 49.064 A, I_{dc3} = 52.004 A and V_{bus} = 257.10 V respectively. Hence, the calculated current sharing ratios between the converters and normalised bus voltage regulation are n_1 = 0.8984, n_2 = 0.9523 and V_{bn} = 0.9522 respectively. It can be observed that there is an error in the current sharing ratio as expected due to the influence of the unequal line resistance. However, the error in the current sharing ratio is eliminated or significantly reduced using the optimal droop coefficient settings obtained using the proposed design strategy (as shown in Figure 7.9).

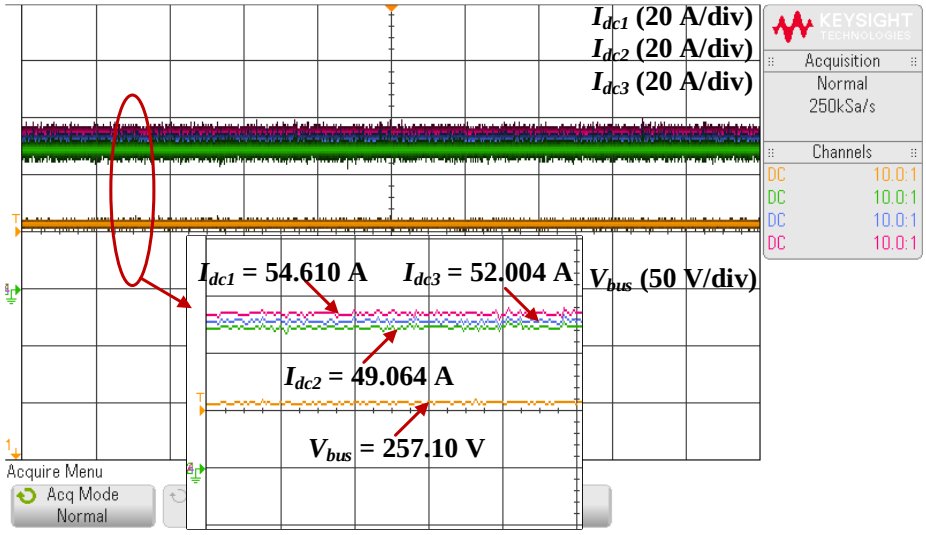


Figure 7.10 HIL experimental results for steady-state current sharing and bus voltage regulation using the conventional droop coefficient.

7.2.3 Load fluctuations

To test the robustness of the selected optimal droop coefficient setting to load variation, a variation of the CPL from 40 kW to 20 kW, 30 kW and then back to 40 kW is applied during the HIL experiment as shown in Figure 7.11. Only the optimal droop coefficient setting from the first design example is used here due to space limitations. It can be observed from Figure 7.11 that the optimal droop coefficient setting is robust to load variation and can share the current demand by the load equally among the converters as desired despite the load fluctuation. Also, the voltage regulation gets better when the load demand is small. For instance, the output current shared and bus voltage regulation for the 20-kW load are I_{dc1} = 25.29 A, I_{dc2} = 25.28 A, I_{dc3} = 25.29 A and V_{bus} = 263.60 V respectively as shown in Figure 7.11.

7.2.4 Fault condition

The robustness of the optimal droop coefficient setting to maintain accurate current sharing if one of the generators is under fault is tested in an HIL experiment as shown in Figure 7.12. The optimal droop coefficient setting from the second design example is used here due to space limitations. A CPL of 40 kW was applied during the HIL experiment. It can be observed from Figure 7.12 that before the disconnection of the PMSG2, the three converters are operating in parallel and able to share the load current demand in the ratio of n_1 = 0.9991 and n_2 = 1 (with a current sharing of 51.805 A, I_{dc2} = 51.760 A, I_{dc3} = 51.835 A). When the second PMSG2 is disconnected, converters 1 and 3 shared the load current demand between them (with current sharing of I_{dc1} = 79.801 A, and I_{dc3} = 79.849 A) after the loss of converter 2. Furthermore, the bus voltage is well regulated within the acceptable limits for the MEA applications, even though its value dropped from 257.40 V (when the three sources are supplying together) to 250.53 V after PMSG2 is disconnected as shown in Figure 7.12. Hence, the optimal droop coefficient performs well even under fault conditions and has a good transient performance.

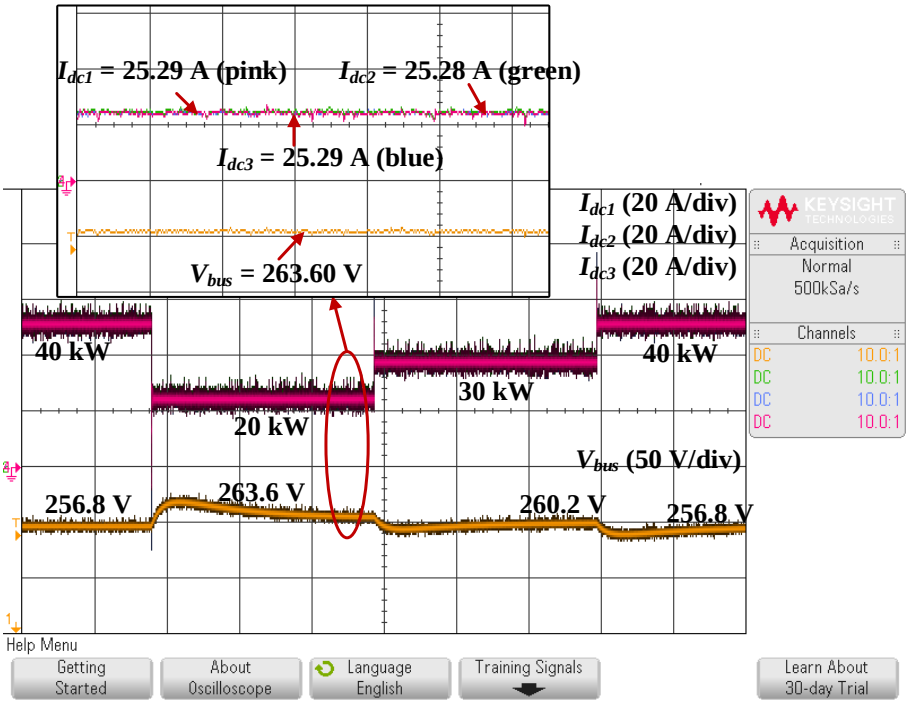


Figure 7.11 HIL experimental results for current sharing and bus voltage regulation using the optimal droop coefficient from the first design example under load variation conditions.

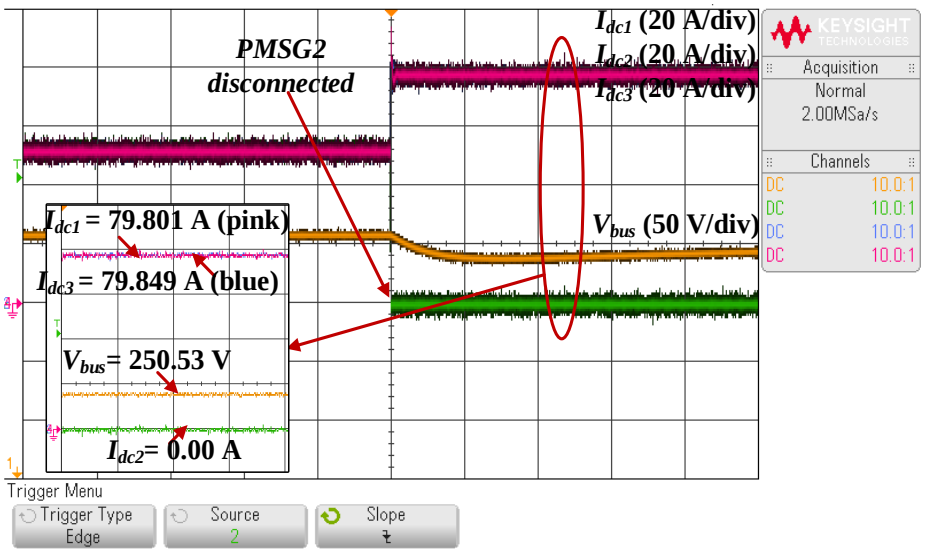


Figure 7.12 HIL experimental results for current sharing and bus voltage regulation using the optimal droop coefficient from the second design example under source disconnection condition.

7.2.5 Robustness to DC-link Capacitance Parameter variations

The robustness of the optimal droop coefficient settings to variations in the internal model parameter is validated in the HIL experiment. Among the EPS parameters that could change due to operating temperature or other factors is the capacitance of the DC-link capacitor C_b. A test was carried out for a 20% reduction in the value of C_b shown in Table 3-1 (i.e., new C_b = 0.96 mF). A load step from 20 kW to 40 kW is applied during the demonstration. Only the optimal droop coefficient setting from the first design example is used. As shown in Figure 7.13, the control algorithm is robust to parameter uncertainties. The reduction in C_b mainly affects the output current of the converters, hence, the little ripple as seen in Figure 7.13. Despite the oscillations, the current sharing and bus voltage regulation is as desired.

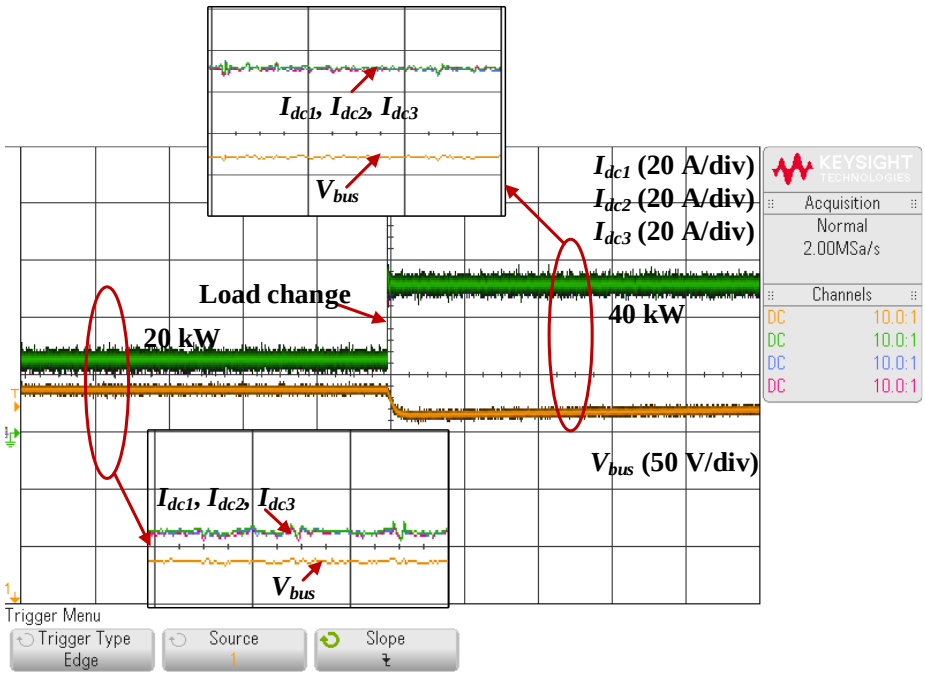


Figure 7.13 HIL experimental results for current sharing and bus voltage regulation using the optimal droop coefficient from the first design example. A response to a 20% reduction in C_b.

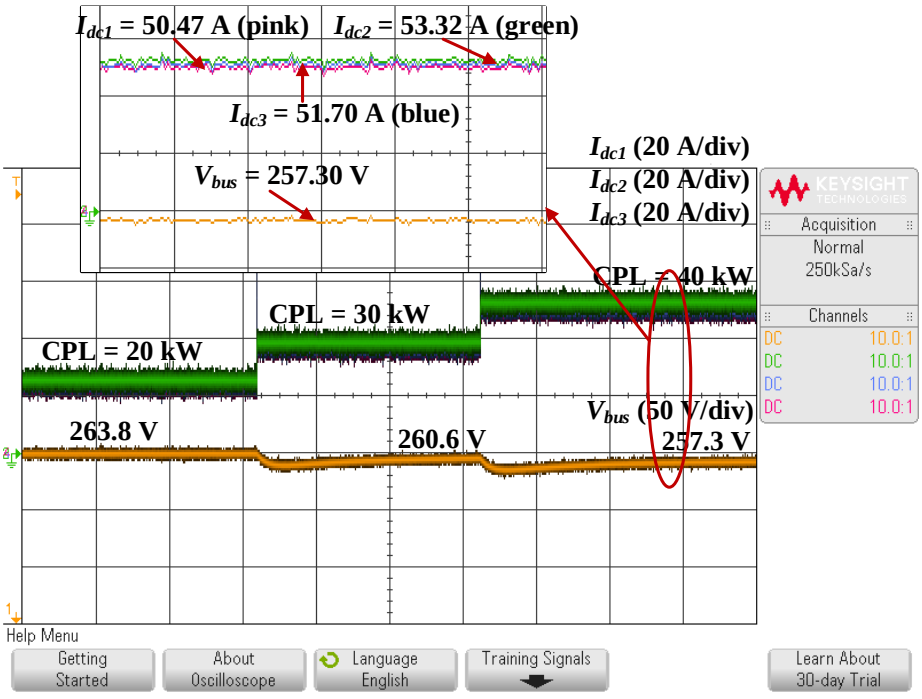
7.2.6 Robustness to variation in line resistance and inductance

This case study demonstrates the robustness of the optimal droop coefficient settings to a variation in the interconnecting cable resistance and inductance. The test is carried out for a $\pm$ 50% variation in the nominal values of the cable's parasitic resistance and inductance shown in Table 3-1. The optimal droop coefficient settings from the first design example are used in

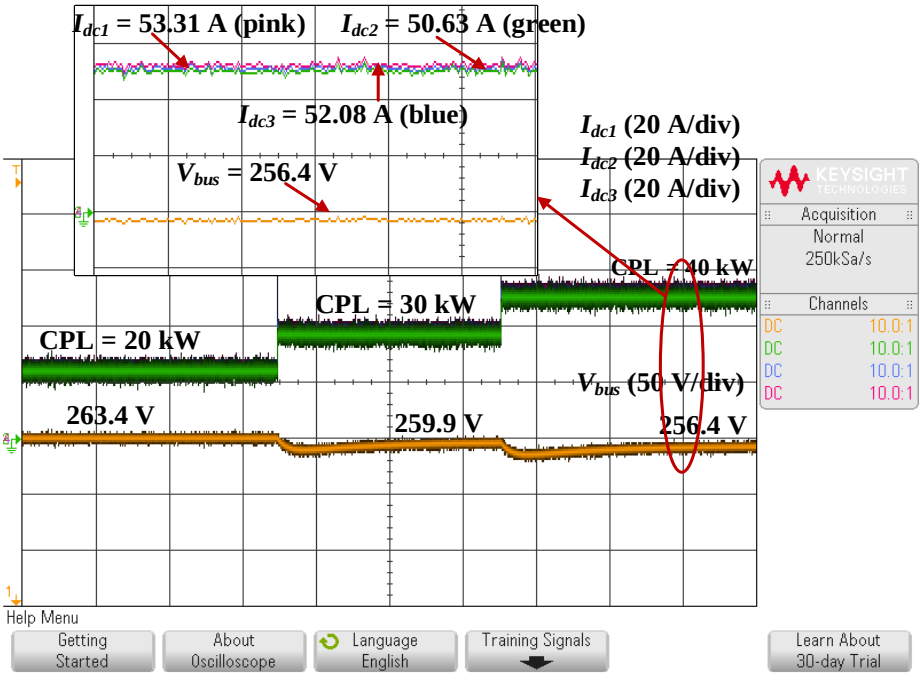
this case study. Furthermore, CPLs of 20 kW, 30 kW and 40 kW are applied during the HIL experiment. The results obtained are shown in Figure 7.14 (a) and (b).

It is observed that the optimal droop coefficient settings obtained using the proposed approach are still able to guarantee a reduction in the current sharing error and regulate the bus voltage within an acceptable range despite the variation in the interconnecting cable parameters. For the case of a 50% decrease in the line parameters (as shown in Figure 7.14 (a)), the computed error in the current sharing ratios (n_1 and n_2) and bus voltage deviation is 5.65%, 2.44%, and 4.70% respectively. Similarly, for the case of a 50% increase in the line parameters (as shown in Figure 7.14 (b)), the computed error in the current sharing ratios (n_1 and n_2) and bus voltage deviation are 5.03%, 2.30%, and 5.04% respectively. This verifies the robustness of the obtained optimal droop coefficient settings to variations in the cable resistance.

However, if there is a huge variation in the line resistance (exceedingly above the range considered) due to temperature or other factors from the line resistance value under which the data used to train the surrogate model is extracted, then the selected optimal droop gain settings may not yield desired control performance. In that case, new data may need to be collected to retrain the surrogate model for the selection of new optimal droop gain settings. Even in that case, the data collection process and training of the surrogate mode can still be carried out fast.



(a)



(b)

Figure 7.14 HIL experimental results for current sharing and bus voltage regulation to validate the robustness of the optimal droop coefficient settings to a (a) 50% decrease in the line resistance and inductance (b) 50% increase in line resistance and inductance.

7.2.7 Performance evaluation under different converter ratings

This case study demonstrates the applicability of our proposed approach for power sharing and bus voltage regulation in a situation where the generators have different power ratings. To achieve this, the design space and control objectives are carefully selected before data collection and training of the surrogate model. It is assumed that the $PMSG_1$ power rating is twice that of $PMSG_2$ and $PMSG_3$ (i.e., $I_{dc1}^{rated} = 2I_{dc2}^{rated} = 2I_{dc3}^{rated}$). Therefore, the total load demand is expected to be shared among the sources according to their power capacity. After using our proposed design strategy, the optimal droop gain settings are found to be k_{d1}^{opt} = 1/8.230, k_{d2}^{opt} = 1/4.565 and k_{d3}^{opt} = 1/4.275. Consequently, the optimal droop gain settings are used in the HIL experiment and CPLs of 20 kW, 30 kW and 40 kW are applied during the HIL experiment. The HIL experimental results for the current sharing and bus voltage regulation are shown in Figure 7.15. It can be observed that the proposed approach can yield proportional current sharing according to the source's power capacity and regulate the bus voltage within acceptable limits.

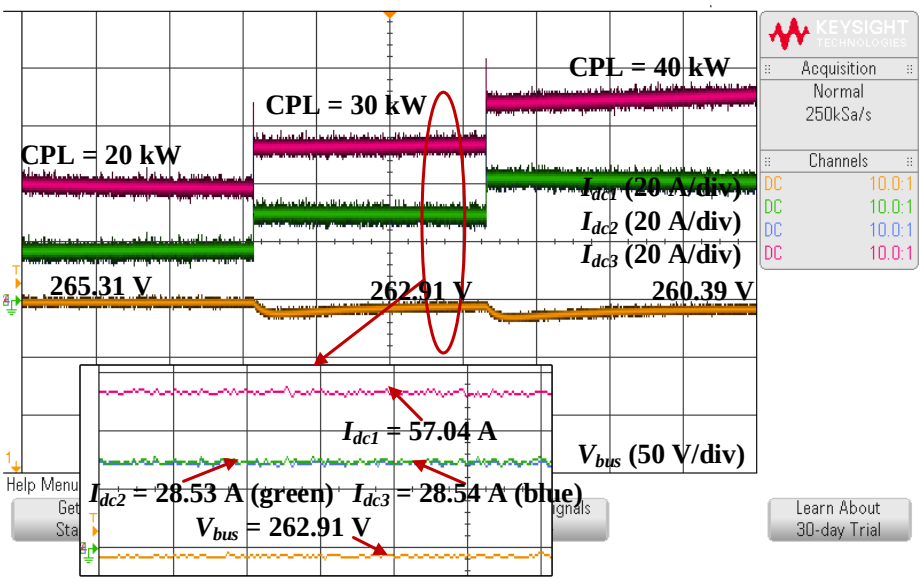


Figure 7.15 HIL experimental results for unequal current sharing and bus voltage regulation.

7.3 HIL Experimental Results for Realtime Tuning of Optimal Droop Gain Settings

The proposed ANN-based approach has undergone HIL experimental verification using a C-HIL setup, illustrated in Figure 7.1, with its corresponding parameters listed in Table 3-1. The primary objective of the study in chapter 4 is to achieve real-time computation of the optimal droop gain settings (k_{d1}^{opt}, k_{d2}^{opt}, and k_{d3}^{opt}) for the converters to enable the controller to adapt quickly to reference changes as shown in Figure 4.8. As mentioned in Chapter 4, Section 4.3, the ANN models, trained offline, can be employed either offline or implemented in a digital microprocessor for online applications. Besides, one of the contributions of Chapter 4 is the comparison of the controller's performance using the computed optimal droop gain settings obtained from both the proposed design approach and the ANN optimisation-based design (presented in chapter 3) [186]. For this comparison, the trained ANN models will be used offline. Hence, the HIL experimental validation section is divided into two parts: validation of the offline computation of optimal droop gain settings using both design approaches and the assessment of real-time implementation performance using the proposed approach in Chapter 4. The parameters used in the HIL experimental setup are shown in Table 3-1.

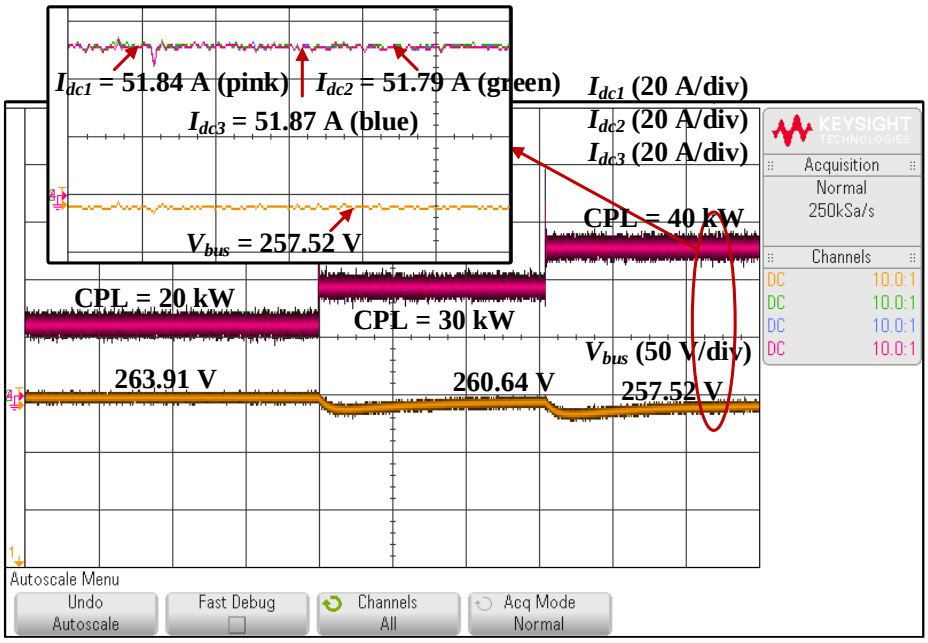
7.3.1 HIL experimental validation of the offline computed optimal droop gain settings

Within this section, an evaluation and validation of the controller's performance are conducted by comparing the offline computed optimal droop gain settings obtained through both the ANN optimisation-based design [186] and the newly proposed design approach in chapter 4. To that end, the offline computed optimal droop coefficient settings are validated in the TI DSP TMS320F28379D control card using the controller hardware-in-the-loop (C-HIL) experiment shown in Figure 7.1 (a). The control algorithms as shown in Figure 4.1 (a) are implemented in the control card. The PMSGs, converters and interconnecting cable impedance as shown in Figure 4.1 (b) are emulated using the typhoon HIL (HIL604) real-time emulator.

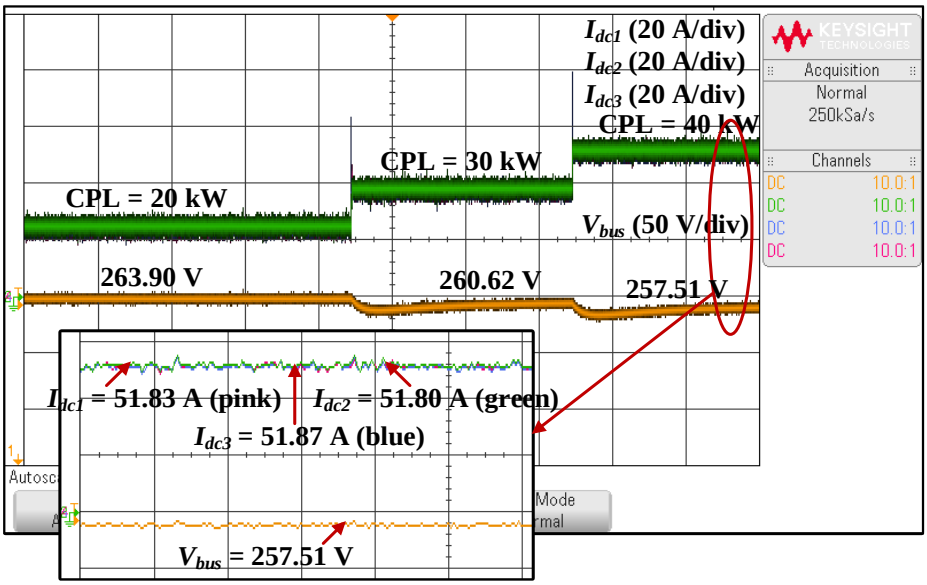
7.3.1.1 Load Changes

In this case study, the optimal droop gain settings obtained from the first design example using both the ANN optimisation-based design and the proposed design approach (see Section 4.3.3) are further validated in the C-HIL experiment. Additionally, the current sharing and voltage regulation performance of both approaches when the system experiences load changes are also assessed. The HIL experimental results are presented in Figure 7.16 (a) and (b) for the ANN optimisation-based design and the proposed design approach, respectively, with CPLs of 20 kW, 30 kW, and 40 kW applied during the HIL experiment.

Figure 7.16 (a) displays the current sharing and voltage regulation results obtained using the optimal droop gain settings from the ANN optimisation-based design for the 40-kW load. In this case, the calculated current sharing ratios and normalised bus voltage regulation in steady state are n_1 = 0.9990, n_2 = 1.0006, and V_{bn} = 0.9537, respectively. Similarly, Figure 7.16 (b) illustrates the current sharing and voltage regulation results obtained using the computed optimal droop gain settings from the proposed approach for the 40-kW load, resulting in n_1 = 0.9994, n_2 = 1.0008, and V_{bn} = 0.9537 in steady state. These results affirm that both design approaches effectively achieve the desired user-defined control objectives, minimising the error in current sharing ratios between the generators and ensuring good bus voltage regulation.



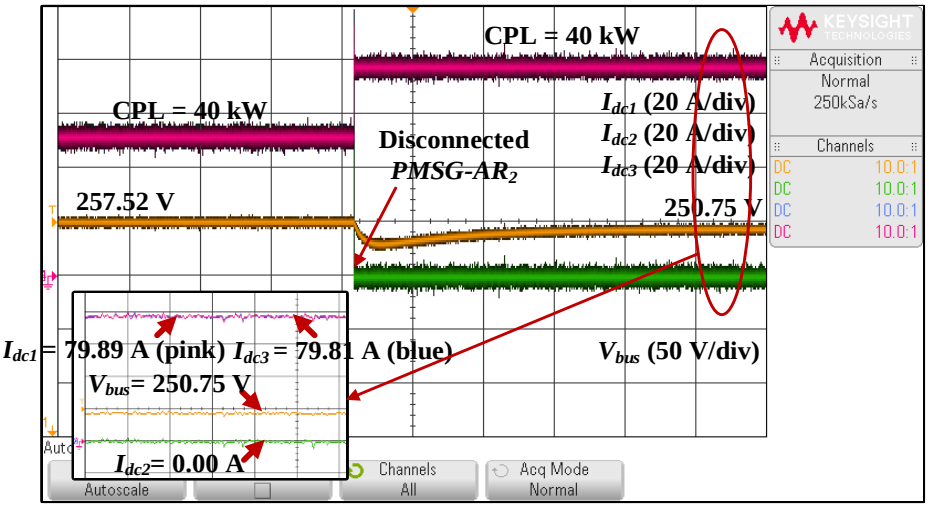
(a)



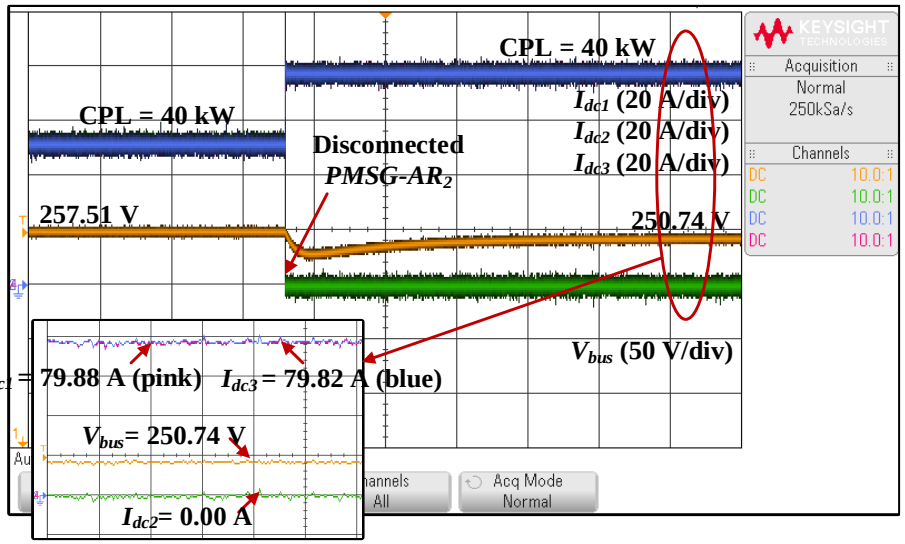
(b)

Figure 7.16 Comparative performance assessment using optimal droop gain settings from the first design example. (a) ANN optimisation-based design [186] (b) Proposed design approach.

Furthermore, it is evident from Figure 7.16 (a) and (b) that both design approaches maintain equal current sharing and good voltage regulation even when the load conditions change.



(a)



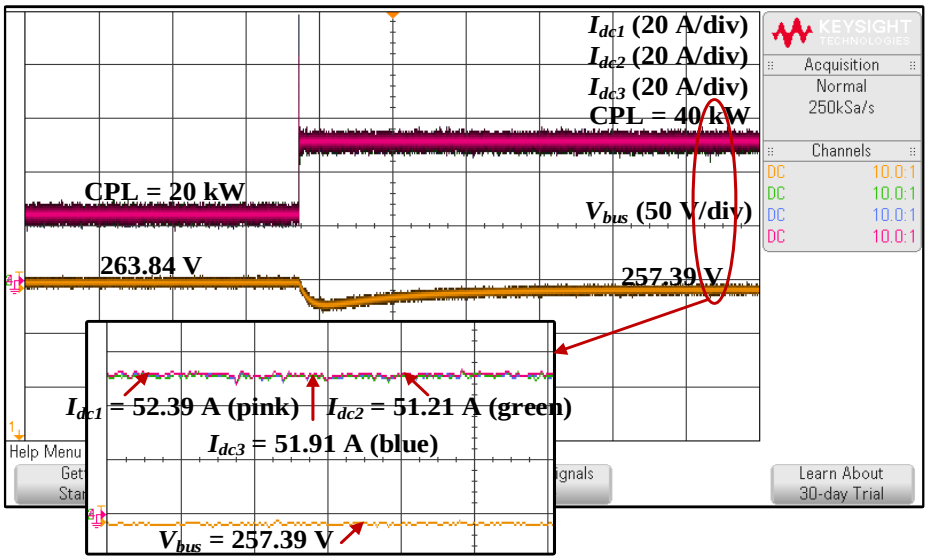
(b)

Figure 7.17 Comparative performance assessment under fault conditions using optimal droop gain settings from the first design example. (a) ANN optimisation-based design [186] (b) Proposed design approach.

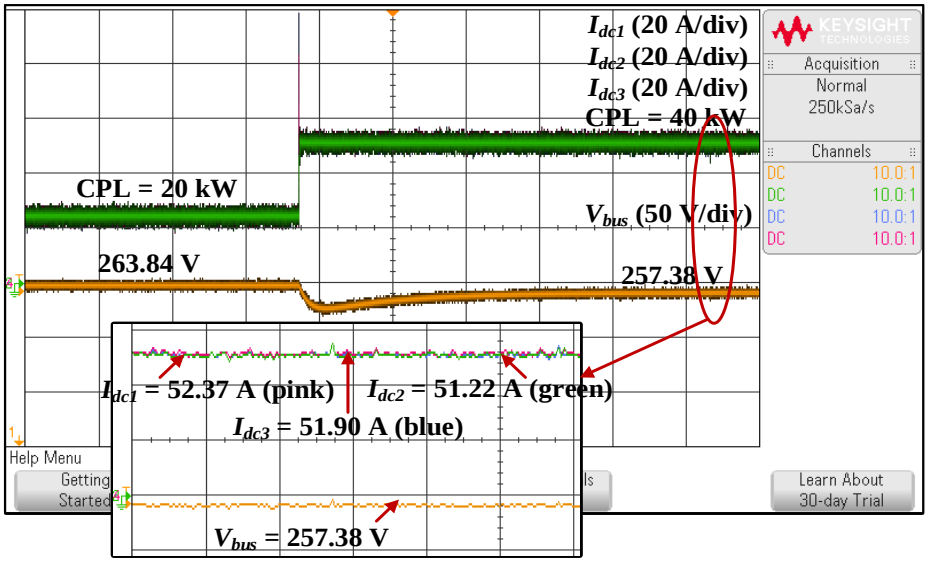
7.3.1.2 Generator disconnection

In this fault scenario, a CPL of 40 kW is applied during the HIL experiment. The optimal droop gain settings obtained from the first design example are utilised in this scenario. Initially, all three *PMSG-AR*$_{1\text{-}3}$ systems work in parallel, sharing the load current demand equally among themselves and regulating the bus voltage as desired, as shown in Figure 7.17 (a) and (b). When the second *PMSG-AR*$_2$ is disconnected (assumed to be under fault), converters 1 and 3 take over the responsibility of supplying the load power demand, as indicated in Figure 7.17 (a) and

(b). It is observed that there is a drop in the bus voltage for both approaches when *PMSG-AR2* is disconnected. However, despite the drop in the bus voltage under the fault condition, the bus voltage regulations remain within the acceptable limits (250 V < V_{bus} < 280 V) for the MEA application. Therefore, it can be concluded that both design approaches are robust to generator disconnection and exhibit good and similar transient performance.



(a)



(b)

Figure 7.18 Comparative performance assessment under line resistance variation using optimal droop gain settings from the first design example. (a) ANN optimisation-based design [186] (b) Proposed design approach.

7.3.1.3 Line resistance variation

In this HIL experimental study, the robustness of the optimal droop gain settings obtained using the ANN optimisation-based design and the proposed design approach from the first design example is assessed under the scenario where the line resistance values shown in Table 3-1 are increased by 20%. The HIL experiment is conducted with a 40-kW load, and the results are presented in Figure 7.18 (a) and (b) for the conventional ANN optimisation-based design and the proposed design approach, respectively.

In Figure 7.18 (a), the output currents and bus voltage regulation obtained from the conventional ANN optimisation-based design are shown. The calculated current sharing ratios between the converters are n_1 = 0.977 and n_2 = 0.991, resulting in an error of 2.30% and 0.90% in n_1 and n_2, respectively. Similarly, in Figure 7.18 (b), the output currents and bus voltage regulation obtained from the proposed design approach are shown. The calculated current sharing ratios between the converters are n_1 = 0.978 and n_2 = 0.991, resulting in an error of 2.20% and 0.90% in n_1 and n_2, respectively. The HIL experimental results demonstrate that both design approaches exhibit a similar and significant reduction in the power sharing error while maintaining the bus voltage regulation within an acceptable range, even in the presence of variation in the line resistance.

7.3.1.4 Comparison with conventional droop gain

This test is conducted to compare the current sharing and voltage regulation performance of the conventional droop gain design with the proposed design approach. The parallel-connected PMSG-ARi system is controlled using two different droop gain settings: traditional identical fixed droop gain settings (as shown in Table 3-1) and computed optimal droop gain settings obtained for case 1 (as shown in Table 4-2). The HIL experimental results are depicted in Figure 7.19, where a CPL of 40 kW is applied during the HIL experiment.

Figure 7.19 shows the output currents flowing through the three converters and the bus voltage regulation for the traditional droop gain setting. The calculated current sharing ratios between the converters and normalised bus voltage regulation in steady state are n_1 = 0.8984, n_2 = 0.9523, and V_{bn} = 0.9522, respectively. These results indicate a 10% error in the current sharing ratio between converters 1 and 2, a 4.77% error in the current sharing ratio between converters 1 and 3, and a 4.78% deviation of the bus voltage from its nominal value. These deviations

demonstrate that the current sharing using the traditional droop gain settings is not as desired, likely due to the impact of unequal cable resistance on the conventional droop control method. Nevertheless, the bus voltage regulation is within the acceptable range for the MEA application. On the other hand, when the predicted optimal droop gain settings for case 1 are applied, the desired control objectives (as presented in Table 4-2) are achieved, and the current sharing and bus voltage regulation improve significantly, as shown in Figure 7.19. The calculated current sharing ratio and normalised bus voltage regulation in steady state are n_1 = 1.0002, n_2 = 1.0003, and V_{bn} = 0.9534, respectively.

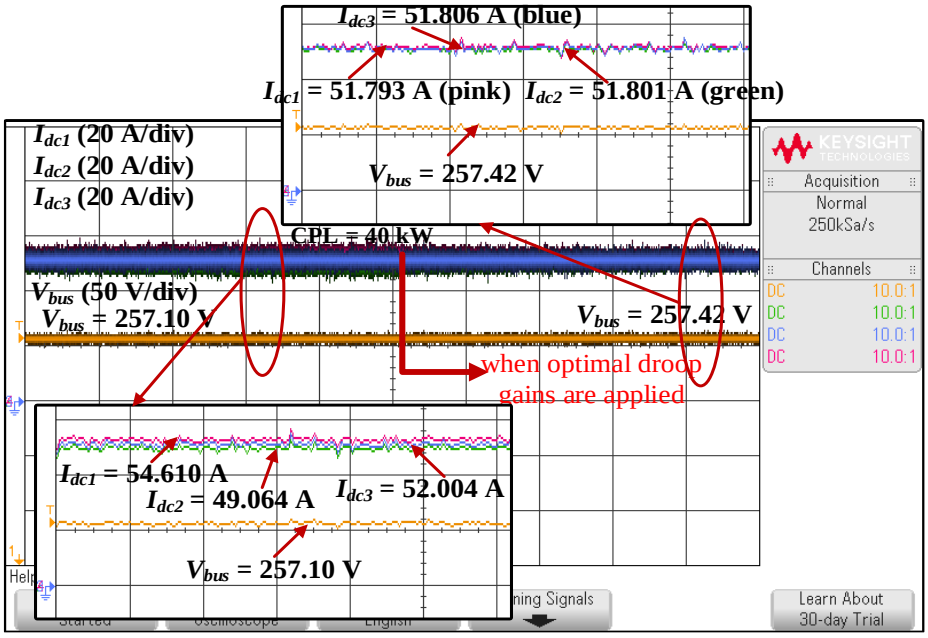


Figure 7.19 Comparative performance assessment using different droop gain settings (a) Traditional identical fixed droop gain settings (b) Optimal droop gain settings for case 1.

These results demonstrate a noteworthy enhancement in the current sharing performance of the proposed design approach compared to the conventional droop gain design. The optimal droop gain settings obtained using the proposed approach effectively mitigate the influence of subsystem cable resistance on the current sharing performance of the droop control method. The effectiveness of the proposed approach is a key motivation of this study, as it enables the quick determination of appropriate droop gain settings for desired control objectives based on sample data collected from a simulation loop, without the need for extensive derivations or detailed information about the system.

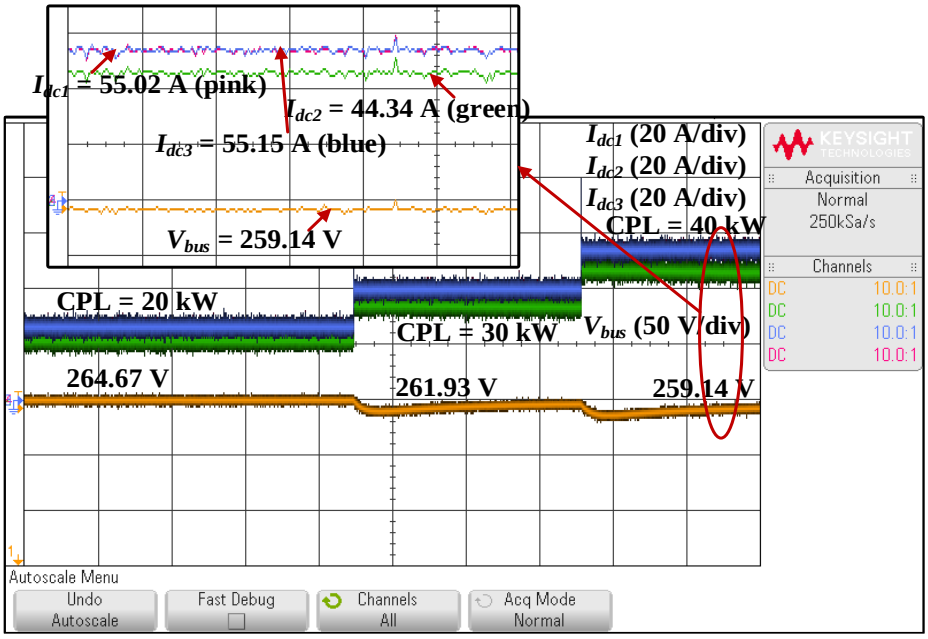


Figure 7.20 HIL experimental results demonstrating unequal current sharing and bus voltage regulation using the optimal droop gain settings from Case 2.

7.3.1.5 Unequal power sharing

In this case study, the optimal droop gain settings for case 2, as obtained from the other design examples (shown in Table 4-2), are validated for unequal power sharing. Figure 7.20 displays the current sharing and bus voltage regulation results for the 40-kW load. The computed current sharing ratios and normalised bus voltage regulation in steady state are n_1 = 0.8058, n_2 = 1.0024, and V_{bn} = 0.9592, respectively. These performance metrics closely match the desired control performance used as input to the surrogate model (as shown in Table 4-2). Hence, it is confirmed that the proposed design approach can effectively share the load current demand and regulate the bus voltage based on user-defined design criteria.

Furthermore, this validation demonstrates that when a different design criterion is considered within the considered design space, the proposed design approach can directly compute the optimal droop gain settings without requiring another round of data collection, as might be the case with heuristic methods [182], [245]. This highlights the flexibility and efficiency of the proposed design approach, enabling quick adaptation to various control objectives without the need for additional data gathering or extensive trial-and-error iterations.

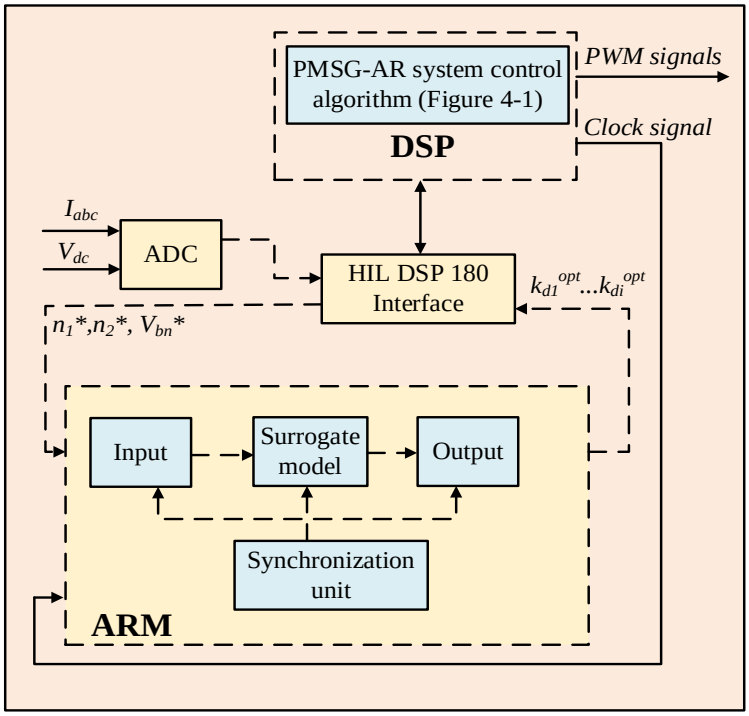


Figure 7.21 Block diagram of the proposed approach for the real-time tuning of the optimal droop gains.

7.3.2 Evaluation of Real-Time Implementation Performance

7.3.2.1 Digital Implementation

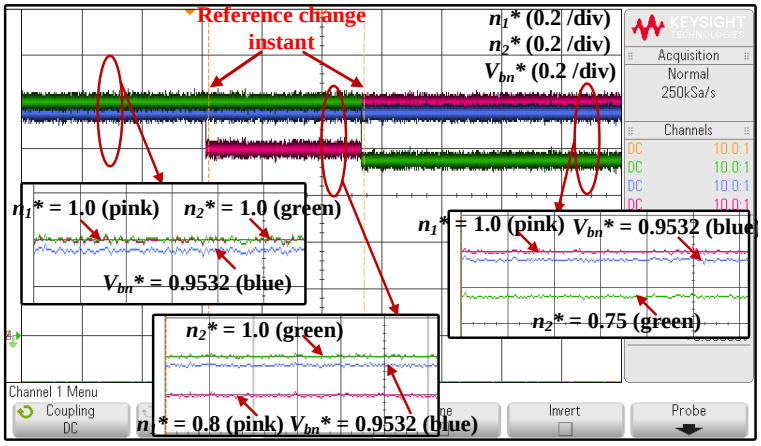
Prior to assessing the real-time implementation performance, this section presents an overview of the digital implementation process. Power system designers leverage the capabilities of Field Programmable Gate Arrays (FPGAs) and advanced Reduced Instruction Set Computing (RISC) machines (such as ARM processors) as these technologies enable the implementation of machine learning algorithms and real-time tuning of control variables (an example is the weighting factor for the FCS-MPC) [187], [246], [247]. ARM refers to a family of processors known for their power efficiency and widespread use in various applications, including mobile devices and embedded systems. They are commonly found in control and communication systems [248].

As shown in Figure 7.21, the PMSG-AR systems control algorithm is implemented and runs on the DSP F28379D control card, while the ANN model's compiled C code runs on the HIL's ARM (ARM Cortex A9) real-time processor [249]. The real-time tuning of optimal droop gain

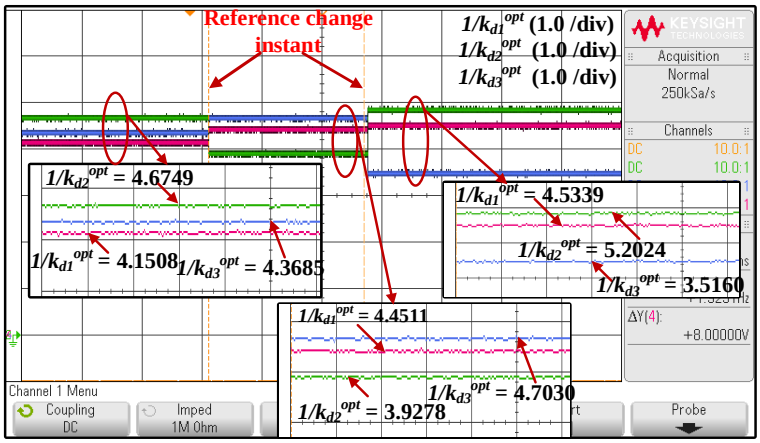
settings is achieved through the ARM-based implementation of the ANN model. The ARM processor efficiently runs the ANN algorithm, providing predictions of the optimal droop gain settings. The ANN model, trained offline in MATLAB, is compiled into a Simulink block and then converted into a Functional Mock-up Unit (FMU) file, including its C source code. This FMU contains the ANN model's mathematical representation, including weights, biases, and activation functions. The inclusion of C source code in the FMU is important for real-time tuning of optimal droop gain in the Typhoon HIL toolchain [250]. Consequently, the ANN model's FMU file is integrated into the Typhoon HIL toolchain via a Functional Mock-up Interface (FMI), allowing the ARM processor to execute the ANN model inference and making it accessible to the DSP control card for real-time communication through the HIL DSP 180 interface board as shown in Figure 7.21. During the C-HIL experiment, the control algorithm running on the DSP control card continuously interacts with the ARM processor on the Typhoon HIL device to obtain optimised droop gain settings in real-time. This ARM-based implementation ensures low latency, high-speed execution, enabling adaptive control and quick adjustments to the optimal droop gain settings based on user-defined references.

7.3.2.2 Real-time Assessment HIL experimental Results

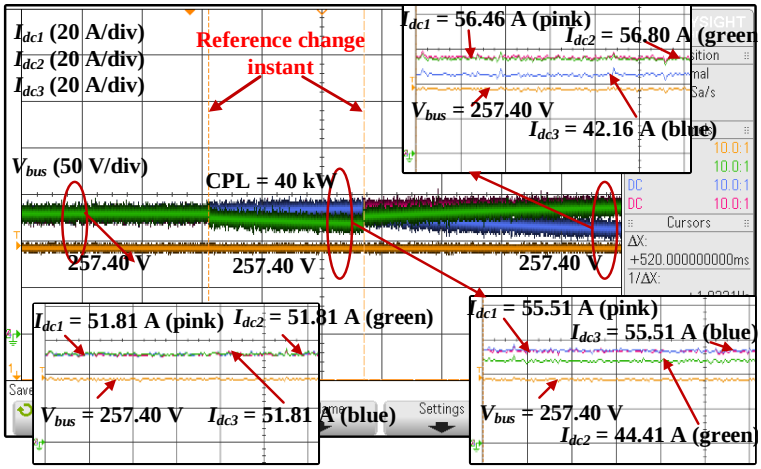
In this section, the feasibility and effectiveness of the proposed approach for real-time tuning of optimal droop gain settings is experimentally validated using the C-HIL setup. Firstly, we investigate the transient state performance under varying current-sharing ratios while maintaining constant voltage regulation references. A CPL of 40 kW was applied during the HIL experiment. Figure 7.22 (a) displays the user-defined references supplied as input to the ANN model (V_{bn}^{*} = 0.9532 (constant), with step changes in current sharing ratios: n_1^{*} = 1.0, n_2^{*} = 1.0; n_1^{*} = 0.8, n_2^{*} = 1.0 and n_1^{*} = 1.0, n_2^{*} = 0.75). Figure 7.22 (b) shows the response of the ANN, continuously updating the computed optimal droop gain settings following each transient. Figure 7.22 (c) exhibits the controller's response, adeptly adjusting the current sharing and bus voltage regulation to achieve the desired system responses. Remarkably, the ANN response is nearly instantaneous, presenting a distinctive advantage of the proposed approach compared to alternative solutions based on heuristic and ANN optimisation-based design methods. In contrast to those methods, which are confined to the offline computation of the optimal droop gain settings, the approach empowers real-time adaptation and control, enhancing the dynamic performance and responsiveness of the system.



(a)



(b)

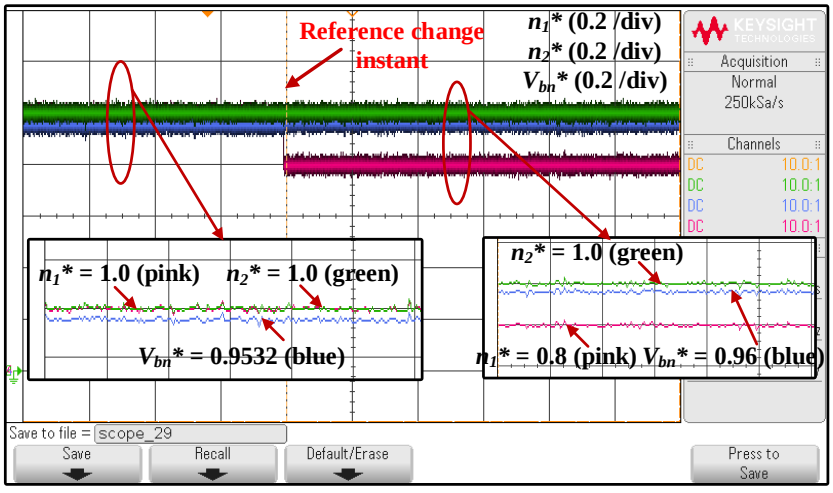


(c)

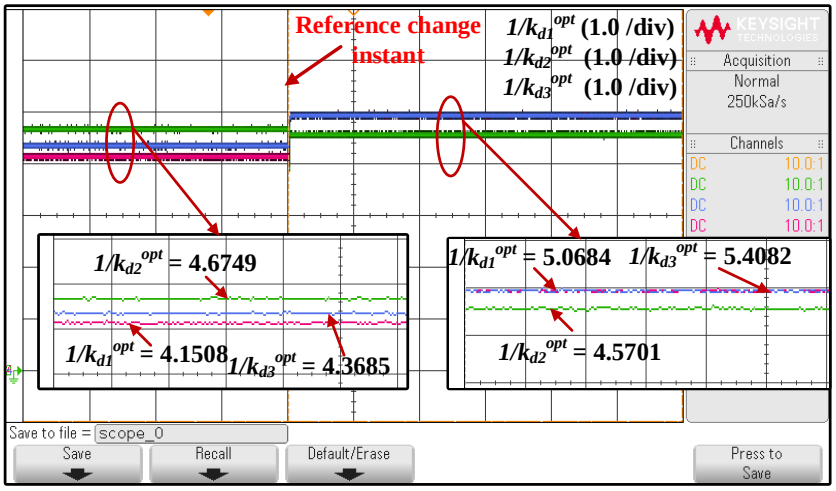
Figure 7.22 Transient-state HIL experimental results under CPL = 40-kW. (a) ANN model references. (b) Computed optimal droop gain settings by the ANN model (c) Current sharing and bus voltage regulation.

Hence, it can be confidently asserted that the proposed strategy functions effectively during transient state operation. In addition, the ANN reliably delivers the correct optimal droop gain settings (k_{di}^{opt}) for each operational point, empowering the controller to achieve the desired system response effectively.

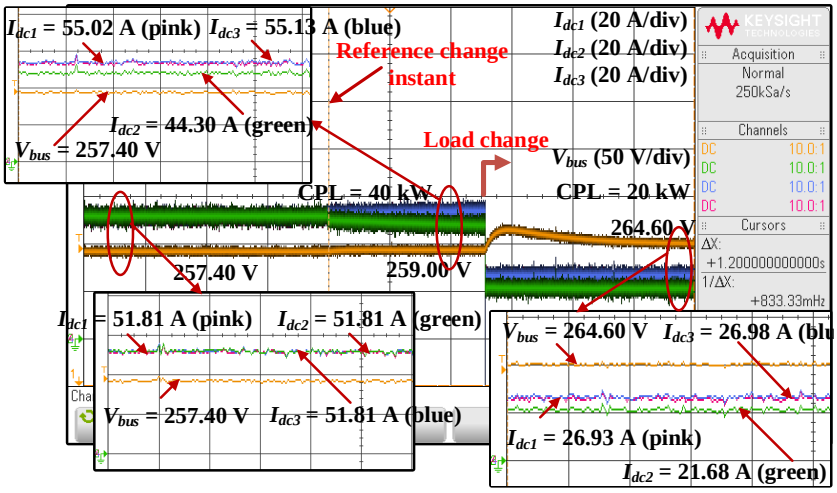
Figure 7.23 presents the transient HIL experimental results, capturing load changes. Specifically, Figure 7.23 (a) illustrates the step change in the desired system responses, serving as the input to the ANN model. Figure 7.23 (b) showcases the corresponding step changes in the computed optimal droop gain settings by the ANN model, responding to the reference modifications. Additionally, Figure 7.23 (c) displays the outcomes of current sharing and voltage regulation before and after the applied step-change transient. As depicted in Figure 7.23 (c), the controller successfully maintains the desired current sharing ratios between the converters even in the face of load changes. Moreover, the droop control mechanism leads to improved bus voltage regulation as the load power demand decreases from 40 kW (assumed maximum load) to 20 kW. Nonetheless, for the 40-kW power demand, the controller achieves desired bus voltage regulation, following the defined reference. Of note, the ANN rapidly and autonomously adjusts the optimal droop gain settings to match the actual operating conditions. Furthermore, through the proposed approach, the controller demonstrates quick adaptability to reference changes, facilitating efficient and accurate control of the system.



(a)



(b)



(c)

Figure 7.23 Transient-state HIL experimental results under CPLs = 40-kW and 20-kW. (a) ANN model references. (b) Computed optimal droop gain settings by the ANN model (c) Current sharing and bus voltage regulation.

7.4 HIL Experimental Results for AI-Based Hierarchical Control Design.

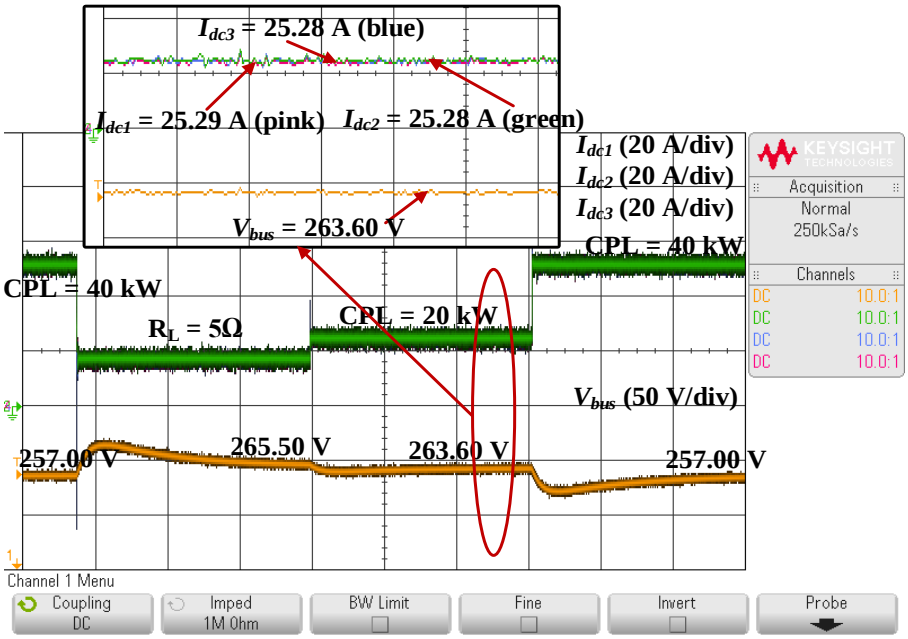
The proposed approach is verified by carrying out a C-HIL experiment. The experimental setup is made up of a Typhoon HIL real-time power electronics emulator and a Digital Signal Processor (DSP) controller (i.e., Texas Instrument (TI) DSP TMS320F28379D) as shown in Figure 7.1 (a). The Typhoon HIL real-time emulator is used to emulate the power stage consisting of multiple generators (i.e., the PMSGs), converters and interconnecting cables and load shown in Figure 5.4, while the DSP controller is used to control the emulated system. The proposed control strategy as shown in Figure 5.2 and the optimised control parameters are

implemented in the TI DSP TMS320F28379D control card to generate control signals for the control of the three PMSG-AR systems. The DSP controller and the typhoon HIL emulator communicate via an interface board, which facilitates the exchange of data between the two systems. The parameters used for the HIL experiment are the same as those shown in Table 3-1.

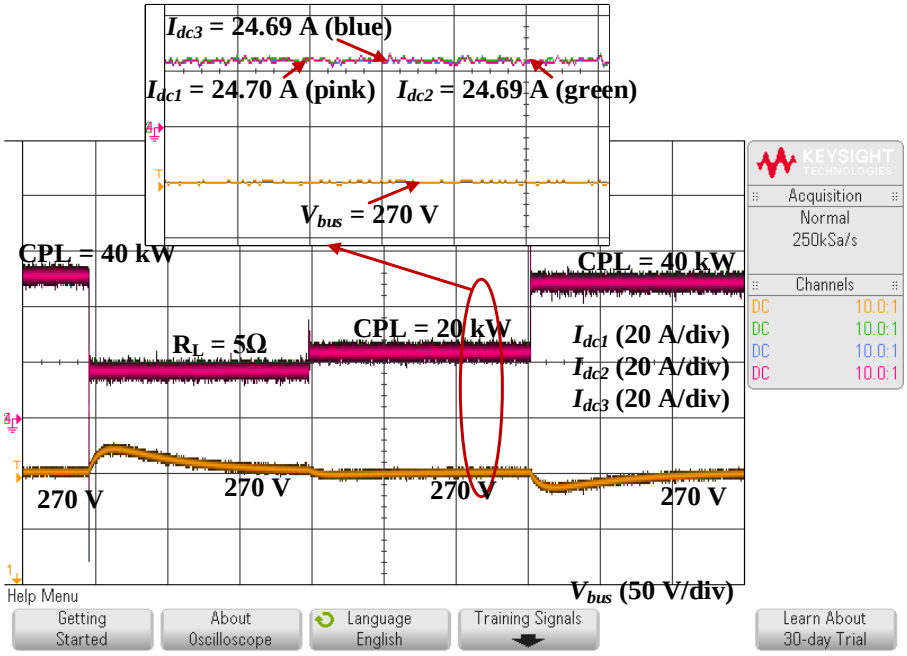
7.4.1 Equal power sharing and bus voltage compensation

In this case study, our proposed control strategy is demonstrated with a mix of resistive and CPLs changes for equal power sharing and bus voltage regulation as shown in Figure 7.24. The results of the HIL experiment using only the optimal droop coefficient settings from the design example 1 and with only the PC activated is shown in Figure 7.24 (a). It can be observed that the optimal droop coefficient can yield equal current sharing among the converters in the desired sharing ratio (with computed n_1 = 1.00, and n_2 = 1.00). However, due to the droop control action, the bus voltage decreases with an increase in the load demand. The normalised bus voltage is computed as V_{bcn} = 0.976 for the 20-kW load bus voltage regulation shown in Figure 7.24 (a). Nevertheless, the bus voltage regulation is still within the steady-state acceptable range (i.e., a voltage range of between 250 V to 280 V) for the MEA application [49].

On the other hand, when the optimal droop and compensation coefficient settings (i.e., SC activated) from design example 1 are used in this case study, the bus voltage is maintained at its nominal value of 270 V (i.e., $V_{bcndesired}$ =1) despite the load changes as shown in Figure 7.24 (b). At the same time, the current is shared equally among the participating converters in the desired sharing ratio (i.e., $n_{1desired}$ = 1 and $n_{2desired}$ = 1). Based on the output current of the converters and bus voltage obtained from the HIL experiment as shown in Figure 7.24 (b), the computed current sharing ratios and normalised bus voltage are n_1 = 0.9996 ≈ 1.00, n_2 = 0.9996 ≈ 1.00, and V_{bcn} = 1.00. These results show that both equal load sharing and bus voltage compensation can be achieved simultaneously as designed and based on user-defined desired control objectives using the proposed approach. In addition, each of the branch currents is reduced after the bus compensation is implemented as shown in Figure 7.24. Thus, it can be said that the proposed SC can reduce interconnecting cable losses compared to the conventional droop control method.



(a)



(b)

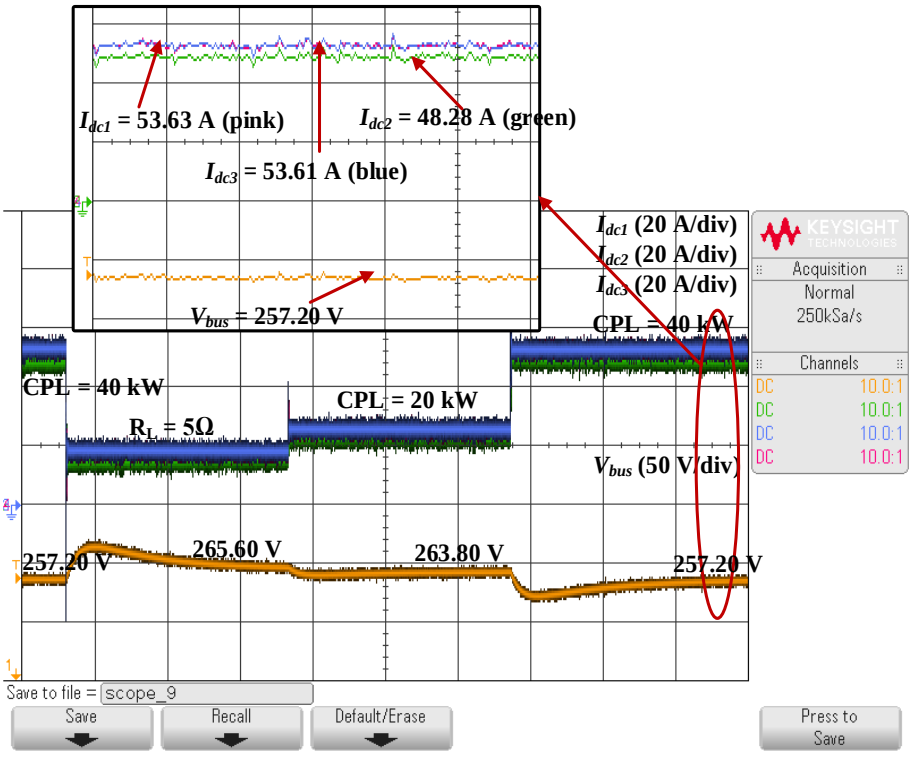
Figure 7.24 HIL experimental results for mixed load with equal current sharing and bus voltage regulation using the proposed approach (a) without bus voltage compensation (b) with bus voltage compensation.

7.4.2 Unequal power sharing and bus voltage compensation

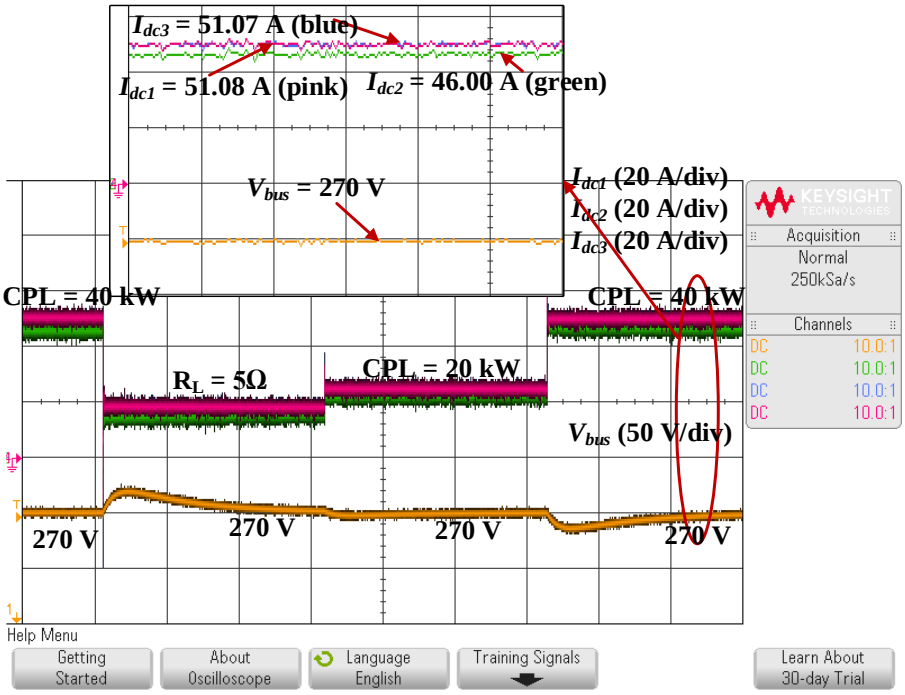
In case 2, the flexibility and applicability of the proposed approach are tested for unequal load sharing ($n_{1desired}$ = 0.9 and $n_{2desired}$ = 1) and bus voltage regulation ($V_{bcndesired}$ =1). The load

changes in this case study are the same as in case 1. The results of the HIL experiment using only the optimal droop coefficient settings from design example 2 and with only the PC activated is shown in Figure 7.25 (a). It can be observed that the optimal droop coefficient can yield unequal current sharing among the converters in the desired sharing ratio (i.e., with computed n_1 = 0.9 and n_2 = 1.00). However, due to the droop control action, the bus voltage decreases with an increase in the load demand. The normalised bus voltage is computed as V_{bcn} = 0.953 for the 40-kW load bus voltage regulation shown in Figure 7.25 (a). Nevertheless, the bus voltage regulation is still within the steady-state acceptable range (i.e., a voltage range of between 250 V to 280 V) for the MEA application [49].

Conversely, by using the optimal droop and compensation coefficient settings from design example 2 and the SC activated, the HIL experimental result is shown in Figure 7.25. It can be observed that the desired unequal load sharing among the converters and bus voltage restoration is realised simultaneously despite the load fluctuation. The calculated current sharing ratios between the converters and normalised bus voltage in steady state using the output current of the converters and bus voltage obtained from the HIL experiment as shown in Figure 7.25 (b) are n_1 = 0.90, n_2 = 1.00 and V_{bcn} = 1.00 respectively. Thus, yielding the user-defined desired control performance.



(a)



(b)

Figure 7.25 HIL experimental results for mixed load with unequal current sharing and bus voltage regulation using the proposed approach (a) without bus voltage compensation (b) with bus voltage compensation.

7.4.3 Traditional Droop Control Method

In this case study, the performance of the proposed control strategy is compared with the conventional droop controller. The HIL experiment is carried out using the traditional fixed and identical droop coefficients shown in Table 3-1 (obtained using the convention droop gain design in (3-2)). As shown in Figure 7.26, the bus voltage regulations are within the acceptable range (i.e., less than 5% of the nominal bus value). However, due to the droop control, the bus voltage regulation will increase with an increase in load demand. On the other hand, the power sharing performance of the droop control method is affected by the unequal interconnecting cable resistance. Based on the output current of the converters shown in Figure 7.26, the computed current sharing ratios are n_1 = 0.8984 and n_2 = 0.9523. Thus, representing 10.16% and 4.77% deviations of the current sharing ratio from the desired value.

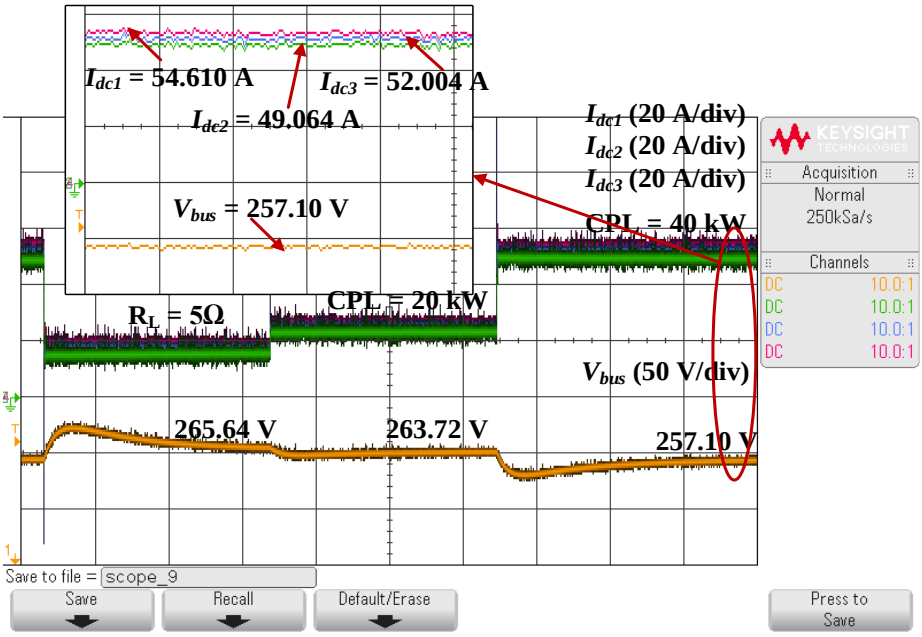


Figure 7.26 HIL experimental results for power sharing and bus voltage regulation using the conventional droop control method.

It can therefore be said that, unlike the conventional droop controller, our proposed control strategy can achieve both accurate power sharing and bus voltage restoration simultaneously. Besides, compared to the conventional fixed and identical droop coefficient, the obtained optimal droop coefficient settings using the proposed design strategy can enhance the current sharing performance of the droop control at the PC level as shown in Figure 7.24 (a).

7.4.4 Fault Scenario

The robustness of the proposed approach under a source fault condition is demonstrated in the HIL experiment. The optimal coefficient settings from design example 1 are used here. A CPL of 25 kW is used in the HIL experiment and the SC is also implemented. The HIL experimental result is shown in Figure 7.27. As shown in Figure 7.27, it can be observed that the three parallel-connected converters are initially operating together and shared the load current equally as desired. Furthermore, the bus voltage is regulated at its reference value of 270 V. When *PMSG-AR*$_2$ is disconnected from the system (assumed to be under fault), the current demand is shared equally as desired by the two remaining converters after the loss of converter 2. However, the bus voltage experienced a little drop to about 266.07 V during the fault duration (representing a voltage drop of 1.42% of the nominal bus value). However, immediately after the optimal compensation coefficient k_{copt} is updated (new k_{copt} = 1/7.9649)

based on the EPS condition, the bus voltage is restored to its nominal value. Hence, this demonstrates the robustness and good fault tolerance capability of the proposed approach.

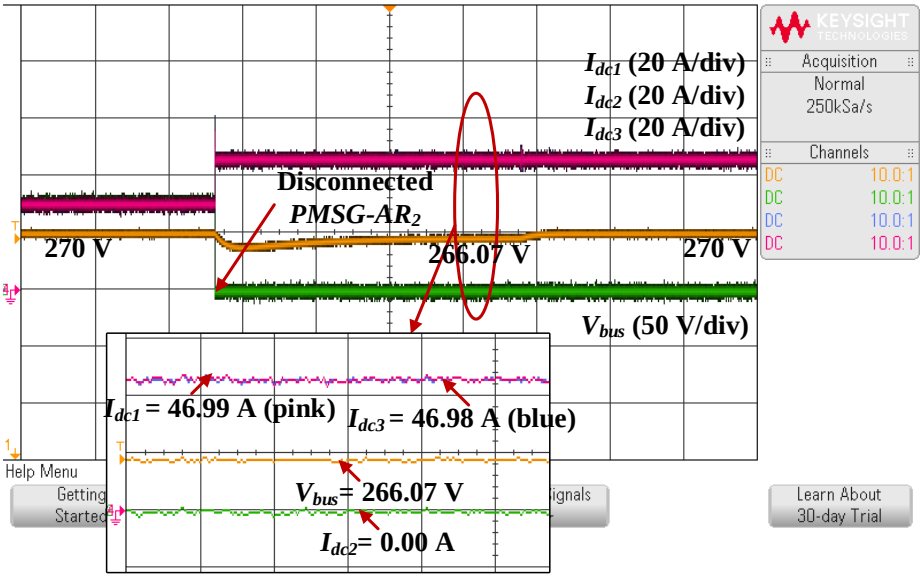


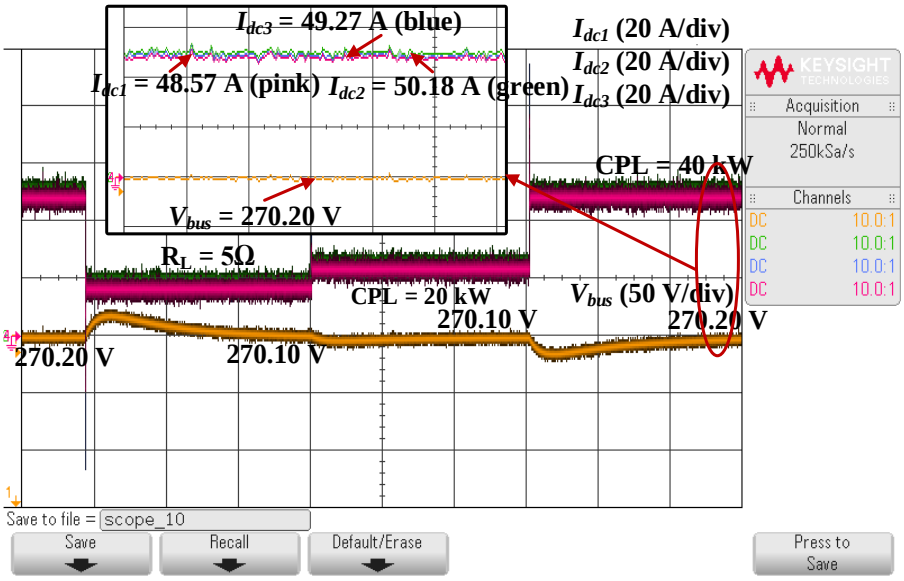
Figure 7.27 HIL experimental results for fault scenario with equal current sharing and voltage regulation using the proposed approach.

7.4.5 Parameter Uncertainty

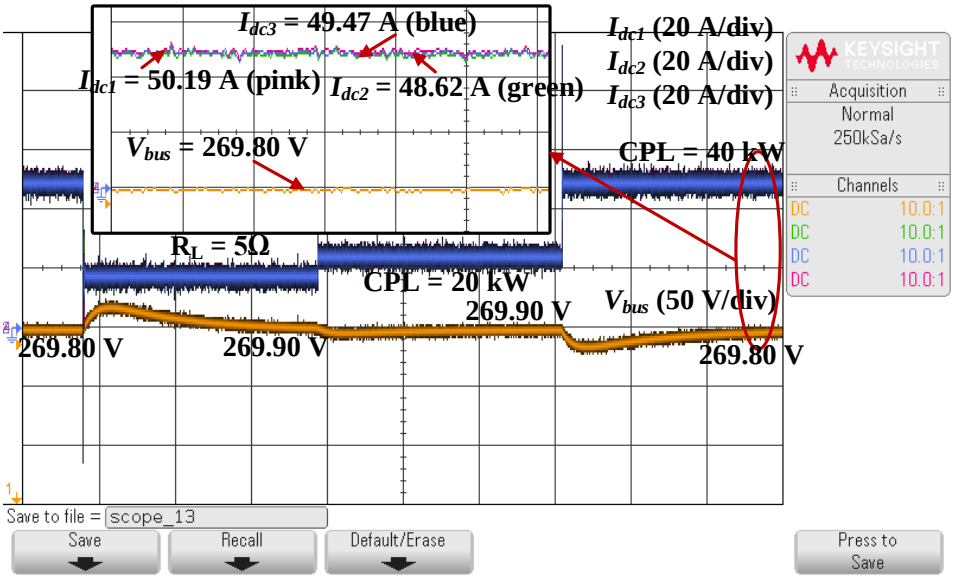
In this case study, the robustness of the proposed control approach to parameter changes in the power system is assessed, this is particularly important when there are no parameter estimation algorithms to adapt to the changes. Some of the parameters that could change during the system operation due to operating temperature or other factors include the cable impedance (i.e., L_{ci} and R_{ci}), DC-link capacitance C_b, stator winding inductance and resistance (i.e., $L_{d,q}$ and R_s) and the machine flux, ψ_m. However, we are only going to assess the variation in the cable impedance and DC-link capacitance. The optimal coefficient settings from design example 1 are used in this case study (see Section 5.4).

To demonstrate the variation in the cable impedance in the HIL experiment, the conductor's parasitic inductance and resistance are varied by - 30% and 30% of their nominal values shown in Table 3-1. The HIL experimental result is shown in Figure 7.28 (a) and (b) respectively. Based on the output current of the converters and voltage regulation shown in Figure 7.28 (a), the computed current sharing ratios and normalised bus voltage are n_1 = 1.033, n_2 = 1.014, and V_{bcn} = 1.00074 respectively. These correspond to 3.30%, and 1.40% deviations of the current

sharing ratios from the desired value. The bus voltage deviation from its nominal value is only 0.074%.



(a)

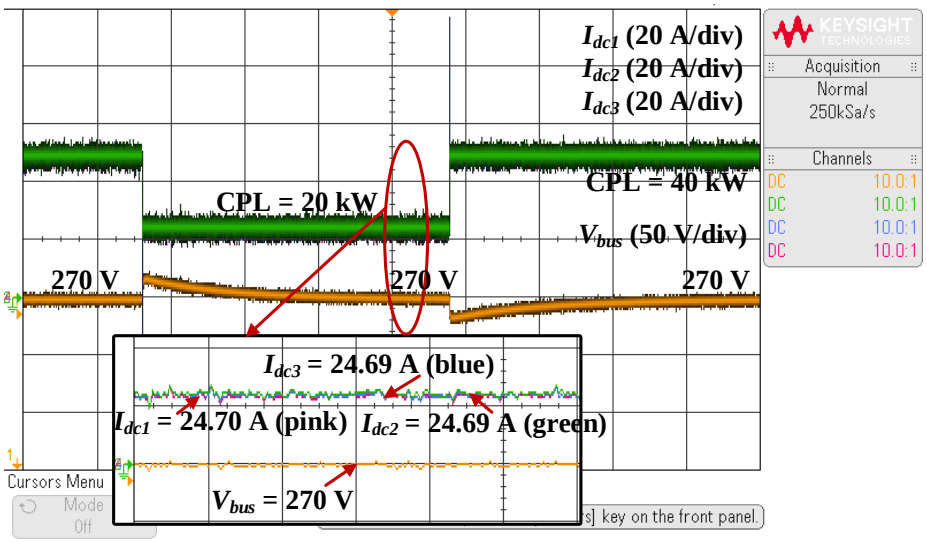


(b)

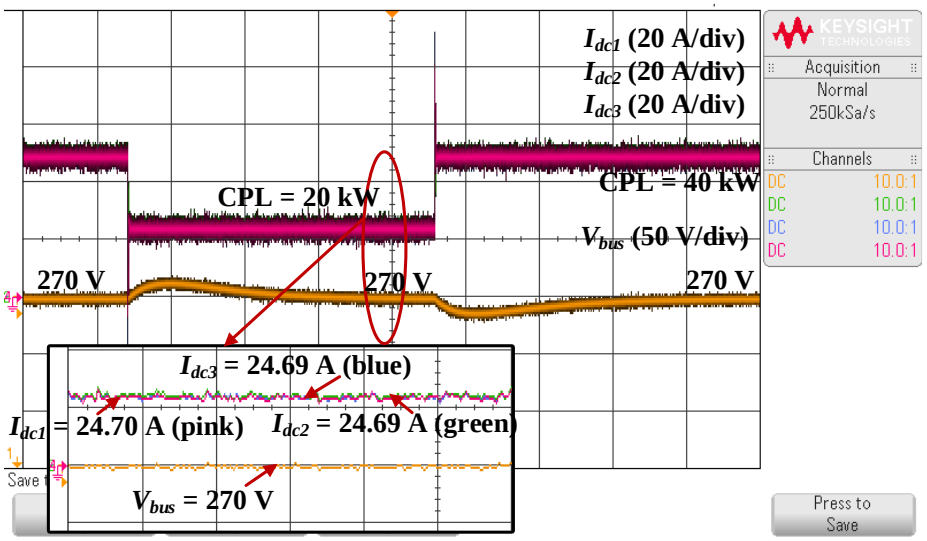
Figure 7.28 HIL experimental results for load sharing and bus voltage compensation using the proposed control method, a response to (a) a 30% decrease in the cable parameters and (b) a 30% increase in the cable parameters.

Similarly, based on the output current of the converters and voltage regulation shown in Figure 7.28 (b), the computed current sharing ratios and normalised bus voltage are n_1 = 0.9687, n_2 = 0.9857, and V_{bcn} = 0.9993 respectively. These correspond to 3.13%, and 1.43% deviations of

the current sharing ratios from the desired value. The bus voltage deviation from its nominal value is only 0.074%.



(a)

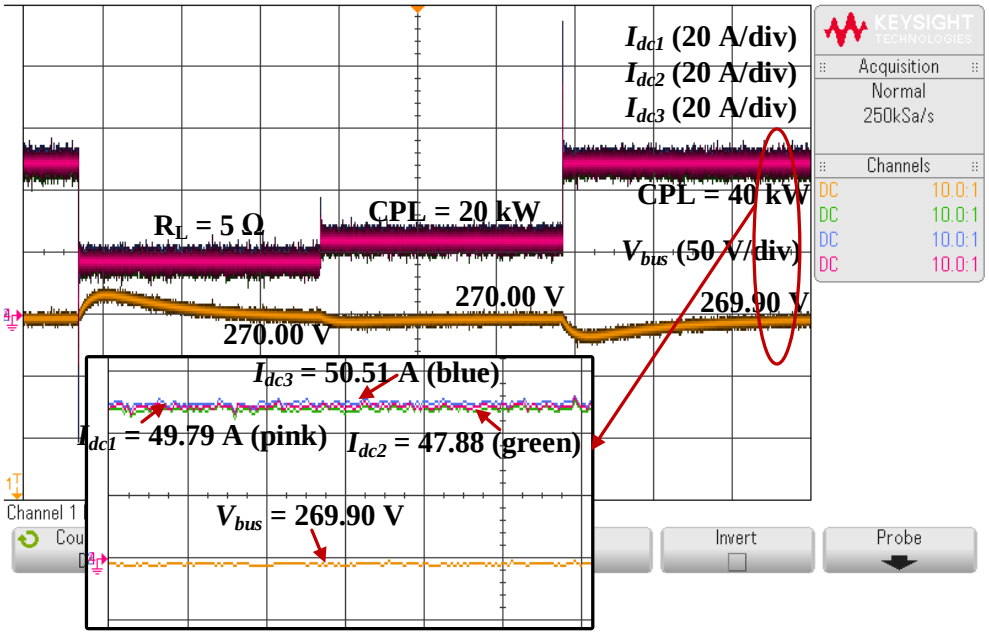


(b)

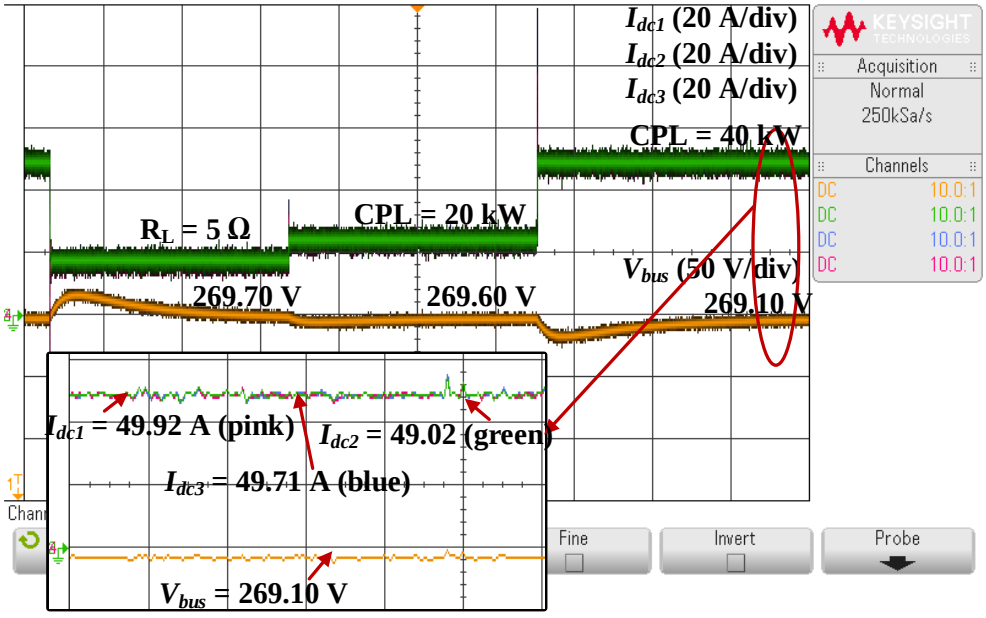
Figure 7.29 HIL experimental results for load sharing and bus voltage compensation using the proposed control method, a response to (a) a 30% decrease in the dc-link capacitance and (b) a 30% increase in the dc-link capacitance.

Though the deviation in the interconnecting cable impedance from their nominal value affects the designed and desired control performance as shown in Figure 7.28 (a) and (b), it is observed that the proposed control method is still able to guarantee a significant reduction in the power

sharing error and maintain the bus voltage near its nominal value despite the variation in the line impedance. Thus, the proposed approach can be said to be robust to a variation in the interconnecting cable impedance.



(a)



(b)

Figure 7.30 HIL experimental results for current sharing and bus voltage compensation. The response to a +/- 30% variation is shown for both (a) the proposed method and (b) the method described in [94].

Also, the dc-link capacitance C_b is varied by - 30% and 30% of its nominal value shown in Table 3-1. The 30% decrease and increase in the dc-link capacitance did not affect the designed and desired control performance of the proposed control approach as shown in Figure 7.29 (a) and (b) respectively. The 30% reduction in the dc-link capacitance mainly causes some small oscillations in the output current of the converters as shown in Figure 7.29 (a), however, the control is still stable. Based on the results shown in Figure 7.28 and Figure 7.29, it can be said that the proposed control approach is robust and will perform well under system parameter uncertainty.

7.4.6 Comparison with the method in [94] under Parameter Uncertainty

In this case study, the steady-state control performance of the proposed method is further validated and compared to the approach proposed in [94] under parameter uncertainty by considering opposite changes to the parameters in the different cables. To that end, the line impedance parameters in cables 1 and 3 are decreased by 30% while the line impedance in cable 2 is increased by 30%. In the proposed control scheme, the droop and compensation coefficients obtained from design example 1 are used (i.e., k_{d1opt} = 1/4.0305, k_{d2opt} = 1/4.5211, k_{d3opt} = 1/4.2342, and k_{copt} = 1/11.9501). For the scheme described in [94], the parameters are $k_{d1} = k_{d2} = k_{d3} = 2$, and $k_c = 2/3$. The HIL experimental results are shown in Figure 7.30.

Based on the output current of the converters and voltage regulation shown in Figure 7.30 (a), the computed current sharing ratios and normalised bus voltage are n_1 = 0.9616, n_2 = 1.0145, and V_{bcn} = 0.9996 respectively for our proposed method. These values correspond to a deviation of 3.84% and 1.45% in the current sharing ratios from the desired value. Furthermore, the bus voltage deviation from its nominal value is merely 0.037%. On the other hand, according to the output current of the converters and voltage regulation depicted in Figure 7.30 (b), the calculated current sharing ratios and normalised bus voltage for the method proposed in [94] are as follows: n_1 = 0.9820, n_2 = 0.9958, and V_{bcn} = 0.9967, respectively. These values indicate that there is a deviation of 1.80% and 0.42% in the current sharing ratios from the desired value. Additionally, the bus voltage shows a deviation of only 0.33% from its nominal value.

Based on the presented results, it is evident that both approaches are influenced by variations in the line impedance parameter, affecting their control performance. The approach proposed in [94], which involves setting high droop gains for the converters, as expected demonstrates

better adaptability to changes in the line impedance parameter in terms of current sharing. However, our detailed case study comparison between the proposed method and the approach in [94] (see case 2 Section 5.4.2) reveals that employing large droop gains at the PC level has certain drawbacks. One of the drawbacks is inadequate voltage regulation, particularly noticeable during secondary control failure and under source fault conditions. Such scenarios can result in unstable voltage levels, which are unfavourable for practical applications, especially for loads onboard the MEA. Furthermore, setting large droop gains can lead to increased interconnecting cable losses under such scenarios due to the voltage drops, reducing the overall system efficiency. In contrast, the proposed approach offers a combination of satisfactory power sharing and improved voltage regulation performance across various operating conditions of the EPS. This capability to maintain acceptable power sharing while ensuring stable voltage regulation represents a significant contribution to the proposed control method.

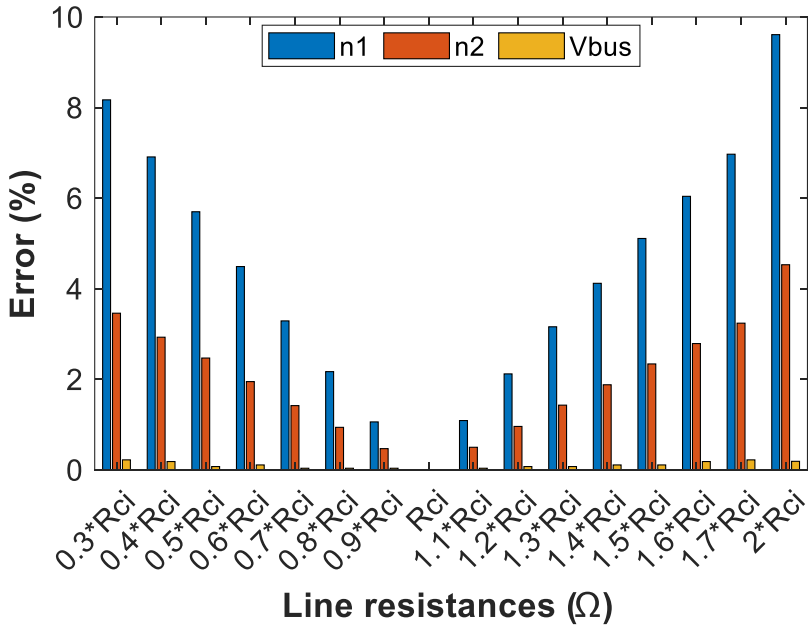


Figure 7.31 Summary of the deviations in control performance resulting from the variations between the line resistances used in data generation and the HIL setup.

7.4.7 Analysis of the impact of variation between simulation and HIL parameters

The purpose of this case study is to analyse the impact of parameter variations between the simulation model used for generating training data and the HIL experimental setup on the control performance. It aims to determine the acceptable differences in parameters while maintaining satisfactory control performance. Additionally, practical conditions may not perfectly align with the training data, leading to discrepancies between expected and actual performance. While the system comprises multiple parameters, this analysis specifically focuses on the variation in interconnecting cable resistance. The line resistance is considered the primary parameter influencing the control performance of the system [161].

In this case study, we examine various adjustments to the line resistance parameters in the HIL experiment. These adjustments involve different percentages of variation, such as -/+ 10%, -/+ 20%, -/+ 30%, and so on. Each percentage corresponds to a specific range of values, for example, 0.9/1.1, 0.8/1.2, and 0.7/1.3, respectively, relative to the line resistance values used in the simulation model for generating the training data (referred to as R_{ci} in Table 3-1). To illustrate this concept, refer to Figure 7.31, which provides a visual representation of how the different variations relate to the line resistance values employed in the simulation model. By considering these variations, we can assess the impact of changes in line resistance on the system's performance and evaluate the robustness of the proposed approach.

As depicted in Figure 7.31, if the line resistance values used in the simulation model for generating the training data match those in the HIL experiment, the desired and designed control performance is achieved with perfect accuracy. Furthermore, it is important to acknowledge that changes in the interconnecting cable resistance can have an impact on the distribution of current among the various sources. These changes lead to deviations from the intended current sharing ratios. It is worth noting that the observed deviations in the current sharing ratios are within tolerable limits [161], being around 5% for n_1 and below 3% for n_2, for a variation of up to -/+ 50%. As shown in Figure 7.31, for a variation beyond -/+ 50%, the steady-state control performance becomes deteriorated, especially for the current ratio n_1. Nevertheless, across the examined variations, the maximum deviation in the current sharing ratios is less than 10% for n_1 and less than 5% for n_2, for a 200% variation in the cable resistance

parameter. On the other hand, the bus voltage is well-regulated despite the different variations in the line resistance.

7.5 HIL Experimental Real-time Line Resistance Identification Using AI

The proposed approach is further validated using C-HIL experiments. The typhoon HIL real-time emulator platform and the TMS320F28379D DSP control card from Texas Instrument (TI) are used in the C-HIL set-up as shown in Figure 7.1 (a). To that end, the power stage which includes the PMSGs, converters and interconnecting cable impedance is emulated by the HIL-604 device in real-time and with ultra-high fidelity. Specifically, the interconnecting cable resistances that link the parallel-connected PMSG-AR systems to the main bus are emulated using fixed resistors [214]. In the C-HIL set-up, the proposed control algorithm (shown in Figure 6.7) which is realized in the DSP controller is used to control the emulated power stage by Typhon (HIL-604) device. The compiled C code of the ANN model operates on the on the typhoon HIL's ARM (ARM Cortex A9) real-time processor. The parameters used in the C-HIL experiments are the same as those used for the simulation, as shown in Table 6-1.

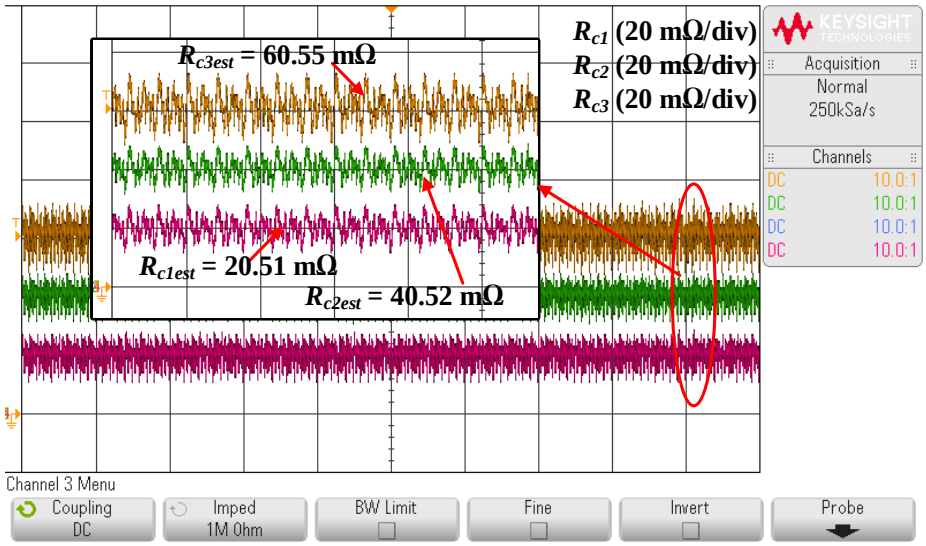


Figure 7.32 HIL experimental result of the online estimation of the initial line resistances.

7.5.1 Validation of the Online Initial Line Resistance identification

To verify the effectiveness of the proposed initial line resistance estimation, a steady-state HIL experiment has been carried out. Figure 7.32 shows the online HIL experimental results of the estimated initial line resistances after implementing equations (6-5), (6-6) and (6-7) in the

controller. As shown in Figure 7.32, it can be observed that the identified line resistances are stable around their nominal values shown in Table 6-1 and the estimation error is less than 3%. Through this HIL experiment, it can be said that the proposed method can accurately estimate the initial line resistances.

7.5.2 Validation of the Accuracy of the Identification Model

The estimation accuracy of the developed identification model for different line resistance values is further validated in the HIL experiment. To achieve this goal, a set of randomly chosen resistor values are used in the HIL test. At the end of each test case, the corresponding current sharing ratios between the converters (n_1 and n_2) are automatically computed and given as input to the identification model. A comparison between the model's estimation (denoted as est.) is shown in Figure 7.33. The corresponding errors in the identification model's estimation are shown in Figure 7.34, which are less than 1%. Thus, it can be said that the developed identification model is effective in the online identification of line resistances. Furthermore, this shows the high level of accuracy in estimation and robustness of the identification model against variation in the line resistance.

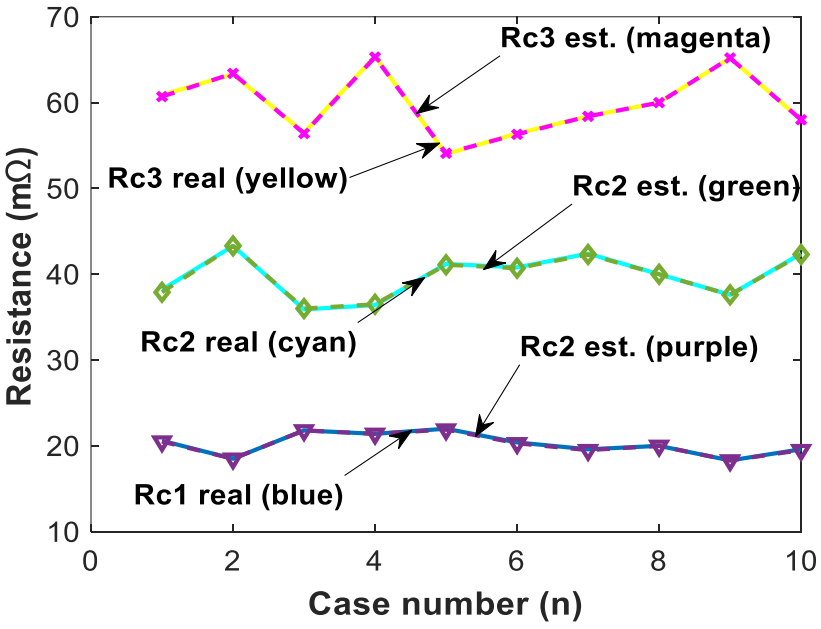


Figure 7.33 Comparison between emulated line resistance and identification model estimation.

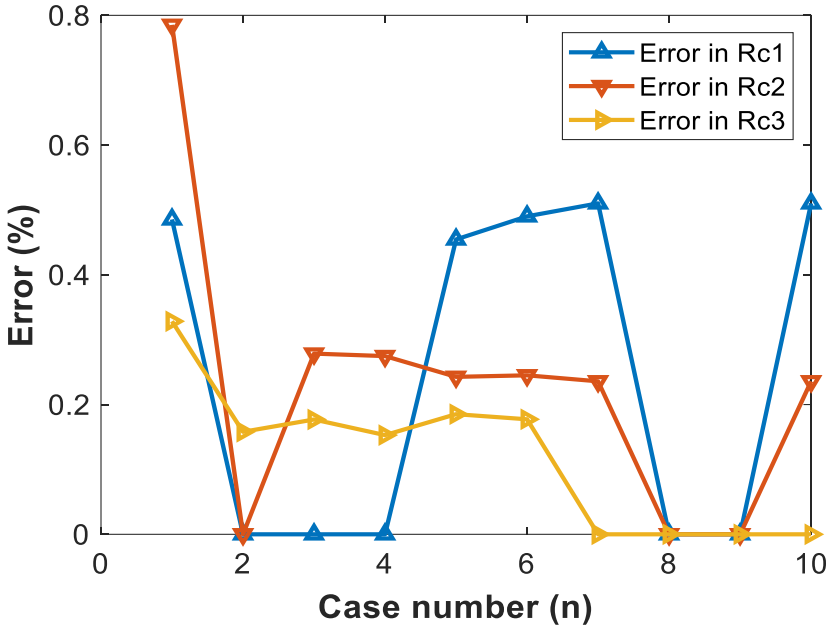


Figure 7.34 Percentage error in the estimation of the emulated line resistances.

7.5.3 Load Current Sharing

In this HIL experimental test case, the converters are assumed to have the same rating and thus are expected to share the load current demand equally. The HIL experimental parameters are as shown in Table 6-1, except for the line resistances which were varied from their nominal values shown in Table 6-1 as follows: R_{c1} = 19 mΩ, R_{c2} = 44 mΩ, and R_{c3} = 63 mΩ. As expected, the load current sharing is unequal (as shown in Figure 7.35) while using the optimal droop gain settings obtained from ANN_1 due to the variation of the line resistances from their nominal values.

When the proposed control strategy is activated, the converters shared the load current demand equally among themselves as shown in Figure 7.35. The estimated line resistances by the identification model are shown in Figure 7.36. It can be observed that the estimated line resistances by the identification model matched excellently well with the emulated line resistances in the HIL experiment. The equal load current sharing is maintained even when the load changes. Also, the bus voltage is well-regulated and within the acceptable range under the proposed control method.

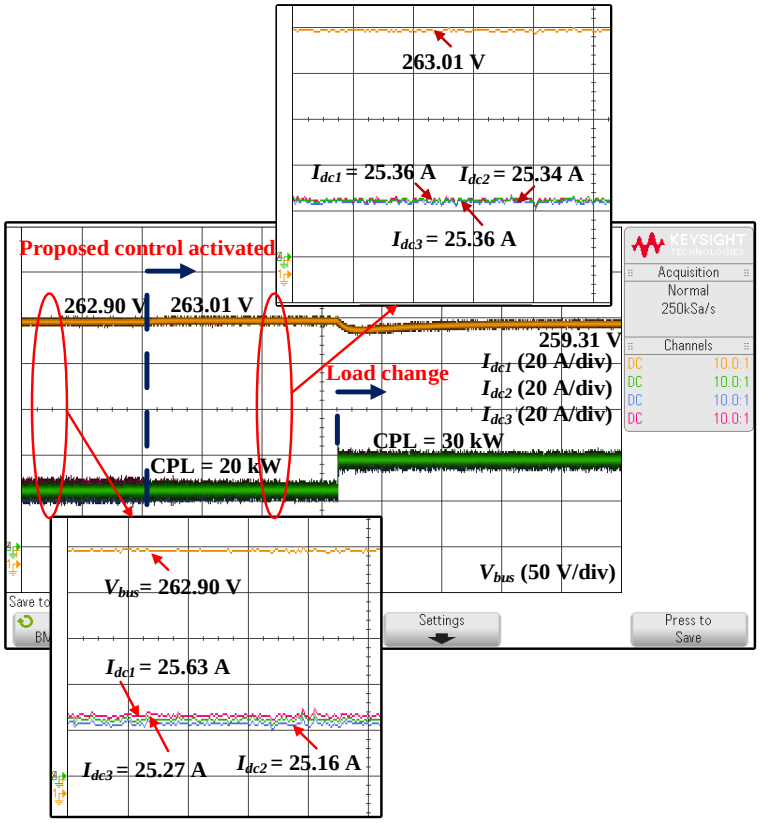


Figure 7.35 HIL experimental result of load current sharing and bus voltage regulation while using the optimal droop gain settings and under the proposed control approach.

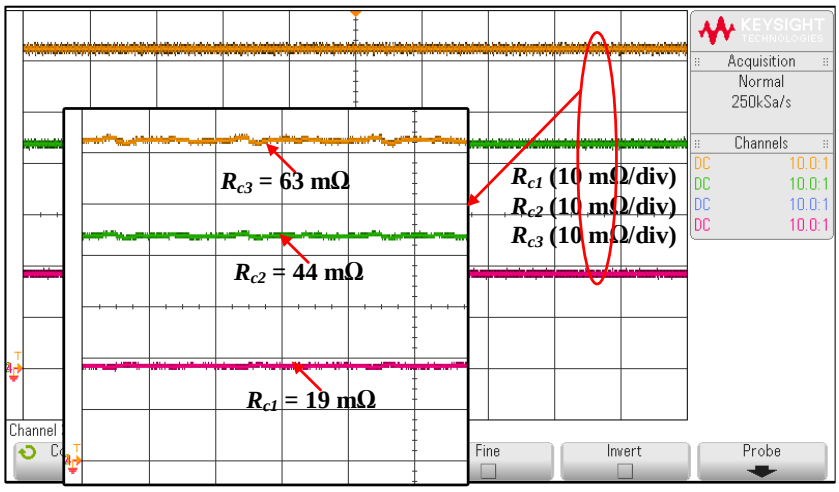


Figure 7.36 HIL experimental result of the online estimation of the line resistances by the identification model.

7.5.4 Fault Scenario

In this case study, the reliability and effectiveness of the proposed control strategy are demonstrated under a source fault condition. As shown in Figure 7.37, the load current demand is shared equally between converters 1 and 2 after the disconnection of the *PMSG-AR*$_3$ (assumed to be under fault) from the system under the proposed control strategy. This is achievable due to the utilisation of pre-estimated line resistance values by the local controller of each converter, eliminating the need for readjusting these values in the event of a source failure. As a result, the proposed control strategy offers the additional benefit of ensuring reliability during abnormal operating conditions.

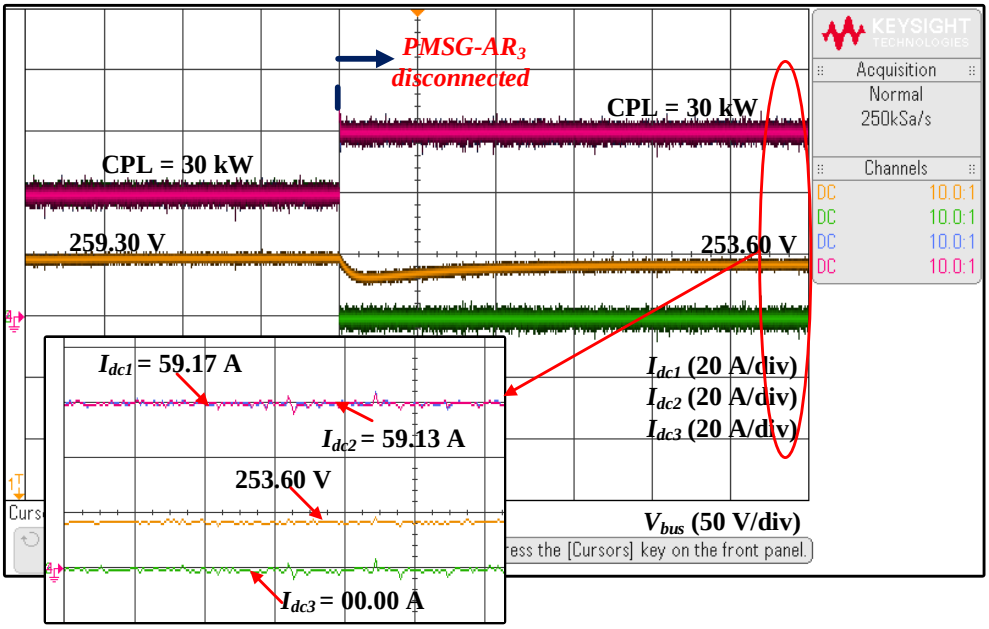


Figure 7.37 HIL experimental result of load current sharing and bus voltage regulation under a generator failure.

A comparison between the proposed control method with the existing control techniques involving online impedance estimation is summarised in Table 7-2, which highlights the benefits of the proposed approach.

Table 7-2 Comparison between proposed control strategy and different techniques for online line resistance identification.

Ref.	Identification technique used	No. of measured quantities used for identification	Accuracy of parameter identification	Current sharing accuracy	Control complexity
[206], [220]	RLS algorithm	3	Medium	Medium	High
[170]	Active pulse disturbance injection	3	Low	Low	Medium
[Proposed]	Data-driven	1	High	High	Low

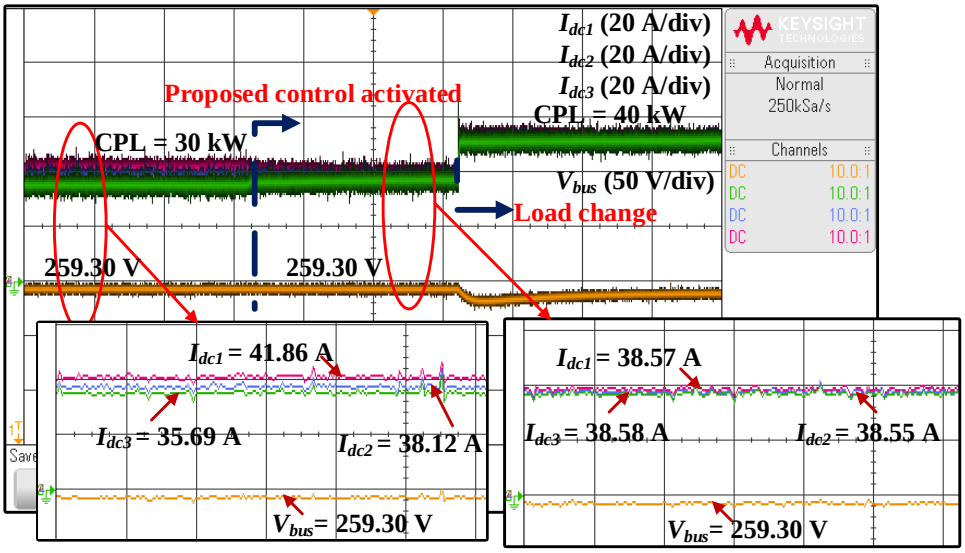


Figure 7.38 Experimental result of load current sharing and bus voltage regulation using the traditional fixed and identical droop gain.

7.5.5 Comparison with Conventional Droop Control

In this case study, the performance of the proposed control strategy is compared with the conventional droop control method using fixed and identical droop gains shown in Table 6-1. The droop gains were obtained using the conventional droop gain design in in (3-2). The HIL experimental result is shown in Figure 7.38. As shown in Figure 7.38., this method fails to

achieve accurate current sharing among the converters due to the mismatch in the interconnecting cable resistances. In contrast, the proposed control method as shown in Figure 7.38 exhibits superior performance in terms of current sharing compared to the conventional droop control approach.

7.6 Summary

This chapter focused on the HIL experimental validation of the theoretical results obtained from the previous chapters. It provided an overview of the HIL setup and presented the HIL experimental results used to validate various proposed approaches. The key experimental findings can be summarized as follows:

- ✓ The offline computed optimal droop gain settings have been validated in the HIL experiment, and the results demonstrate their capability to enhance the performance of the traditional droop control method.
- ✓ The real-time tuning of the optimal droop gain settings allows the controller to quickly adapt to any reference changes.
- ✓ The hierarchical control design of optimal droop and voltage compensation coefficients enhances bus voltage regulation and dynamic performance in various MEA EPS operation conditions while simultaneously achieving optimal load power sharing among power sources compared to state-of-the-art methods.
- ✓ This real-time line resistance identification technique provides a data-driven solution that eliminates the need for system perturbations, paving the way for improved control performance and stability in the MEA EPS distribution network.

In summary, the experimental results presented in this chapter have validated all the theoretical findings of this thesis.

Chapter 8 Conclusion and Future Work

8.1 Conclusion and Discussion

The research presented in this thesis focuses on the application of AI techniques for parameter identification and control design in the DC MG of the More Electric Aircraft (MEA). The primary goal of the study was to enhance the performance, reliability, and efficiency of the MEA's electrical power system (EPS) through intelligent and efficient computing methods. In the earlier chapters, a comprehensive review of the conventional droop control method was provided, highlighting its limitations in achieving accurate load sharing and voltage regulation. The impact of unequal interconnecting cable resistance and droop gains on current sharing among converters was discussed, emphasising the need for improved control strategies. The main contributions brought by the proposed AI-based methodologies are highlighted as follows:

- The use of ANN optimisation-based design for selecting the optimal droop coefficient settings for the droop control of parallel-connected converter is a new approach not previously explored in the literature.
- The development and validation of a real-time method for online tuning of the optimal droop gain settings for the droop control of parallel-connected converters, addressing power-sharing and bus voltage control effectively.
- The development of a new neural network-based design strategy for hierarchical control design to ensure accurate power sharing and improved bus voltage regulation in different EPS operating conditions.
- The development and implementation of an online initial line resistance estimation algorithm in the MG controller, the use of an ANN-based identification model for real-time line resistance estimation during EPS operation, and the achievement of accurate current sharing and improved voltage regulation in steady-state and transient conditions.

In Chapter 3, a new design strategy for the selection of the optimal droop gain for the control of power converters in a MEA EPS multi-source DC grid. The surrogate model is trained

offline by using data obtained from the traditional droop control method. The effectiveness of the proposed approach was demonstrated using a detailed simulation model of the studied system and with a C-HIL-based experiment. The C-HIL experimental results show that the proposed approach can enhance the current sharing and voltage regulation performance of the traditional droop control method compared to the conventional droop gain design. Furthermore, the surrogate model predictions matched excellently well with the results from the simulation and HIL experiment and the selected optimal droop coefficient settings are robust to transient conditions and parameter uncertainty.

In Chapter 4, a new and efficient method for computing optimal droop gain settings in the droop control of parallel-connected converters is presented. By utilising reverse data training of an ANN, the proposed approach enables real-time determination of droop gain settings based on power sharing and voltage regulation references. This method overcomes the complexities and time-consuming aspects of traditional heuristic and ANN optimisation-based approaches, providing a fast and practical solution for online tuning of optimal droop gains. The experimental validation using the C-HIL approach confirms the effectiveness and superiority of the proposed design approach compared to ANN optimisation-based methods, demonstrating its simplicity, flexibility, and low computational burden.

In Chapter 5, a new design strategy for optimising power sharing and bus voltage compensation coefficients in the islanded DC MG of the MEA EPS is investigated. The approach utilises an ANN-based surrogate model to compute the optimal droop and bus voltage compensation settings. Simulation and C-HIL experimental results demonstrate that the proposed approach outperforms the method proposed in [94], achieving superior power sharing and bus voltage regulation performance under various EPS conditions. Moreover, the implementation of the proposed approach does not require additional digital communication lines and controllers, making it an efficient and practical solution for enhancing the performance of the MEA EPS distribution network.

In Chapter 6, a control strategy to enhance power sharing in the islanded DC MG of the MEA by incorporating real-time estimated line resistances using an ANN-based model is presented. The proposed strategy effectively compensates for terminal voltage deviations, eliminating the impact of line resistances and achieving proportional load sharing and improved bus voltage regulation among parallel-connected converters. Additionally, the data-driven solution for line

resistance identification prevents the injection of perturbations into the system. The simulations and HIL-based experimental results validate the effectiveness of the proposed method, demonstrating remarkable accuracy in identifying interconnecting cable resistance parameters with at least 99% accuracy.

Chapter 7 provides an overview of the C-HIL setup and presents HIL experimental results for the validation of various proposed approaches. The validation includes the optimal droop control design using ANN (Chapter 3), the real-time tuning of optimal droop gain settings on a hardware control platform (Chapter 4), the hierarchical control design for enhanced bus voltage regulation under different EPS operating conditions (Chapter 5), and the real-time estimation of line resistances using ANN-model to improve droop control performance (Chapter 6).

8.2 Future Work

This research thesis has explored the application of AI techniques for parameter identification and control design in the DC MG of More Electric Aircraft (MEA) EPS. Based on the theories and results presented in this thesis, several promising areas for future research can be considered, which are listed as follows:

1. Due to the real-time implementation of the ANN on a control hardware platform, one potential avenue for future research could involve utilising the presented approach to create a pre-trained ANN-based surrogate model, which can then be fine-tuned and adapted using online learning techniques. This approach has the potential to accelerate and simplify the process of online training, making it more efficient and effective.
2. Based on the proposed approach for real-time estimation of line resistances, a possible future research direction would be stability analysis based on the identified line resistances.
3. A compelling future research direction lies in exploring the coordinated control and integration of an Energy Storage System (ESS) within the MEA EPS. The incorporation of an ESS offers numerous advantages, such as reducing generator ratings, improving the dynamic performance of the main DC bus voltage, providing backup electrical power supply, and enabling power flow control, including peak shaving to meet load demand [251]. To achieve efficient power management and balance between main

generators and ESS, the development of a coordinated control strategy is essential. This strategy should enable the ESS to operate in discharging mode when load power demand exceeds generator capacity, effectively supplying power to meet the load demand. Additionally, determining the optimal droop gain settings of the interfacing converters for these sources under varying operating conditions would further enhance power sharing and control efficiency.

Appendix A List of Publications

The findings and research outcomes of the Ph.D. study have been disseminated through various channels, including journal papers and conference presentations. The list provided below comprises papers that have already been published and presented at conferences and those currently under review for publication in journals.

Refereed Journal Papers

[J1] **H. Hussaini**, T. Yang, Y. Gao, C. Wang, M. Urrutia and S. Bozhko, "Optimal Droop Control Design Using Artificial Intelligent Techniques for Electric Power Systems of More-Electric Aircraft," *IEEE Transactions on Transportation Electrification*, 03 May 2023, doi: 10.1109/TTE.2023.3271763.

[J3] **H. Hussaini**, T. Yang, G. Bai, M. Urrutia and S. Bozhko, "A Low-Complexity Artificial Neural Network Based Optimal Droop Gain Design Strategy for DC Microgrids of More Electric Aircraft", in *IEEE Transactions on Transportation Electrification,* **accepted (02-Nov-2023).**

[J3] **H. Hussaini**, T. Yang, G. Bai, M. Urrutia and S. Bozhko, "Artificial Intelligence-Based Hierarchical Control Design for Current Sharing and Voltage Restoration in DC Microgrid of More Electric Aircraft", in *IEEE Transactions on Transportation Electrification,* 03 July 2023, doi: 10.1109/TTE.2023.3289773.

[J4] **H. Hussaini**, T. Yang, G. Bai, M. Urrutia and S. Bozhko, "Real-time Line Resistance Identification with Artificial Intelligence for Accurate Current Sharing and Improved Voltage Regulation in DC Microgrids", *in IEEE Transactions on Transportation Electrification,* **under review.**

Refereed Conference Papers

[C1] **H. Hussaini**, T. Yang, C. Wang, and S. Bozhko, "An Enhanced and Cost Saving Droop Control Method for Improved Load Sharing for the MEA Application," *2021 IEEE Transportation Electrification Conference & Expo (ITEC)*, 2021, pp. 84-89.

[C2] **H. Hussaini**, T. Yang, Y. Gao, C. Wang, M. A. A. Mohamed, and S. Bozhko, "Artificial Neural Network Aided Cable Resistance Estimation in Droop-Controlled Islanded DC Microgrids," *IECON 2021 – 47th Annual Conference of the IEEE Industrial Electronics Society*, 2021, pp. 1-7.

[C3] **H. Hussaini**, T. Yang, Y. Gao, C. Wang, T. Dragicevic, and S. Bozhko, "Droop Coefficient Design in Droop Control of Power Converters for Improved Load Sharing: An Artificial Neural Network Approach," *2021 IEEE 30th International Symposium on Industrial Electronics (ISIE)*, 2021, pp. 1-6.

[C4] **H. Hussaini**, T. Yang, Y. Gao, C. Wang, G. Bai, and S. Bozhko, "Droop Coefficient Design and Optimisation Using Genetic Algorithm-A Case Study of the More Electric Aircraft DC Microgrid," *IECON 2022 – 48th Annual Conference of the IEEE Industrial Electronics Society*, 2022, pp. 1-6.

[C5] **H. Hussaini** *et al*., "Accurate Line Resistance Estimation in a Multi-source Electrical Power System of the More Electric Aircraft: An Intelligent and Data-Driven Approach," *2022 IEEE Transportation Electrification Conference & Expo (ITEC)*, 2022, pp. 1254-1258.

[C6] **H. Hussaini**, T. Yang, C. Wang, and S. Bozhko, "An Enhanced Droop Control Method for Multi-source Electric Power System of More Electric Aircraft", *MEA2021 More Electric Aircraft*, 2021, pp. 1-6.

The following articles were published during the PhD; however, they have not been included in the current thesis.

[J5] C. Wang, T. Yang, **H. Hussaini**, Z. Huang and S. Bozhko, "Power Quality Improvement Using an Active Power Sharing Scheme in More Electric Aircraft," in *IEEE Transactions on Industrial Electronics*, vol. 69, no. 4, pp. 3588-3598, April 2022, doi: 10.1109/TIE.2021.3076401.

[J6] C. Wang, T. Yang, **H. Hussaini** and S. Bozhko, "Using DC–DC Converters as Active Harmonic Suppression Device for More Electric Aircraft Applications," in *IEEE Transactions on Industrial Electronics*, vol. 69, no. 7, pp. 6508-6518, July 2022, doi: 10.1109/TIE.2021.3099239.

Appendix B Reference Frame Transformation

Three-phase quantities represented in the *abc* frame can be transformed into a two-axis frame (*dq* frame) rotating at a synchronous speed denoted by ω. This transformation is known as the *dq* transformation. If the d-axis is aligned with phase a (*vd* = *va*) as the reference point for both frames (θ=0), then:

$$\begin{bmatrix} v_d \\ v_q \end{bmatrix} = k_{dq} \begin{bmatrix} v_a \\ v_b \\ v_c \end{bmatrix} \tag{B-1}$$

The *dq* transformation matrix is defined as:

$$k_{dq} = \frac{2}{3} \begin{bmatrix} \cos(\theta) & \cos\left(\theta - \frac{2\pi}{3}\right) & \cos\left(\theta + \frac{2\pi}{3}\right) \\ -\sin(\theta) & -\sin\left(\theta - \frac{2\pi}{3}\right) & -\sin\left(\theta + \frac{2\pi}{3}\right) \end{bmatrix} \tag{B-1}$$

The diagram of *dq* transformation is shown in Figure B-1

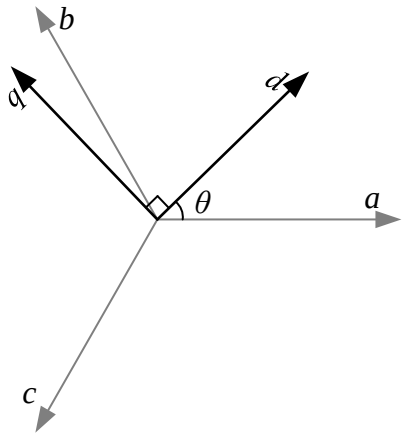


Figure B-1 Three phase and *dq* phasor diagram.

Appendix C Voltage Equations for Stator Windings of a Permanent Magnet Machine in the DQ Frame

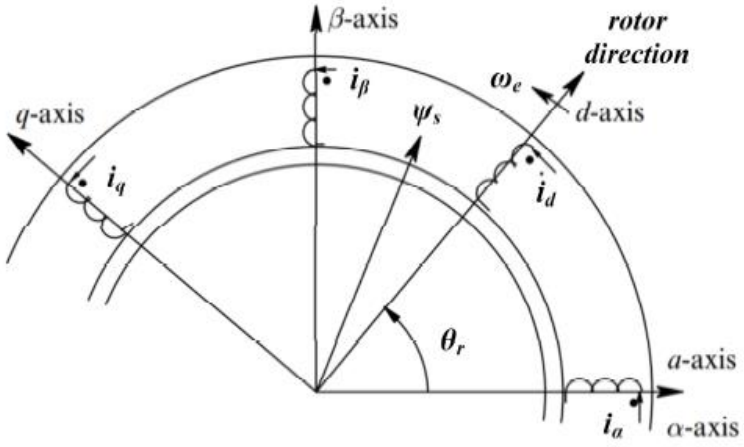


Figure C-1 Stator αβ and *dq* equivalent windings [252]

To calculate the *dq* winding voltages, we will begin by examining a set of orthogonal *αβ* windings attached to the stator, as depicted in Figure C-1. In this configuration, the *α*-axis is aligned with the stator's *a*-axis. In all windings, the positive voltage polarity is indicated at the terminal marked with a dot. When considering the *αβ* windings and their respective variables, we obtain

$$\begin{cases} v_\alpha = R_s i_\alpha + \dfrac{d}{dt}\psi_\alpha \\ v_\beta = R_s i_\beta + \dfrac{d}{dt}\psi_\beta \end{cases} \tag{C-1}$$

Here, v_α and v_β represent the stator winding voltages in the *αβ* frame. Similarly, i_α and i_β denote the stator winding currents in the *αβ* frame, while ψ_α and ψ_β indicate the stator winding flux linkage in the *αβ* frame. Finally, R_s corresponds to the stator winding resistance.

Appendix C Voltage Equations for Stator Windings of a Permanent Magnet Machine in the DQ Frame

The two equations in (C-1) can be merged by multiplying the β-axis voltage equation with the operator j and subsequently adding it to the α-axis voltage equation. As a result, the stator winding voltage can be expressed in space vectors as follows:

$$\vec{v}_{\alpha\beta} = R_s \vec{i}_{\alpha\beta} + \frac{d}{dt}\vec{\psi}_{\alpha\beta} \tag{C-2}$$

where $\vec{v}_{\alpha\beta} = v_\alpha + jv_\beta$ and so on. As shown in Figure C-1, the space vectors of current, voltage, and flux linkage concerning the α-axis are interconnected with those pertaining to the d-axis as follows:

$$\begin{cases} \vec{v}_{\alpha\beta} = \vec{v}_{dq}.e^{j\theta_r} \\ \vec{i}_{\alpha\beta} = \vec{i}_{dq}.e^{j\theta_r} \\ \vec{\psi}_{\alpha\beta} = \vec{\psi}_{dq}.e^{j\theta_r} \end{cases} \tag{C-3}$$

where $\vec{v}_{dq} = v_d + jv_q$ and so on. Substituting (C-3) into (C-2), we obtain

$$\vec{v}_{dq}.e^{j\theta_r} = R_s \vec{i}_{dq}.e^{j\theta_r} + \frac{d}{dt}(\vec{\psi}_{dq}.e^{j\theta_r}) \tag{C-4}$$

Re-arranging C-4, we obtain the expression in (C-5)

$$\vec{v}_{dq}.e^{j\theta_r} = R_s \vec{i}_{dq}.e^{j\theta_r} + \frac{d\vec{\psi}_{dq}}{dt}.e^{j\theta_r} + j\underbrace{\frac{d\theta_r}{dt}}_{\omega_e}.e^{j\theta_r}.\vec{\psi}_{dq} \tag{C-5}$$

Eliminating the common term $e^{j\theta r}$ from both sides in (C-5), the stator winding voltage equations can be reformulated as follows:

$$\vec{v}_{dq} = R_s \vec{i}_{dq} + \frac{d\vec{\psi}_{dq}}{dt} + j\omega_e \vec{\psi}_{dq} \tag{C-6}$$

The flux linkages in the *dq* frame are given as:

$$\begin{cases} \psi_d = L_d i_d + \psi_m \\ \psi_q = L_q i_q \end{cases} \tag{C-7}$$

where L_d and L_q denote the stator inductances in the *dq* frame, respectively, while ψ_m represents the flux linkage in the airgap generated by the permanent magnets mounted on the rotor. By substituting (C-7) into (C-6) and separating the real and imaginary components in (C-6), the stator winding voltage equations of a PMM in the *dq* frame can be derived as follows:

$$\begin{cases} v_d = R_s i_d + L_d \dfrac{di_d}{dt} - \omega_e L_q i_q \\ v_q = R_s i_q + L_q \dfrac{di_q}{dt} + \omega_e L_d i_d + \omega_e \varphi_m \end{cases} \tag{C-8}$$

References

[1] J. Laurence K. Loftin, “The Evolution of Modern Aircraft,” 1985. [Online]. Available: https://www.hq.nasa.gov/pao/History/SP-468/cover.htm. [Accessed 26 October 2023].

[2] “Aerospace,” [Online]. Available: https://www.nottingham.ac.uk/workingwithbusiness/services/aerospace.aspx. [Accessed 26 October 2023].

[3] U.S Energy Information Administration (EIA), “Annual Energy Outlook 2020,” EIA, 2019.

[4] “Climate Action,” European Commision, [Online]. Available: https://climate.ec.europa.eu/eu-action/transport-emissions/reducing-emissions-aviation_en. [Accessed 08 07 2023].

[5] Airbus, “Airbus, Rolls-Royce, and Siemens team up for electric future Partnership launches E-Fan X hybrid-electric flight demonstrator,” [Online]. Available: https://www.airbus.com/en/newsroom/press-releases/2017-11-airbus-rolls-royce-and-siemens-team-up-for-electric-future. [Accessed 26 October 2023].

[6] K. Emadi and M. Ehsani, “Aircraft power systems: technology, state of the art, and future trends,” *IEEE Aerospace and Electronic Systems Magazine,* vol. 15, no. 1, pp. 28-32, 2000.

[7] B. Sarlioglu and C. T. Morris, “More electric aircraft: Review, challenges, and opportunities for commercial transport aircraft,” *IEEE transactions on Transportation Electrification,* vol. 1, no. 1, pp. 54-64, 2015.

References

[8] J. A. Rosero, J. A. Ortega, E. Aldabas and L. A. R. L. Romeral, “Moving towards a more electric aircraft,” *IEEE Aerospace and Electronic Systems Magazine,* vol. 22, no. 3, pp. 3-9, 2007.

[9] P. Wheeler and S. Bozhko, “The more electric aircraft: Technology and challenges,” *IEEE Electrification Magazine,* vol. 2, no. 4, pp. 6-12, 2014.

[10] P. Wheeler, “Technology for the more and all electric aircraft of the future,” in *2016 IEEE International Conference on Automatica (ICA-ACCA) (pp. 1-5). IEEE,* 2016, October.

[11] S. J. Cutts, “A collaborative approach to the more electric aircraft,” in *2002 International Conference on Power Electronics, Machines and Drives (Conf. Publ. No. 487),* Sante Fe, NM, USA, 2002.

[12] V. Madonna, P. Giangrande and M. Galea, “Electrical Power Generation in Aircraft: Review, Challenges, and Opportunities,” *IEEE Transactions on Transportation Electrification,* vol. 4, no. 3, pp. 646-659., 2018.

[13] I. Moir, A. Seabridge and M. Jukes, Civil Avionics Systems 2nd Edition, John Wiley & Sons, 2013, pp. 235-290.

[14] “Clean Aviation,” [Online]. Available: https://www.clean-aviation.eu/. [Accessed 26 October 2023].

[15] M. Sinnett, “787 No-Bleed Systems: Saving Fuel and Enhancing Operational Efficiencies,” 2007. [Online]. Available: https://www.boeing.com/commercial/aeromagazine/articles/qtr_4_07/AERO_Q407_article2.pdf. [Accessed 26 October 2023].

[16] A. Abdel-Hafez, “Power generation and distribution system for a more electric aircraft-A review,” in *Recent advances in aircraft technology,* InTech, 2012, pp. 290-308.

References

[17] Y. Tao, Development of dynamic phasors for the modelling of aircraft electrical power systems, PhD Dissertation, University of Nottingham, 2013.

[18] C. L. Bowman, "Visions of the future: Hybrid electric aircraft propulsion.," AIAA Aircraft Electric/Hybrid-Electric Power & Propulsion Workshop, July 28, 2016. [Online]. Available: https://ntrs.nasa.gov/archive/nasa/casi.ntrs.nasa.gov/20170002633.pdf. [Accessed 7 August 2019].

[19] A. Schwab, A. Thomas, J. Bennett, E. Robertson and S. Cary, "Electrification of Aircraft: Challenges, Barriers, and Potential Impacts (No. NREL/TP-6A20-80220)," National Renewable Energy Lab (NREL), Golden, CO, United States, 2021.

[20] J. A. Weimer, "The role of electric machines and drives in the more electric aircraft," in *IEEE International Electric Machines and Drives Conference. IEMDC'03. (Vol. 1, pp. 11-15). IEEE.,* 2003.

[21] X. Roboam, B. Sareni and A. De Andrade, "More electricity in the air: Toward optimized electrical networks embedded in more-electrical aircraft," *IEEE industrial electronics magazine,* vol. 6, no. 4, pp. 6-17, 2012.

[22] V. C. Cavalcanti and C. R. de Andrade, "A trade-off study of a bleedless and conventional air conditioning systems (No. 2008-36-0001)," *SAE Technical Paper,* 2008.

[23] "More Open Electrical Technologies," [Online]. Available: https://trimis.ec.europa.eu/project/more-open-electrical-technologies. [Accessed 26 October 2023].

[24] L. Faleiro, "Summary of the European power optimised aircraft (POA) project," in *25th International Congress of the Aeronautical Sciences, ICAS (pp. 3-8),* September 2006.

References

[25] S. J. Cutts, “Totally Integrated More Electric Systems (TIMES) Refer to: A Collaborative Approach to the More Electric Aircraft,” in *Power Electronics, Machines and Drives, 2002. International Conference (pp. 223-228).*, 2002.

[26] M. Brunet, S. Aubry and R. Lafage, “The Clean Sky programme: environmental benefits at aircraft level,” in *15th AIAA Aviation Technology, Integration, and Operations Conference (p. 2390).*, 2015.

[27] M. C. Gelhausen, W. Grimme, A. Junior, C. Lois and P. Berster, “Clean Sky 2 Technology Evaluator—Results of the First Air Transport System Level Assessments,” *Aerospace,* vol. 9, no. 204, pp. 1-27, 2022.

[28] F. Gao, Decentralised control and stability analysis of a multi-generator based electrical power system for more electric aircraft, PhD thesis, University of Nottingham, 2016.

[29] J. C. Swierczek, F. Mollet, C. Saudemont, R. Meuret and B. Robyns, “Power management of a regenerative local HVDC aircraft network using supercapacitors,” in *2012 15th International Power Electronics and Motion Control Conference (EPE/PEMC) (pp. LS4a-5). IEEE.*, Novi Sad, Serbia, 2012, September.

[30] E. Commission, “More Open Electrical Technologies,” [Online]. Available: https://cordis.europa.eu/project/id/30861#:~:text=MOET%20is%20a%20consortium%20of,set%20up%20the%20PbW%20standard.. [Accessed 26 October 2023].

[31] X. Lang, T. Yang, C. Li, H. B. Enalou, S. Bozhko and P. Wheeler, “A dual-channel-enhanced power generation architecture with back-to-back converter for MEA application,” *IEEE Transactions on Industry Applications,* vol. 56, no. 3, pp. 3006-3019, 2020.

[32] D. Kumar, F. Zare and A. Ghosh, “DC microgrid technology: system architectures, AC grid interfaces, grounding schemes, power quality, communication networks, applications, and standardizations aspects,” *IEEE Access,* vol. 5, pp. 12230-12256, 2017.

References

[33] H. Kakigano, Y. Miura and T. Ise, “Low-voltage bipolar-type DC microgrid for super high quality distribution,” *IEEE transactions on power electronics,* vol. 25, no. 12, pp. 3066-3075, 2010.

[34] A. Emadi, K. Rajashekara, S. S. Williamson and S. M. Lukic, “Topological overview of hybrid electric and fuel cell vehicular power system architectures and configurations,” *IEEE Transactions on vehicular technology,* vol. 54, no. 3, pp. 763-770, 2005.

[35] F. Gao and S. Bozhko, “Modeling and impedance analysis of a single DC bus-based multiple-source multiple-load electrical power system,” *IEEE Transactions on Transportation Electrification,* vol. 2, no. 3, pp. 335-346, 2016.

[36] T. Dragičević, J. M. Guerrero, J. C. Vasquez and D. Škrlec, “Supervisory control of an adaptive-droop regulated DC microgrid with battery management capability,” *IEEE Transactions on power Electronics,* vol. 29, no. 2, pp. 695-706, Feb. 2014.

[37] F. Chen, R. Burgos, D. Boroyevich, J. C. Vasquez and J. M. Guerrero, “Investigation of nonlinear droop control in DC power distribution systems: Load sharing, voltage regulation, efficiency, and stability,” *IEEE Transactions on Power Electronics,* vol. 34, no. 10, pp. 9404-9421, 2019.

[38] F. Blaabjerg, Z. Chen and S. B. Kjaer, “Power electronics as efficient interface in dispersed power generation systems,” *IEEE transactions on power electronics,* vol. 19, no. 5, pp. 1184-1194, 2004.

[39] T. Dragičević and M. Novak, “Weighting factor design in model predictive control of power electronic converters: An artificial neural network approach,” *IEEE Transactions on Industrial Electronics,* vol. 66, no. 11, pp. 8870-8880, Nov. 2019.

[40] X. Lu, J. M. Guerrero, K. Sun and J. C. Vasquez, “ An improved droop control method for dc microgrids based on low bandwidth communication with dc bus voltage restoration and enhanced current sharing accuracy,” *IEEE Transactions on Power Electronic,* vol. 29, no. 4, pp. 1800-1812, April 2014 .

References

[41] D. E. Olivares, A. Mehrizi-Sani, A. H. Etemadi, C. A. Cañizares, R. Iravani, M. Kazerani and N. D. Hatziargyriou, " Trends in microgrid control," *IEEE Transactions on smart grid,* vol. 5, no. 4, pp. 1905-1919, July 2014.

[42] J. M. Kern and H. L. N. Wiegman, "U.S. Patent No. 7,605,483. Washington, DC: U.S," *Patent and Trademark Office,* 2009.

[43] H. B. Enalou, X. Lang, M. Rashed and S. Bozhko, "Time-scaled emulation of electric power transfer in the more electric engine," *IEEE Transactions on Transportation Electrification,* vol. 6, no. 4, pp. 1679-1694, December 2020.

[44] J. M. Kern and H. L. N. Wiegman, "U.S. Patent No. 7,468,561," in *U.S. Patent and Trademark Office*, Washington, DC, 2008.

[45] G. B. Gharehpetian and S. M. M. Agah, Distributed generation systems: design, operation and grid integration, Butterworth-Heinemann, 2017.

[46] I. Moir and A. Seabridge, Aircraft Systems: Mechanical, electrical, and avionics subsystems integration (Vol. 52), John Wiley & Sons, 2011.

[47] W. K. Boice and L. G. Levoy, "Basic considerations in selection of electric systems for large aircraft," *Electrical Engineering,* vol. 63, no. 6, pp. 279-287, 1944.

[48] T. B. Holliday, "Applications of electric power in aircraft," *Electrical Engineering,* vol. 60, no. 5, pp. 218-225, 1941.

[49] MIL-STD-704F, "Department of Defense Interface Standard. Aircraft Electric Power Characteristics," [Online]. Available: http://everyspec.com/MIL-STD/MIL-STD-0700-0799/MIL-STD-704F_1083/. [Accessed 26 October 2023].

[50] P. E. Gartz, "Commercial systems development in a changed world," *IEEE Transactions on Aerospace and Electronic Systems,* vol. 33, no. 2, pp. 632-636, 1997.

References

[51] J. A. DeSantis, “Engines turn or passengers swim: A case study of how ETOPS improved safety and economics in aviation,” *Journal of Air Law and Commerce,* vol. 78, no. 1, pp. 3-68, 2013.

[52] B. Khandelwal, J. Cronly, I. S. Ahmed, C. J. Wijesinghe and C. Lewis, “The effect of alternative fuels on gaseous and particulate matter (PM) emission performance in an auxiliary power unit (APU),” *The Aeronautical Journal,* vol. 123, no. 1263, pp. 1-19, 2019.

[53] A. Eid, H. El-Kishky, M. Abdel-Salam and T. El-Mohandes, “Modeling and characterization of an aircraft electric power system with a fuel cell-equipped APU paralleled at main AC bus,” in *2010 IEEE International Power Modulator and High Voltage*, 2010, May.

[54] S. S. Yeoh, M. Rashed, M. Sanders and S. Bozhko, “Variable-Voltage Bus Concept for Aircraft Electrical Power System,” *IEEE Transactions on Industrial Electronics,* vol. 66, no. 7, pp. 5634-5643, 2018.

[55] L. Setlak, “Overview of Aircraft Technology solutions compatible with the concept of MEA,” *Czasopismo Techniczne.,* pp. 67-76, 2015.

[56] L. Andrade and C. Tenning, “Design of Boeing 777 electric system,” *IEEE Aerospace and Electronic Systems Magazine,* vol. 7, no. 7, pp. 4-11, 1992.

[57] A. Eid, H. El-Kishky, M. Abdel-Salam and M. T. El-Mohandes, “On power quality of variable-speed constant-frequency aircraft electric power systems,” *IEEE Transactions on Power Delivery,* vol. 25, no. 1, pp. 55-65, 2009.

[58] M. J. Cronin, “Aircraft providing variable and constant electric power.,” *Washington, DC: U.S. U.S. Patent No. 4,587,436. Patent and Trademark Office.,* 1986.

[59] V. V. Vadher, I. R. Smith and S. Williams, “Mathematical modeling of a VSCF aircraft generating system,” *IEEE transactions on aerospace and electronic systems,* Vols. AES-22, no. 5, pp. 573-582, 1986.

References

[60] X. Roboam, “New trends and challenges of electrical networks embedded in “more electrical aircraft”,” in *2011 IEEE International Symposium on Industrial Electronics (pp. 26-31). IEEE,* Gdansk, Poland, 2011, June.

[61] P. W. Wheeler, J. C. Clare, A. Trentin and S. Bozhko, “An overview of the more electrical aircraft,” *Proceedings of the Institution of Mechanical Engineers, Part G: Journal of Aerospace Engineering,* vol. 227, no. 4, pp. 578-585, 2013.

[62] P. W. Wheeler, J. Rodriguez, J. C. Clare, L. Empringham and A. Weinstein, “Matrix converters: A technology review,” *IEEE Transactions on industrial electronics,* vol. 49, no. 2, pp. 276-288, 2002.

[63] P. Wheeler, J. Clare, L. de Lillo, K. Bradley, M. Aten, C. Whitley and G. Towers, “A reliability comparison of a matrix converter and an 18-pulse rectifier for aerospace applications,” in *2006 12th International Power Electronics and Motion Control Conference (pp. 496-500). IEEE.,* 2006, September.

[64] D. Makarov, S. Kharitonov, G. Zinoviev, D. Korobkov and A. Sidorov, “Variable frequency generation system for aircraft,” in *2014 IEEE Energy Conversion Congress and Exposition (ECCE) (pp. 917-922). IEEE,* 2014, September.

[65] M. Olaiya and N. Buchan, “High power variable frequency generator for large civil aircraft,” in *IEE Colloquium on Electrical Machines and Systems for the More Electric Aircraft (Ref. No. 1999/180), pp. 3-1,* November 1999.

[66] B. H. Nya, J. Brombach and D. Schulz, “Benefits of higher voltage levels in aircraft electrical power systems,” in *2012 Electrical Systems for Aircraft, Railway and Ship Propulsion (pp. 1-5). IEEE,* 2012, October.

[67] S. Shoujun, L. Weiguo, D. Peitsch and U. Schaefer, “Detailed design of a high speed switched reluctance starter/generator for more/all electric aircraft,” *Chinese Journal of Aeronautics,* vol. 23, no. 2, pp. 216-226, April 2010.

References

[68] B. S. Bhangu and K. Rajashekara, “Electric starter generators: Their integration into gas turbine engines,” *IEEE Industry Applications Magazine,* vol. 20, no. 2, pp. 14-22, 2013.

[69] Z. Yang, F. Shang, I. P. Brown and M. Krishnamurthy, “Comparative study of interior permanent magnet, induction, and switched reluctance motor drives for EV and HEV applications,” *IEEE Transactions on Transportation Electrification,* vol. 1, no. 3, pp. 245-254, October 2015.

[70] A. Griffo, R. Wrobel, P. H. Mellor and J. M. Yon, “Design and characterization of a three-phase brushless exciter for aircraft starter/generator,” *IEEE Transactions on Industry Applications,* vol. 49, no. 5, pp. 2106-2115, 2013.

[71] M. van der Geest, H. Polinder, J. A. Ferreira and D. Zeilstra, “Machine selection and initial design of an aerospace starter/generator,” in *2013 International Electric Machines & Drives Conference (pp. 196-203). IEEE,* Chicago, IL, USA, 2013, May.

[72] Z. Chen, H. Wang and Y. Yan, “A doubly salient starter/generator with two-section twisted-rotor structure for potential future aerospace application,” *IEEE Transactions on industrial electronics,* vol. 59, no. 9, pp. 3588-3595, 2011.

[73] M. E. Elbuluk and M. D. Kankam, “Potential starter/generator technologies for future aerospace applications,” *IEEE Aerospace and Electronic Systems Magazine,* vol. 12, no. 5, pp. 24-3, 1997.

[74] “AC Motors: General Principles of Operation (Motors And Drives),” [Online]. Available: http://what-when-how.com/motors-and-drives/ac-motors-general-principles-of-operation-motors-and-drives/. [Accessed 8 July 2023].

[75] C. Terron-Santiago, J. Martinez-Roman, R. Puche-Panadero and A. Sapena-Bano, “A review of techniques used for induction machine fault modelling,” *Sensors,* vol. 21, no. 14, 4855, pp. 1-18, 2021.

[76] R. Anbarasu, R. K. Gupta, N. D. Sharma, G. Gauthaman, A. K. Wankhede, P. H. Chavda, J. Nataraj and B. Bhattacharjee, “Design and experimental investigation of

high speed squirrel cage induction motor," in *Proceedings of International Conference on Power Electronics, Drives and Energy Systems for Industrial Growth (Vol. 2, pp. 920-926). IEEE,* 1996, January.

[77] T. Finken, M. Felden and K. Hameyer, "Comparison and design of different electrical machine types regarding their applicability in hybrid electrical vehicles," in *2008 18th International Conference on Electrical Machines (pp. 1-5). IEEE,* 2008, September.

[78] K. Vijayakumar, R. Karthikeyan, S. Paramasivam, R. Arumugam and K. N. Srinivas, "Switched reluctance motor modeling, design, simulation, and analysis: a comprehensive review," *IEEE Transactions on Magnetics,* vol. 44, no. 12, pp. 4605-4617, 2008.

[79] A. Griffo, D. Drury, T. Sawata and P. H. Mellor, "Sensorless starting of a wound-field synchronous starter/generator for aerospace applications," *IEEE Transactions on Industrial Electronics,* vol. 59, no. 9, pp. 3579-3587, 2011.

[80] C. Li, T. Yang, P. Kulsangcharoen, G. L. Calzo, S. Bozhko, C. Gerada and P. Wheeler, "A modified neutral point balancing space vector modulation for three-level neutral point clamped converters in high-speed drives," *EEE Transactions on Industrial Electronics,* vol. 66, no. 2, pp. 910-921, February 2019.

[81] S. Bozhko, M. Rashed, C. I. Hill, S. S. Yeoh and T. Yang, "Flux-weakening control of electric starter–generator based on permanent-magnet machine," *IEEE Transactions on Transportation Electrification,* vol. 3, no. 4, pp. 864-877, December 2017.

[82] A. Eid, M. Abdel-Salam, H. El-Kishky and T. El-Mohandes, "Simulation and transient analysis of conventional and advanced aircraft electric power systems with harmonics mitigation," *Electric Power Systems Research,* vol. 79, no. 4, pp. 660-668, 2009.

[83] R. Abdel-Fadil, A. Eid and M. Abdel-Salam, "Electrical distribution power systems of modern civil aircrafts," in *2nd International Conference on Energy Systems and Technologies (pp. 201-210),* Cairo, Egypt, 2013, February.

References

[84] A. Eid, H. El-Kishky, M. Abdel-Salam and T. El-Mohandes, “Constant frequency aircraft electric power systems with harmonic reduction,” in *2008 34th Annual Conference of IEEE Industrial Electronics (pp. 623-628). IEEE*, 2008, November.

[85] J. Chen, C. Wang and J. Chen, “Investigation on the selection of electric power system architecture for future more electric aircraft,” *IEEE Transactions on Transportation Electrification*, vol. 4, no. 2, pp. 563-576, 2018.

[86] T. Jomier, More open electrical technologies, EU FP6 Project, 2009.

[87] S. Bozhko, “Modern trends in aircraft electric power systems and in onboard electric power generation,” in *IQPC Conference More Electric Aicraft* , Seattle, USA, 2017.

[88] T. Wu, S. V. Bozhko and G. M. Asher, “High speed modeling approach of aircraft electrical power systems under both normal and abnormal scenarios,” in *2010 IEEE International Symposium on Industrial Electronics, pp. 870-877*, Bari, Italy, July 2010.

[89] G. Buticchi, S. Bozhko, M. Liserre, P. Wheeler and K. Al-Haddad, “On-board microgrids for the more electric aircraft—Technology review,” *IEEE Transactions on Industrial Electronics*, vol. 66, no. 7, pp. 5588-5599, July 2019.

[90] C. Spagnolo, S. Sumsurooah, C. I. Hill and S. Bozhko, “Finite state machine control for aircraft electrical distribution system,” *The Journal of Engineering*, vol. 2018, no. 13, pp. 506-511, 2018.

[91] Y. Zhang, Y. Yu, R. Su and J. Chen, “Power scheduling in more electric aircraft based on an optimal adaptive control strategy,” *IEEE Transactions on Industrial Electronics*, vol. 67, no. 12, pp. 10911-10921, December 2020.

[92] F. Gao, S. Bozhko, A. Costabeber, G. Asher and P. Wheeler, “Control design and voltage stability analysis of a droop-controlled electrical power system for more electric aircraft,” *IEEE Transactions on Industrial Electronics*, vol. 64, no. 12, pp. 9271-9281, December 2017.

References

[93] Y. Zhang, G. O. H. Peng, J. K. Banda, S. Dasgupta, M. Husband, R. Su and C. Wen, "An energy efficient power management solution for a fault-tolerant more electric engine/aircraft," *IEEE Transactions on Industrial Electronics,* vol. 66, no. 7, pp. 5663-5675, July 2019.

[94] F. Gao, S. Bozhko, G. Asher, P. Wheeler and C. Patel, "An improved voltage compensation approach in a droop-controlled DC power system for the more electric aircraft," *IEEE Transactions on Power Electronics,* vol. 31, no. 10, pp. 7369-7383, October 2016.

[95] M. K. AL-Nussairi, R. Bayindir, S. Padmanaban, L. Mihet-Popa and P. Siano, "Constant Power Loads (CPL) with Microgrids: Problem Definition, Stability Analysis and Compensation Techniques," *Energies,* vol. 10, no. 10:1656, pp. 1-20, 2017.

[96] S. Chapman, Electric machinery fundamentals, Tata McGraw-Hill Education, 2005.

[97] S. S. Yeoh, F. Gao, S. Bozhko and G. Asher, "Control design for PMM-based starter generator system for More Electric Aircraft," in *2014 16th European Conference on Power Electronics and Applications, pp. 1-10,* 2014.

[98] T. M. Jahns, "Flux-weakening regime operation of an interior permanent-magnet synchronous motor drive.," *IEEE Transactions on Industry Applications,* Vols. IA-23, no. 4, pp. 681-689, 1987.

[99] C. Wang, H. Hussaini, F. Gao and T. Yang, "Modeling and control of DC grids within more-electric aircraft," in *Modeling, Operation, and Analysis of DC Grids*, Academic Press, 2021, pp. 337-366.

[100] T. Dragičević, X. Lu, J. C. Vasquez and J. M. Guerrero, "DC microgrids—Part I: A review of control strategies and stabilization techniques," *IEEE Transactions on power electronics,* vol. 31, no. 7, pp. 4876-4891, 2015.

[101] X. Sun, Y. S. Lee and D. Xu, "Modeling, analysis, and implementation of parallel multi-inverter systems with instantaneous average-current-sharing scheme," *IEEE Transactions on Power Electronics,* vol. 18, no. 3, pp. 844-856, May 2003.

[102] A. P. Martins, A. S. Carvalho and A. S. Araujo, "Design and implementation of a current controller for the parallel operation of standard UPSs," in *Proceedings of IECON'95-21st Annual Conference on IEEE Industrial Electronics, Vol. 1, pp. 584-589,* Orlando, FL, USA, November 1995.

[103] G. Byeon, T. Yoon, S. Oh and G. Jang, " Energy management strategy of the DC distribution system in buildings using the EV service model," *IEEE Transactions on Power Electronics,* vol. 28, no. 4, pp. 1544-1554, April 2013.

[104] K. T. Tan, X. Y. Peng, P. L. So, Y. C. Chu and M. Z. Chen, "Centralized control for parallel operation of distributed generation inverters in microgrids," *IEEE Transactions on Smart Grid,* vol. 3, no. 4, pp. 1977-1987, December 2012.

[105] M. Saleh, Y. Esa and A. Mohamed, "Centralized control for DC microgrid using finite state machine," in *2017 IEEE Power & Energy Society Innovative Smart Grid Technologies Conference (ISGT), pp. 1-5,* April 2017.

[106] S. K. Mazumder, M. Tahir and K. Acharya, "Master–slave current-sharing control of a parallel DC–DC converter system over an RF communication interface," *IEEE Transactions on Industrial Electronics,* vol. 55, no. 1, pp. 59-66, 2008.

[107] H. H. C. Iu, V. Pjevalica and B. Robert, "Implementation of a simple rotating master control scheme for parallel converters," in *2004 IEEE 35th Annual Power Electronics Specialists Conference (IEEE Cat. No. 04CH37551) (Vol. 2, pp. 1494-1499),* Aachen, Germany, 2004, June.

[108] S. Pan and P. K. Jain, "A precisely-regulated multiple output forward converter with automatic master-slave control," in *2005 IEEE 36th Power Electronics Specialists Conference (pp. 969-975). IEEE,* Recife, Brazil, 2005, June.

[109] M. S. Mahmoud, Microgrid: advanced control methods and renewable energy system integration, Elsevier, 2016.

[110] L. Meng, Q. Shafiee, G. F. Trecate, H. Karimi, D. Fulwani, X. Lu and J. M. Guerrero, "Review on control of DC microgrids and multiple microgrid clusters," *IEEE Journal of Emerging and Selected Topics in Power Electronics,* vol. 5, no. 3, pp. 928-948, 2017.

[111] J. M. Guerrero, J. C. Vasquez, J. Matas, L. G. De Vicuña and M. Castilla, "Hierarchical control of droop-controlled AC and DC microgrids—A general approach toward standardization," *IEEE Transactions on industrial electronics,* vol. 58, no. 1, pp. 158-172, January 2011.

[112] L. Che and M. Shahidehpour, "DC microgrids: Economic operation and enhancement of resilience by hierarchical control," *IEEE Transactions on Smart Grid,* vol. 5, no. 5, pp. 2517-2526, 2014.

[113] C. Jin, P. Wang, J. Xiao, Y. Tang and F. H. Choo, "Implementation of hierarchical control in DC microgrids," *IEEE transactions on industrial electronics,* vol. 61, no. 8, pp. 4032-4042, August 2014.

[114] B. Wang, M. Sechilariu and F. Locment, "Intelligent DC microgrid with smart grid communications: Control strategy consideration and design," *IEEE transactions on smart grid,* vol. 3, no. 4, pp. 2148-2156, 2012.

[115] Q. Shafiee, T. Dragičević, J. C. Vasquez and J. M. Guerrero, "Hierarchical control for multiple DC-microgrids clusters," *IEEE Transactions on Energy Conversion,* vol. 29, no. 4, pp. 922-933, 2014.

[116] R. Olfati-Saber and R. M. Murray, "Consensus problems in networks of agents with switching topology and time-delays," *IEEE Transactions on automatic control,* vol. 49, no. 9, pp. 1520-1533., 2004.

[117] L. Meng, T. Dragicevic, J. M. Guerrero and J. C. Vasquez, "Dynamic consensus algorithm based distributed global efficiency optimization of a droop controlled DC

microgrid," in *2014 IEEE International Energy Conference (ENERGYCON) (pp. 1276-1283). IEEE,* Cavtat, Croatia, 2014, May.

[118] A. Bidram, A. Davoudi, F. L. Lewis and Z. Qu, "Secondary control of microgrids based on distributed cooperative control of multi-agent systems," *IET Generation, Transmission & Distribution,* vol. 7, no. 8, pp. 822-831, 2013.

[119] V. Nasirian, S. Moayedi, A. Davoudi and F. L. Lewis, "Distributed cooperative control of DC microgrids," *IEEE Transactions on Power Electronics,* vol. 30, no. 4, pp. 2288-2303, April 2015.

[120] T. Dragičević, J. M. Guerrero and C. V. Juan, "A distributed control strategy for coordination of an autonomous LVDC microgrid based on power-line signaling," *IEEE Transactions on Industrial Electronics,* vol. 61, no. 7, pp. 3313-3326, 2013.

[121] H. Han, X. Hou, J. Yang, J. Wu, M. Su and J. M. Guerrero, "Review of power sharing control strategies for islanding operation of AC microgrids," *IEEE Transactions on Smart Grid,* vol. 7, no. 1, pp. 200-215, 2015.

[122] H. Behjati, A. Davoudi and F. Lewis, "Modular DC–DC converters on graphs: Cooperative control," *IEEE Transactions on Power Electronics,* vol. 29, no. 12, pp. 6725-6741, 2014.

[123] Q. Shafiee, J. M. Guerrero and J. C. Vasquez, "Distributed secondary control for islanded microgrids—A novel approach," *IEEE Transactions on power electronics,* vol. 29, no. 2, pp. 1018-1031, Feb. 2014.

[124] A. Bidram, A. Davoudi and F. L. Lewis, "A multiobjective distributed control framework for islanded AC microgrids," *IEEE Transactions on industrial informatics,* vol. 10, no. 3, pp. 1785-1798, 2014.

[125] H. Xin, L. Zhang, Z. Wang, D. Gan and K. P. Wong, "Control of island AC microgrids using a fully distributed approach," *IEEE Transactions on Smart Grid,* vol. 6, no. 2, pp. 943-945, 2014.

[126] M. C. Chandorkar, D. M. Divan and R. Adapa, "Control of parallel connected inverters in standalone AC supply systems," *IEEE Transactions on Industry Applications,* vol. 29, no. 1, pp. 136-143, 1993.

[127] K. Visscher and S. W. H. De Haan, "Virtual synchronous machines (VSG's) for frequency stabilisation in future grids with a significant share of decentralized generation," in *CIRED Seminar 2008: SmartGrids for Distribution*, 2008, June.

[128] F. Gao, Y. Gu, S. Bozhko, G. Asher and P. Wheeler, "Analysis of droop control methods in DC microgrid," in *2014 16th European Conference on Power Electronics and Applications, pp. 1-9*, 2014.

[129] J. W. Kim, H. S. Choi and B. H. Cho, "A novel droop method for converter parallel operation," *IEEE Transactions on Power Electronics,* vol. 17, no. 1, pp. 25-32, 2002.

[130] T. M. Haileselassie and K. Uhlen, "Impact of DC line voltage drops on power flow of MTDC using droop control," *IEEE Transactions on Power Systems,* vol. 27, no. 3, pp. 1441-1449, 2012.

[131] N. R. Chaudhuri and B. Chaudhuri, "Adaptive droop control for effective power sharing in multi-terminal DC (MTDC) grids," *IEEE Transactions on Power Systems,* vol. 28, no. 1, pp. 21-29, 2012.

[132] H. Kakigano, Y. Miura and T. Ise, "Distribution voltage control for DC microgrids using fuzzy control and gain-scheduling technique," *IEEE transactions on power electronics,* vol. 28, no. 5, pp. 2246-2258, May 2013.

[133] S. Zhao, F. Blaabjerg and H. Wang, "An overview of artificial intelligence applications for power electronics," *IEEE Transactions on Power Electronics,* vol. 36, no. 4, pp. 4633 - 4658, 2021.

[134] T. Wu, Z. Wang, B. Ozpineci, M. Chinthavali and S. Campbell, "Automated heatsink optimization for air-cooled power semiconductor modules," *IEEE Transactions on Power Electronics,* vol. 34, no. 6, pp. 5027-5031, 2018.

[135] X. Zhan, W. Wang and H. Chung, "A neural-network-based color control method for multi-color LED systems," *IEEE Transactions on Power Electronics,* vol. 34, no. 8, pp. 7900-7913, 2018.

[136] I. Bandyopadhyay, P. Purkait and C. Koley, "Performance of a classifier based on time-domain features for incipient fault detection in inverter drives," *IEEE Transactions on Industrial Informatics* , vol. 15, no. 1, pp. 3-14, 2018.

[137] G. Bramerdorfer, J. A. Tapia, J. J. Pyrhönen and A. Cavagnino, "Modern electrical machine design optimization: Techniques, trends, and best practices," *IEEE Transactions on Industrial Electronics,* vol. 65, no. 10, pp. 7672-7684, 2018.

[138] M. A. Hassan and M. A. Abido, "Optimal design of microgrids in autonomous and grid-connected modes using particle swarm optimization," *IEEE Transactions on power electronics,* vol. 26, no. 3, pp. 755-769, March 2011.

[139] I. Y. Chung, W. Liu, D. A. Cartes, E. G. Collins and S. I. Moon, "Control methods of inverter-interfaced distributed generators in a microgrid system," *IEEE Transactions on Industry Applications,* vol. 46, no. 3, pp. 1078-1088, 2010.

[140] Z. Peng, J. Wang, D. Bi, Y. Wen, Y. Dai, X. Yin and Z. J. Shen, "Droop Control Strategy Incorporating Coupling Compensation and Virtual Impedance for Microgrid Application," *IEEE Transactions on Energy Conversion,* vol. 34, no. 1, pp. 277-291, March 2019.

[141] A. Maulik and D. Das, "Optimal Operation of Droop-Controlled Islanded Microgrids," *IEEE Transactions on Sustainable Energy,* vol. 9, no. 3, pp. 1337-1348. doi: 10.1109/TSTE.2017.2783356., July 2018.

[142] M. Mokhtar, M. I. Marei and A. A. El-Sattar, "Improved current sharing techniques for DC microgrids," *Electric Power Components and Systems,* vol. 46, no. 7, pp. 757-767, 2018.

[143] A. Abraham and S. Das, Eds., Computational intelligence in power engineering (Vol. 302), Springer, 2010.

[144] Y. Zeng, A. I. Maswood, J. Pou, X. Zhang, Z. Li, C. Sun, S. Mukherjee, A. K. Gupta and J. Dong, "Active Disturbance Rejection Control Using Artificial Neural Network for Dual-Active-Bridge-Based Energy Storage System," *IEEE Journal of Emerging and Selected Topics in Power Electronics*, 2021.

[145] T. Guillod, P. Papamanolis and J. W. Kolar, "Artificial neural network (ANN) based fast and accurate inductor modeling and design," *IEEE Open Journal of Power Electronics,* vol. 1, pp. 284-299., 2020.

[146] M. I. Jordan and T. M. Mitchell, "Machine learning: Trends, perspectives, and prospects," *Science,* vol. 349, no. 6245, pp. 255-260, 2015.

[147] T. Hastie, R. Tibshirani, J. Friedman, T. Hastie, R. Tibshirani and J. Friedman, "Overview of supervised learning. The elements of statistical learning: Data mining, inference, and prediction," in *The Elements of Statistical Learning*, New York, NY, Springer , 2009, pp. 9-41.

[148] G. James, D. Witten, T. Hastie, R. Tibshirani and J. Taylor, "Unsupervised learning," in *An Introduction to Statistical Learning: with Applications in Python*, Cham: Springer International Publishing., 2023, pp. 503-556.

[149] M. A. Wiering and M. Van Otterlo, "Adaptation, learning, and optimization," in *Reinforcement learning*, vol. 12, 2012.

[150] C. Wei, Z. Zhang, W. Qiao and L. Qu, "Reinforcement-learning-based intelligent maximum power point tracking control for wind energy conversion systems," *IEEE Transactions on Industrial Electronics,* vol. 62, no. 10, p. 6360–6370, 2015.

[151] B. K. Bose, "Neural network applications in power electronics and motor drives—An introduction and perspective," *IEEE Transactions on Industrial Electronics*, vol. 54, no. 1, pp. 14-33, 2007.

[152] M. Naguib, P. Kollmeyer and A. Emadi, “Application of Deep Neural Networks for Lithium-Ion Battery Surface Temperature Estimation Under Driving and Fast Charge Conditions,” *IEEE Transactions on Transportation Electrification,* vol. 9, no. 1, pp. 1153 - 1165, March 2023.

[153] J. Zhao and B. K. Bose, “Neural-network-based waveform processing and delayless filtering in power electronics and AC drives,” *IEEE transactions on industrial electronics,* vol. 51, no. 5, pp. 981-991, 2004.

[154] S. K. Mondal, J. O. Pinto and B. K. Bose, “A neural-network-based space-vector PWM controller for a three-level voltage-fed inverter induction motor drive,” *IEEE Transactions on industry applications,* vol. 38, no. 3, pp. 660-669, 2002.

[155] T. Dragičević, P. Wheeler and F. Blaabjerg, “Artificial intelligence aided automated design for reliability of power electronic systems,” *IEEE Transactions on Power Electronics,* vol. 38, no. 4, pp. 7161-7171, August 2019.

[156] A. Keane, A. Forrester and A. Sobester, Engineering design via surrogate modelling: a practical guide, American Institute of Aeronautics and Astronautics, Inc., 2008.

[157] R. A. Ferreira, H. A. Braga, A. A. Ferreira and P. G. Barbosa, “Analysis of voltage droop control method for dc microgrids with Simulink: Modelling and simulation,” in *2012 10th IEEE/IAS International Conference on Industry Applications* , November, 2012.

[158] A. Tah and D. Das, “ An enhanced droop control method for accurate load sharing and voltage improvement of isolated and interconnected DC microgrids,” *IEEE Transactions on Sustainable Energy,* vol. 7, no. 3, pp. 1194-1204, 2016.

[159] J. M. Guerrero, M. Chandorkar, T. L. Lee and P. C. Loh, “Advanced control architectures for intelligent microgrids—Part I: Decentralized and hierarchical control,” *IEEE Transactions on Industrial Electronics,* vol. 60, no. 4, pp. 1254-1262, April 2013.

[160] J. Chen and Q. Song, "A decentralized dynamic load power allocation strategy for fuel cell/supercapacitor-based APU of large more electric vehicles," *IEEE Transactions on Industrial Electronics,* vol. 66, no. 2, pp. 865-875, Feb. 2019.

[161] S. Anand, B. G. Fernandes and J. Guerrero, "Distributed control to ensure proportional load sharing and improve voltage regulation in low-voltage DC microgrids," *IEEE Transactions on Power Electronics,* vol. 28, no. 4, pp. 1900-1913, April 2013.

[162] K. Sun, L. Zhang, Y. Xing and J. M. Guerrero, "A distributed control strategy based on DC bus signaling for modular photovoltaic generation systems with battery energy storage," *IEEE Transactions on Power Electronics,* vol. 26, no. 10, pp. 3032-3045, 2011.

[163] S. Liu, J. Zheng, Z. Li and X. Liu, "A general piecewise droop design method for DC microgrid," *International Journal of Electronics,* vol. 108, no. 5, pp. 758-776, 2021.

[164] T. Hailu and J. A. Ferreira, "Piece-wise linear droop control for load sharing in low voltage DC distribution grid," in *2017 IEEE Southern Power Electronics Conference (SPEC), pp. 1-6,* Puerto Varas, Chile, 2017.

[165] M. Mokhtar, M. I. Marei and A. A. El-Sattar, "An adaptive droop control scheme for DC microgrids integrating sliding mode voltage and current controlled boost converters," *IEEE Transactions on Smart Grid,* vol. 10, no. 2, pp. 1685-1693, March 2019.

[166] Y. Lin and W. Xiao, "Novel piecewise linear formation of droop strategy for DC microgrid," *IEEE Transactions on Smart Grid,* vol. 10, no. 6, pp. 6747-6755, 2019.

[167] V. Nasirian, A. Davoudi, F. L. Lewis and J. M. Guerrero, "Distributed adaptive droop control for DC distribution systems," *IEEE Transactions on Energy Conversion,* vol. 29, no. 4, pp. 944-956, 2014.

References

[168] N. Ghanbari and S. Bhattacharya, “Adaptive droop control method for suppressing circulating currents in dc microgrids,” *IEEE Open Access Journal of Power and Energy,* vol. 7, pp. 100-110, 2020.

[169] W. Jiang, J. Zhao, K. Qu, L. Mao, Y. Zhu and H. Liu, “An Enhanced Drop Control Method for DC Microgrids with Accurate Current Sharing and DC Bus Voltage Restoration,” in *2019 4th International Conference on Intelligent Green Building and Smart Grid (IGBSG),* Hubei, China, 2019.

[170] C. Liu, J. Zhao, S. Wang, W. Lu and K. Qu, “Active identification method for line resistance in DC microgrid based on single pulse injection,” *IEEE Transactions on Power Electronics,* vol. 33, no. 7, pp. 5561-5564, July 2018.

[171] F. Cingoz, A. Elrayyah and Y. Sozer, “Optimized settings of droop parameters using stochastic load modeling for effective DC microgrids operation,” *IEEE Transactions on Industry Applications,* vol. 53, no. 2, pp. 1358-1371, March-April 2017.

[172] M. Novak, T. Dragicevic and F. & Blaabjerg, “Weighting factor design based on Artificial Neural Network for Finite Set MPC operated 3L-NPC converter,” in *2019 IEEE Applied Power Electronics Conference and Exposition (APEC) (pp. 77-82). IEEE,* Anaheim, CA, USA, March 2019.

[173] J. Schmidhuber, “Deep learning in neural networks: An overview,” *Neural networks,* vol. 61, pp. 85-117, 2015.

[174] F. Gao, S. Bozhko, A. Costabeber, C. Patel, P. Wheeler, C. I. Hill and G. Asher, “Comparative stability analysis of droop control approaches in voltage-source-converter-based DC microgrids,” *IEEE Transactions on Power Electronics,* vol. 32, no. 3, pp. 2395 - 2415, March 2017.

[175] F. Cingoz, A. Elrayyah and Y. Sozer, “Optimized droop control parameters for effective load sharing and voltage regulation in DC microgrids,” *Electric Power Components and Systems,* vol. 43, no. 8-10, pp. 879-889, 2015.

[176] Shivam and R. Dahiya, “Distributed control for DC microgrid based on optimized droop parameters,” *IETE journal of research,* vol. 66, no. 2, pp. 192-203, 2018.

[177] A. M. Dissanayake and N. C. Ekneligoda, “Multiobjective optimization of droop-controlled distributed generators in DC microgrids,” *IEEE Transactions on Industrial Informatics,* vol. 16, no. 4, pp. 2423-2435, April 2020.

[178] K. Yu, Q. Ai, S. Wang, J. Ni and T. Lv, “Analysis and optimization of droop controller for microgrid system based on small-signal dynamic model,” *IEEE Transactions on Smart Grid,* vol. 7, no. 2, pp. 695-705. doi:10.1109/TSG.2015.2501316, March 2016.

[179] V. V. Thanh and W. Su, “Improving current sharing and voltage regulation for DC microgrids: A decentralized demand response approach,” *IEEE Transactions on Smart Grid.,* 2022.

[180] L. Zadeh, “Optimality and non-scalar-valued performance criteria,” *IEEE transactions on Automatic Control ,* vol. 8, no. 1, pp. 59-60, 1963.

[181] K. Deb, Multi-objective optimisation using evolutionary algorithms: an introduction. In Multi-objective evolutionary optimisation for product design and manufacturing, London: Springer, 2011.

[182] P. Zanchetta, “Heuristic multi-objective optimization for cost function weights selection in finite states model predictive control,” in *2011 Workshop on Predictive Control of Electrical Drives and Power Electronics, pp. 70-75*, 2011.

[183] X. Wang, Y. Gao, J. Atkin and S. Bozhko, “Neural Network based Weighting Factor Selection of MPC for Optimal Battery and Load Management in MEA,” in *2020 23rd International Conference on Electrical Machines and Systems (ICEMS) (pp. 1763-1768),* Hamamatsu, Japan, 2020, November.

[184] Y. Gao, T. Yang, S. Bozhko, P. Wheeler and T. Dragičević, “Filter design and optimization of electromechanical actuation systems using search and surrogate

algorithms for more-electric aircraft applications," *IEEE Transactions on Transportation Electrification,* vol. 6, no. 4, pp. 1434-1447, 2020.

[185] M. Novak, H. Xie, T. Dragicevic, F. Wang, J. Rodriguez and F. Blaabjerg, "Optimal cost function parameter design in predictive torque control (PTC) using artificial neural networks (ANN)," *IEEE Transactions on Industrial Electronics,* vol. 68, no. 8, pp. 7309 - 7319, August 2021.

[186] H. Hussaini, T. Yang, Y. Gao, C. Wang, M. Urrutia and S. Bozhko, "Optimal Droop Control Design Using Artificial Intelligent Techniques for Electric Power Systems of More-Electric Aircraft," *IEEE Transactions on Transportation Electrification,* 2023.

[187] S. Vazquez, D. Marino, E. Zafra, M. Valdes, J. J. Rodriguez-Andina, L. G. Franquelo and M. Manic, "An Artificial Intelligence Approach for Real-Time Tuning of Weighting Factors in FCS-MPC for Power Converters," *IEEE Transactions on Industrial Electronics,* November 2021.

[188] S. Skansi, Introduction to Deep Learning: from logical calculus to artificial intelligence, Springer, 2018.

[189] S. Bozhko, T. Yang, J. M. Le Peuvedic, P. Arumugam, M. Degano, A. La Rocca, Z. Xu, M. Rashed and P. Wheeler, "Development of aircraft electric starter–generator system based on active rectification technology," *IEEE Transactions on Transportation Electrification,* vol. 4, no. 4, pp. 985 - 996, December 2018.

[190] P. R. Bana and M. Amin, "Control for Grid-Connected VSC With Improved Damping Based on Physics-Informed Neural Network," *IEEE Journal of Emerging and Selected Topics in Industrial Electronics,* March 2023.

[191] I. Harbi, M. Ahmed, J. Rodriguez, R. Kennel and M. Abdelrahem, "Low-complexity finite set model predictive control for split-capacitor ANPC inverter with different levels modes and online model update," *EEE Journal of Emerging and Selected Topics in Power Electronics,* vol. 11, no. 1, pp. 506-522, Feb. 2023.

References

[192] I. Harbi, M. Ahmed, C. M. Hackl, J. Rodriguez, R. Kennel and M. Abdelrahem, "Low-Complexity Dual-Vector Model Predictive Control for Single-Phase Nine-Level ANPC-Based Converter," *IEEE Transactions on Power Electronics,* vol. 38, no. 3, pp. 2956-2971, March 2023.

[193] A. Nasr, C. Gu, G. Buticchi, S. Bozhko and C. Gerada, " A Low-Complexity Modulated Model Predictive Torque and Flux Control Strategy for PMSM Drives without Weighting Factor," *IEEE Journal of Emerging and Selected Topics in Power Electronics,* February 2022 .

[194] S. Wang, T. Dragicevic, Y. Gao and R. Teodorescu, "Neural network based model predictive controllers for modular multilevel converters," *IEEE Transactions on Energy Conversion,* vol. 36, no. 2, pp. 1562-1571, June 2021.

[195] B. Wang, G. Vakil, Y. Liu, T. Yang, Z. Zhang and C. Gerada, "Optimization and analysis of a high power density and fault tolerant starter–generator for aircraft application," *Energies,* vol. 14, no. 1:113, pp. 1-16, 2021.

[196] "DO-160E Environmental Conditions and Test Procedures for Airborne Equipment," RTCA Standard, 2004.

[197] Y. Han, X. Ning, P. Yang and L. Xu, "Review of power sharing, voltage restoration and stabilization techniques in hierarchical controlled DC microgrids," *IEEE Access,* vol. 7, pp. 149202-149223, 2019.

[198] F. Gao, R. Kang, J. Cao and T. Yang, "Primary and secondary control in DC microgrids: a review," *Journal of Modern Power Systems and Clean Energy,* vol. 7, no. 2, pp. 227-242, 2019.

[199] N. Yang, D. Paire, F. Gao, A. Miraoui and W. Liu, "Compensation of droop control using common load condition in DC microgrids to improve voltage regulation and load sharing," *International Journal of Electrical Power & Energy Systems,* vol. 64, pp. 752-760, 2015.

[200] P. H. Huang, Liu, P. C., W. Xiao and M. S. El Moursi, “A novel droop-based average voltage sharing control strategy for DC microgrids,” *IEEE transactions on Smart Grid,* vol. 6, no. 3, pp. 1096-1106, May 2015.

[201] P. Prabhakaran, Y. Goyal and V. Agarwal, “A novel communication-based average voltage regulation scheme for a droop controlled DC microgrid,” *IEEE Transactions on Smart Grid,* vol. 10, no. 2, pp. 1250-1258, March 2019.

[202] P. Wang, X. Lu, X. Yang, W. Wang and D. Xu, “An improved distributed secondary control method for DC microgrids with enhanced dynamic current sharing performance,” *IEEE Transactions on Power Electronics,* vol. 31, no. 9, pp. 6658-6673, September 2016.

[203] F. Gao, S. Bozhko and P. Wheeler, “An enhanced secondary control approach for voltage restoration in the DC distribution system,” *SAE Technical Paper. No. 2016-01-1985,* 2016.

[204] F. Guo, Q. Xu, C. Wen, L. Wang and P. Wang, “ Distributed secondary control for power allocation and voltage restoration in islanded DC microgrids,” *IEEE Transactions on Sustainable Energy ,* vol. 9, no. 4, pp. 1857-1869, October 2018.

[205] L. Xing, Y. Mishra, F. Guo, P. Lin, Y. Yang, G. Ledwich and Y. C. Tian, “Distributed secondary control for current sharing and voltage restoration in DC microgrid,” *IEEE Transactions on Smart Grid,* vol. 11, no. 3, pp. 2487-2497, May 2020.

[206] N. Mohammed, L. Callegaro, M. Ciobotaru and J. M. Guerrero, “Accurate power sharing for islanded DC microgrids considering mismatched feeder resistances,” *Applied Energy,* vol. 340, no. 121060, 2023.

[207] C. Deng, F. Guo, C. Wen, D. Yue and Y. Wang, “Distributed resilient secondary control for DC microgrids against heterogeneous communication delays and DoS attacks,” *IEEE Transactions on Industrial Electronics,* vol. 69, no. 11, pp. 11560-11568, November 2022.

[208] M. S. Sadabadi, N. Mijatovic and T. Dragičević, "A Robust Cooperative Distributed Secondary Control Strategy for DC Microgrids with Fewer Communication Requirements," *IEEE Transactions on Power Electronics,* 2022.

[209] S. Peyghami, H. Mokhtari, P. C. Loh, P. Davari and F. Blaabjerg, "Distributed primary and secondary power sharing in a droop-controlled LVDC microgrid with merged AC and DC characteristics," *IEEE Transactions on Smart Grid,* vol. 9, no. 3, pp. 2284-2294, May 2018.

[210] S. Peyghami, H. Mokhtari and F. Blaabjerg, "Decentralized load sharing in a low-voltage direct current microgrid with an adaptive droop approach based on a superimposed frequency," *IEEE Journal of Emerging and Selected Topics in Power Electronics,* vol. 5, no. 3, pp. 1205-1215, September 2017.

[211] F. Gao, S. Bozhko, G. Asher, P. Wheeler and C. Patel, "An Improved Voltage Compensation Approach in a Droop-Controlled DC Power System for the More Electric Aircraft," *IEEE Transactions on Power Electronics,* vol. 31, no. 10, pp. 7369 - 7383, 2016.

[212] H. Hussaini, T. Yang, G. Bai, M. Urrutia-Ortiz and S. Bozhko, "Artificial Intelligence-Based Hierarchical Control Design for Current Sharing and Voltage Restoration in DC Microgrid of the More Electric Aircraft," *IEEE Transactions on Transportation Electrification,* 03 July 2023 .

[213] S. Anand, B. G. Fernandes and J. Guerrero, "Distributed control to ensure proportional load sharing and improve voltage regulation in low-voltage DC microgrids," *IEEE transactions on power electronics,* vol. 28, no. 4, pp. 1900-1913, April 2013.

[214] S. Sharma, V. M. Iyer, S. Bhattacharya and K. Zou, "New Mesh Configurations with Decentralized Droop Control Method for DC Microgrids," *IEEE Transactions on Industrial Electronics,* pp. 1 - 10, February 2023.

[215] H. Hussaini, T. Yang, Y. Gao, C. Wang, M. A. Mohamed and S. Bozhko, "Artificial Neural Network Aided Cable Resistance Estimation in Droop-Controlled Islanded DC

Microgrids," in *IECON 2021–47th Annual Conference of the IEEE Industrial Electronics Society (pp. 1-7)*, 2021, October.

[216] H. Hussaini, T. Yang, Y. Gao, C. Wang, T. Dragicevic and S. Bozhko, " Droop Coefficient Design in Droop Control of Power Converters for Improved Load Sharing: An Artificial Neural Network Approach," in *2021 IEEE 30th International Symposium on Industrial Electronics (ISIE) (pp. 1-6). IEEE.*, June, 2021.

[217] J. C. Vasquez, J. M. Guerrero, A. Luna, P. Rodríguez and R. Teodorescu, "Adaptive droop control applied to voltage-source inverters operating in grid-connected and islanded modes," *IEEE transactions on industrial electronics,* vol. 56, no. 10, pp. 4088-4096, October 2009.

[218] P. M. Le, D. V. D. Hoang, H. T. X. Pham and H. M. Nguyen, "New adaptive droop control with combined line impedance estimation method for parallel inverters," *Science and Technology Development Journal,* vol. 19, no. 4, pp. 45-64, 2016.

[219] N. Mohammed and M. Ciobotaru, "Adaptive Power Control Strategy for Smart Droop-based Grid-connected Inverters," *IEEE Transactions on Smart Grid*, 2022.

[220] N. Mohammed, A. Lashab, M. Ciobotaru and J. M. Guerrero, "Accurate reactive power sharing strategy for droop-based islanded AC microgrids," *IEEE Transactions on Industrial Electronics,* vol. 70, no. 3, pp. 2696-2707, March 2023.

[221] S. Liu, Y. Li, J. Xiang and F. Ji, "Islanding detection method based on system identification," *IET Power Electronics,* vol. 9, no. 10, pp. 2095-2102, 2016.

[222] A. Vijayakumari, A. T. Devarajan and N. Devarajan, "Decoupled control of grid connected inverter with dynamic online grid impedance measurements for micro grid applications," *International Journal of Electrical Power & Energy Systems,* vol. 68, pp. 1-14, 2015.

References

[223] M. Zhang, Q. Xu and X. Wang, "Physics-Informed Neural Network Based Online Impedance Identification of Voltage Source Converters," *IEEE Transactions on Industrial Electronics,* vol. 70, no. 4, pp. 3717-3728, April 2023.

[224] M. Ciobotaru, V. Agelidis and R. Teodorescu, "Line impedance estimation using model based identification technique," in *2011 14th European Conference on Power Electronics and Applications (pp. 1-9). IEEE,* August 2011.

[225] M. K. De Meerendre, E. Prieto-Araujo, K. H. Ahmed, O. X. L. Gomis-Bellmunt and A. Egea-Alvarez, "Review of local network impedance estimation techniques," *IEEE access,* vol. 8, pp. 213647-213661, November 2020.

[226] K. Wang, Y. Yang, M. Fan, Y. Tang, H. Li, R. Chen, J. Hu, W. Zeng and J. Rodriguez, "Grid Impedance Detection Based on Complex Coefficient Filter and Full-order Capacitor Current Observer for Three-phase Grid-connected Inverters," *IEEE Transactions on Power Electronics,* vol. 38, no. 2, pp. 2408 - 2420, October 2022 .

[227] S. Cobreces, P. Rodriguez, D. Pizarro, F. J. Rodriguez and E. J. Bueno, "Complex-space recursive least squares power system identification," in *2007 IEEE Power Electronics Specialists Conference, pp. 2478-2484,* 2007.

[228] N. Hoffmann and F. W. Fuchs, "Minimal invasive equivalent grid impedance estimation in inductive–resistive power networks using extended Kalman filter," *IEEE Transactions on Power Electronics,* vol. 29, no. 2, pp. 631-641, February 2014.

[229] N. Mohammed, L. Callegaro, M. Ciobotaru and J. M. Guerrero, "Accurate power sharing for islanded DC microgrids considering mismatched feeder resistances," *Applied Energy,* vol. 340, no. 121060, pp. 1-11, 2023.

[230] M. Ciobotaru, R. Teodorescu and F. Blaabjerg, "On-line grid impedance estimation based on harmonic injection for grid-connected PV inverter," in *2007 IEEE international symposium on industrial electronics, pp. 2437-2442,* June 2007.

[231] R. A. Fantino, C. A. Busada and J. A. Solsona, “Grid Impedance Estimation by Measuring Only the Current Injected to the Grid by a VSI With LCL Filter,” *IEEE Transactions on Industrial Electronics,* vol. 68, no. 3, pp. 1841-1850, March 2021.

[232] M. Ciobotaru, R. Teodorescu, P. Rodriguez, A. Timbus and F. Blaabjerg, “Online grid impedance estimation for single-phase grid-connected systems using PQ variations,” in *2007 IEEE Power Electronics Specialists Conference, pp. 2306-2312,* June 2007.

[233] M. M. Mardani, R. D. Lazar, N. Mijatovic and T. Dragičević, “ Artificial Neural Network Based Constrained Predictive Real-Time Parameter Adaptation Controller for Grid-Tied VSCs,” *IEEE Journal of Emerging and Selected Topics in Power Electronics,* vol. 11, no. 2, pp. 1507 - 1517, April 2023.

[234] H. Hussaini, T. Yang, M. A. Mohamed, G. Bai, Y. Gao, Y. Chen and S. Bozhko, “Accurate Line Resistance Estimation in a Multi-source Electrical Power System of the More Electric Aircraft: An Intelligent and Data-Driven Approach,” in *2022 IEEE Transportation Electrification Conference & Expo (ITEC), pp. 1254-1258,* Anaheim, CA, USA, June, 2022.

[235] S. Sharma, V. M. Iyer, P. P. Das and S. Bhattacharya, “A modified droop control algorithm for dc microgrids to achieve accurate current sharing and improved voltage regulation,” in *2021 IEEE Applied Power Electronics Conference and Exposition (APEC), pp. 119-125,* Phoenix, USA, June 2021.

[236] H. Soliman, I. Abdelsalam, H. Wang and F. Blaabjerg, “Artificial neural network based DC-link capacitance estimation in a diode-bridge front-end inverter system,” in *2017 IEEE 3rd International Future Energy Electronics Conference and ECCE Asia (IFEEC 2017-ECCE Asia) (pp. 196-201),* 2017, June.

[237] T. Kamel, Y. Biletskiy and L. Chang, “ Capacitor aging detection for the DC filters in the power electronic converters using ANFIS algorithm,” in *2015 IEEE 28th Canadian Conference on Electrical and Computer Engineering (CCECE) (pp. 663-668),* 2015, May.

[238] H. Soliman, P. Davari, H. Wang and F. Blaabjerg, "Capacitance estimation algorithm based on DC-link voltage harmonics using artificial neural network in three-phase motor drive systems," in *2017 IEEE Energy Conversion Congress and Exposition (ECCE) (pp. 5795-5802)*, 2017, October.

[239] H. Soliman, H. Wang and F. Blaabjerg, "A review of the condition monitoring of capacitors in power electronic converters," *IEEE Transactions on Industry Applications*, vol. 52, no. 6, pp. 4976-4989, 2016.

[240] H. Hussaini, T. Yang, Y. Gao, C. Wang, M. A. A. Mohamed and S. Bozhko, "Artificial Neural Network Aided Cable Resistance Estimation in Droop-Controlled Islanded DC Microgrids," in *IECON 2021–47th Annual Conference of the IEEE Industrial Electronics Society*, 2021, October.

[241] H. Hussaini, T. Yang, C. Wang and S. Bozhko, "An Enhanced and Cost Saving Droop Control Method for Improved Load Sharing for the MEA Application," in *2021 IEEE Transportation Electrification Conference & Expo (ITEC)*, Chicago, USA, 2021.

[242] S. Wang, T. Dragicevic, Y. Gao, S. K. Chaudhary and R. Teodorescu, "Machine learning based operating region extension of modular multilevel converters under unbalanced grid faults," *IEEE Transactions on Industrial Electronics*, vol. 68, no. 5, pp. 4554-4560, May 2021.

[243] T. D. C. Busarello, J. F. Guerreiro, M. G. Simões and J. A. Pomilio, "Hardware-in-the-loop experimental setup of a lcl-filtered grid-connected inverter with digital proportional-resonant current controller," in *2021 IEEE 22nd Workshop on Control and Modelling of Power Electronics (COMPEL), pp. 1-8*, November 2021.

[244] "Typhoon HIL Documentation," [Online]. Available: https://www.typhoon-hil.com/documentation/typhoon-hil-hardware-manual/hil_dsp_180_interface/concepts/overview.html. [Accessed 28 07 2023].

[245] H. Hussaini, T. Yang, Y. Gao, C. Wang, G. Bai and S. Bozhko, "Droop Coefficient Design and Optimization Using Genetic Algorithm-A Case Study of the More Electric

Aircraft DC Microgrid," in *IECON 2022–48th Annual Conference of the IEEE Industrial Electronics Society, pp. 1-6*, October, 2022.

[246] H. Bai, C. Liu, E. Breaz and F. Gao, "Artificial neural network aided real-time simulation of electric traction system," *Energy and AI*, vol. 1, no. 2020: 100010., pp. 1-12, 2020.

[247] I. Harbi, J. Rodriguez, E. Liegmann, H. Makhamreh, M. L. Heldwein, M. Novak, M. Rossi, M. Abdelrahem, M. Trabelsi, M. Ahmed, P. Karamanakos, S. Xu, T. Dragicevic and R. Kennel, " Model Predictive Control of Multilevel Inverters: Challenges, Recent Advances, and Trends," *IEEE Transactions on Power Electronics,* 2023.

[248] M. D. V. Pena, J. J. Rodriguez-Andina and M. Manic, "The internet of things: The role of reconfigurable platforms," *IEEE Industrial Electronics Magazine,* vol. 11, no. 3, pp. 6-19, September 2017.

[249] "Typhoon HIL Documentation," Typhoon HIL Inc., [Online]. Available: https://www.typhoon-hil.com/documentation/typhoon-hil-application-notes/References/terrestrial_microgrid_%28switching%29.html. [Accessed 15 7 2023].

[250] "Typhoon HIL Documentation," Typhoon HIL Inc., [Online]. Available: https://www.typhoon-hil.com/documentation/typhoon-hil-software-manual/References/fmu_import.html#fmi_import__fig_vns_2fd_zvb. [Accessed 15 07 2023].

[251] H. Zhang, F. Mollet, C. Saudemont and B. Robyns, "Experimental validation of energy storage system management strategies for a local dc distribution system of more electric aircraft," *IEEE Transactions on Industrial Electronics,* vol. 57, no. 12, pp. 3905-3916, 2010.

[252] N. Mohan, Advanced electric drives: analysis, control, and modeling using MATLAB/Simulink, John wiley & sons, 2014.